



Injection de spin dans le germanium : de l'injecteur ferromagnétique métallique à l'injecteur semiconducteur (Ge,Mn)

Abhinav Jain

► To cite this version:

Abhinav Jain. Injection de spin dans le germanium : de l'injecteur ferromagnétique métallique à l'injecteur semiconducteur (Ge,Mn). Autre [cond-mat.other]. Université de Grenoble, 2011. Français. NNT : 2011GRENY049 . tel-00647310

HAL Id: tel-00647310

<https://theses.hal.science/tel-00647310>

Submitted on 1 Dec 2011

HAL is a multi-disciplinary open access archive for the deposit and dissemination of scientific research documents, whether they are published or not. The documents may come from teaching and research institutions in France or abroad, or from public or private research centers.

L'archive ouverte pluridisciplinaire **HAL**, est destinée au dépôt et à la diffusion de documents scientifiques de niveau recherche, publiés ou non, émanant des établissements d'enseignement et de recherche français ou étrangers, des laboratoires publics ou privés.

THÈSE

Pour obtenir le grade de

DOCTEUR DE L'UNIVERSITÉ DE GRENOBLE

Spécialité : **PHYSIQUE/ PHYSIQUE DE MATIERE CONDENSEE
& RAYONNEMENT**

Arrêté ministériel : 7 août 2006

Présentée par

Abhinav JAIN

Thèse dirigée par **Dr. Matthieu JAMET**

préparée au sein de l'**Institut Nanoscience et Cryogenie, CEA-
GRENOBLE**
dans l'**École Doctorale de Physique de Grenoble**

Injection de spin dans le germanium: de l'injecteur ferromagnétique métallique à l'injecteur semiconducteur (Ge,Mn)

Thèse soutenue publiquement le **26 Octobre 2011**,
devant le jury composé de :

Dr. Joel CIBERT

Directeur de Recherche, Institut Néel, CNRS Grenoble (Président)

Dr. Ron JANSEN

Docteur, Spintronics Research Center AIST Tsukuba Japan (Rapporteur)

Dr. Pierre RENUCCI

Maitre de Conférences, INSA Toulouse (Rapporteur)

Dr. Matthieu JAMET

Directeur de Recherche, INAC-SP2M, CEA Grenoble (Directeur)

Dr. Jean-Marie GEORGE

Directeur de Recherche, CNRS Thales, Palaiseau (Examineur)

Dr. Emmanuel AUGENDRE

Docteur-Ingenieur, CEA-LETI Grenoble (Examineur)



Acknowledgements

This thesis work is part of my three years research done with two laboratories of Institute of Nanosciences and Cryogenics (INAC/SP2M) in CEA Grenoble: Nanostructures and Magnetism (NM) group and Silicon Nanoelectronics, Photonics and Structures (SiNaPS) group. I am sincerely thankful to Jean-Michel Gerard, director of the division on Physics of Materials and Microstructures (SP2M) and Emmanuel Hadji, head of the SiNaPs lab to host me as a PhD student. I am thankful to CEA for granting me a CFR funding and giving me an opportunity to work in world-class research facility.

It is a great pleasure for me to express my sincere gratitude and indebtedness to my thesis supervisor Dr. Matthieu Jamet for his invaluable guidance and constant encouragement to complete this work. You are one of the most passionate researcher I have worked with and you are my role model. I learned a lot from you during three years both on scientific and personal level. You were always available for discussions and I am thankful for your patience and high expertise in field of spintronics and nanomagnetism. I have enjoyed working with you.

I am also thankful to my second supervisor Andre Barski who guided me on the aspects of epitaxial growth and structural characterization. It was a great opportunity for me to work with you and learn so many things from you. I still remember the initial days, the first few months of MBE installment, it was very educative. You were always helpful and your valuable guidance has helped me solve some difficult problems in my PhD.

I would also like to express my deep gratitude to the members of my PhD jury : Joel Cibert, Ron Jansen, Pierre Renucci, Jean-Marie George and Emmanuel Augendre who kindly accepted to be respectively president of the jury, referees of this manuscript, and examiner of the PhD defense. I greatly benefited by their constructive comments which helped me improve the manuscript to its current shape.

I would like to thank Porret Clement for giving hands-on training on MBE instrument. You were very helpful and always took interest in my PhD work. We also had some good time outside the lab discussing on all possible topics. I am also thankful to Celine, Ing-Song, Thibaut, Samuel, Eric and Lamis for their help and support in this PhD work.

I gratefully acknowledge the efforts of Stephane Auffret and Vincent Baltz (from Spintec lab) and Celine Portemont and Clarisse Ducruet (from Crocus Technology) for their help in growth of high quality magnetic tunnel junctions.

I would like to convey my special thanks and appreciation to the staff in the technology platform (PTA) especially to Thibaut Haccart for introducing me to this field of fabrication.

I am grateful to Jean-Francois Jacquot for giving me training on SQUID instrument and also Serge Gambarelli, Vincent Maurel, Gerard Desfonds (team of FMR) for their expertise and inputs. Special thanks to Eric Delamadeleine for his efforts and motivation to repair the Silicon electron gun and other technical support.

I am thankful to Pascale Bayle-Guillemaud and Vincent Favre-Nicolin for their help on structural characterization of (Ge,Mn) films. I take opportunity to thank people from NM lab (Laurent, Ariel, Lucien, Cyrille and Alain) and from SiNaPS lab (Pascal, Nicolas and Vincent) who helped me with their expertise during my PhD work.

Concerning the external collaboration, I am thankful to Emmanuel Augendre for providing us GOI Substrates. I would also like to thank the team of CNRS Thales (Jean-Marie George, Henri Jaffres, Jean Christophe and Julien) for their support and expertise in this work.

My special acknowledgments to Carmelo and Cecile, for their indispensable help dealing with travel, administration and bureaucratic matters efficiently during my stay.

Individual acknowledgments are owed to my friends and colleagues at NM and SiNaPS: Irina, Jyo, Damien, Dai, Piotr, Andrei, Thu-nhi, Louis, Amit, Dimitri, Quentin, Guillaume and Claude... for giving such a pleasant time working together.

I am extraordinarily thankful to Pankaj (with whom I shared the apartment), Somani, Sandeep, Nitin, Prem, Veeresh, Parveen and Karthick for creating such a great friendship network together and sharing your thoughts.

Finally, my parents require a special mention for their support, enthusiasm and appreciation towards my pursuit of higher education. Thank you!

Contents

| | | |
|----------|--|-----------|
| 1 | Spintronics | 11 |
| 1.1 | Spintronics in Semiconductors | 12 |
| 1.1.1 | Spin Injection and Detection in Semiconductors | 13 |
| | Solution to conductivity mismatch- Introduction of a tunnel barrier . . . | 16 |
| | Tailored Schottky tunnel barriers | 19 |
| | Oxide tunnel barrier | 22 |
| | Ferromagnetic Semiconductors | 25 |
| 1.1.2 | Spin Relaxation in Semiconductors | 28 |
| | Spin-Orbit Coupling | 29 |
| | Different mechanisms for spin relaxation | 30 |
| 1.1.3 | Manipulation of spin polarization | 32 |
| | Manipulation of spins by external magnetic field | 32 |
| | Manipulation of spins by electric field | 33 |
| 1.2 | Spin injection into Germanium | 34 |
| 1.3 | Conclusion | 35 |
| 2 | Experimental techniques | 37 |
| 2.1 | Molecular Beam Epitaxy | 37 |
| 2.1.1 | Reflection High Energy Electron Diffraction (RHEED) | 39 |
| 2.2 | Transmission Electron Microscopy | 40 |
| 2.3 | Superconducting Quantum Interference Device | 40 |
| 2.4 | Ferromagnetic Resonance | 41 |
| 2.5 | Sputtering | 42 |
| 2.6 | Sample Processing | 43 |
| 2.7 | Cryostat | 44 |
| 3 | Spin Injection in Germanium | 47 |
| 3.1 | Metal-Germanium contact | 47 |
| 3.2 | Spin injection in Germanium using tunnel barrier | 51 |
| 3.2.1 | Literature Review | 51 |
| 3.2.2 | Results and discussion | 52 |
| | Co/FeNi/Al ₂ O ₃ layers for spin injection into Ge | 53 |
| | CoFeB/MgO layers for spin injection into Ge | 66 |
| 3.3 | Discussion | 72 |
| 3.4 | Conclusion | 73 |

| | | |
|----------|--|------------|
| 4 | Towards (Ge,Mn) as a spin injector | 77 |
| 4.1 | Literature Review | 77 |
| 4.2 | Investigation of magnetic anisotropy in (Ge,Mn) nanostructures | 79 |
| 4.2.1 | Superparamagnetism | 82 |
| 4.3 | Results and Discussion | 84 |
| 4.3.1 | Ge ₃ Mn ₅ thin films on Ge(111) | 84 |
| 4.3.2 | Crystalline (Ge,Mn) nanocolumns / Ge(001) | 86 |
| 4.3.3 | Amorphous (Ge,Mn) nanocolumns / Ge(001) | 90 |
| 4.3.4 | Ge ₃ Mn ₅ clusters/Ge(001) | 94 |
| 4.4 | Growth on Germanium-on-insulator substrates | 98 |
| 4.4.1 | Optimization of growth | 99 |
| 4.4.2 | Towards (Ge,Mn) as a spin injector- A concept | 103 |
| 4.5 | Conclusion | 104 |
| A | Appendix | 111 |
| A.1 | Derivation of resonance equation | 111 |
| A.2 | Comment on the FMR measurements | 114 |
| | Bibliography | 117 |

Introduction

The trend in scaling down of silicon (Si)-based conventional complementary metal-oxide-semiconductor (CMOS) transistors has almost reached its ultimate physical limitation, challenging *Moore's Law* which has been valid for almost half a century. This led to exploration of new materials and need for alternative innovative solutions. Spintronics has emerged as one of the most promising alternatives where extra degree of freedom of spin along with the charge can be exploited.

The trigger in spintronics can be attributed to the discovery of giant magneto-resistance (GMR) in metallic layers by A. Fert and P. Grünberg in 1988. Today it has led to unbelievable storage capacity of hard disks and magnetic random access memories (MRAM). However combining both memory and logic on the same device can solve the current issues of high power consumption and slow speeds. A spin transistor proposed by Datta and Das in 1990s has motivated many researchers and tremendous improvements have been done in last decades. The important challenge for such devices had been the creation of a non-equilibrium spin polarization in semiconductors, which is the main theme of this thesis.

In this thesis the motivation and the possible ways to demonstrate spin injection in Germanium are presented. This thesis is divided into five chapters.

The *first* chapter of this thesis gives a quick insight to the field of spintronics. The advantages of using semiconductors for spintronics applications are discussed. The four essential requirements in order to achieve spin-based devices are discussed in detail: spin injection from ferromagnetic source, spin transport in semiconducting channel, spin manipulation and finally the spin detection to determine the output. Different geometries and techniques used in literature for spin injection and detection are discussed.

A brief chapter describing the *experimental techniques* used in this work is then included.

In the first part of my PhD, I was mainly involved in the growth and characterization of epitaxial (Ge,Mn) thin films on Germanium substrate. The films were grown by molecular beam epitaxy and characterized using reflection high-energy electron diffraction (RHEED), transmission electron microscopy (TEM), superconducting quantum interference device (SQUID) and ferromagnetic resonance (FMR). The knowledge of fundamental properties of this material (Ge,Mn): Curie temperature, saturation magnetization, magnetic anisotropy (to control magnetization direction) is a prerequisite to use it in spintronics devices.

The second part of my PhD was focused on achieving spin injection in Ge using tunnel barrier and ferromagnetic metals with the final aim to use (Ge,Mn) films to inject spins in Ge. Before achieving a 'full semiconductor' device GeMn/Ge, one has to investigate basic properties of spins in Ge and analyze the different spin injection mechanisms. Then from the knowledge of basic properties of (Ge,Mn) and of spin injection/relaxation mechanisms (using well known ferromagnetic metals first), we can plan to use GeMn/Ge as a prototype spintronic device.

At the beginning of the *third* chapter, the metal/n-doped Ge contact is discussed and the issue

of Fermi level pinning in Ge is pointed out. The rest of the chapter deals with the results obtained for electrical spin injection and detection in n-Ge using FM/oxide contacts. Germanium-on-insulator (GOI) substrates were used to define the Ge channel and three-terminal geometry was used. The results are divided into two parts: first part dealing with Py/Al₂O₃ devices (low RA) and second part dealing with CoFeB/MgO devices (high RA). Hanle measurements giving unambiguous proof of spin accumulation in Ge are reported. The effect of surface roughness on spin accumulation is also discussed.

In the *fourth* chapter, the motivation of using (Ge,Mn) as a spin injector in Ge is presented. The structural and magnetic properties of (Ge,Mn) thin films grown by MBE are discussed. Different (Ge,Mn) nanostructures have been obtained on bulk Ge by changing the growth conditions. The magnetic anisotropy in these nanostructures has been investigated using complementary techniques: SQUID and FMR. At the end, the successful growth of (Ge,Mn) layers on Germanium-on-insulator (GOI) substrates is shown and the first step towards using (Ge,Mn) as a spin injector is discussed.

Finally, the *conclusion* of the thesis and future scope are discussed.

The operation of current semiconductor devices is based on the motion of charges. The absence or presence of the charges (electrons or holes) leads to the basic functioning of a device. In past decades, there has been tremendous increase in functionality and performance-to-cost ratio of semiconductor devices by downscaling of device dimensions. This trend is referred to as Moore's law and it projects that the number of transistors per unit area will approximately double every 18 months [1]. However in near future, simple reduction of length scale cannot continue indefinitely since existing device architectures as well as the material properties will reach their fundamental limitations. In this situation spintronics offers an opportunity to develop new class of materials which could have significant impact on the future of electronics as we move into the 21st century.

Spintronics is a field based on the manipulation of spin degrees of freedom [2]. It uses the spin angular momentum as the basic functional unit rather than charge. An electron can rotate either clockwise or anticlockwise around its own axis with constant frequency, representing two spin states of spin-up ($+1/2$) and spin-down ($-1/2$) respectively. The two possible spin states represent the '0' and '1' states in logical operations. A two spin channel model was proposed by Mott in 1930s, stating that spin-up and spin-down conduction electrons are two independent families of charge carriers each with its own distinct transport properties [3, 4]. This two-current conduction was then confirmed, quantified and modeled around 1970 [5–7].

The first experiments on spin-dependent electron transport phenomena has been performed by Tedrow and Messervey et al. in the early 70s by studying the magnetoresistance of a ferromagnet/insulator/superconductor (F/I/S) junction [8]. Julliere [9] extended this work to F/I/F junctions leading to discovery of tunneling magnetoresistance (TMR) in this magnetic tunnel junction (MTJ) (Fig. 1.1). In MTJ the insulating layer is thin enough (typically a few nanometers) for electrons to tunnel from one ferromagnet into the other. TMR is a magnetoresistive effect where the resistance of the junction is lower when the moments of the ferromagnetic layers are parallel. Since tunneling is forbidden in classical physics, the TMR is a strictly quantum mechanical phenomenon. With the advancements of nano-fabricating technologies, Magnetic Random Access Memory (MRAM) and reprogrammable magnetic logic devices have been realized based on this effect.

Another great advancement in spintronics was the discovery of giant magnetoresistance (GMR) effect observed independently by the group of Albert Fert [10] and of Peter Grünberg [11]. The GMR is observed in stacks of metallic materials, alternatively magnetic and non-magnetic, as illustrated in Fig. 1.2. There is significant change in the electrical resistance depending on whether the magnetization of adjacent ferromagnetic layers are in a parallel or an antiparallel alignment. The overall resistance can be tuned depending on the relative orientations of the magnetic layers. The first GMR experiments were performed in the current in plane (CIP) geometry. After 1991, experiments in the current perpendicular to the plane of the layers (CPP)

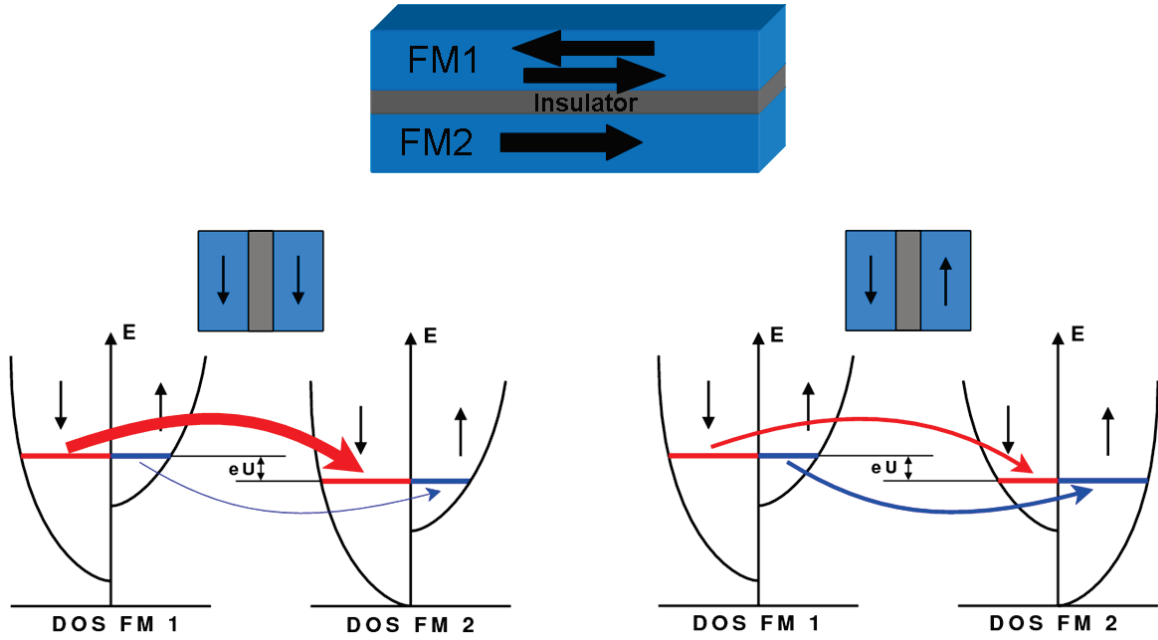


Figure 1.1 : A standard magnetic tunnel junction (MTJ) and illustration of Julliere's model of TMR in MTJ.

geometry have also been performed and have led to the analysis of the physics of spin accumulation. The GMR has important applications, in particular for the read heads of hard disks. A hard disk storing binary information can use the difference in resistance between parallel and antiparallel layer alignments as a method of storing 1s and 0s.

The extension of the spintronics in semiconductors promises many new avenues and opportunities that are simply inaccessible in metallic structures. These concepts are discussed in the section below.

1.1 Spintronics in Semiconductors

For extending the applications of spintronics to microelectronics, researchers are interested in the integration of magnetic materials and semiconductors. This is due to the ability to readily control carrier concentrations and transport characteristics in semiconductors via doping and gate voltages. In 1990s experimental studies in GaAs demonstrated spin diffusion lengths of many microns [12, 13], spin lifetimes of > 100 ns [14, 15] and coherent transport of spin polarized electrons over distances larger than conventional channel lengths. These parameters were many orders of magnitude larger in semiconductors than in metals. This generated excitement for utilizing semiconductors as hosts for spin.

Reduced power consumption is also a major attraction for a spintronic device where the electron spin would transfer and process the information without moving the electron charge. This would lower the power dissipated which is a major issue of conventional electronic semiconductor industry. Thus, it would lead to higher speeds and enhanced functionality of the device. Quantum Computing is another possible application of spintronics. There is an advantage of using (electron or nuclear) spins as quantum bits as they can deliver significant speed-up over classical computers.

A semiconductor-based spintronics technology has at least four essential requirements for implementation [16]:

- efficient electrical injection of spin-polarized carriers from an appropriate contact into the

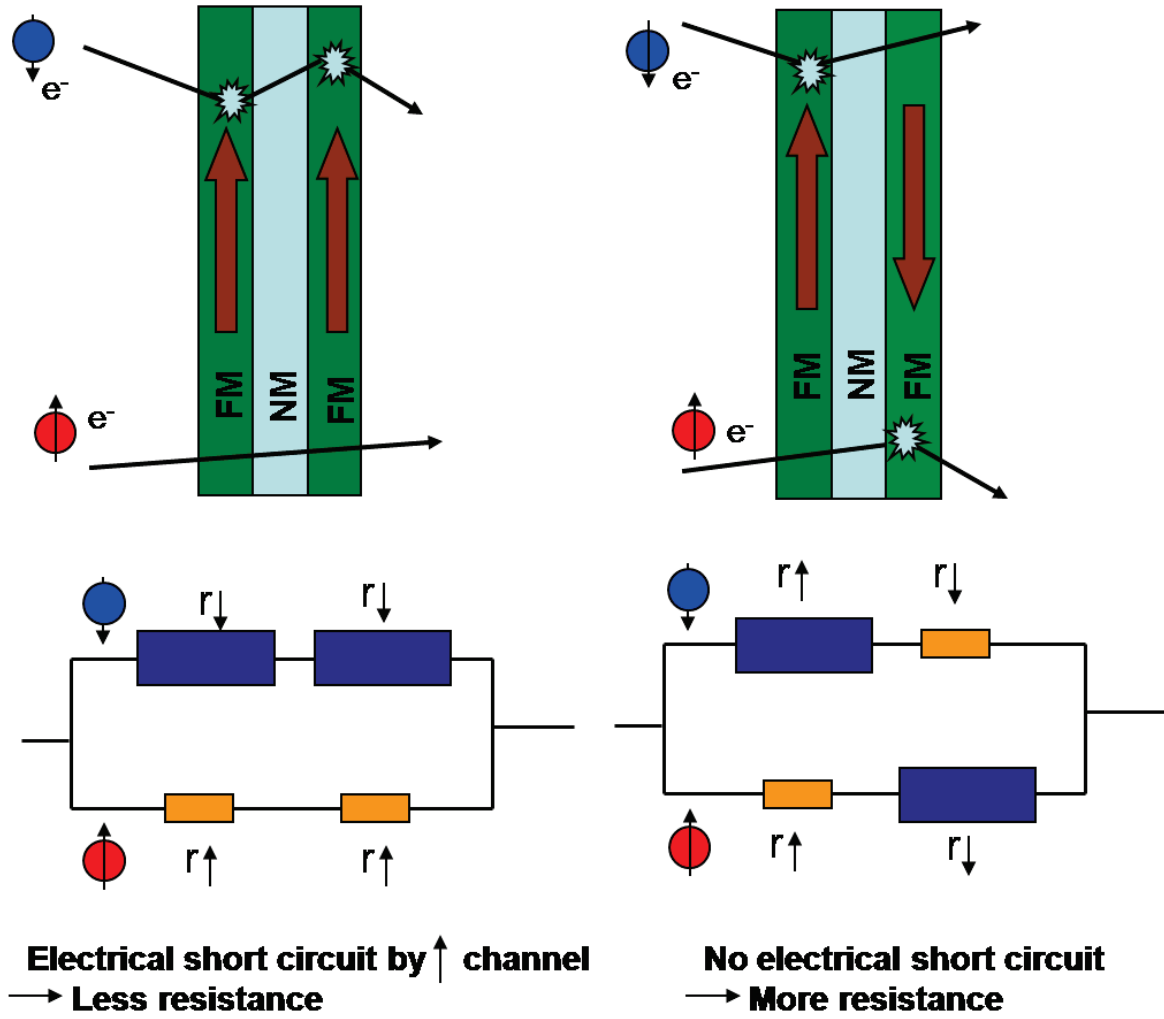


Figure 1.2 : Schematic picture of the GMR mechanism.

device heterostructure,

- understanding spin relaxation and knowledge of spin lifetimes,
- effective control and manipulation of the spin system to implement the desired function, and
- efficient detection of the spin system to determine the output.

1.1.1 Spin Injection and Detection in Semiconductors

In a ferromagnetic metal (FM), the current is spin polarized whereas in non-magnetic material (NM) this is not the case. Spin injection refers to creation of a non-equilibrium spin population in this non-magnetic material. This may be achieved by applying potential difference across FM/NM interface causing spin-polarized electrons from the FM to diffuse into the NM and create a net spin-polarized electron population. Based on this concept Datta and Das [17] in 1990 proposed a first spintronic device concept, a spin transistor, as shown in Fig. 1.3. It consists of two ferromagnetic contacts (FM1 and FM2) on both sides of a 2-dimensional electron gas (2DEG). This 2DEG is formed by a heterojunction between two narrow gap semiconductor materials, here $\text{In}_x\text{Al}_{1-x}\text{As}$ and $\text{In}_x\text{Ga}_{1-x}\text{As}$. The FM1 source acts as a spin polarizer and FM2

as a spin analyzer. There is injection of spin current from FM1 contact into the 2DEG. The length of the channel L , given by the distance between the FM contacts, is less than the spin flip length (l_{sf}) in 2DEG. The spin polarized electrons can enter the analyzer if they both have same spin orientation. By applying gate voltage, perpendicular to the two dimensional electron gas plane, an effective magnetic field is generated by Rashba spin-orbit interaction (for details see section 1.1.3). This effective magnetic field causes the electron spins to precess and the spin direction is no longer parallel to the source and drain magnetizations direction, hence reducing the flow of spin current. This modulation of electric current by the degree of precession of the electron spin can be introduced by the gate field. The researchers perceive this spin field effect transistor to have technological impact for a variety of new applications in digital semiconductor technology.

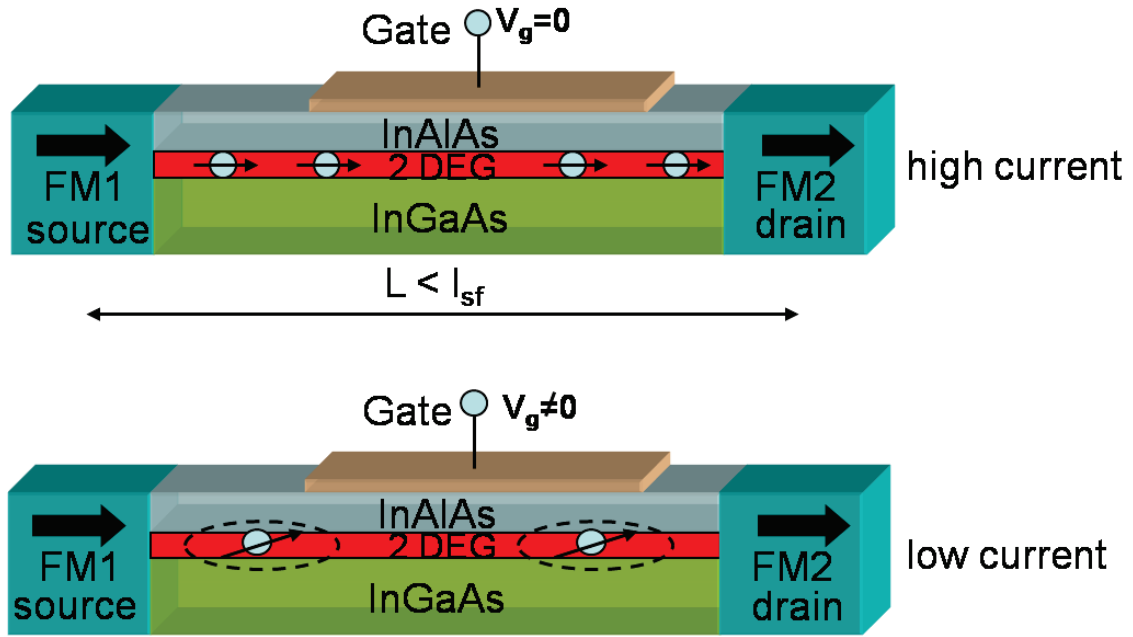


Figure 1.3 : Schematic diagram of SFET proposed by Datta and Das [17].

Hammar et. al. made the first attempt to inject spin current in InAs semiconductor having 2DEG using NiFe electrodes [18]. An ohmic contact was formed between NiFe and InAs due to high density of surface states. By changing the relative magnetizations of two electrodes, 0.8% change in resistance was observed. However interpretation of these results was complicated due to the large spurious effects of electrodes eg. anisotropic magnetoresistance and local hall effects. These results are debatable and were rejected by Van Wees [19] and Monzon et al. [20].

In order to avoid the spurious effects of electrodes and local Hall effect, a non-local geometry was proposed (Fig. 1.4(b)). In this geometry, the current path and the detected voltage path are separated. When current flows from ferromagnetic contact (FM1) into a non-magnetic (NM) material (to contact 1), the spin-up electrons are injected into NM, so that the population of spin-up electrons increase by shifting the electrochemical potential (ECP) by $\Delta\mu/2$, while those of spin-down electrons decrease by shifting the ECP by $\Delta\mu/2$. The total splitting in ECP becomes $\Delta\mu$ which corresponds to spin accumulation in NM (Fig. 1.4(a)). This spin accumulation diffuses over characteristic length l_{sf}^{NM} , the spin diffusion length in non-magnetic material [21]. The second ferromagnet electrode (FM2) is placed such that it is lying within the l_{sf}^{NM} from FM1. When the magnetization of FM2 is parallel to FM1, the ECP of spin-up of FM2 is probed by ECP of spin-up of NM and when they are antiparallel, the spin-down ECP is probed. Therefore, the output voltage (ΔV_{NL}) depends on whether the magnetization of FM2

is parallel or antiparallel to that of FM1. Contact 2 is placed beyond the spin diffusion length l_{sf}^{NM} in the non-magnetic material.

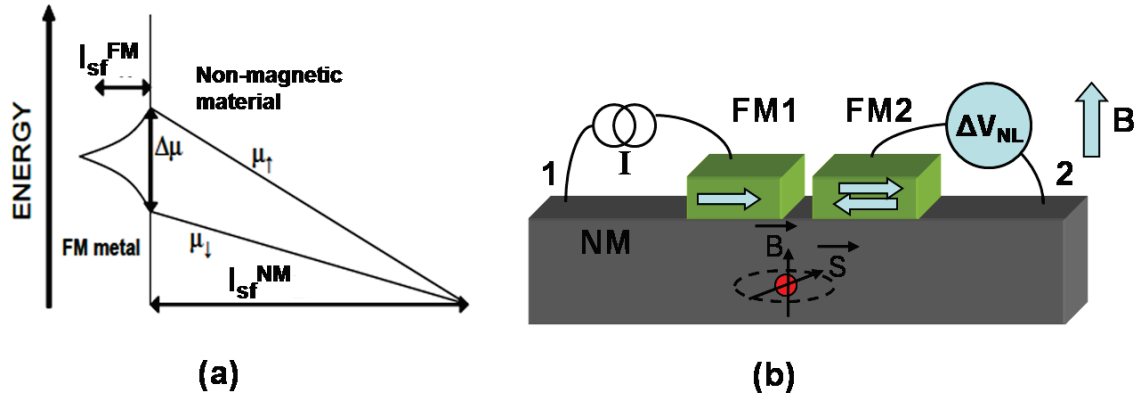


Figure 1.4 : (a) Spatial variation of electrochemical potential (ECP) for spin up and spin down electrons at FM/NM interface. (b) Non-local geometry for the spin valve structure. FM1 and FM2 are two ferromagnetic electrodes and NM is the non-magnetic channel. The spin current passing from FM1 to contact 1 creates splitting of the spin-dependent electrochemical potential near the interface. This spin accumulation diffuses to FM2 if its placed below spin diffusion length of the NM and creates a voltage difference between FM2 and contact 2. By applying transverse magnetic field spin-polarized carriers precess and dephase in the transport channel.

The spin transport in the non-magnetic channel can be confirmed by observing Hanle effect [22] (see section 1.1.3 for details). A small magnetic field perpendicular to the electron spin direction is applied which causes the spin-polarized carriers to precess and dephase in the transport channel. During the time the electrons will travel to FM2, their spins have certain angle. Since ΔV_{NL} is sensitive to the projection of the spins along the FM2 magnetization, it changes as a function of the field. Hence in non-local geometry electrical injection of spin, accumulation of non-equilibrium spin and electrical detection can be observed. Successful attempts have been done in metallic systems using this non-local geometry with demonstration of Hanle effect [23].

However in the case of semiconductors having ohmic contacts with ferromagnetic electrodes, successful spin injection and detection have been difficult. Several attempts were made in non-local geometry with ohmic contacts between ferromagnetic electrodes like Ni,Co and NiFe on InAs semiconductor having 2DEG but no spin injection was observed [24].

It was finally theoretically demonstrated by Schmidt et al. [25] that negligible spin signal is expected for an ohmic contact between a high-conductivity metallic ferromagnet and a low-conductivity non-magnetic semiconductor. The fundamental reason for the suppression in the spin polarization is the *conductivity mismatch*. As shown in Fig. 1.5, the current of electrons is spin polarized on the left in FM and non-polarized far on the right in the semiconductor SC. In between, there must be a transfer of current between one of the spin channel to the other one. As discussed before, there is spin accumulation at the interface. The progressive depolarization of the current is related to the spin flips generated by this spin accumulation. The intermediate level of polarization at the interface is simply related to the proportion of the spin flips on the F and N sides. In case of FM/SC interface, the density-of-states is much higher on the FM side and similar spin-accumulation splittings on both sides correspond to a much higher spin accumulation density in FM. For similar spin relaxation times in FM and SC, this leads to a much higher number of spin flips in FM, so that the depolarization of the electron current occurs in FM before the interface. The same depolarization also occurs if DOS are similar, but the spin lifetime is much shorter in the FM.

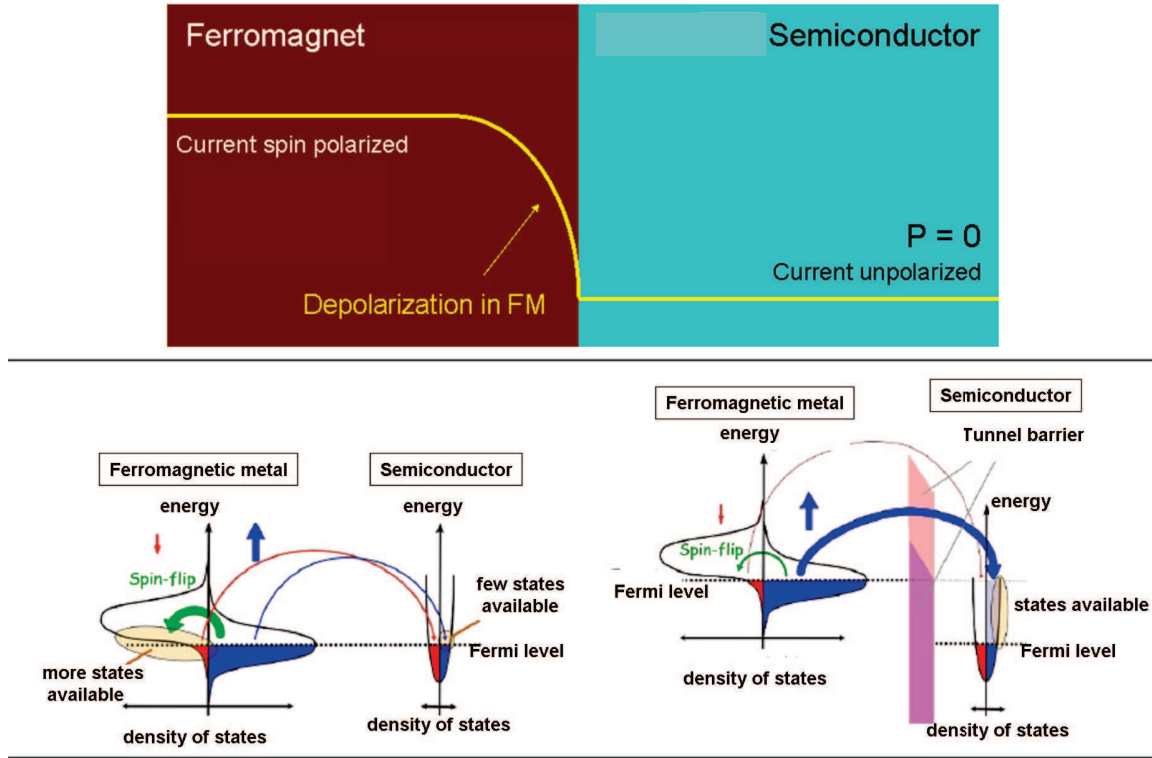


Figure 1.5 : (a) Variation of current spin polarization at FM/SC interface where spin flips on FM side are predominant. (b) Schematic representation of FM/SC contact with and without tunnel barrier. Image taken from ref. [26].

Rashba and Fert proposed that in order to have efficient spin injection from a ferromagnetic metal FM to a semiconductor SC, a spin dependent interface resistance like a tunnel barrier at the FM/SC interfaces can be introduced to promote transfer of one spin type [27, 28]. Also by introducing this tunnel barrier, it will not be energetically favorable for spins to flip back in FM leading to increase in spin accumulation in semiconductor (Fig. 1.5(b)). This is discussed in more detail in section below.

Solution to conductivity mismatch- Introduction of a tunnel barrier

In this section, the spin polarization of current at the metal-semiconductor (FM/NM) interface is calculated and how it changes with introduction of a tunnel barrier. These calculations are taken from ref. 28.

Here it is assumed that FM/NM interface is parallel to the xy plane and a current density J parallel to the z axis. For $z < 0$ there is a ferromagnetic metal. In this ferromagnet, the spin-up and spin-down electrons have different conductivities and their resistivities can be given by: $\rho_{\uparrow(\downarrow)}^{FM} = 2[1 - (+)\beta]\rho^F$. Here β is dimensionless bulk asymmetry parameter given by $\beta = \frac{\rho_{\uparrow}^{FM} - \rho_{\downarrow}^{FM}}{\rho_{\uparrow}^{FM} + \rho_{\downarrow}^{FM}}$, here the spin direction of the electrons $\uparrow(\downarrow)$ refers to the majority (minority) spin direction in a ferromagnetic material and ρ_{\uparrow}^{FM} , ρ_{\downarrow}^{FM} are the resistivities for the spins \uparrow and \downarrow respectively. For $z > 0$, there is a semiconductor with equal conductivities of spin-up and spin-down electrons. Their resistivity is given by $\rho_{\uparrow}^{NM} = \rho_{\downarrow}^{NM} = 2\rho^{NM}$.

Here assuming that the spin-scattering occurs on a much slower timescale than other electron scattering events, there exists two electrochemical potentials (μ_+ , μ_-) which need not be equal. $+$ ($-$) refers to the absolute spin direction of the electrons. If the current flow is one dimensional,

e.g. in the z direction, the electrochemical potentials are connected to the current via the resistivity, the diffusion constant D and the spin-flip time constant τ_{sf} by the following drift-diffusion equations:

$$j = j_+ + j_- \quad (1.1)$$

$$\frac{\partial \mu_{+,-}}{\partial z} = -e\rho_{+,-}j_{+,-} \quad (1.2)$$

$$\frac{\mu_+ - \mu_-}{\tau_{sf}} = \frac{D\partial^2(\mu_+ - \mu_-)}{\partial x^2} \quad (1.3)$$

These equations can be solved by following boundary conditions:

$$\Delta\mu(z = -\infty) = \Delta\mu(z = +\infty) = 0 \quad (1.4)$$

At $z=0$, there exists continuity in j_+ and j_- :

$$\Delta j(z = 0^-) = \Delta j(z = 0^+) \quad (1.5)$$

There is also continuity in electrochemical potentials (μ_+ and μ_-), however there is discontinuity with existence of an interface resistance:

$$\mu_{+(-)}^{NM}(z = 0^+) - \mu_{+(-)}^{FM}(z = 0^-) = er_{+(-)}j_{+(-)}(z = 0) \quad (1.6)$$

where $r_{+(-)} = 2r_b^*[1 - (+)\gamma]$ and r_b^* is the resistance of interface layer and γ is its spin asymmetry coefficient. In absence of an interface resistance $r_{\uparrow(\downarrow)}$ becomes zero.

The solution of the above equations can be written as:

$$\mu_{+(-)}^{FM} = e\rho_{FM}^*(1 - \beta^2)J_z - (+)B[1 - (+)\beta]\exp(\frac{z}{l_{sf}^{FM}}) + C \quad (1.7)$$

$$J_{+(-)}^{FM} = [1 + (-)\beta]\frac{J}{2} - (+)\frac{B}{2e\rho_{FM}}\exp(\frac{z}{l_{sf}^{FM}}) \quad (1.8)$$

$$\mu_{+(-)}^{NM} = e\rho_N J_z - (+)D\exp(-\frac{z}{l_{sf}^{NM}}) \quad (1.9)$$

$$J_{+(-)}^{NM} = \frac{J}{2} + (-)\frac{D}{2e\rho_N}\exp(-\frac{z}{l_{sf}^{NM}}) \quad (1.10)$$

Hence we get,

$$\Delta\mu^{FM} = E\exp(z/l_{sf}^{FM}) \quad (1.11)$$

$$\Delta\mu^{NM} = F\exp(-z/l_{sf}^{NM}) \quad (1.12)$$

here B , C , D , E and F are constants and can be calculated using boundary conditions. So in absence of interface, the spin accumulation ($\mu_+ - \mu_-$) has the same value on both sides of the interface and when one goes away from the interface it decreases exponentially with decay lengths l_{sf}^{FM} on FM side and l_{sf}^{NM} on NM side (Fig. 1.6(a)). The polarization of current injected into the semiconductor is given by:

$$(SP)^{NM}(z) = \frac{j_+^{NM}(z) - j_-^{NM}(z)}{j_+^{NM}(z) + j_-^{NM}(z)} \quad (1.13)$$

$$= \frac{\beta r_{FM} + \gamma r_b^*}{r_{FM} + r_{NM} + r_b^*} \quad (1.14)$$

here r_{FM} and r_{NM} are given by the products of the resistivity by the spin diffusion length for the ferromagnetic and nonmagnetic materials, respectively: $r_{FM} = \rho_{FM}^* \times l_{sf}^{FM}$ and $r_{NM} = \rho_{NM}^* \times l_{sf}^{NM}$. If we consider the case when both FM and NM are metals, without any interface layer, then the equation can be written as:

$$SP = \frac{\beta}{1 + r_{NM}/r_{FM}} \quad (1.15)$$

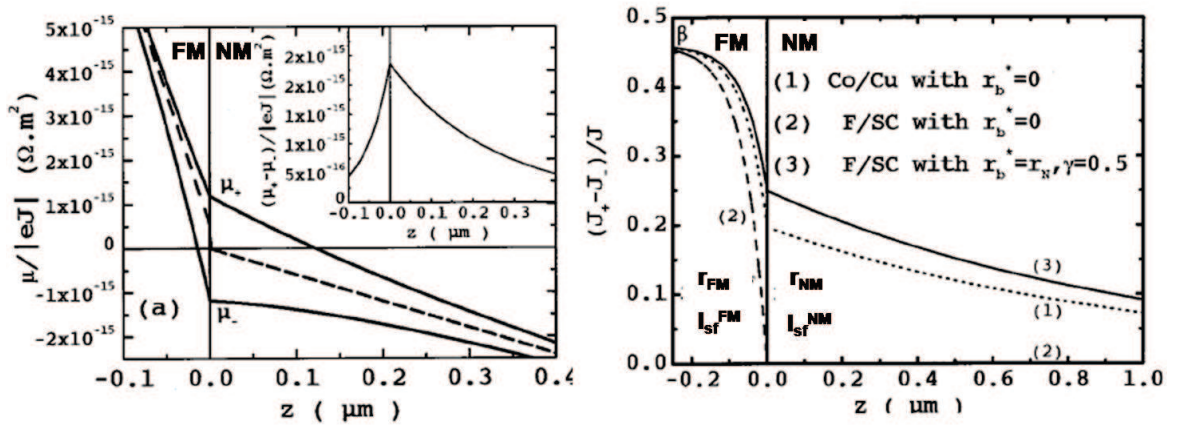


Figure 1.6 : (a) Variation of the electrochemical potentials (μ_+ and μ_-) as a function of z at a Co/Cu interface without interface resistance. The inset shows the variation of the spin accumulation parameter, $\Delta\mu = (\mu_+ - \mu_-)$. (b) Spin polarization of the current as a function of z at the FM/NM interface. Curve 1 is for Co and Cu without interface resistance. Curve 2 is for Co and a semiconductor without interface resistance. Curve 3 is for Co and a semiconductor with a spin dependent resistance (tunnel junction) at the interface. The spin polarization is $\gamma/2$ at the interface for the particular case $r_b^* = r_{NM} \gg r_{FM}$ of curve 3.

Taking example of Co and Cu ($r_{Cu} = 6 \times 10^{-15} \Omega m^2$ and $(r_{Co} = 4.5 \times 10^{-15} \Omega m^2)$, the spin-polarization penetrating the NM becomes $SP = \beta/2.33$, indicating that the current penetrating the non-magnetic metal is only moderately reduced from its value β inside the ferromagnet.

Now if we consider only a FM and a semiconductor, we have six orders of magnitude of difference in the resistance, hence leading to a strong reduction of the spin polarization. Also from calculations it is found that the current spin polarization on either side is proportional to the total numbers of spin flips and these spin flips are proportional to $1/r_{FM}$ and $1/r_{NM}$ in FM and NM respectively. With $r_{FM} \ll r_{NM}$, this means that there are much more spin-flips and a stronger depolarization of the current in FM than in NM. In other words, the current is already completely depolarized when it crosses the interface (Fig. 1.6b).

Inserting a high interface resistance with $r_b^* > r_{NM}$ leads to high spin polarization. For $r_b^* = r_{NM} \gg r_{FM}$, this spin-polarization is given by $\gamma/2$. In the limiting case for $r_b^* \gg r_{NM} > r_{FM}$, the spin polarization at the interface is simply the spin asymmetry coefficient of the interface resistance:

$$SP = \gamma \quad (1.16)$$

The high interface resistance and the high asymmetry coefficient γ can be obtained by introducing ultra-thin insulating layers i.e. tunnel barriers of Al_2O_3 or MgO at the interface. This tunnel barrier brings discontinuity in the $\Delta\mu$, being much higher in NM. This leads to a more balanced number of spin flips in FM and NM, and hence restores the spin polarization at the interface and in the semiconductor.

Tailored Schottky tunnel barriers

Tailored Schottky barriers can act as effective tunnel barriers by heavily doping the semiconductor surface layer. In a normal Schottky barrier between a semiconductor and a FM, e.g. in the case of GaAs with doping of $N_D \approx 10^{17} \text{ cm}^{-3}$ and a FM (like Fe, Co, Ni) there is a barrier height of $0.5 - 0.8 \text{ eV}$ and a depletion width of 90 nm (Fig. 1.7(a)). This large barrier height and high depletion width leads to negligible spin injection in reverse bias condition from FM to semiconductor. However when the depletion region of the Schottky diode is sufficiently narrow, tunneling between the ferromagnetic metal and the semiconductor becomes the dominant transport process. The surface layers of semiconductor can be highly doped by introducing a n^{++} layer between FM and n-GaAs, reducing the depletion width to around $10\text{-}15 \text{ nm}$ which acts as a tunnel barrier for spin injection. This is also known as tailored Schottky contact. The tunnel barrier hence formed circumvents the constraint of mismatched conductivity between the contact and semiconductor.

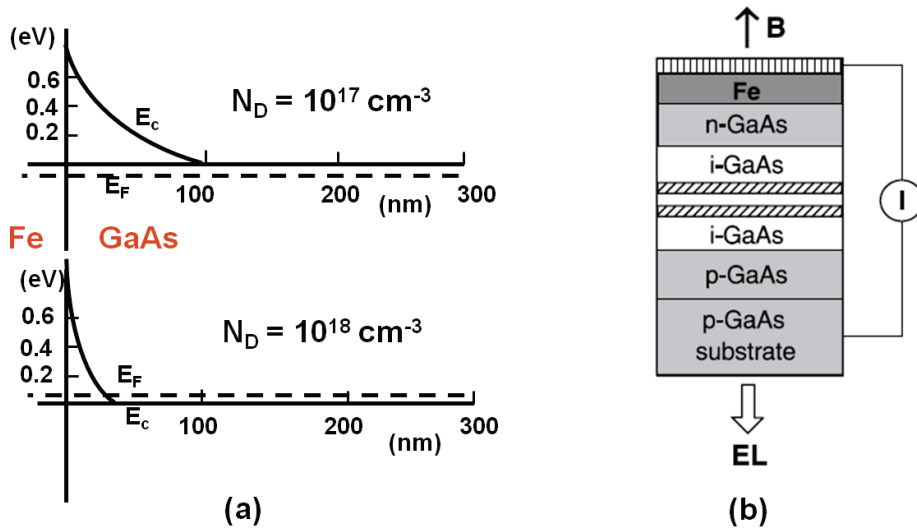


Figure 1.7 : (a) Band diagram of Schottky barriers for Fe/GaAs junctions of different doping densities. As the doping density increases, the depletion layer width becomes thinner and the Fermi level merges with the conduction band. The electrons can tunnel through the thin Schottky barrier. (b) Spin-LED structure used by Zhu et al. [29] consisting of an Fe Schottky contact to a GaAs/InGaAs Quantum well LED detector.

The first evidence of spin injection in GaAs semiconductor from ferromagnetic Fe contact was shown in 2001 by Zhu et al. [29]. They used an Fe film epitaxially grown onto a GaAs/GaInAs LED structure (Fig. 1.7(b)). The spin injection efficiency was investigated by analyzing the

degree of circular polarization of light emitted by the LED. They observed spin injection with circular polarization degrees of about 2% up to room-temperature.

Eventually, in 2003 Hanbicki et al. [30, 31] tailored the Schottky barrier between Fe and AlGaAs by heavily doping the surface layers of semiconductor, steeply increasing the doping level from 10^{16}cm^{-3} to 10^{19}cm^{-3} . The detailed analysis of the transport process over the Fe/GaAs interface showed a single-step tunneling mechanism as dominant conduction mechanism. They used spin-LED structure having a GaAs quantum well and measured the circular polarization of the emitted light. They reported a spin injection polarization of about 30% at room-temperature.

In 2005, Crooker et al. [32] directly imaged electrical spin injection and accumulation in the GaAs channel of lateral spin-transport device having Fe/GaAs tailored Schottky contacts (Fig. 1.8(a)). Scanning Kerr microscopy was used to image the spin transport in the 300 μm long channel region. Images of the steady-state perpendicular component of spin polarization in the n-GaAs channel near the source and drain contacts (Fig. 1.8(b)) show injection and lateral flow of spin-polarized electrons. The perpendicular component is studied because Kerr effect is much higher in polar geometry and this component is present due to precession of spins in perpendicular magnetic field. The injected spins are accumulated near the injector contact and decay with distance due to spin relaxation in GaAs. Also there is spin accumulation at detector contact due to selective extraction of electron spins.

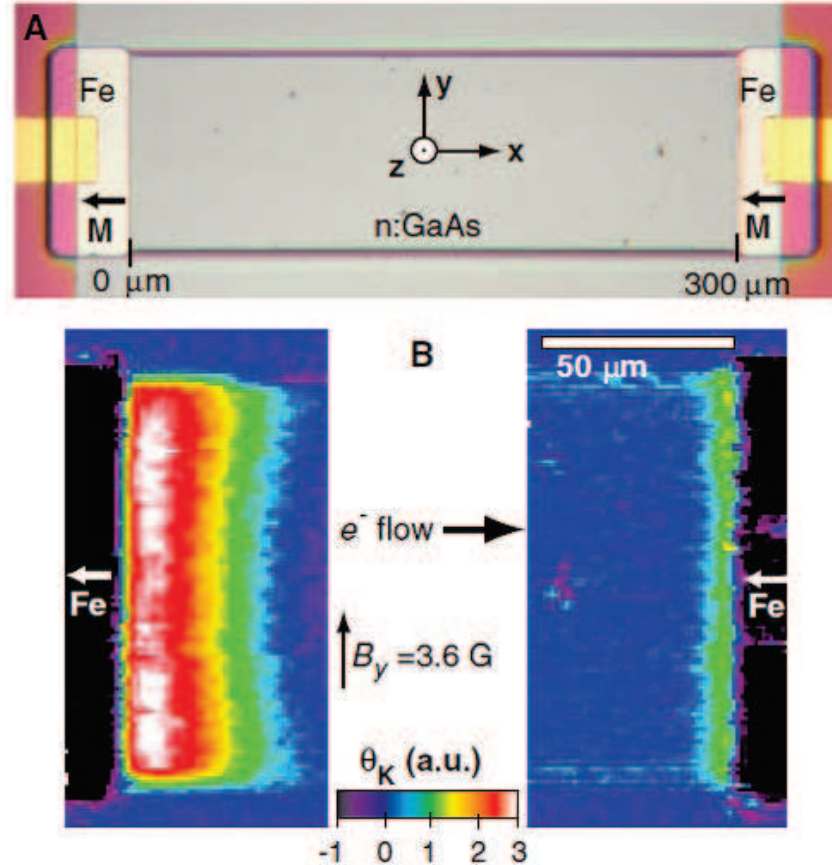


Figure 1.8 : (a) Photo-micrograph of the spin injection device. Spin polarized electrons are injected from Fe into GaAs. (b) Image of the perpendicular component of spin accumulation in a GaAs channel by a scanning Kerr microscope.

Lou et al. in 2006, demonstrated electrical spin injection and detection in Fe/GaAs tailored Schottky contact [33]. The geometry of their device is shown in Fig. 1.9. The n-GaAs channel had a doping level of $3.6 \times 10^{16}\text{cm}^{-3}$ with a surface layer with doping level of $5 \times 10^{18}\text{cm}^{-3}$.

They observed accumulation of spin polarized electrons in forward-biased Fe/GaAs contact. Their results were in agreement with the model of Ciuti et al.[34], where the effective resistance of the Schottky barrier is higher when a spin accumulation in the semiconductor is present. The barrier is less transmissive for the spin state that accumulates in the semiconductor. Moreover, the Hanle effect, modulation of spin current by applying transverse magnetic field, was also shown. The spin signal was observed up to 60 K.

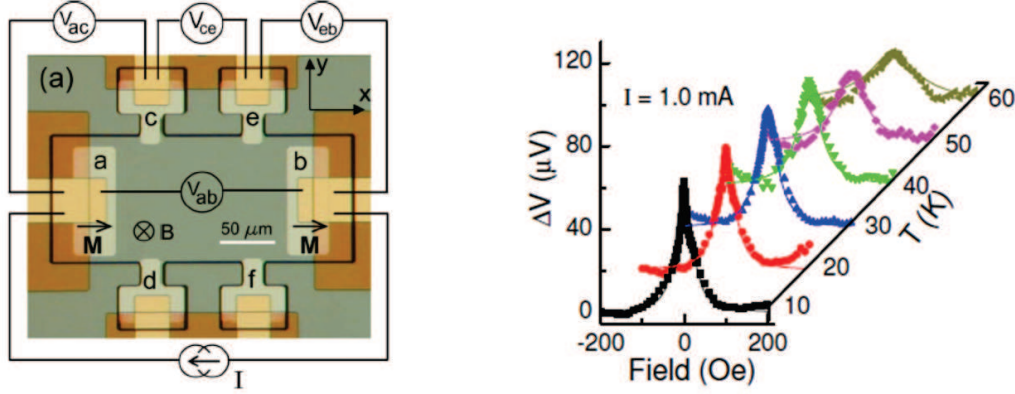


Figure 1.9 : Photomicrograph of the Fe/GaAs device used by Lou [33]. Hanle-effect observed at different temperatures is also shown.

In 2007, Lou et al. demonstrated the first successful electrical detection of spin injection using a non-local geometry in Fe/GaAs contact at 50K [35]. The schematic diagram of their device is shown in Fig. 1.10. Spin-polarized electrons are injected from Fe into the GaAs channel through a tunneling Schottky barrier at contact 3 towards contact 1. This causes spin accumulation in GaAs as the population of spin up and spin down electrons becomes unequal. Although electrons flow from 3 to 1, the non-equilibrium spin polarization in GaAs, represented by purple arrows can diffuse in either direction from the source. The non-local voltage is thus measured between contacts 4 and 5. A change of $16.8\mu\text{V}$ in non-local voltage (V_{4-5}) was observed for parallel and anti-parallel orientations of the two contacts. They also observed the Hanle effect. The difference in two Hanle signal for different orientation of electrodes was found to be $18\mu\text{V}$. This voltage difference is given as:

$$V_{\uparrow\downarrow} - V_{\uparrow\uparrow} = \frac{2\gamma\beta_{Fe}(SP)_{GaAs}E_f}{3e} \quad (1.17)$$

here γ is the spin transmission efficiency of the interface ≈ 0.5 , e the electronic charge, β_{Fe} the spin polarization in Fe ≈ 0.42 , E_f the Fermi energy and $(SP)_{GaAs}$ the spin polarization in GaAs to be calculated. At distance of $12\mu\text{m}$ from the source, the value of SP_{GaAs} was found to be 0.02, hence successfully demonstrating the electrical spin injection and detection using Schottky-tunnel barrier contacts.

However in case of spin injection from Schottky barrier, the quality of interface plays a very important role. Since the ferromagnetic metal and semiconductor are in direct contact, any structural disorder at the interface will drastically reduce the spin polarization. A good chemical stability of the interface is the prerequisite for high efficiency of device. The growth temperature of metal on semiconductor is of crucial importance because magnetic atoms can diffuse into the semiconductor. These magnetic atoms carrying a local magnetic moment scatter the spin in semiconductor channel and hence degrades the spin polarization. The second disadvantage of Schottky barrier for spin injection is that tunneling is not possible on both ends of the device. When the spin injection is carried by reverse biasing the injector FM-SC Schottky contact, the detector end will be automatically forward biased. This would remove the Schottky tunnel

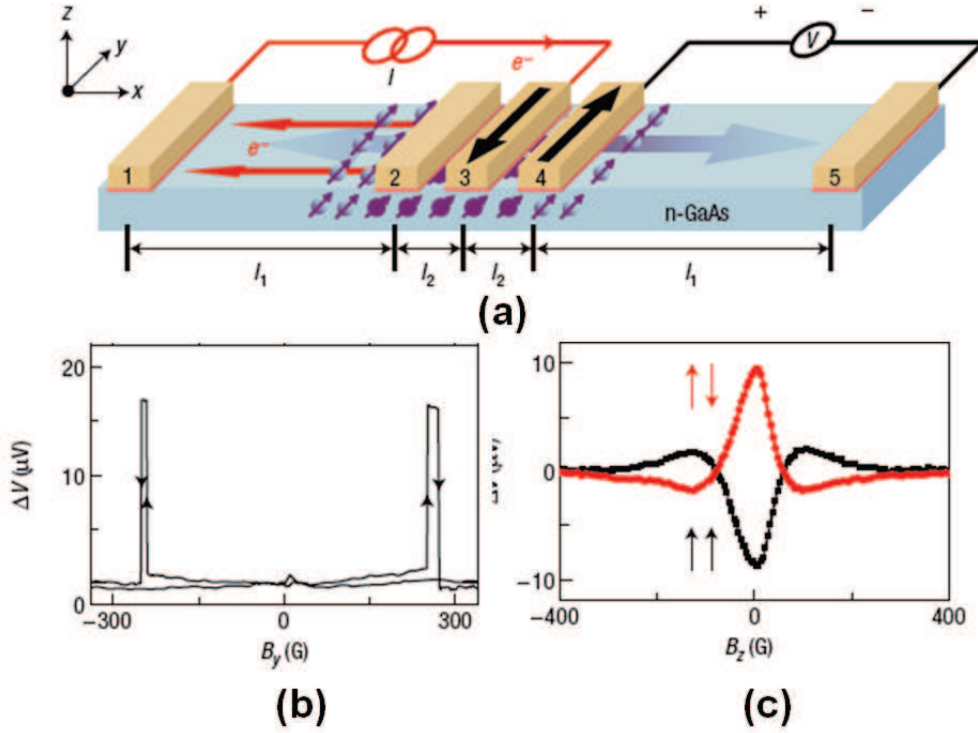


Figure 1.10 : (a) A schematic diagram of the non-local experiment used in ref. 35. The five Fe contacts having in-plane easy axes on GaAs channel. The large arrows indicate the magnetizations of the source and detector. Electrons are injected along the path shown in red. The injected spins (purple) diffuse in either direction from contact 3. The non-local voltage is detected at contact 4. (b) Non-local voltage, V_{4-5} , versus in-plane magnetic field at a current $I_{1-3} = 1$ mA at $T=50$ K. (c) Non-local voltage, V_{4-5} , versus perpendicular magnetic field, B_z , for the same contacts and bias conditions.

barrier and both spin-up and spin-down electrons can enter into the detector without spin filtering. This reduces the spin detection efficiency. Both the above problems can be solved by using a insulating tunnel barrier between FM and a semiconductor for efficient spin injection.

Oxide tunnel barrier

The insertion of insulating tunnel barrier like Al_2O_3 , MgO or SiO_2 between a FM/semiconductor interface can be employed for efficient spin injection. It introduces a spin-dependent drop of the electrochemical potentials at the interface with discontinuous $\Delta\mu$ at the interface and an enhancement of the spin accumulation in semiconductor. It also provides chemical stability at the interface and tunnel barriers are formed at both ends of device (injector and detector).

The maximum tunneling spin polarization which can be obtained in case of FM/ Al_2O_3 is 50%. This is due to the amorphous nature of the layer which causes spin scattering and depolarization of spin [36, 37]. However for crystalline MgO , the tunneling spin polarization of FM/ MgO is predicted to be very high due to coherent tunneling of spin polarized electrons [38]. It has been found that in a structure like $\text{Fe}/\text{MgO}(001)/\text{Fe}$, the tunneling magnetoresistance ratio is in excess of 1000% for an MgO (100) barrier of ≈ 20 atomic planes.

In a device with lateral geometry, it was theoretically explained by Fert et al. that high values of magnetoresistance (MR) for FM/I/NM/I/FM structure can be observed only if the

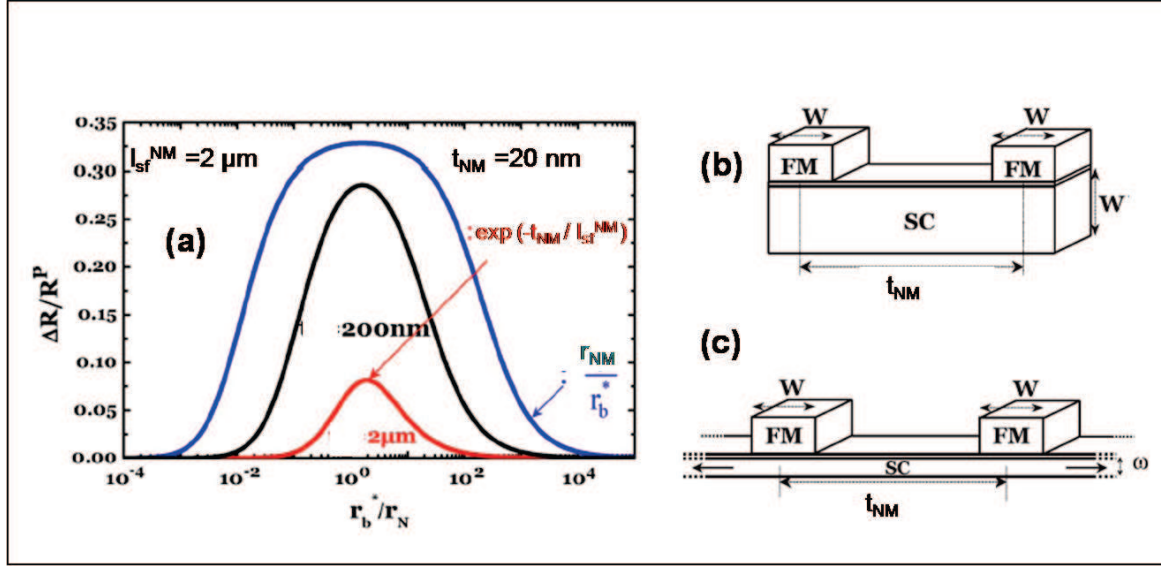


Figure 1.11 : (a) $\Delta R/R_p$ for the lateral geometry given in (b) as a function of r_b^*/r_{NM} for different values of t_{NM}/l_{sf}^{NM} . The calculations were performed for $r_{FM} = 4.5 \times 10^{-15} \Omega m^2 \ll r_{NM} = 4 \times 10^{-9} \Omega m^2$, $\beta = 0.46$, $\gamma = 0.5$. (b) Lateral geometry with the same widths W for the FM and NM channels. (c) Lateral geometry with different widths W and w for FM and NM channels. Also the NM channel extends to infinity at both ends. Images taken from ref. [28]

resistance-area (RA) product of both the FM/I/NM contacts lie in a narrow range [28]. The tunnel barrier resistance r_b^* (the RA product of the tunnel contact) should lie in this optimum range:

$$r_{NM}t_{NM}/l_{sf}^{NM} < r_b^* < r_{NM}l_{sf}^{NM}/t_{NM} \quad (1.18)$$

This condition is true only for $t_{NM} \ll l_{sf}^{NM}$ and the value of MR obtained as a function of r_b^* for different values of t_{NM}/l_{sf}^{NM} is shown in Fig. 1.11(a). This is for lateral geometry shown in Fig. 1.11(b). The lower edge condition $r_{NM}t_{NM}/l_{sf}^{NM} < r_b^*$ is required so that the resistance of the tunnel contact is larger than a critical value to overcome the conductivity mismatch. If $r_b^* \ll r_{NM}t_{NM}/l_{sf}^{NM}$, then the discontinuities in the electrochemical potentials (μ_{\uparrow} and μ_{\downarrow}) introduced by the interface resistances are too small to generate a high enough splitting $\Delta\mu_{NM}$ and polarize the current in semiconductor. The condition corresponding to the upper edge of the window, $r_b^* < r_{NM}l_{sf}^{NM}/t_{NM}$, is the condition for spin conservation, or more precisely, optimal conservation of the spin accumulation occurring in the anti-parallel configuration. If $r_b^* \gg r_{NM}l_{sf}^{NM}/t_{NM}$, the spin accumulation $\Delta\mu_{NM}$ of the AP configuration is completely relaxed by the spin flips in the volume t_{NM} of the semiconductor leading to negligible MR.

In the structure of Fig. 1.11(c), where FM and NM channels have different widths (W and w) and also the NM layer spreads from $-\infty$ to $+\infty$ towards the left and the right in the horizontal plane, the spin accumulation $\Delta\mu$ spreads over l_{sf}^{NM} on both sides of t_{NM} . Consequently, the relaxation in NM is enhanced by the factor $(W/w)(l_{sf}^{NM}/t_{NM})$ and the condition for large MR becomes $r_{NM}(t_{NM}/l_{sf}^{NM})^2(W/w) < r_b^* < r_{NM}(W/w)$ [28]. The correction factor W/w applies only when the lateral dimensions of the contact are smaller than the spin-diffusion length.

For electrical injection and optical detection of spin polarization the lower edge condition should be satisfied. However for both electrical injection and detection both conditions should be satisfied. The tailoring of the RA product of the tunnel contact to satisfy these conditions can be done by either by heavily doping the semiconductor surface layer (to reduce the depletion

zone) or by changing the resistance of tunnel barrier.

The electrical spin injection in semiconductor using Al_2O_3 tunnel barrier was demonstrated in GaAs LED system in vertical geometry by Motsnyi et al. [37]. The detection was done optically by oblique Hanle-effect and measuring the circular polarization of the emitted light. They found spin injection efficiency of more than 9% at 80 K. By replacing the Alumina barrier by crystalline MgO by Jiang et al., the efficiency was improved to 50% [39]. Similarly in Si, successful injection of spin-polarized electrons through an Al_2O_3 tunnel barrier was shown by Jonker et al. [40]. The spins were electrically injected from a thin ferromagnetic Fe film through an Al_2O_3 tunnel barrier into a Si(001) n-i-p doped heterostructure, and the detection was done optically. A spin polarization of 3% was measured optically and by using correction factor a value of 30% was obtained at 5 K.

The first results of electrical spin injection and detection in Si were published by Appelbaum et al. in 2007 [41]. They showed the injection of high energy hot electrons from a source of Aluminium and polarized by CoFe electrode at 85 K (Fig. 1.12). After vertical transport through undoped Si, the spin polarization of the conduction-band electrons was detected electrically by another ferromagnetic NiFe electrode. The proof of spin transport in Si was seen by change in collector current by changing the relative magnetizations of two ferromagnetic electrodes. Also dephasing spin by applying weak transverse magnetic field, precession angles of up to 4π were observed.

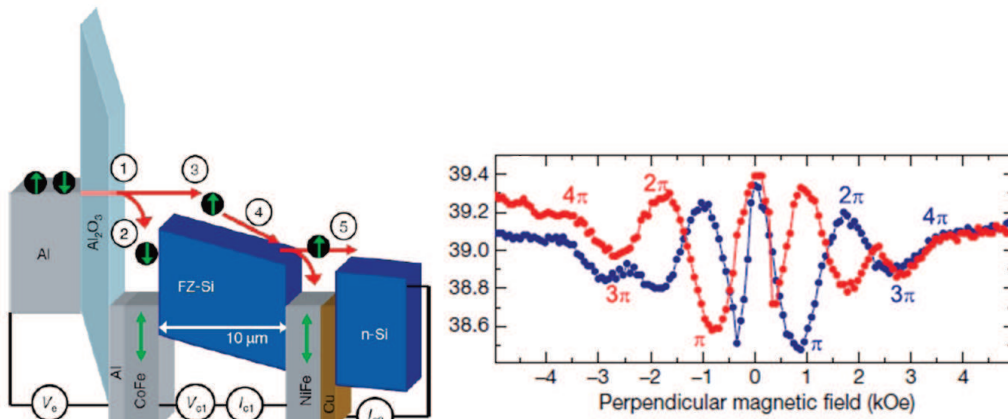


Figure 1.12 : Schematic band diagram of the device used by Appelbaum [41] for transport of hot electrons in Silicon. Precession angles up to 4π were observed by applying perpendicular magnetic field at 85 K.

In the same year, van't Erve et al. demonstrated electrical spin injection and detection in n-Si at 5K using Fe/ Al_2O_3 tunnel barrier contacts in non-local lateral geometry (1.13(a))[42]. They observed change in non-local voltage with change in relative magnetizations of the electrodes. The confirmation of spin transport and a demonstration of spin modulation in the silicon was provided by the Hanle effect. Eventually the first results of spin injection in Silicon at room temperature were published by Dash et al. [43]. They used a three-terminal geometry in which injection and detection is done under the same electrode (1.13(b)). They demonstrated electrical injection of spin polarization into n-type and p-type silicon from a ferromagnetic tunnel contact, spin manipulation using the Hanle effect and the electrical detection of the induced spin accumulation. A spin splitting of 2.9 meV was observed in n-type silicon, corresponding to an estimated electron spin polarization of 4.6%. The spin lifetime greater than 140 ps was extracted for conduction electrons in heavily doped n-type silicon at 300 K and greater than 270 ps for holes in heavily doped p-type silicon at the same temperature. The spin diffusion length greater than 230 nm for electrons and 310 nm for holes in the corresponding materials was found.

(The low values of spin lifetime was found due to artificial broadening of the Hanle curves. The surface roughness at the interface leads to magnetostatic charges which produces local fields and drastically affect spin accumulation [44]. This phenomenon is discussed in detail in chapter 3). Since then, the experimental progress for spin transport in semiconductors has been fascinating by utilizing oxide tunnel barrier and various works have been published.

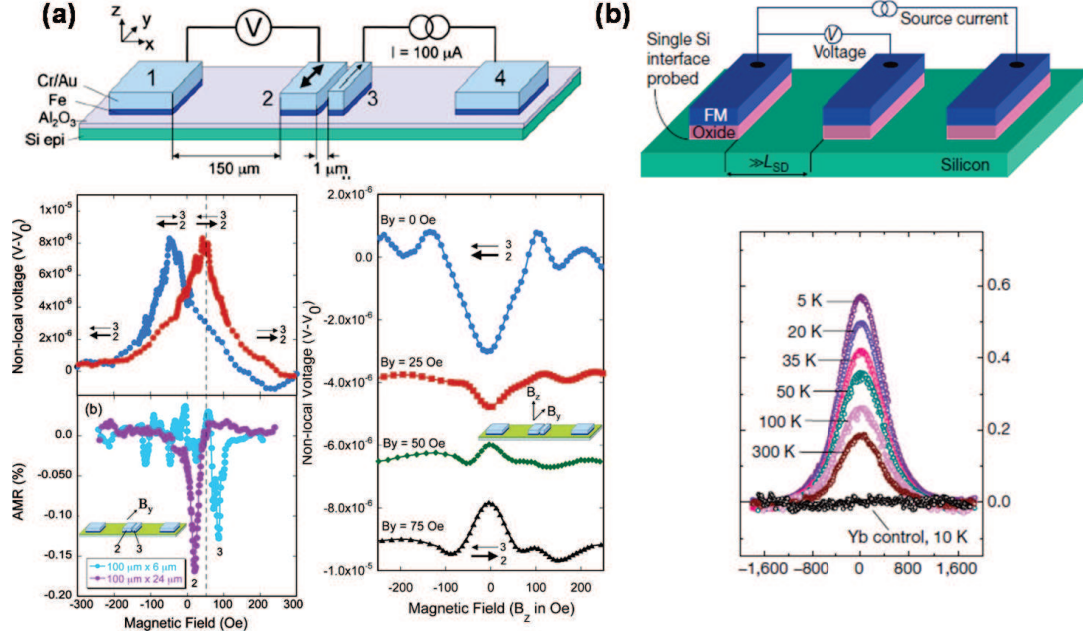


Figure 1.13 : (a) Non-local geometry used by van't Erve et al. [42] for spin injection in Si using Fe/Al₂O₃ spin injector. The non-local voltage measured as a function of in-plane and out-of-plane magnetic field at 10 K is also shown. (b) Three terminal geometry employed by Dash et al. [43] where injection and detection is done under same contact. Change in detected voltage as a function of perpendicular field is also shown at different temperatures.

Thus, using a insulating tunnel barrier between FM and semiconductor interface solves the problem of conductivity mismatch and leads to efficient spin injection. This barrier should be free of any pin-holes and thermally stable for the device to function properly at higher temperatures. The crystalline MgO barrier provides more tunneling spin polarization than amorphous Al₂O₃ barrier. Finally the RA product of the barrier should lie in an optimum range to have the highest values of magnetoresistance.

Ferromagnetic Semiconductors

One more solution to have spin injection in semiconductors is to use magnetic semiconductors as spin injectors instead of metals. The magnetic semiconductors exhibit both ferromagnetism and semiconductor properties and hence match the resistance of the semiconductors. The magnetic semiconductors can be divided into three categories depending on the distribution of magnetic atoms:

- Concentrated Magnetic Semiconductors

Concentrated magnetic semiconductors (CMS) are alloys of magnetic atoms with semiconducting materials. Here the magnetic atoms sit in well defined lattice sites in the crystalline structure. Some examples are europium chalcogenides (Eus, EuSe) and semiconducting spinels like CdCr₂Se₄ or CuCr₂S₄ (the proportion of magnetic atoms being

28.6%). However these materials have different crystal structure than that of Si, GaAs limiting their integration in existing semiconductor industry.

- Dilute Magnetic Semiconductors (DMS)

The non-magnetic semiconductors are doped with small amount of magnetic atoms (few percent) to make them magnetic, called as Diluted Magnetic Semiconductors. The magnetic atoms substitute the atoms of semiconductor matrix without changing significantly the crystalline structure. In beginning the research was focused on II-VI-based compound semiconductors such as CdTe or ZnSe, doping them with magnetic 3d transition metals. However, their Curie temperatures was quite low.

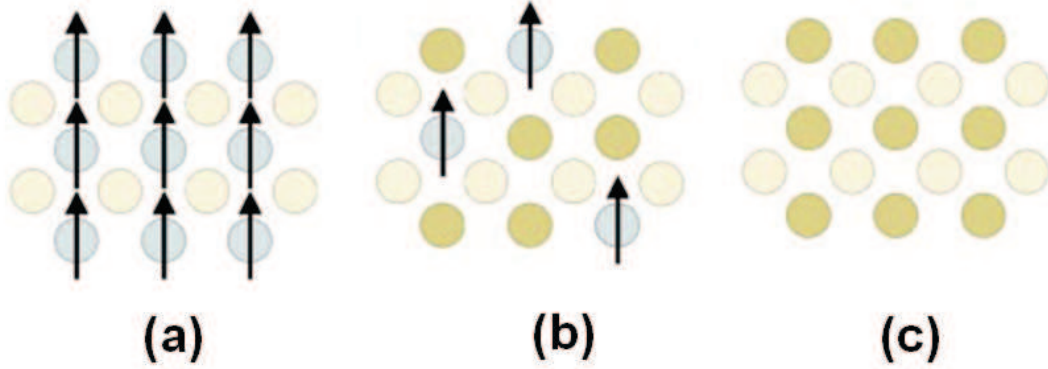


Figure 1.14 : *Three types of semiconductors: (A) a magnetic semiconductor, in which a periodic array of magnetic element is present; (B) a diluted magnetic semiconductor, an alloy between nonmagnetic semiconductor and magnetic element; and (C) a nonmagnetic semiconductor, which contains non magnetic ions. (from ref. 45)*

In the 1990s, III-V based DMS were fabricated by doping with Mn atoms. However the low solubility of Mn in III-V was improved by using non-equilibrium growth techniques like low temperature molecular beam epitaxy. It was also observed that the carrier density plays important role in the mediation of ferromagnetism. In 2000 a model (Zener Model and mean field approximation) was proposed to explain the origin of magnetism in II-VI and III-V DMS and the relation of T_c with the concentration of magnetic atoms and the carrier density [46].

In III-V DMS Mn atoms replace Ga atoms and provide both magnetic moments and holes due to their valence different from Ga. However in II-VI DMS, Mn atoms have the same valence as the cations and act as localized magnetic moments without changing the carrier density. Thus, additional conventional doping is required to tune the carrier density. Despite those advances, experimental results in II-VI systems have shown rather low T_c and focus moved on to III-V and IV semiconducting hosts. The theoretical prediction of Curie temperatures T_c by Zener model for different DMSs is shown in Fig. 1.15. Up to now, T_c up to 190 K have been achieved in (Ga,Mn)As, and major efforts are made to reach T_c 's above room temperature [47, 48].

- Non-uniform magnetic semiconductors

Non-uniform magnetic semiconductors, also known as heterogeneous semiconductors, are group of magnetic semiconductors which originates from DMS. During non-equilibrium growth of DMS systems, when the magnetic element concentration far exceeds the solubility limit, there may be formation of unknown, metastable phases. A spinodal decomposition occurs for such systems leading to the formation of such metastable phases

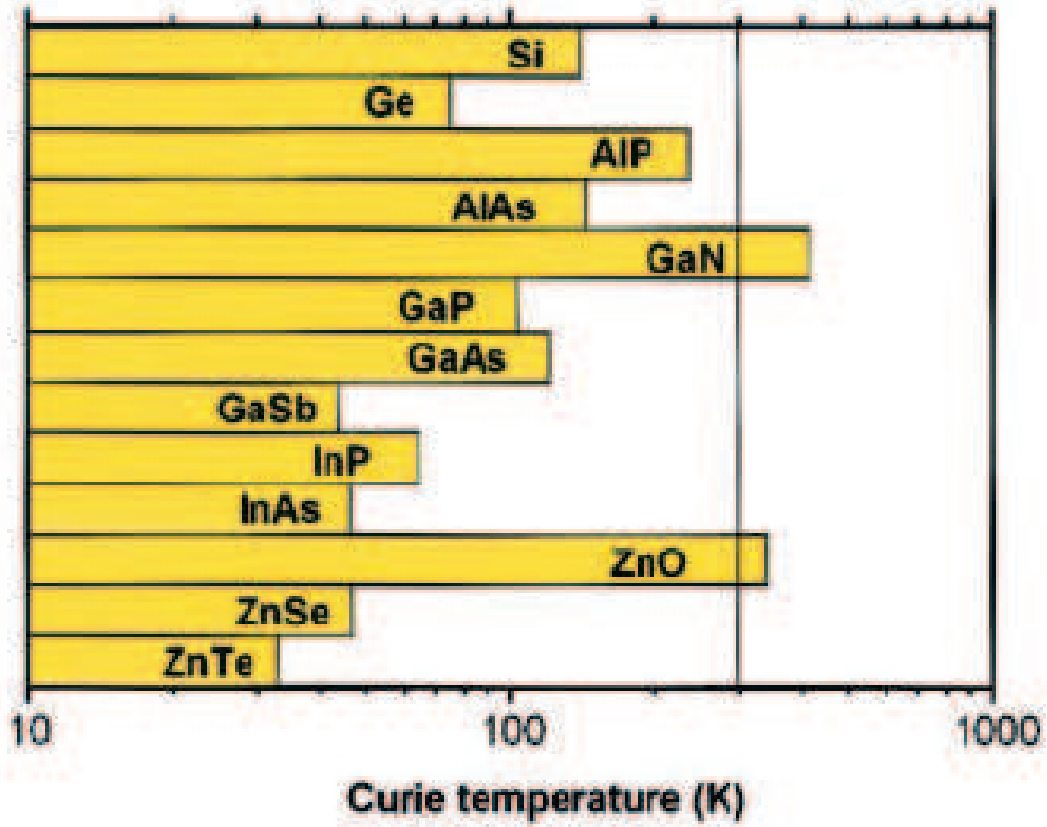


Figure 1.15 : Computed value of the Curie temperature T_C by Zener's model for various p-type semiconductors containing 5% Mn and 3.5×10^{20} holes at different temperatures [46].

which exhibit higher T_c than the DMS films. These phases are fully coherent with the surrounding matrix but still show locally higher concentration of magnetic atoms. The first theoretical explanation for this phenomenon was given by Sato et. al. who calculated an increase of T_c upon phase decomposition due the extended magnetic networks in the system [49]. This spinodal decomposition has been reported in different II-VI, III-V and IV systems, such as, e.g., in (Zn,Cr)Te by Kuroda et al. [50], in (Ga,N)Fe by Bonanni et al. [51], in (Ga,Mn)As by Hai et al. [52], or in (Ge,Mn) by Jamet et al. [53].

The first result of using DMS as a spin aligner (Fig. 1.16) was shown in $\text{Be}_x\text{Mn}_y\text{Zn}_{1-x-y}\text{Se}$ by Fiederling et al. [54]. A large magnetic field parallel to the growth direction was applied and full polarization of carriers in the DMS layer was created by giant Zeeman splitting. The polarized spins entered the AlGaAs channel and 90% spin polarization was observed by electroluminescence. Jonker et al. also achieved similar results using $\text{Zn}_{1-x}\text{Mn}_x\text{Se}$ as a spin-injecting contact on a GaAs-based light-emitting diode [55]. At the same time, Y. Ohno et al. [56] published results showing the injection of spin polarized holes from magnetic GaMnAs into the active region of a spin LED (InGaAs/GaAs quantum well). The circular polarization of the light emitted along the edge of the sample (perpendicular to the growth direction) was measured to be about 1%. However, these results are debated and it is argued that there are different selection rules for edge-emission (side emission) and surface emission using quantum wells [57].

In 2003, Mattana et al. illustrated electrical spin injection and detection in GaAs quantum well using GaMnAs ferromagnetic electrodes [58]. A vertical structure of GaMnAs/AlAs/GaAs/AlAs/GaMnAs having double tunnel junction and two GaMnAs electrodes with different thicknesses and dif-

ferent Mn concentrations was used in order to obtain different coercive fields. A TMR ratio of 38% was observed at 4 K.

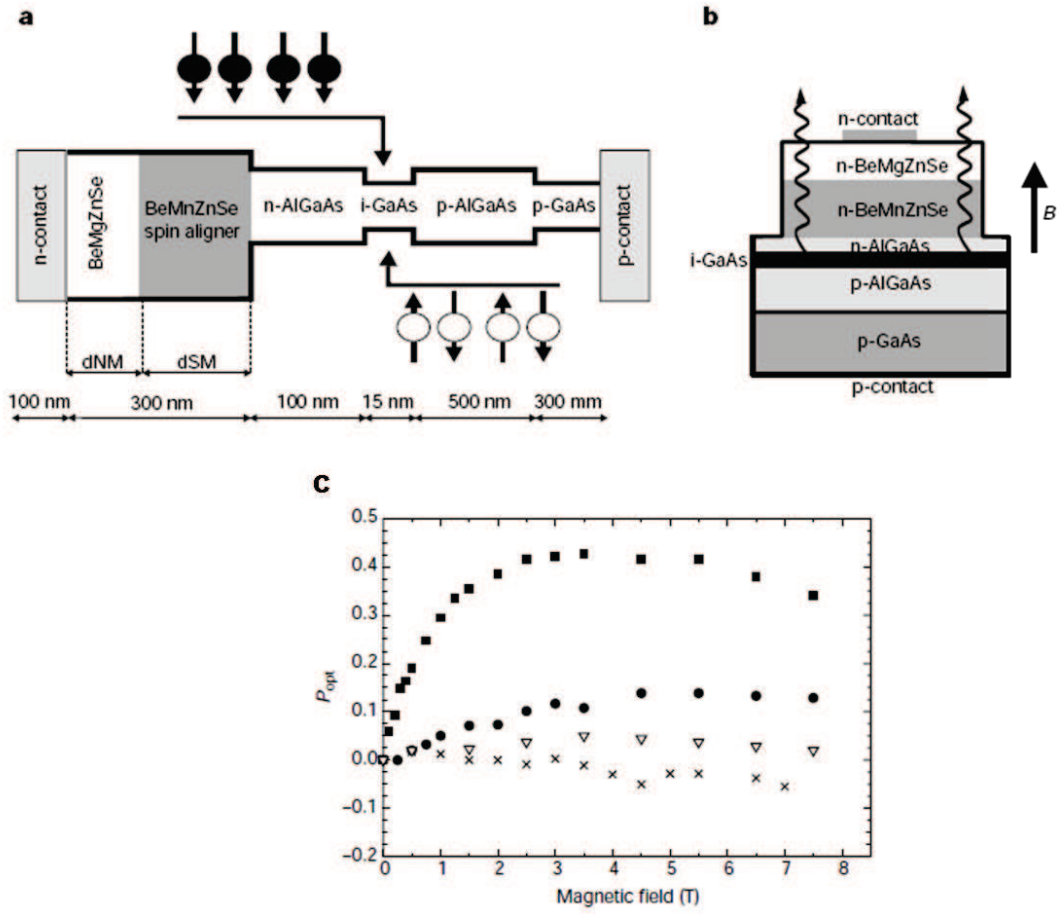


Figure 1.16 : (a) Schematic band structure of the spin-aligner light-emitting diode. Spin-polarized electrons are injected from the left into the active GaAs layer, unpolarized holes from the right, (b) Side view of the device showing the direction of the magnetic field and the emitted light. (c) Degree of circular polarization of the electroluminescence observed for different values of dSM and dNM. For more details see ref. 54.

The electrical spin injection and detection in non-local lateral geometry using GaMnAs DMS was done by Ciorga et al in 2009 [59]. They used $p^+GaMnAs/n^+GaAs$ ferromagnetic Esaki diodes [60] as spin aligning contacts for spin injection and detection in n-GaAs channel. This Esaki diode under reverse-bias allows spin-polarized tunneling of electrons from the valence band of (Ga,Mn)As to the conduction band of n^+GaAs . They successfully demonstrated the spin-valve effect, Hanle-effect and extracted the value of 50% for spin-injection efficiency. The results may open new possibilities for spin-current-induced magnetization switching (CIMS) in (Ga,Mn)As and one could realize all-semiconductor spin devices.

1.1.2 Spin Relaxation in Semiconductors

Spin relaxation is the decaying of initial non-equilibrium spin polarization. It can occur due to combination of momentum scattering and spin-orbit interaction or due to precession of spins around a random fluctuating magnetic field or due to emission/absorption of magnetic excitations (like magnons in FM). The random magnetic field can be described by two parameters:

its amplitude, referred to by the average spin precession frequency in the random field, ω and its correlation time τ_c , the time during which the field may be considered as constant.

The spin makes a precession around the (random) direction of the effective magnetic field with a typical frequency ω and during a typical time τ_c . After a time τ_c the direction and the absolute value of the field change randomly, and the spin starts its precession around the new direction of the field. After a certain number of such steps the initial spin direction will be completely lost. The dimensionless parameter $\omega\tau_c$ is the typical angle of spin precession during the correlation time. We can consider two limiting cases for the product $\omega\tau_c$:

- $\omega\tau_c \ll 1$

In this case the electron spin undergoes a very small precession during the correlation time $\omega\tau_c$ and the spin undergoes a small angular diffusion. During a time t , the number of random steps is t/τ_c , for each step the squared precession angle is $(\omega\tau_c)^2$. These steps are not correlated, so that the total squared angle after a time t is $(\omega\tau_c)^2(t/\tau_c)$. The spin relaxation time τ_s may be defined as the time at which this angle becomes of the order of 1. Hence,

$$\frac{1}{\tau_s} \approx \omega^2 \tau_c \quad (1.19)$$

- $\omega\tau_c \gg 1$

This means that during the correlation time the spin will make many rotations around the direction of the magnetic field. Hence the spin will be lost in a time of the order of τ_c :

$$\tau_s \approx \tau_c \quad (1.20)$$

This consideration is quite general and applies to any mechanism of spin relaxation. We only have to estimate the values of the relevant parameters ω and τ_c for a given mechanism.

In most cases spin-orbit coupling is responsible for spin relaxation.

Spin-Orbit Coupling

A particle moving with velocity \vec{v} in an electric field \vec{E} will experience a magnetic field given by $\vec{B} = (1/c^2)\vec{E} \times \vec{v}$, where c is the velocity of light. Similarly in a rest frame of electron, the electric field from charge $+Ze$ in nucleus is seen as a magnetic field. This magnetic field acts on the electron magnetic moment. The radial electric field can be given as $\vec{E} = \frac{1}{e} \frac{\partial U(r)}{\partial r} \vec{u}_r$, where $U(r)$ is potential of the electron. Also the angular momentum \vec{L} can be written as $\vec{L} = \vec{u}_r \times m\vec{v}$. This makes the effective magnetic field as:

$$\vec{B}_{eff} = \frac{1}{m_e e c^2} \frac{1}{r} \frac{\partial U(r)}{\partial r} \vec{L} \quad (1.21)$$

This field is perpendicular both to \vec{E} and \vec{v} is normal to the plane of the orbit, thus it is parallel to the orbital angular momentum L . This is the physical origin of the spin-orbit interaction and this effect is relativistic and quantum mechanical.

The magnetic moment of an electron with spin \vec{S} is given by $\vec{\mu} = -\frac{g\mu_B}{\hbar} \vec{S}$ where g is the Lande factor and μ_B is Bohr magneton. In a magnetic field this magnetic moment will have energy, Zeeman energy, $H = -\vec{\mu} \cdot \vec{B}$. Thus in the above magnetic field due to spin-orbit coupling, the energy associated can be given as:

$$H = \frac{\mu_B}{\hbar m_e e c^2} \frac{1}{r} \frac{\partial U(r)}{\partial r} \vec{L} \cdot \vec{S} \quad (1.22)$$

Thus the spin-orbit interaction can be written as $A(\vec{L} \cdot \vec{S})$, the constant A depending on the electron state in an atom. This interaction results in a splitting of atomic levels, which strongly increases for heavy atoms. This spin-orbit interaction is responsible for band split-off in valence band which is observed in semiconductors at $\vec{k} = \vec{0}$ and is given in the table 1.1.

| Material | $E_{split-off}$ |
|----------|-----------------|
| GaAs | 0.34 eV |
| Ge | 0.29 eV |
| Si | 0.05 eV |

Table 1.1 : *The band split-off in valence band for different semiconductors.*

Different mechanisms for spin relaxation

There are several possible mechanisms responsible for spin relaxation.

- The Elliott-Yafet (EY) Mechanism

Elliott-Yafet (EY) spin scattering refers to processes in which an electron scatters from a specific defect within the semiconductor in a manner that causes the electron to flip its spin. These defects may be structural defects such as misfit dislocations, grain boundaries, or local impurities, or they may be dynamic defects such as phonons. The electrical field, accompanying lattice vibrations, or the electric field of charged impurities is transformed to a magnetic field through a spin-orbit coupling [61, 62].

Due to this spin-orbital interaction, real crystals Bloch states (i.e momentum eigenstates) are not spin-eigenstates anymore. The magnetic field lifts-off the spin degeneracy of the Bloch states and mixes spin-up and spin-down states. This occurs because the spin component of wave functions do not factorize into a single product of a purely orbital wave function and a purely spin component. The correlation between the spin component of the wave function and the orbital component of the wave function differs for electronic states with different momenta, and thus non-magnetic scattering from one state with momentum \vec{k}_1 to another state with momentum \vec{k}_2 will lead to a small probability of a spin flip. This happens even when the materials are inversion symmetric, and the dispersion relations are doubly degenerate at each momentum k , because it is still not possible to factorize states at a given momentum into an orbital and a spin part.

The spin relaxation rate is proportional to momentum scattering rate and hence it increases with increase in the impurity concentration. For temperature dependence, spin relaxation by impurities occurs at lower temperatures and by phonons at higher temperatures. Therefore a weak temperature dependence of the spin relaxation rate ($1/\tau_s$) is observed at lower temperatures but as temperature increases phonon scattering becomes dominant and much higher temperature dependence is observed. This scattering mechanism is dominant for inversion-symmetric materials, such as simple metals and semiconductors like Silicon and Germanium.

- The D'yakonov-Perel' mechanism

This spin relaxation mechanism is related to the spin-orbit splitting of the conduction band of semiconductors that lack inversion symmetry. As the electron moves, the combination of spin-orbit interaction and the inversion asymmetry of the material causes it to feel an effective magnetic field. This field lifts the degeneracy of the momentum states of the spin-up and spin-down electrons: $E_{k\uparrow} \neq E_{k\downarrow}$ i.e. having the same momentum state but different energies. Most prominent examples of materials without inversion symmetry come from groups III-V (such as GaAs) and II-VI (ZnSe) semiconductors, where inversion symmetry

is broken by the presence of two distinct atoms in the Bravais lattice. In heterostructures the symmetry is broken by the presence of asymmetric confining potentials.

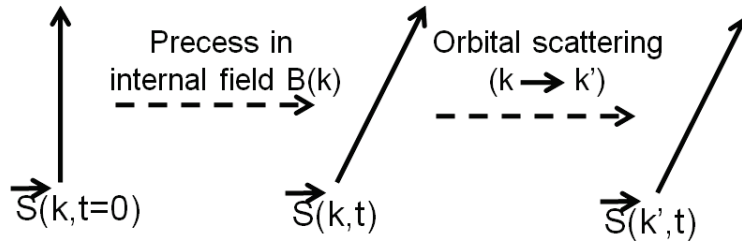
For bulk semiconductors, this splitting was first pointed out by Dresselhaus [63]. The additional spin-dependent term in the electron Hamiltonian can be presented as $g\mu\vec{B}(\vec{k})\cdot\vec{S} = \hbar\vec{\Omega}(\vec{k})\cdot\vec{S}$, which can be viewed as the energy of a spin in an effective magnetic field. Here $\vec{\Omega}(\vec{k})$ is a vector depending on orientation of the electron momentum with respect to the crystal axes. Hence the energy of an electron in the conduction band, should be written in the form:

$$E(\vec{k}) = \frac{(\hbar k)^2}{2m^*} + \hbar\vec{\Omega}(\vec{k})\cdot\vec{S} \quad (1.23)$$

For a given \vec{k} , $\vec{\Omega}(\vec{k})$ is the spin precession frequency. In an effective field \vec{B}_{eff} , this frequency is given by $\vec{\Omega}(\vec{k}) = \frac{e\hbar}{m}\vec{B}_{eff}(\vec{k})$. This effective magnetic field is inhomogeneous in momentum space. This implies that the effective magnetic field changes in time because the direction of \vec{k} varies due to electron collisions. Thus the correlation time τ_c is on the same order of the momentum relaxation time τ_k and if $\Omega\tau_k$ is small, the spin relaxation rate from eqn. 1.19 is given by:

$$\frac{1}{\tau_s} \approx \Omega^2\tau_k \quad (1.24)$$

(a) Single carrier



(b) Population of carriers

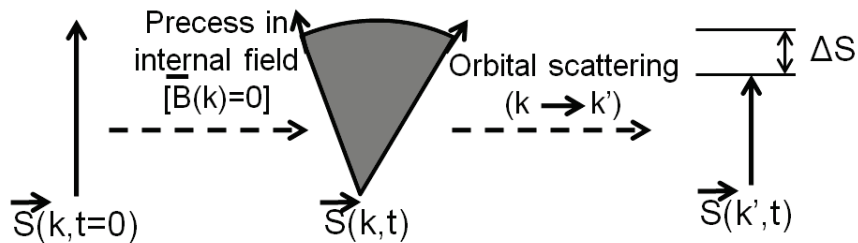


Figure 1.17 : (a) Evolution of a single carrier in the presence of the effective magnetic field $B(k)$ and orbital scattering. Both the spin orientation and the momentum of the carrier is altered. (b) Evolution of a population of carriers under the same conditions. Different precession rates and orientations of carriers with different momenta lead to different spin directions for different carriers. Orbital decoherence averages spin orientation, yielding a spin polarization reduced from the initial value.

In contrast to the Elliott-Yafet mechanism, now the spin relaxation rate is inversely proportional to momentum scattering rate. The spin rotates not during but between the collisions

and therefore the relaxation rate increases when the impurity concentration decreases.

For an electron gas in equilibrium, the average magnetic field vanishes, but the variance of the magnetic field does not. As carriers scatter from momentum state to momentum state, they feel a time-dependent effective fluctuating field.

This spin relaxation mechanism is predominant at higher temperatures ($> 70\text{K}$). Elemental semiconductors like Si, Ge possess inversion symmetry in the bulk, so the D'yakonov-Perel' mechanism does not apply to them. Hence the spin lifetime in these systems can exceed the spin lifetimes in III-V semiconductors by orders of magnitude [64].

- The Bir-Aronov-Pikus mechanism

This is a mechanism of spin relaxation of non-equilibrium electrons in p-type semiconductors due to the exchange interaction between the electron and hole spins. This was first observed by Bir et al. in 1975 [65]. The exchange interaction between electrons and holes is governed by the Hamiltonian:

$$H = A\vec{S}\cdot\vec{J}\delta(\vec{r}) \quad (1.25)$$

where A is proportional to the exchange integral between the conduction and valence states, \vec{J} is the angular momentum operator for holes, \vec{S} is the electron-spin operator, and \vec{r} is the relative position of electrons and holes. The spin-flip scattering probability depends on the state of the holes (degenerate or non-degenerate, bound on acceptors or free). Holes have shorter spin coherence times, and spin exchange between electrons and holes is very effective. Ultimately, it will lead to spin decoherence of electrons. This spin relaxation rate, being proportional to the number of holes, may become the dominant one in heavily p-doped semiconductors. This mechanism is of importance at low temperatures [66].

- Hyperfine-interactions

Hyperfine-interaction comes from the magnetic interaction between the magnetic momentum of nuclei and electrons. The electron spin interacts with the spins of the lattice nuclei which provide a random effective magnetic field. In most III-V semiconductors, all the nuclei have non-zero spin, and can engage in mutual spinflip processes with electrons and holes in a process analogous to the BAP process described above. A key difference is the short-range, weak coupling that characterizes the hyperfine interaction. The hyperfine interaction is only significant for electrons in localized states such as quantum dots or dilute dopant levels.

1.1.3 Manipulation of spin polarization

For realization of spin-transistor as proposed by Datta and Das, its necessary to manipulate the spins in the channel of the transistor. This can be mostly done in two ways: either by applying external magnetic field or utilizing Rashba effect by applying electric field. However, recently it was shown that temperature gradient (Spin Seebeck effect [67]) and optical methods [68] can be used to manipulate spin, but these are not discussed here.

Manipulation of spins by external magnetic field

Upon the application of a magnetic field \vec{B} the electron spins, or rather the spin magnetization \vec{m} experiences a torque. This torque $\vec{\Gamma}$ is given by:

$$\vec{\Gamma} = \vec{m} \times \vec{B} \quad (1.26)$$

Under this torque, the spins will precess around the field at a frequency, known as Larmor frequency given by

$$\Omega = \left| \frac{ge}{2m} B \right| \quad (1.27)$$

The precessional motion is altered by damping caused by spin relaxation and the creation or recombination of electrons. This precession, along with spin creation, spin relaxation, and recombination is described by the following simple equation of motion of the average spin vector \vec{S} :

$$\frac{d\vec{S}}{dt} = \frac{\vec{S}_o - \vec{S}}{\tau} - \frac{\vec{S}}{\tau_s} + \vec{\Omega} \times \vec{S} \quad (1.28)$$

Here the first term on right-side denotes the spin generation (S_o/τ) and recombination (S/τ) with electron lifetime τ , the second term describes spin relaxation with spin relaxation time τ_s and third term denotes the spin precession in magnetic field with frequency Ω . The spin lifetime is defined as ($\tau_{sf}^{-1} = \tau^{-1} + \tau_s^{-1}$).

In the stationary state ($dS/dt = 0$) and in the absence of a magnetic field, one finds:

$$S_z(0) = \frac{S_o}{1 + \tau/\tau_s} \quad (1.29)$$

where $S_z(0)$ is projection of the spin on the direction of S_o (z-axis). In the presence of magnetic field we obtain:

$$S_z(B) = \frac{S_z(0)}{1 + (\Omega\tau_{sf})^2} \quad (1.30)$$

Hence in static conditions, the spin projection S_z decreases as a function of the Larmor frequency or transverse magnetic field due to spin precession in the semiconductor. This effect is called the Hanle effect. The spin transport in a non-magnetic channel can be confirmed by observing this effect. Also the spin lifetime, an important parameter can be found by making use of this phenomenon.

A spin transistor is possible if spin injection and detection is done in lateral geometry and manipulated by controlling spin precession. The external field should be applied in such a way that it is perpendicular to the magnetization direction of electrodes and sufficient for the spins to precess 180° during their trajectory in the channel. The application and removal of the magnetic field should decide the 'on' and 'off' state of the transistor. The demonstration of such spin-valve was first done by Jedema et al. in metallic systems [23].

Manipulation of spins by electric field

Applying a magnetic field is an easy way to manipulate the spins however this option is not feasible for integration into the application technology. The other way to manipulate spins is by applying electric field by utilizing Rashba effect as proposed by Datta and Das in 1990 [17].

In a non-centro-symmetric quantum well, due to the band offsets at the interface of two different materials the electrons are confined in a quantum well. A two-dimensional electron gas (2DEG) is formed. In an electric field, these electrons due to spin-orbit coupling experience a magnetic field which leads to splitting of energies of spin up and spin down electrons. This happens even in the absence of external magnetic field. This splitting is described by the so-called Rashba [69], or Bychkov-Rashba [70] term in the Hamiltonian:

$$H = \alpha(\vec{S} \times \vec{k}) \cdot \vec{n} \quad (1.31)$$

here α is a constant reflecting strength of spin-orbit coupling and \vec{n} is the unit vector perpendicular to the sample layer usually in the growth direction for layered structures. The Hamiltonian for electrons confined in y-direction is given by:

$$H = \alpha(s_z k_x - s_x k_z) \quad (1.32)$$

Considering a case where electrons propagate in x-direction and having polarization in z-direction, this Hamiltonian gives a splitting of $E = \alpha s_z k_x$. The value of α will determine the difference in energy and hence a difference in wave vector between electrons with their spins aligned along +z and -z. This difference in wave vector is translated into a phase shift that can be detected at the drain contact due to a change in magnetoresistance. Varying the potential applied to the gate contact changes the strength of the Rashba Hamiltonian and thus the conduction properties of the device.

This aspect of controlling the spin-orbit interaction by applying gate voltage was demonstrated by Nitta et al. in 1997 [71]. They successfully demonstrated that in an inverted $\text{In}_{0.53}\text{Ga}_{0.47}\text{As}/\text{In}_{0.52}\text{Al}_{0.48}\text{As}$ quantum well, α can be controlled by the interface electric field because the Rashba mechanism is dominant. Recently, the successful control of Spin precession in a spin-injected field effect transistor was shown by Koo et al [72]. By electrical injection and detection of spins in non-local geometry from FeNi electrodes into a 2DEG made of InAs, they showed modulations in collector voltage as a function of gate voltage. This effect was directly related to the precession of spins due to Rashba mechanism.

1.2 Spin injection into Germanium

The subject of this thesis is to demonstrate electrical spin injection and detection in Germanium. As a group IV semiconductor, Germanium is receiving high attention as a candidate for metal-oxide-semiconductor field-effect transistors (MOSFETs) due to its high electron and hole mobilities. The combination of Ge channel MOSFETs and spintronics can lead to high performance and low power-consumption devices.

Germanium has inversion-symmetric crystal structure, hence D'yakonov-Perel' relaxation mechanism is not possible. This increases spin-diffusion lengths and spin-relaxation occurs by Elliot-Yafet mechanism (except in nanostructures and heterostructures). This makes Ge more interesting for spintronics applications.

Since Germanium is a indirect band-gap semiconductor optical methods for spin detection are not so effective to detect carrier spin polarization. Electrical detection is the best way to demonstrate spin transport in Ge and Hanle-effect gives an unambiguous proof for this phenomenon. In this thesis we discuss the following two methods to realize spin transport in Germanium:

- Spin injection using ferromagnetic metals and tunnel barrier

Spin injection in Ge can be realized using ferromagnetic metal electrodes and a tunnel barrier. The electrodes of ferromagnetic metals have high Curie temperature and moderate spin polarization. The tunnel barrier removes the conductivity mismatch problem and can be formed by tailored-Schottky contact or by inserting thin insulating layer at the interface. In this work, Py/ Al_2O_3 and CoFeB/MgO have been used as spin injector. These electrodes have in-plane magnetization due to shape anisotropy.

A three-terminal geometry is employed for spin injection and detection in order to remove the spurious effects and local Hall-effect of electrodes. A tunneling transport and Hanle-effect have been observed. The dependence of spin lifetime on temperature and bias have been studied. The effect of surface roughness on spin polarization in the Ge channel has also been shown.

- Towards (Ge,Mn) as a spin injector

Magnetic semiconductor (Ge,Mn) appears to be a promising candidate as spin injector in semiconductors and in particular in Ge. Doping of Germanium by Mn to make it a magnetic semiconductor can solve the problem of conductivity-mismatch. Also it has high potential in spintronics applications due to its compatibility with existing Si technology and possible electric control of carrier mediated ferromagnetism.

In this thesis we discuss growth of thin $\text{Ge}_{1-x}\text{Mn}_x$ films by molecular beam epitaxy on Ge(111) and Ge(001) substrates. We have studied the following (Ge,Mn) systems: thin Ge_3Mn_5 films grown on Ge(111) substrate, randomly distributed spherical Ge_3Mn_5 clusters and finally crystalline and amorphous (Ge,Mn) nanocolumns grown on Ge(001) substrates. The crystalline structure and morphology of these nanostructures have been investigated by transmission electron microscopy and X-ray diffraction.

We also present a study of magnetic anisotropy in (Ge,Mn) nanostructures investigated using complementary techniques: superconducting quantum interference device (SQUID) and ferromagnetic resonance (FMR). For future spintronics applications, the knowledge of magnetic anisotropy of (Ge,Mn) material is very important since it determines the direction of magnetization, coercive fields, and domain sizes.

Finally we discuss the growth of (Ge,Mn) films on Germanium-on-Insulator (GOI) substrates with 40nm Ge-channel thickness, a step towards realization of (Ge,Mn) as a spin injector.

1.3 Conclusion

In this chapter, we have seen the importance of integrating spintronics with semiconductor technology. The long spin diffusion and coherence lengths along with the typical semiconductor advantages are some of the benefits in this integration. A spin-FET can work with higher speeds, enhance the functionality and reduce the power consumption as compared to existing technology.

We discussed the four conditions for realization of semiconductor-based spintronics technology: spin injection from ferromagnetic source, spin transport in channel, spin manipulation and finally the spin detection to determine the output. The problem of conductivity mismatch leading to unsuccessful spin injection from ferromagnetic metal into semiconductor and different solutions have been explained.

Finally we presented the motivation for realization of electrical spin injection and detection in Germanium.

Experimental techniques

In this chapter, the experimental techniques used for sample preparation and characterization are discussed. For the growth of (Ge,Mn) thin-films, a molecular beam epitaxy (MBE) system was used. The surface morphology and crystal structure were analyzed in-situ by reflection high-energy electron diffraction (RHEED). The crystalline quality of these thin-films was studied using high resolution transmission electron microscopy (HRTEM). Magnetic measurements were performed using superconducting quantum interference device (SQUID) magnetometry and ferromagnetic resonance (FMR) spectroscopy.

For spin injection experiments, a sputtering system was used to grow the oxide barrier and the ferromagnetic metals. The samples were processed using lithography and dry etching in order to make devices for spin injection. The measurements were done in an Oxford helium cryostat setup.

2.1 Molecular Beam Epitaxy

Epitaxy is a method to deposit a single-crystalline film on to a single-crystalline substrate. It consists in depositing atoms on a crystalline substrate such that the atoms arrange themselves in the same crystallographic arrangement as that of the substrate. If the grown film and the substrate are the same material then it is called homoepitaxy and if they are different it is called heteroepitaxy. Different techniques can be used to grow epitaxial films: molecular beam epitaxy (MBE), chemical vapor deposition (CVD), pulsed laser deposition (PLD) and atomic layer deposition (ALD).

In this present work we have used a ultra high vacuum molecular beam epitaxy (UHV-MBE) system for the growth of (Ge,Mn) epitaxial films. This technique for epitaxial growth was invented in the late 1960s at Bell Laboratories by J. R. Arthur and Alfred Y. Cho [73]. The principle of MBE growth involves the migration of atoms or clusters of atoms which are produced by heating a solid source on a hot substrate. In UHV conditions, these atoms have very long mean free path between collisions (longer than the chamber dimension). After reaching the substrate the atoms diffuse and eventually incorporate into the growing film. Using this technique high quality epitaxial structures with monolayer (ML) control can be obtained.

The schematic diagram of the MBE chamber is shown in Fig. 2.1. The base pressure in the MBE system is of the order of 10^{-11} mbar, obtained by a pumping system consisting of turbo-molecular and ion pumps. The liquid nitrogen panel surrounds the growth chamber to prevent re-evaporation from other than the hot cells, to provide the thermal isolation from cell to cell and to pump residual gases. The chamber is equipped with different effusion cells which are co-focused on the substrate heater, to optimize flux uniformity. In an effusion cell, a crucible with the material to be deposited is heated by a Ta filament. The substrate is fixed on a molybloc and can be rotated with the help of a manipulator. The heater behind the sample is designed to

maximize temperature uniformity and minimize power consumption and impurity outgassing.

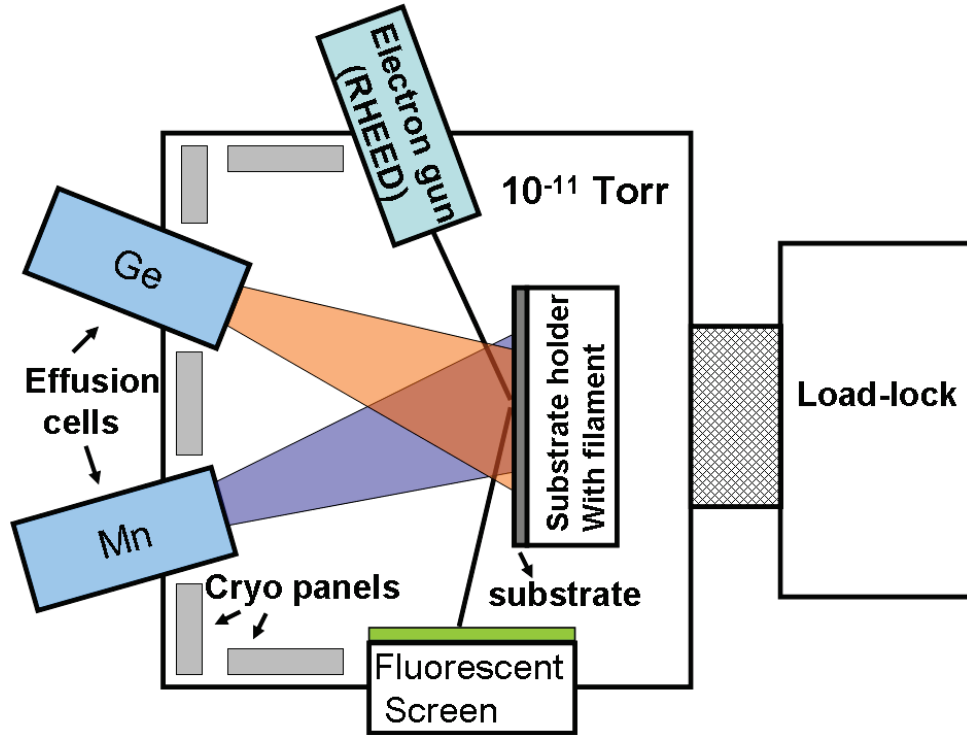


Figure 2.1 : *Schematic drawing of the MBE system.*

The crystal growth mechanisms on the sample surface by MBE include the adsorption of atoms, atom diffusion on the surface, nucleation of phases and desorption, which mainly depend on the growth temperature of the surface (Fig. 2.2). At higher growth temperature, the atoms have more energy for diffusion on the surface and higher possibility for the growth of new phases. Desorption of atoms from the growth surface can also occur at much higher growth temperatures. On the other hand, if the growth temperature is too low, atoms do not have enough energy for diffusion, there could be a polycrystal or amorphous growth. Therefore, to well control the growth mechanisms of thin films by MBE, the growth temperature (T_g) is a key parameter.

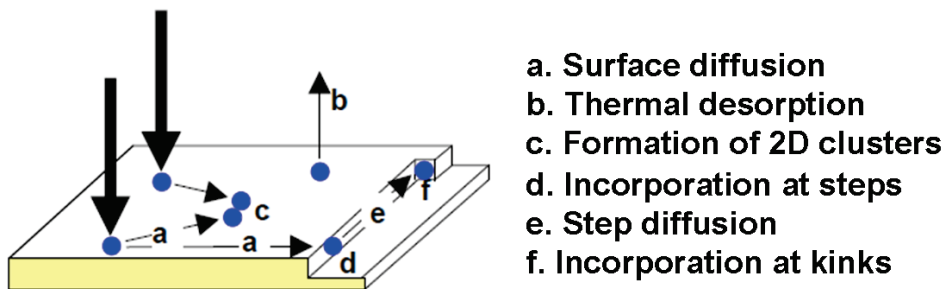


Figure 2.2 : *Illustration of different processes on the sample surface during the MBE growth.*

For the growth of (Ge,Mn) films, the Ge substrates are glued on molybdenum Molyblocks using indium. This ensures good mechanical stability of the sample and a good thermal conductivity with the sample holder. The growth temperature which has been thoroughly calibrated can be adjusted by changing the filament current. The Ge and Mn knudsen cells are connected to the main chamber and are focused on the substrate. Using the individual filaments, the

temperature in the cells can be increased to evaporate the atoms on the sample. The ratio of pressures between different cells with different elements will control the stoichiometry of the film. There are individual and common shutters covering the cells which control the start and end of the growth. The Ge flux is calibrated using RHEED oscillations and will be discussed in the next section. The Mn concentration is calibrated using the Rutherford backscattering technique.

The advantages of using the MBE technique for growth of epitaxial films are: a very low base pressure which limits the contamination of samples, possible to make in-situ characterization of samples using RHEED or X-ray diffraction and finally low growth rates which permits to control the thickness of layers with a precision of the order a monolayer.

2.1.1 Reflection High Energy Electron Diffraction (RHEED)

RHEED is employed to check the sample surface at grazing incidence (a few degrees) by high energy electron beam (up to 20 keV in our system). The grazing incidence limits the interaction of electrons to the first few atomic planes and ensures surface sensitivity. The diffraction pattern is observed on a phosphorescent screen. This pattern represents the intersection of the Ewald sphere with the reciprocal lattice of the surface and results in a series of spots placed on a half circle (Fig. 2.3). However the surface imperfections and thermal vibrations cause the reciprocal lattice rods to have a finite thickness, while the Ewald sphere itself has some finite thickness, due to divergence and dispersion of the electron beam.

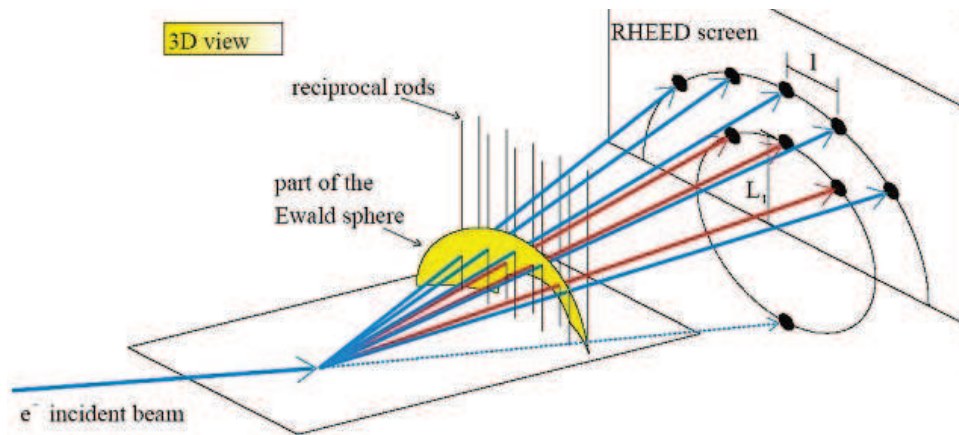


Figure 2.3 : Schematic drawing functioning of RHEED. A high energy electron beam is diffracted from the surface and the resulting pattern is observed on the fluorescent screen. Image taken from ref 74.

The RHEED pattern provides the information regarding the crystalline quality and flatness of the surface. If the surface is completely crystalline and flat, the pattern consists in a series of streaks and the distance between these streaks gives an estimation of the lattice parameter. However, if the surface is rough or 3D the pattern becomes spotty. Also one can study the change of in-plane lattice parameter during the growth which is given by the change in distance between the streaks.

Moreover a layer-by-layer growth mode can lead to oscillations of the RHEED pattern. For example during homoepitaxy of Ge on Ge(111), by measuring the period of intensity oscillations, one can calibrate the growth rate. The origin of the oscillations is explained in Fig. 2.4. If the initial surface is perfectly flat, the reflectivity of the specular spot will be relatively high. As layer-by-layer growth starts, the incident electron beam gets partially scattered by the island steps of the forming monolayer, thus reducing the reflected intensity. Scattering becomes max-

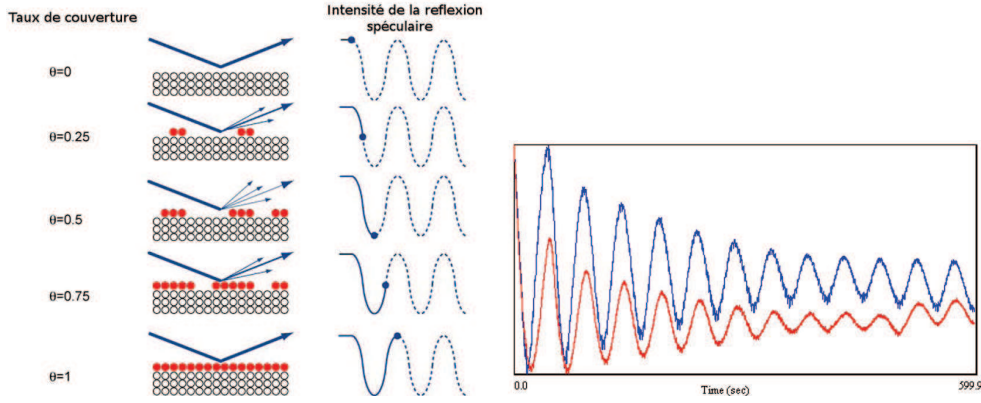


Figure 2.4 : *The mechanism of RHEED intensity oscillations during growth of a monolayer.*

imum at half ML coverage, while as the new monolayer completes, the surface flattens again by coalescence of the islands, and the reflected intensity recovers its value. The persistence of RHEED oscillations can therefore be considered as a measure of the quality of the layer-by-layer epitaxial growth.

2.2 Transmission Electron Microscopy

The structural properties of grown (Ge,Mn) films was studied using Transmission Electron Microscopy (TEM). A beam of high energy electrons (≥ 100 kV) is transmitted through an ultra thin specimen (normally less than 100 nm), interacting with the specimen as it passes through it. An image is formed from the interaction of the electrons transmitted through the specimen; the image is magnified and focused onto an imaging device, such as a fluorescent screen, on a layer of photographic film, or to be detected by a sensor such as a CCD camera.

TEM is capable of imaging at a significantly higher resolution than standard optical microscopes, owing to the small de Broglie wavelength of electrons ($\lambda = h/p$, where h is the Planck's constant, and p is momentum of electrons). This enables the instrument's user to examine fine detail-even as small as a single column of atoms, called High-resolution transmission electron microscopy (HRTEM), which is tens of thousands times smaller than the smallest resolvable object in an optical microscope. At smaller magnifications the TEM image contrast is due to the absorption of electrons in the material, due to its thickness and composition. At higher magnifications complex wave interactions modulate the intensity of the image, requiring expert analysis of observed images. Alternate modes of use allow for the TEM to observe modulations in chemical analysis, crystal orientation, electronic structure and sample induced electron phase shift as well as the regular absorption based imaging [75].

In the present work TEM observations were performed by Pascale Bayle-Guillemaud, Thibaut Devillers and Eric Prestat using a JEOL 4000EX microscope with an acceleration voltage of 400 kV.

2.3 Superconducting Quantum Interference Device

The magnetic properties of (Ge,Mn) films was studied using Superconducting QUantum Interference Device (SQUID). It is a very sensitive device used to measure the magnetization signal as low as 10^{-11} Am². The detailed functioning of the device is not discussed here. In our SQUID system, the applied magnetic field is up to 5 T and its temperature range is from 2 K to 400 K. The raw signal given by the SQUID is in Am² and is normalized on the volume of the magnetic layer to obtain the magnetization in A/m.

During the measurements, the total magnetic signal is given by the sum of the following contributions: the diamagnetic signal from the substrate, the ferromagnetic signal from (Ge,Mn) nanostructures and finally the paramagnetic signal from diluted Mn atoms. The diamagnetic signal from the substrate is proportional to the applied field and this proportionality is given by the diamagnetic susceptibility of the substrate. Since diamagnetic susceptibility is independent of temperature, it is measured at higher temperature to avoid the signal from paramagnetic phases and then removed from the total signal.

In order to separate the magnetic contribution of different phases in (Ge,Mn) films, we use Brillouin function to subtract the paramagnetic component, and a Langevin function is employed to fit out the magnetic moment and size of Mn-rich phases. Here, these two functions are briefly introduced.

The Brillouin function [76] is a special function defined by the following equation:

$$B(x) = \frac{2J+1}{2J} \coth\left(\frac{2J+1}{2J}x\right) - \frac{1}{2J} \coth\left(\frac{x}{2J}\right) \quad (2.1)$$

This function is best known for arising in the calculation of the magnetization of an ideal paramagnet. In particular, it describes the dependence of the magnetization (M) on the applied magnetic field (B) and the temperature (T) for a total angular momentum quantum number (J) of the microscopic magnetic moments. The magnetization is given by:

$$M = Ng\mu_BJB_J(x) \quad (2.2)$$

here N is the number of atoms per unit volume, g is the Landé g-factor, μ_B is the Bohr magneton, x is the ratio of Zeeman energy of the magnetic moment in the external field to the thermal energy ($g\mu_BJB/k_BT$), k_B is the Boltzman constant and T the temperature.

In the classical limit ($B/T \ll 1$), the magnetic moment can be continuously aligned in the field and J can assume all values ($J \rightarrow \infty$). The Brillouin function is then simplified into the Langevin function:

$$L(x) = \coth(x) - \frac{1}{x} \quad (2.3)$$

2.4 Ferromagnetic Resonance

Ferromagnetic Resonance (FMR) spectroscopy is based on the precessional motion of the magnetization in a magnetic field. It is one of the most powerful experimental techniques for the study of ferromagnetic thin films, providing the opportunity for determining their essential properties like magnetic anisotropy, Curie temperature and parameters describing the relaxation of magnetization. In this work, it has been used to study the magnetic anisotropy and calculate anisotropy constants in (Ge,Mn) nanostructures. To determine the anisotropy constants, the free energy approach developed by Smit-Beljers is used (see Appendix for details). This approach neglects the damping effect and assumes that the sample is homogeneously magnetized.

The experiments were performed using Bruker electron paramagnetic resonance (EPR) spectrometer (model ESP 300). The schematic diagram of the instrument is shown in Fig. 2.5(a). The applied DC magnetic field is confined to the horizontal plane, and the weak microwave (rf-) field acting on the sample is vertical. The sample is placed in a sample holder tube inserted into a liquid helium continuous flow cryostat, which is in turn inserted into the microwave cavity of the EPR spectrometer. The experiments are done at both X-band (9.4 GHz) and Q-band (34 GHz). A modulation frequency of 100 kHz and a modulation amplitude of 10 Oe for lock-in detection is used. The resonance spectrum is then the first derivative of a Lorentzian line shape.

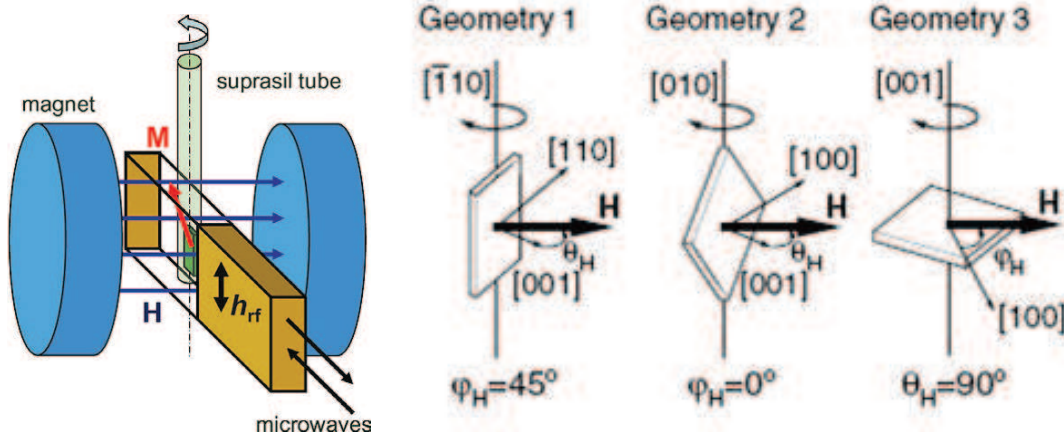


Figure 2.5 : (a) Schematic diagram of the EPR/FMR apparatus. (b) Three experimental configurations which can be used. Images taken from ref 77.

The FMR measurement procedure is similar to nuclear magnetic resonance (NMR) and EPR [78]. However, in the FMR measurements on (Ge,Mn) films, the total magnetization of the system precesses as a whole around the resultant of all static magnetic fields present in the system. The total magnetic field is the sum of the rf-field, the external DC field and internal fields. During the experiments, the microwave frequency is fixed by the resonance frequency of the cavity (9.4 or 34 GHz) and DC magnetic field is swept as the independent variable. When the precessional frequency coincides with the rf-frequency, a resonance takes place. By rotating the sample in the field, one can study the angular dependence of this resonance field B_{res} .

When the magnetic field is oriented along an easy direction of magnetization (i.e. free energy minimum) B_{res} is minimal and when the magnetization is oriented along the hard axis (i.e. free energy maximum) B_{res} exhibits a maximum value. By fitting this angular dependence using the free energy model described in appendix, the anisotropy constants can be calculated. The samples can be rotated in three different configurations as shown in Fig. 2.5(b), in order to obtain different anisotropy constants.

2.5 Sputtering

For spin injection experiments, the oxide barrier and ferromagnetic metallic layers were grown using a sputtering machine. The structures with an alumina barrier i.e. $\text{Al}_2\text{O}_3/\text{NiFe}/\text{Co}/\text{Pt}$ were grown in Spintec lab ¹ ((Actemium Technology)) and structures with a MgO barrier ($\text{Ta}/\text{CoFeB}/\text{MgO}$) were grown in Crocus technology (Singulus machine).

¹CEA/INAC/Spintec

2.6 Sample Processing

The samples were processed in clean-room using optical lithography and dry etching. The processing was done in 'Plateforme Technologique Amont' at CEA Grenoble. The following steps were followed:

- Cleaning the samples using Acetone and Isopropanol.
- Spin coating of positive resist AZ1512HS and baking it at 100°C for 90 seconds.
- UV lithography to define tunnel electrodes ($150 \times 400 \mu\text{m}^2$).
- MESA etching until tunnel barrier at 300 W and Ar pressure of approximately 2×10^{-4} Torr. The etching was followed using secondary ion mass spectrometry.
- Second optical lithography with negative resist AZ5214 to define the ohmic contacts ($300 \times 400 \mu\text{m}^2$)
- Ti/Au deposition with Ti 10 nm and Au 250 nm, in order to have ohmic contacts on n-Ge.
- Lift-off.
- Sample bonding on chip to introduce in the cryostat.

All the contacts on the chip were first grounded before connecting the sample and special caution was always taken to avoid damaging of tunnel contact with residual electrostatic charges or voltage spikes. The schematic diagram of the final device is shown in Fig. 3.8.

2.7 Cryostat

The SPECTROMAG OXFORD SM 4000-8 was used to make spin injection experiments. In this system magnetic fields up to 7 T can be applied, the temperature can be controlled from 2 K to 300 K and the angle between the sample and the applied magnetic field can be changed from 0 to 180 degrees. The cryostat is divided in three parts: liquid nitrogen tank at 77 K, hollow middle part and finally liquid Helium tank at 4.2 K. A vacuum is all around these parts to prevent freezing. The split magnetic coils are dipped in this part with liquid He. The sample on chip is fixed on the transfer rod with variable temperature insert as shown in Fig. 2.6 and entered into the cryostat. The temperature can be regulated with a stability of 0.1 K by controlling the flow of He and by heating the sample. A DC current source Keithley was used to pass the current and a Keithley nano-voltmeter was used to detect the voltage change.

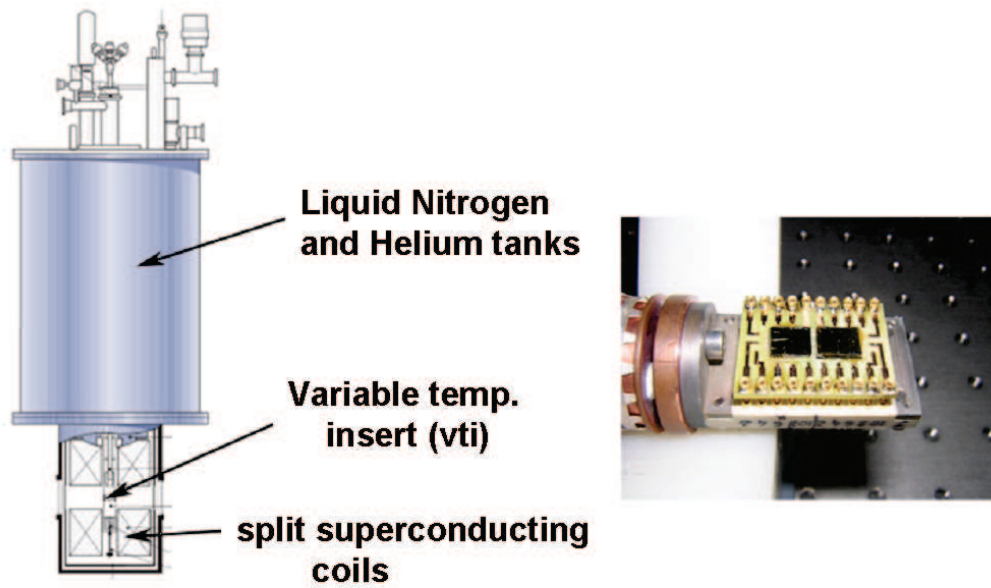


Figure 2.6 : *Schematic diagram of the the cryostat and the sample holder.*

Spin Injection in Germanium

In this chapter, we demonstrate the spin injection in n-doped Germanium using a ferromagnetic metal and an oxide tunnel barrier. The tunnel barrier solves the problem of conductivity mismatch and retains the spin accumulation in the semiconductor. In beginning, we discuss the metal-Ge contact and introduce the problem of Fermi level pinning. Next, the substrates used for experiments and the device geometry are discussed. Finally, we present the results using two different structures: Co/Py/Al₂O₃/Ge and CoFeB/MgO/Ge.

3.1 Metal-Germanium contact

The demonstration of functional MOSFET with high-k gate dielectric in Germanium has increased the interest for next-generation devices [79]. Low effective masses of carriers in Ge leads to high carrier mobilities and thus high current drive as compared to Si. There has been significant progress in developing Ge p-channel MOSFETs, however the performance of n-channel MOSFETs has been poor, largely due to high contact resistances. When a metal is connected to an n-type semiconductor, electrons tend to naturally flow from the semiconductor into the metal as the Fermi levels tend to align. A energy-band diagram of a metal to n-type semiconductor contact in thermal equilibrium is shown in Fig. 3.1(a). Here the metal work function is greater than the semiconductor work function. Following this figure, one can deduce that the Schottky barrier height (SBH) for electrons (ϕ_b) is solely determined by the metal work-function (ϕ_m) and the semiconductor electron affinity (χ) and is given by this Schottky-Mott relation relation: $\phi_b = \phi_m - \chi$. However in case of Germanium, SBH is weakly dependent on the metal work-function. This is due to a strong Fermi level pinning (FLP) near the valence band edge of Ge which results in high Schottky barrier heights (ϕ_b) in metal/n-Ge contacts. This was first reported by Dimoulas et. al. and a pinning factor S (given by $S = \partial\phi_b / \partial\phi_m$) of 0.05 was observed (Fig. 3.2(a))[80]. Similar results were obtained by Nishimura et. al. where metal/p-Ge and metal/n-Ge junctions showing Ohmic and Schottky characteristics, respectively due to strong FLP [81] (Fig. 3.2(b)). They evaluated the Schottky Barrier heights ϕ_b for various metal/semiconductor junctions, with vacuum work functions ϕ_m reported in the literature. The pinning factors extracted experimentally for Ge and Si were obtained to be 0.02 and 0.27, respectively. These results suggests that metals are almost perfectly pinned on Ge.

The cause of FLP can be explained due to high density of interface states (Fig. 3.1(b)). This distribution of states within the forbidden band-gap can be characterized by a charge neutrality level ϕ_0 (also noted CNL) [84]. The surface is neutral if the surface states are occupied up to this energy level. Above this level, the surface states are called acceptor-like (neutral if unoccupied, negatively charged if occupied). Below, they are called donor-like (neutral if occupied by electrons, positively charged if unoccupied). In this figure, there is a narrow insulating layer between metal and SC which is transparent to flow of electrons. Since there are some acceptor

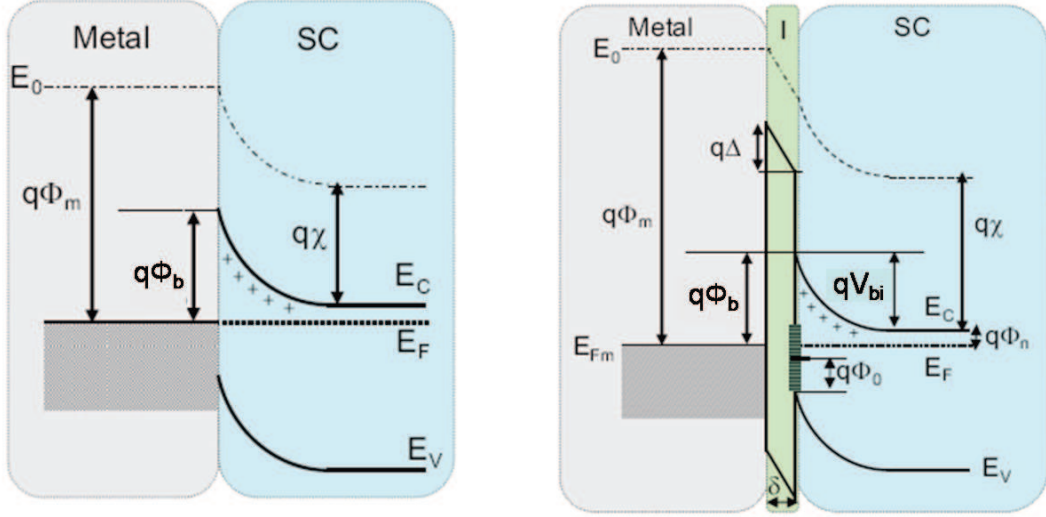


Figure 3.1 : (a) Band diagram of a metal/n-type semiconductor contact, defining the Schottky Barrier Height in the perfect contact limit case [82]. (b) Energy-band diagram of same metal-semiconductor junction with an interfacial layer and interface states [83].

states above ϕ_0 , they will tend to contain electrons and will be negatively charged. It is assumed that the surface state density is constant and equal to D_{it} states/cm²eV. The relation between the surface potential, surface state density, and other semiconductor parameters can be given by [85]:

$$\phi_m - \chi - \phi_b = \sqrt{\frac{2e\epsilon_s N_D \delta^2}{\epsilon_i^2} (\phi_b - \phi_n - \frac{kT}{q})} - \frac{eD_{it}\delta}{\epsilon_i} (E_g - q\phi_0 - q\phi_b) \quad (3.1)$$

here ϵ_o , ϵ_i and ϵ_s are permittivities of vacuum, interfacial layer and semiconductor respectively. The other symbols are explained in Fig. 3.1(b). Given that the interfacial layer is transparent, so $\epsilon_i = \epsilon_o$, the $\frac{2e\epsilon_s N_D \delta^2}{\epsilon_i^2}$ term can be neglected. There can be two limiting cases:

- If one considers that there exists high density of interface states such that $D_{it} \rightarrow \infty$, then the above equation becomes:

$$\phi_b = \frac{1}{q} (E_g - e\phi_0) \quad (3.2)$$

Hence the barrier height is now fixed by the band-gap energy and the potential ϕ_0 . The barrier height is totally independent of the metal work function and the semiconductor electron affinity. The Fermi level becomes 'pinned' at the surface, at the surface potential ϕ_0 . This case is also known as Bardeen's strong pinning limit case [84].

- On the other hand, if one considers that there are no interface states and $D_{it} = 0$, then the above equation reduces to:

$$\phi_b = \phi_m - \chi \quad (3.3)$$

which is the original ideal expression. Thus there is no pinning and the normal Schottky-Mott law applies.

Since the interface state density is not predictable with any degree of certainty, the barrier height must be an experimentally determined parameter. The origin of these interface states can

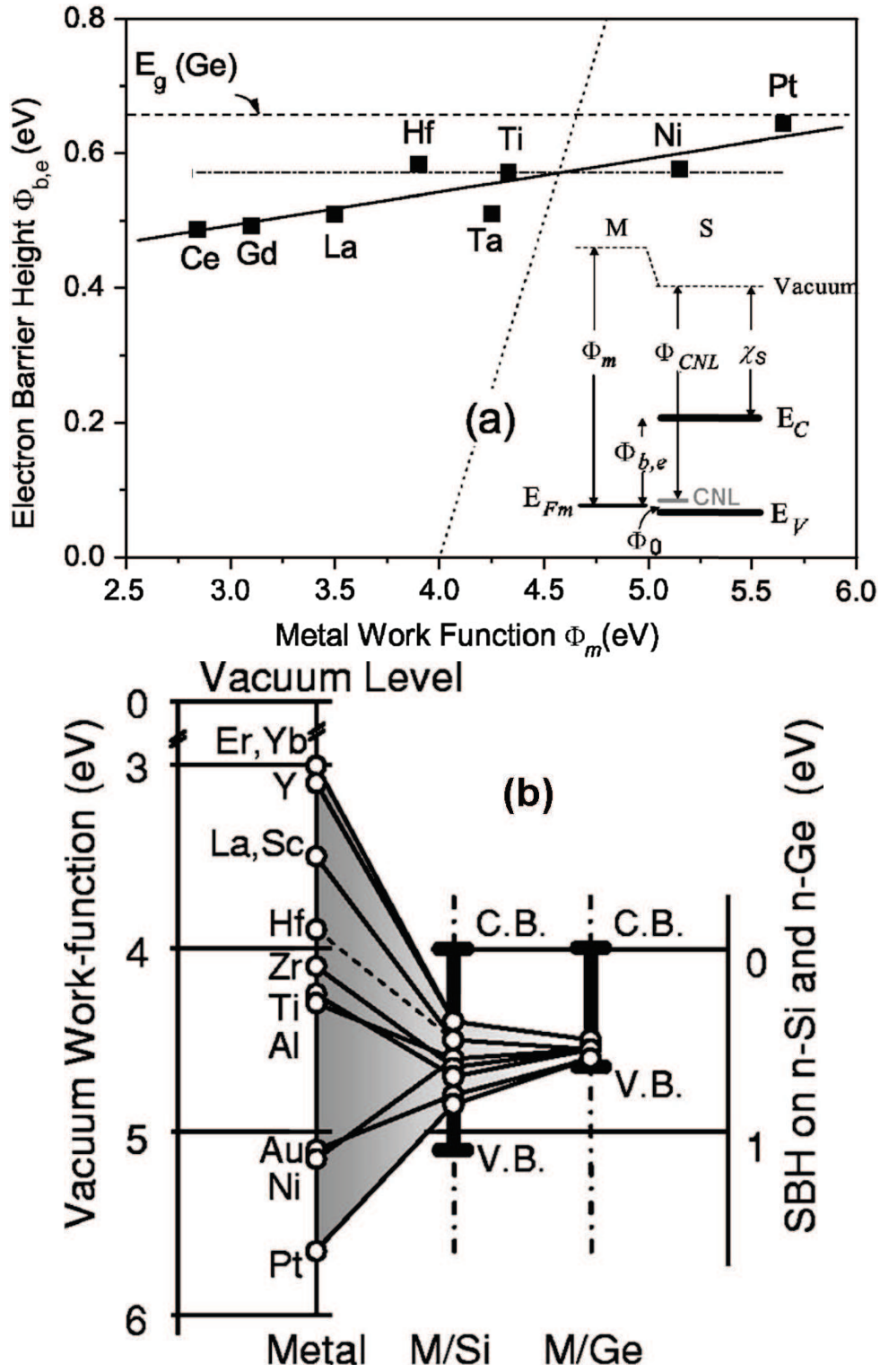


Figure 3.2 : (a) Barrier height for electrons vs metal work function obtained for contact of different metals with Ge. The linear fit gives the pinning factor S of 0.05 [80]. (b) Illustration of the influence of Fermi-level pinning on the Schottky barrier height experimentally obtained for electrons in Si and Ge [81].

be either intrinsic i.e. induced by the atoms of deposited metal or extrinsic i.e. states present at the surface of the semiconductor before metal deposition.

The intrinsic states also referred to as metal-induced gap-states (MIGS) are present within the forbidden band-gap due to the tailing of the wave-functions of electrons of metals into the semiconductor. They originate from the disruption of crystalline periodicity at the interface. Since MIGS follow an exponential decay passed the interface with typical penetration lengths of 4 Å in Ge [85], depinning could be achieved by inserting a thin layer between the metal and Ge substrate. This thin layer blocks the tailing of the metal wave function into Ge and thus reduce the MIGS formation. This have been demonstrated recently by growing thin layers like Si₃N₄, TiO₂, Al₂O₃ and MgO [86–92].

The extrinsic states due to the presence of surface states on the semiconductor surface arise from unsatisfied dangling bonds or other defects before metal deposition [93]. These dangling bonds can be saturated by growing layers like Fe₃Si, Ge₃N₄ or by treating the surface with (NH₄)₂S solution (via bridge-bonding formation) causing depinning of Fermi-level [94–96].

For a moderately doped Ge, the metal-semiconductor contact leads to high SBH (due to FLP) and wide depletion zones (order of μm) (Fig. 3.3(a)). This leads to strong bias dependence of device current (i.e. low currents for reverse bias). Also the contact resistance has strong dependence on temperature due to the dominant thermionic emission transport over the Schottky barrier. For spin injection into semiconductors, these issues are serious and must be solved [97]. Even in the presence of oxide tunnel barrier, only the electrons thermally emitted over the Schottky barrier can tunnel through the oxide barrier. This leads to inefficient spin injection because the electrons injected to Ge originate from the states at elevated energy above the FM Fermi level, which have a reduced spin polarization as compared to those at the lower energy states. Moreover, the high contact resistance i.e. high RA products does not lie in the optimum range in order to observe significant magnetoresistance as discussed in chapter 1.

The contact resistance R_c has the following dependence:

$$\ln(R_c) \propto V_{bi} \quad (3.4)$$

$$\ln(R_c) \propto \frac{1}{\sqrt{N_d}} \quad (3.5)$$

here V_{bi} is build-in potential as shown in Fig. 3.1 and N_d is doping concentration. Hence by decreasing the V_{bi} or the SBH, suitable RA products can be obtained. The SBH in Ge can be decreased by removing the Fermi-level pinning as discussed before. Also increasing the doping concentration in the semiconductor can decrease the contact resistance. If the Ge surface layer is degenerately doped, the depletion zone becomes thin enough and electrons can tunnel through the Schottky barrier. The tunneling probability (T) through a Schottky barrier is given by:

$$T = \exp \left\{ \frac{-4(2m^*)^{1/2}(e\phi_b)^{3/2}}{3eE\hbar} \right\} \quad (3.6)$$

here m^* is the effective mass and E is average electric field in the depletion region given by ($V_{bi}/\text{depletion-width}$). For a doping concentration of $10^{18}/\text{cm}^3$, the depletion width $\sqrt{(2\epsilon V_{bi}/eN_d)}$ becomes 30 nm (assuming $V_{bi} \approx \phi_b \approx 0.5$ eV). This gives the tunneling probability of $\approx \exp(-50)$ which is almost zero. In this case there is no tunneling current. However increasing the doping concentration to $10^{20}/\text{cm}^3$, the depletion width reduces to just 3 nm and tunneling probability increases to $\exp(-5)$ i.e. 0.7 %, leading the electrons to move across the junction through tunneling (Fig. 3.3(b)). A tunneling transport in n-Ge was first shown by Zhou et al. in 2009 using Fe/oxide/n-Ge contacts [98]. By degenerately doping the Ge surface layer by low energy ion-implantation to the order of $10^{19}/\text{cm}^3$, they observed tunneling transport and suitable RA products for spin injection and detection. The surface doping layer sharply reduces the depletion width of the barrier and thus increases its tunneling transparency. These results were promising towards spin injection in Ge.

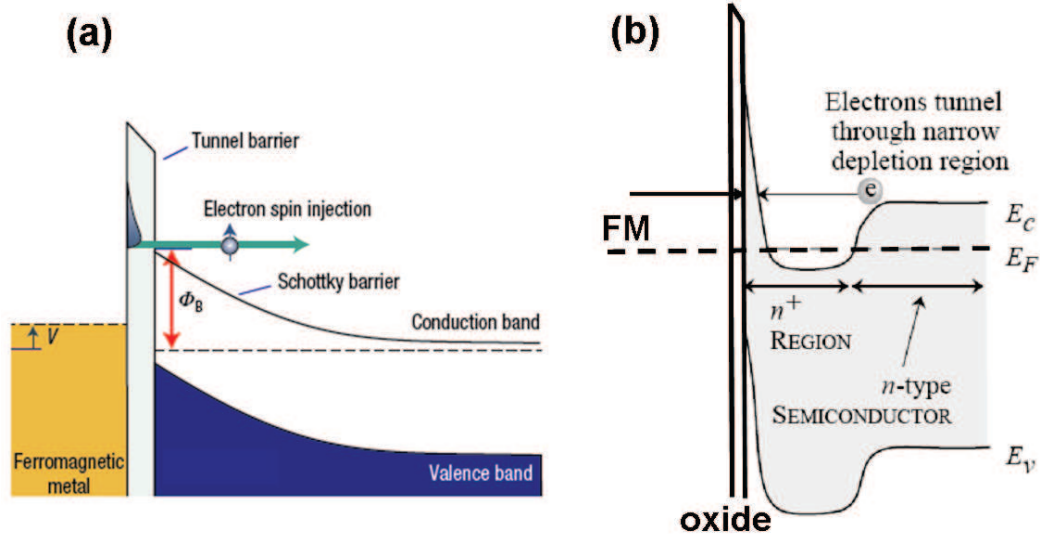


Figure 3.3 : Metal-semiconductor energy band diagrams for moderately and heavily doped semiconductor (image taken from ref [97]).

3.2 Spin injection in Germanium using tunnel barrier

The combination of Ge based high performance MOSFETs and spintronics for non-volatile memory can lead to a next-generation CMOS technology with ultra-low-power consumption. The inversion symmetry of Ge leads to suppression of the Dresselhaus term in the Hamiltonian and hence gives low 'spin-orbit interaction' and high spin diffusion lengths. An electrical spin injection and transport in Ge is a requirement for realization of spintronic based devices. As discussed in the first chapter, this can be achieved by using a tunnel barrier at the FM/Ge interface.

3.2.1 Literature Review

Liu et. al. in 2010 were the first to report electrical spin injection in n-doped Ge nanowires (NWs) using Co/MgO contacts [99]. They performed MR measurements in two-contact and in four-contact non-local geometry (Fig. 3.4(a)). The diameter of their NWs was in range of 80 nm with length of 12 μm . The doping concentration in their NWs was given to be $(5 \pm 2) \times 10^{19} \text{ cm}^{-3}$ and hence the contact resistance between Ge and Co was low leading to RA values lying in the optimum range. They could observe a difference in non-local voltage for parallel and anti-parallel orientations of electrodes. However, they suggested spin diffusion length of order of 100 μm at 4.2 K, which is not reasonable. Moreover, the Hanle effect giving unambiguous evidence of spin injection was not reported.

In the same year, Shen et al. reported spin injection and transport in Ge at room temperature using Ni/Ge/n- $\text{Al}_x\text{Ga}_{1-x}\text{As}$ /GaAs/ p- $\text{Al}_x\text{Ga}_{1-x}\text{As}$ /p-GaAs heterostructure (Fig. 3.4(b)) [100]. The Ge layer was highly doped with a carrier concentration of $3.2 \times 10^{20} \text{ cm}^{-3}$, giving a depletion region of 1-2 nm at Ni/Ge interface. A tunneling transport mechanism was observed due to this tailored-Schottky barrier. The spin polarized carriers were generated in AlGaAs n-i-p junction using optical method and subsequently transported through Ge at the Ni/Ge interface. However for devices based on spintronics applications, an electric means of generation of spin polarized carriers is desired.

Eventually very recently Zhou et al. reported electric spin injection and detection in n-Ge using 4-contact non-local geometry [101]. They used Fe-MgO tunnel contacts on n-doped Ge

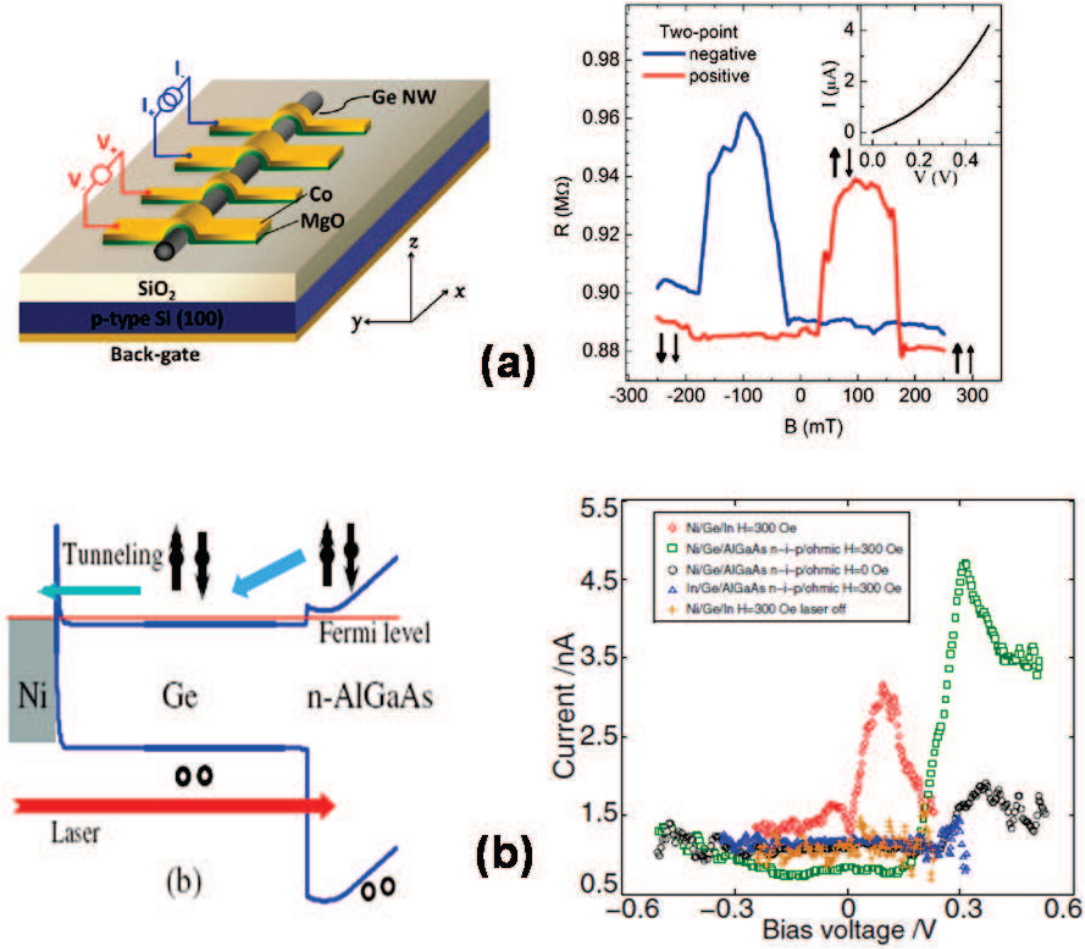


Figure 3.4 : (a) Schematic of Ge NW spin injection device and the MR data obtained by Liu et al. [99] (b) A Simulated band diagram of the Ni/Ge/AlGaAs junction. Helicity dependent photocurrent (HDPC) for different contact combinations is also shown.

having doping concentration of $1 \times 10^{16} \text{ cm}^{-3}$. However a transition layer of 15 nm of highly doped n^+ Ge $2 \times 10^{19} \text{ cm}^{-3}$ was inserted to reduce the interface resistance. They observed non-local MR signal up to 225 K and in Hanle measurements they found spin lifetime of around 1 ns.

Also Saito et al. demonstrated spin injection in p-Ge also using Fe/MgO contacts [102]. The tunneling transport was observed due to absence of the Schottky barrier in metal p-Ge contact. They used 3-terminal geometry and reported direct spin injection into bulk Ge. They found the spin lifetime of around 30 ps. The spin signal was observed till 100 K. Moreover they observed tunneling anisotropic magnetoresistance (TAMR) till room temperature. However, spin injection in n-type Ge is more favorable than in p-type Ge for longer carrier spin diffusion lengths. Indeed s-type conduction band electrons are less sensitive to spin-orbit interaction than p-type valence band electrons.

3.2.2 Results and discussion

Ferromagnetic metals were used as a spin injector since they have high Curie temperature and significant spin polarization. The oxide tunnel barrier between FM/Ge releases the Fermi level pinning and circumvent the problem of conductivity mismatch. In this work Co/FeNi/Al₂O₃ and CoFeB/MgO layers as spin injectors were used.

The experiments were carried out on n-doped germanium-on-insulator substrates (GOI). The substrates were provided by the CEA-LETI and SOITEC company (collaboration with E. Augendre). These substrates were fabricated using the Smart CutTM process and Ge epitaxial wafers (Fig. 3.5) [103]. The original 40-60 nm thick Ge film was transferred onto a SiO₂-capped highly doped Si substrate (B, 10¹⁹cm⁻³) through direct bonding, coarse grinding and chemical removal of the initial Si handle part in a 12% tetramethylammonium hydroxide (TMAH) solution. The transferred Ge film was then n-type doped in two steps: a first step (phosphorus implantation, 3×10¹³cm⁻², 40 keV, annealed for 1h at 550°C) that provided uniform doping in the range of 10¹⁸cm⁻³, and a second step (phosphorus implantation, 2×10¹⁴cm⁻², 3 keV, annealed for 10s at 550°C) that increased surface n⁺ doping to the vicinity of 10¹⁹cm⁻³. The surface of the GeOI was finally capped with amorphous SiO₂ to prevent surface oxidation.

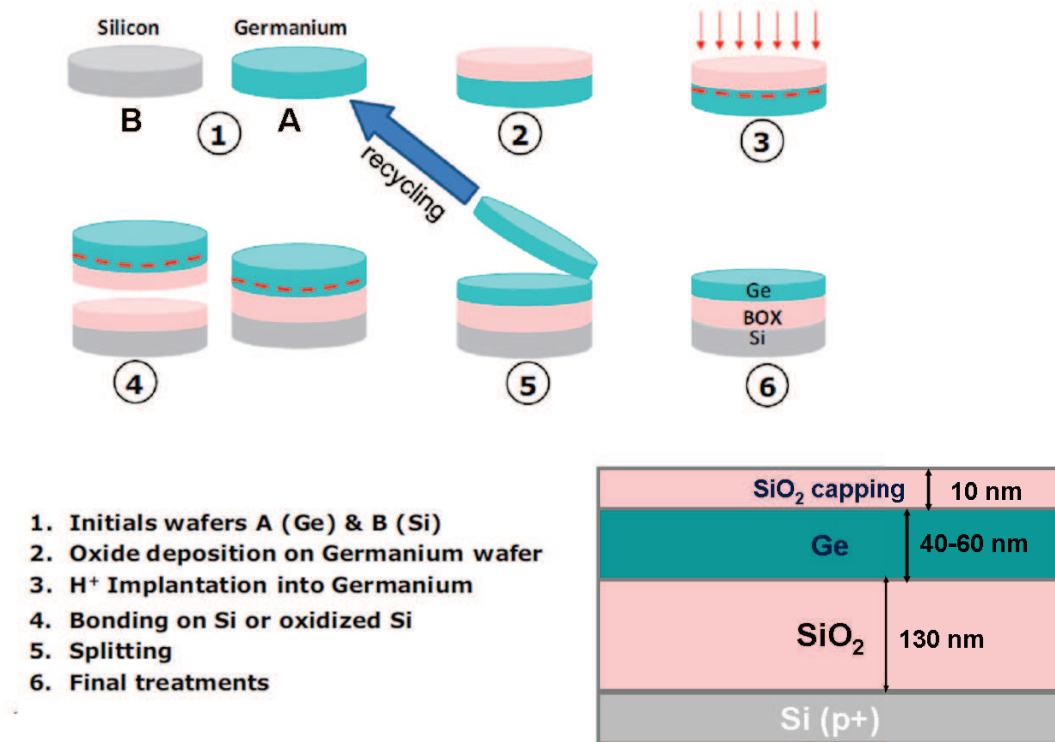


Figure 3.5 : Schematic flow of the Smart CutTM process to manufacture GOI wafers along with a sketch of the GOI wafer used in this work showing the thickness of different layers.

As discussed before there is strong Fermi-level pinning in Germanium close to the valence band which leads to high Schottky barrier height and large depletion width for metal/n-Ge interface. The surface doping of the Ge layer is required to facilitate the tunneling transport. The surface doping layer sharply reduces the thickness of the barrier and increases its tunneling transparency. From simulation by the program of the stopping and range of ions in matter (SRIM) [104], the width of highly doped n⁺ layer was found to be 5-10 nm from the surface (Fig. 3.6).

Co/FeNi/Al₂O₃ layers for spin injection into Ge

The GOI substrates were treated with 10% hydrofluoric acid solution to remove the SiO₂ capping layer and quickly introduced in the sputtering machine. Aluminium layer of 1.6 nm was grown and treated with oxygen plasma to form a Al₂O₃ thin layer of around 2-3 nm. Then a stack of

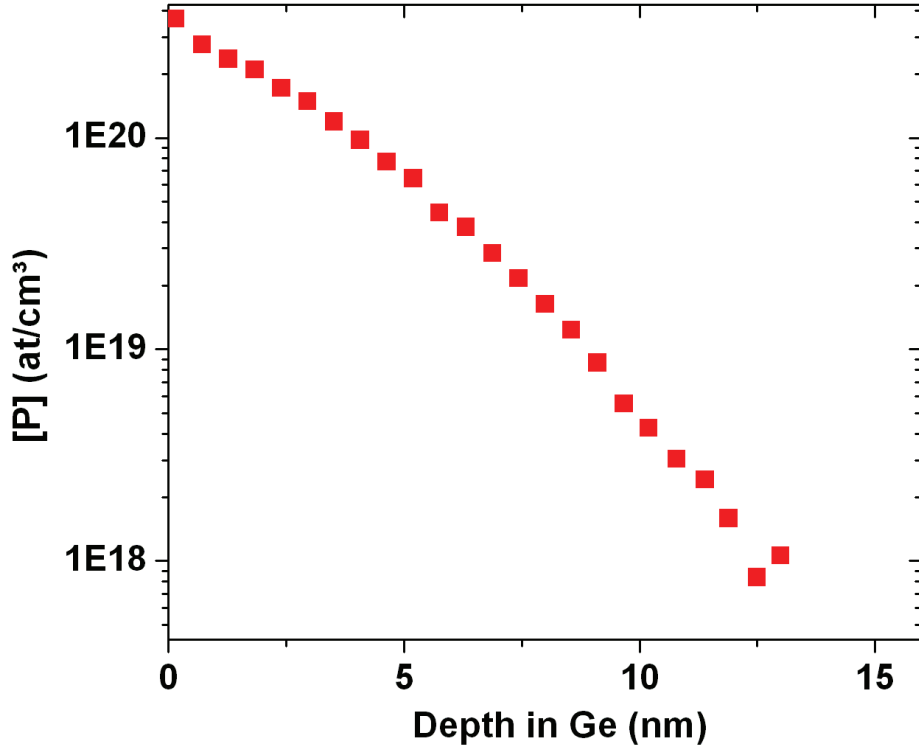


Figure 3.6 : A SRIM simulation of Phosphorus implanted depth profile in Germanium that is expected to remain unchanged after the very short anneal at 550° C

5 nm permalloy (Py), 20 nm Co and 10 nm Pt was grown to have in-plane anisotropy. Adding Co likely helps the Py/Co to be in a single domain state due to its anisotropy and exchange coupling. This stack gives the coercive field to be 10 Oe found by AMR measurements on a 2D film and a single electrode (Fig. 3.7).

The sample was processed using standard optical lithography and dry etching to have $150 \times 400 \mu\text{m}^2$ electrodes. Finally ohmic contacts of Ti/Au with dimensions $300 \times 400 \mu\text{m}^2$ were deposited to form three-terminal geometry. The schematic diagram of the structure is shown in Fig. 3.8. The edge-to-edge distance between contacts A and B or contacts B and C is $125 \mu\text{m}$. The processed sample was fixed on a chip and after wire bonding it was entered into a cryostat.

In order to find the dominant transport mechanism, the current-voltage (I-V) characteristics between the tunnel contact (B) and one of the ohmic contacts (A) was done. A non-linear behavior in IV curves at room temperature is seen which corresponds to a tunneling behavior. The confirmation for tunneling transport was done by performing temperature dependence of IV characteristics. Fig. 3.9 shows non-linear behavior of IV curves and their weak dependence on temperature: $R(10 \text{ K})/R(300 \text{ K}) \approx 8$ for a DC current of $0.5 \mu\text{A}$. This proves that tunneling is the dominant mechanism for the transport. The RA product of the tunnel contact at different temperatures is also shown. This tunneling mechanism is made possible by the specific shape of the Schottky barrier in Ge, thin enough to allow a tunneling transmission through it and low enough to limit its own resistance.

The minimum interface resistance threshold required for spin injection into Ge is given by : ρl_{sf} , where $\rho = 10 \text{ m}\Omega\cdot\text{cm}$ is resistivity of the Ge channel and l_{sf} is spin diffusion length taken to

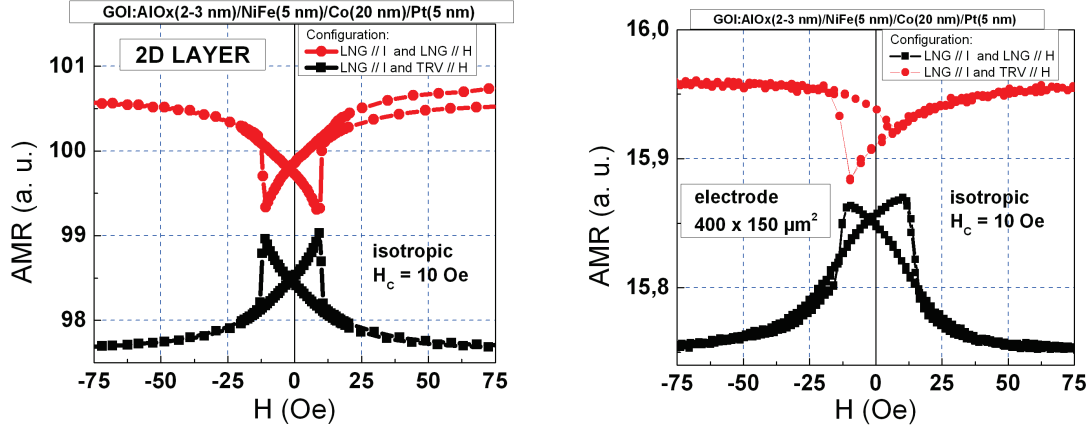


Figure 3.7 : Anisotropic magnetoresistance measurements on a $\text{GOI}/\text{Al}_2\text{O}_3(2-3 \text{ nm})/\text{NiFe}(5 \text{ nm})/\text{Co}(20 \text{ nm})/\text{Pt}(5 \text{ nm})$ stack (a) for a 2D film and (b) for a single $150 \times 400 \text{ } \mu\text{m}^2$ electrode. Here LNG and TRV represent the longitudinal and transverse directions respectively.

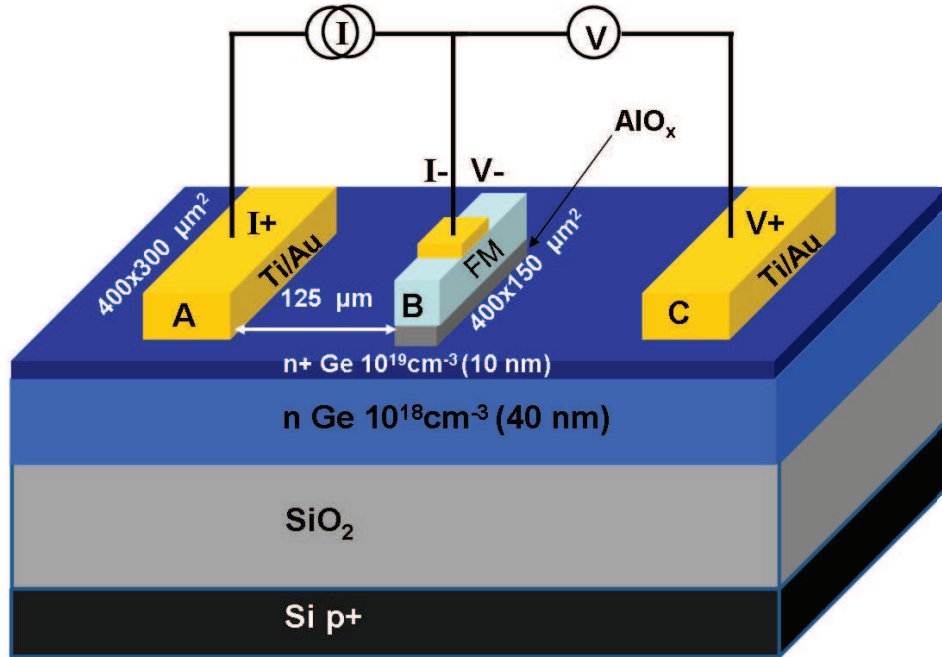


Figure 3.8 : Schematic image of three-terminal geometry used for spin injection in Germanium.

be of the order of $1 \text{ } \mu\text{m}$ from ref. 101. Since the channel thickness ($w = 30 \text{ nm}$) is smaller than the l_{sf} , the minimum threshold becomes: $(\rho l_{sf}^2)/w \approx 10 \text{ k}\Omega \cdot \mu\text{m}^2$. In the whole temperature range, the RA products obtained exceed this threshold value. The resistivity of $10 \text{ m}\Omega \cdot \text{cm}$ was taken from the literature for doping concentration of 10^{18} /cm^3 . However the 'true' resistivity may be less due to the presence of thin n^+ layer. This value was taken for room temperature and since the Ge channel is degenerated (as seen from IV curves), not much difference in resistivity is expected with change in temperature.

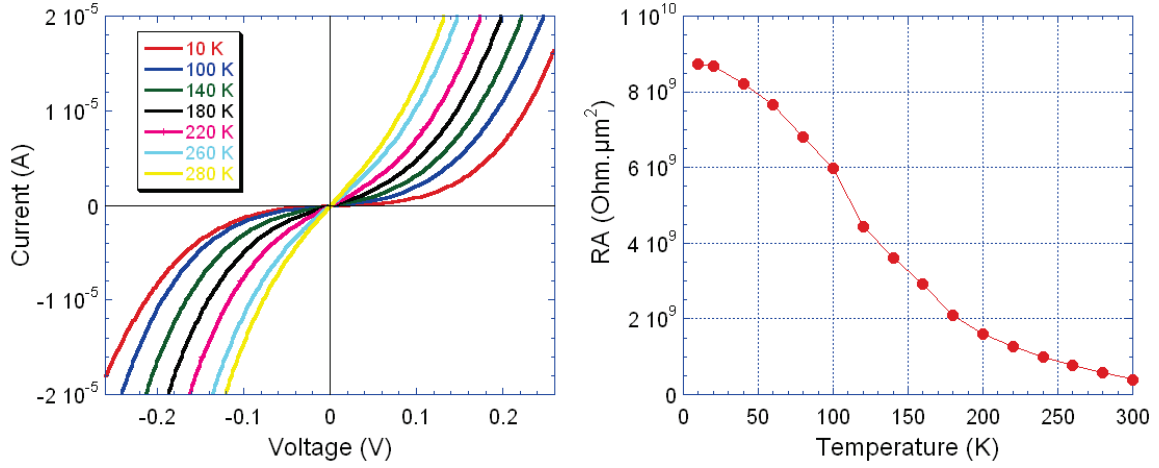


Figure 3.9 : (a) The current voltage characteristics between the tunnel contact and one of the ohmic contact. (b) The dependence of RA product of tunnel contact with temperature.

For spin injection experiments, the magnetic moment of the tunnel electrode was aligned parallel to the film plane by applying a high field of 2 T and to make sure that Py layer is in a single domain state. A constant current I_{AB} was passed between contacts A and B (DC current source). When the current I_{AB} is positive, electrons are flowing from Ge channel into contact A and hence injecting spin polarized electrons from FM into Ge channel at tunnel contact B (contact B is reverse biased). There is accumulation of spin polarized electrons under the electrode (Fig. 3.10). For negative values of I_{AB} , there is spin extraction from Ge channel into FM contact and hence making contact B forward biased. There is still spin accumulation under the electrode but with minority spin polarization because of preferential transmission of majority spin electrons into the FM tunnel contact.

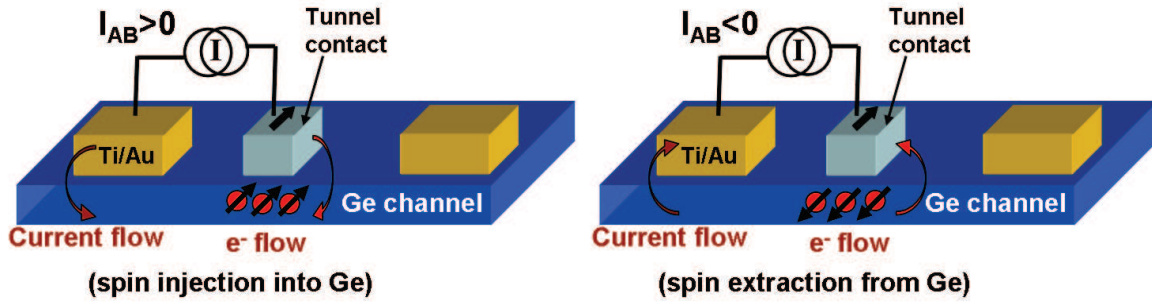


Figure 3.10 : Schematic diagram explaining the flow of current and accumulation of spin polarized electrons in germanium channel.

A small transverse field B_{\perp} was applied to cause precession of the spins in the Ge and hence reducing the spin accumulation (Hanle effect, see section 1.1.3). A voltage change V_{BC} as a function of field B_{\perp} was measured between contacts B and C. Fig 3.11 shows Hanle-effect curves at 10 K for $I_{AB} = -10 \mu\text{A}$ (-0.217 mV) and $-20 \mu\text{A}$ (-0.274 mV) for transverse field ranging from $\pm 0.6 \text{ T}$ (out-of-plane curves). A voltage change of V_{BC} of 0.1 mV is observed, hence providing evidence of spin accumulation and injection in Ge. As described before, the Hanle curves can be described by a Lorentzian shape given by $\Delta V = \frac{\Delta V_0}{1 + (\Omega \tau_{sf})^2}$, where τ_{sf} is spin lifetime and Ω is the Larmor frequency ($\Omega = g \mu_B B_{\perp} / \hbar$). Here $g = 1.6$ is the Landé factor for

Ge ([64]) and μ_B is Bohr magneton.

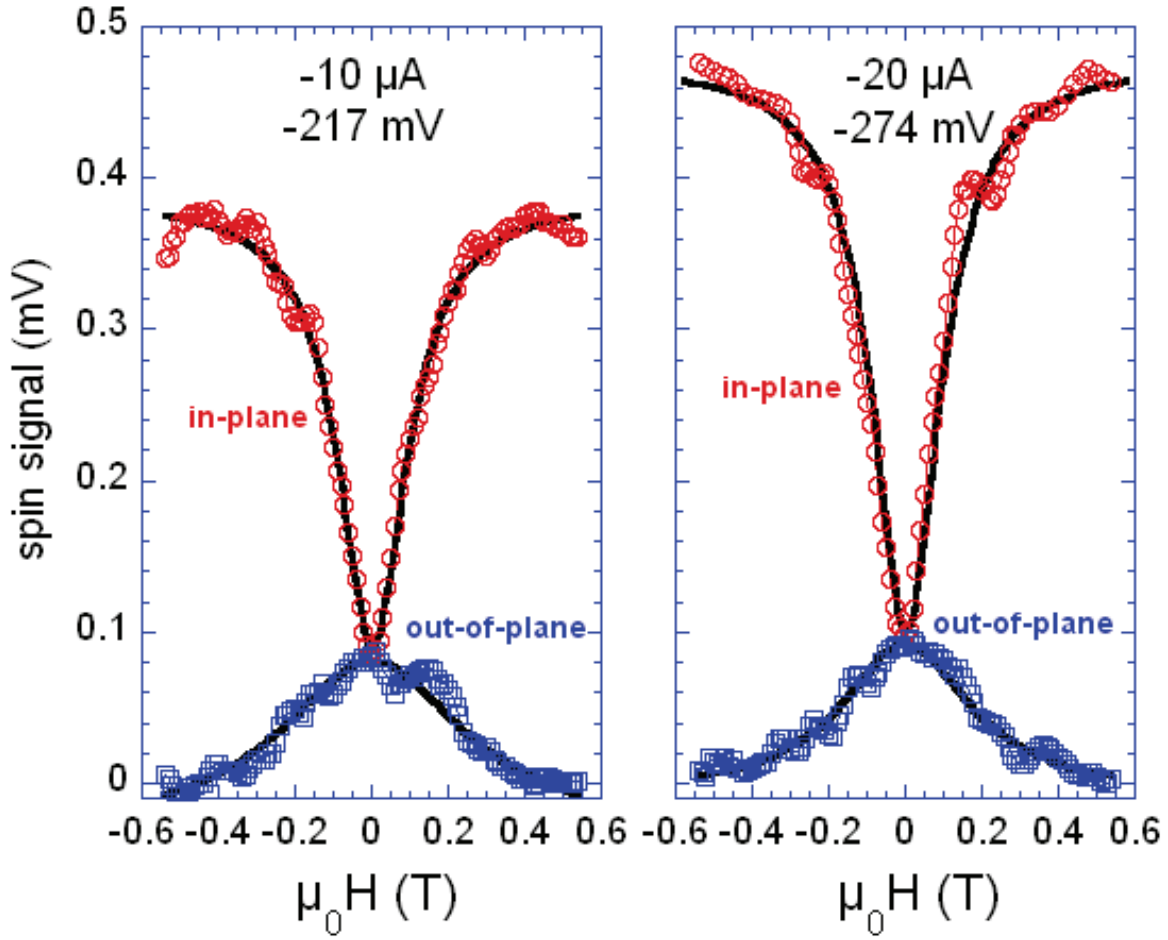


Figure 3.11 : Low magnetic field dependence of the spin signal for two different bias currents $-10\mu A$ (-217 mV) and $-20\mu A$ (-274 mV) showing both Hanle (out-of-plane) and inverted Hanle (in-plane) effects. Measurements were performed at 10 K.

After fitting the Hanle curves, a spin lifetime of 35 ps is extracted which is much shorter than 1 ns reported by Zhou et al in n-Ge at 4 K [101]. This can be explained by local magnetostatic fields (B^{ms}) arising from finite surface roughness at the interface [44]. In Fig. 3.12 these magnetostatic fields are shown for an interface with a sinusoidal profile with period λ . The ferromagnetic electrodes have in-plane magnetization \vec{M} and hence pointing parallel to the global interface. If the interface is completely flat, there will be no magnetostatic charges and hence no magnetostatic fields from the in-plane magnetized electrodes outside the ferromagnet. However in case of rough interface, these magnetostatic fields are present due to presence of magnetic surface charges and can penetrate into the semiconductor channel. These local fields are random i.e. inhomogeneous in magnitude and direction and change sign periodically. The magnitude of these fields increases with the roughness amplitude and also proportional to the magnetization M_s of the ferromagnet. The field strength decays exponentially as one goes away from the interface into the Ge channel. These fields influence the spin precession and severely reduce the spin accumulation.

This phenomenon can be verified by inverted-Hanle curves where an external field is applied in-plane ($B_{||}$) to rotate the total magnetic field (vector sum of B^{ms} and $B_{||}$) into the direction of the magnetization. This reduces the angle between the injected spins and the axis of precession. The precession of spins is suppressed and the spin accumulation increases as a function of $B_{||}$.

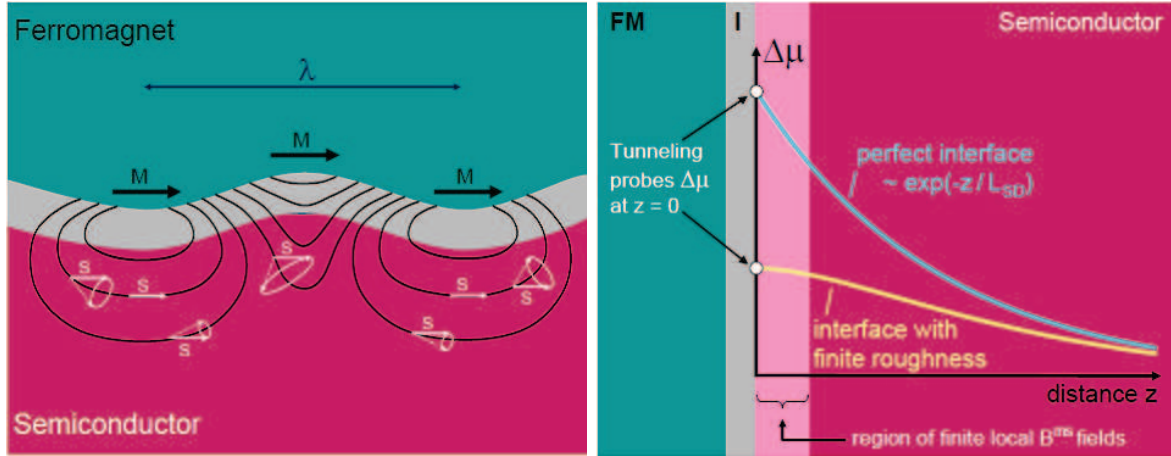


Figure 3.12 : A FM/I/SC interface with a finite roughness creating local interface magnetic fields. In these inhomogeneous local fields, spins precess on different trajectories. The spin accumulation is drastically reduced where the interface has finite roughness as compared to a perfect smooth interface [44].

This phenomenon was shown recently in case of Si and GaAs [44].

The inverted-Hanle curves at 10 K are shown in Fig. 3.11, where a voltage change of 0.36 mV is seen for a current of $-20 \mu\text{A}$ for in-plane field ranging from $\pm 0.6 \text{ T}$. The application of this in-plane magnetic field led to a recovery of the spin accumulation, reaching the ideal value (that would be obtained without any precession) for large enough B_{\parallel} . The total spin signal is defined as the difference between the maximum in-plane and minimum out-of-plane values : $V_{BC} = 0.46 \text{ mV}$ at 10 K and $-20 \mu\text{A}$.

The true spin signal can also be confirmed by application of high magnetic fields during both Hanle-effect and inverted-Hanle effect measurements. During Hanle-effect, when B_{\perp} is increased from zero, initially there is decrease in spin signal due to spin precession but on further increasing the field the magnetization of the FM electrodes starts rotating out of plane. This leads to sharp increase in spin signal since the spins in Ge are getting aligned with B_{\perp} and hence reducing precession. When the magnetization of electrodes becomes totally out-of-plane, the precession completely stops and a maximum spin signal is observed. This signal should be identical to the saturation value of the inverted Hanle curve, for which magnetization, spins in the Ge and B_{\parallel} all are in the same direction and hence precession is stopped too. In Fig. 3.13 both Hanle-effect and inverted-Hanle effect curves are shown for high fields up to $\pm 5 \text{ T}$ and curves saturate and perfectly coincide above the cobalt demagnetization field of 1.8 T. A true spin signal of 0.46 mV is obtained at 10 K and $-20 \mu\text{A}$.

It should be noted that the minimum out-of-plane value may not necessarily coincide with the total loss of spin accumulation since the magnetic moment of the electrode starts to align along the applied field when reaching a fraction of the demagnetizing field. In three-terminal measurements, this spin signal is given by $V_{BC} = \gamma \Delta\mu / 2e$, where γ is spin transmission coefficient, for $\text{Al}_2\text{O}_3/\text{Py}$ interface it is 0.3 [43] and $\Delta\mu$ is the spin accumulation. For $V_{BC} = 0.46 \text{ mV}$, the value of spin accumulation is found to be $\Delta\mu = 3.07 \text{ meV}$ at 10 K.

The spin resistance-area product is proportional to γ^2 , since the spin accumulation depends on the polarization of the injected current and second γ factor comes for the detection of this spin accumulation. As discussed in section 1.1.1, the value expected by theory is given by: $R_s \cdot A(\text{expected}) = \gamma^2 \rho l_{sf}^2 / w$ (for contact width greater than spin diffusion length). It is calculated to be $R_s \cdot A(\text{expected}) = 0.3 \text{ k}\Omega \cdot \mu\text{m}^2$. However, the spin RA product obtained from our data is given by $R_s \cdot A(\text{obtained}) = (\Delta V / I) \cdot A$, hence for $\Delta V = 0.46 \text{ mV}$, $I = -20 \mu\text{A}$ and contact

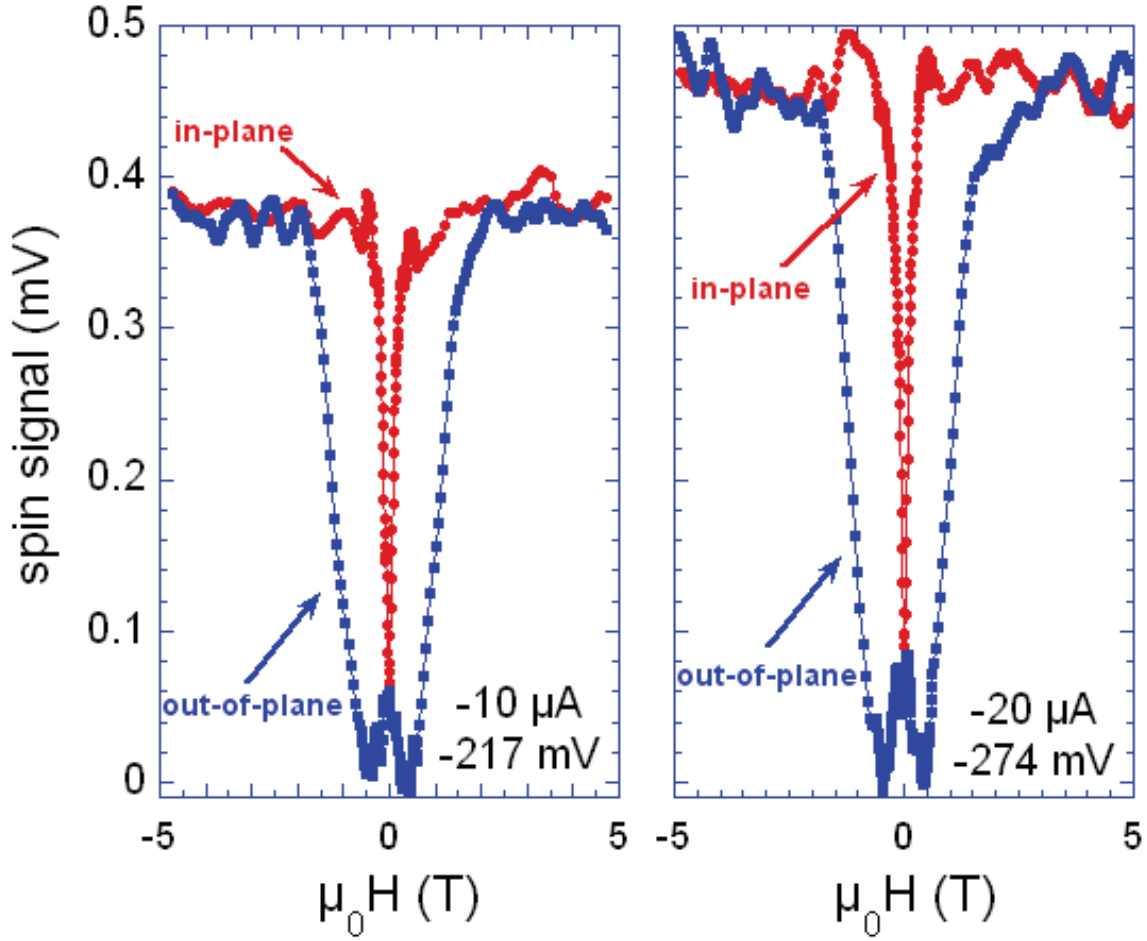


Figure 3.13 : High magnetic field dependence of the spin signal for two different bias currents $-10\mu A$ (-217 mV) and $-20\mu A$ (-274 mV) showing both Hanle (out-of-plane) and inverted Hanle (in-plane) effects. Measurements were performed at 10 K.

area $A = 150 \times 400 \mu m^2$, it becomes $R_s.A(\text{obtained}) = 1380 \text{ k}\Omega.\mu m^2$, which is almost four-orders of magnitude higher than the expected value. The spin diffusion length of $70 \mu m$ extracted from this value is also unrealistic. This enhancement of spin signal have also been observed by other groups [43, 102, 105, 106].

The origin of this huge difference is still unclear, however the possible explanations can be:

- The variations in thickness and composition of the oxide tunnel barrier ([43]). These can create inhomogeneities in the tunnel current which is well known in tunnel junctions, making real tunnel area much smaller than the whole geometric area. The local current density becomes much larger and hence giving large spin accumulation as compared to the average current density.
- Spin accumulation in the localized states. These localized states may be either due to Phosphorus donors in the depletion layer or due to the surface states at the Al_2O_3 interface (large Schottky barrier between bulk bands and the interface states). This was proposed by Tran et al. in case of Co- Al_2O_3 -GaAs and can explain the unexpected large spin signal [105]. In our case of Py- Al_2O_3 -Ge, it is believed that the enhancement of spin-signal by four orders of magnitude through localized states is at play and is discussed below in detail.

In presence of a large Schottky barrier, the interface states and the bulk bands are well

separated (Fig. 3.14). The interface or localized states (LS) act as a confining layer which has bias dependent resistance. A two-step tunneling (or sequential tunneling) occurs via these localized states and spin accumulation in these states can be larger as compared to the Ge channel. The spin accumulation in these LS ($\Delta\mu_{LS}$) and in the bulk Ge ($\Delta\mu_{ch}$) can be written as [105]:

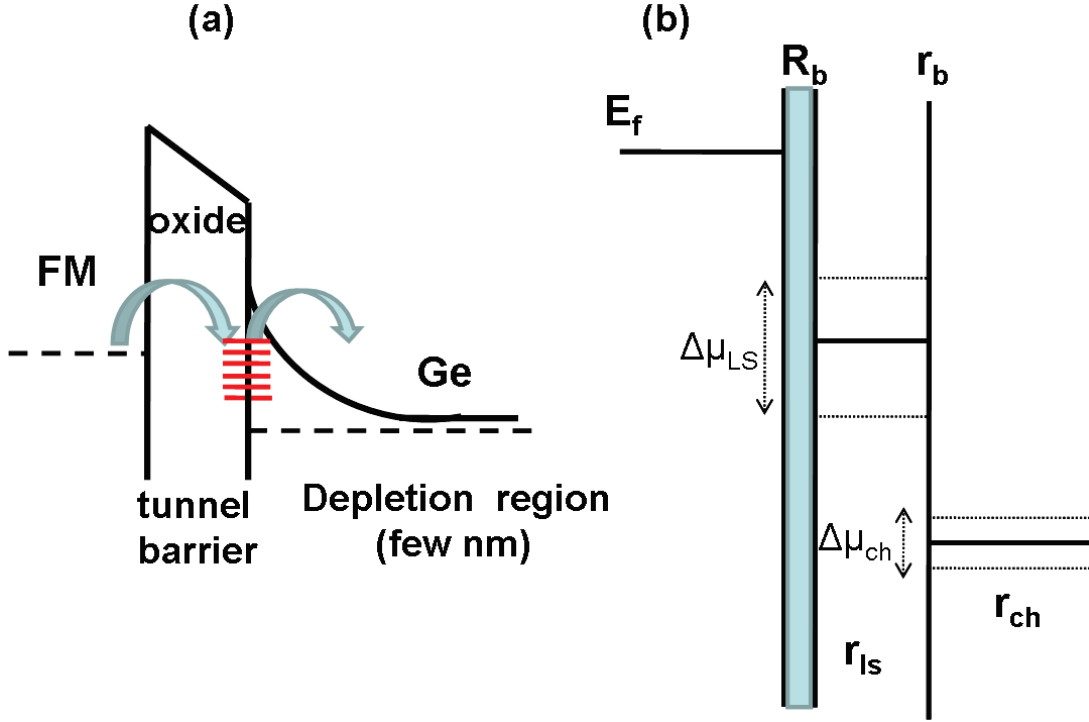


Figure 3.14 : (a) The localized interface states present due to large Schottky barrier which can lead to two-step tunneling. (b) The localized states acts as confining layer and the spin accumulation in these states can be larger than in the semiconductor channel.

$$\Delta\mu_{LS} \approx 2e\gamma j \frac{r_{LS}(r_{ch} + r_b)}{r_{LS} + r_{ch} + r_b} \quad (3.7)$$

$$\Delta\mu_{ch} \approx 2e\gamma j \frac{r_{LS}r_{ch}}{r_{LS} + r_{ch} + r_b} \quad (3.8)$$

here r_{LS} is spin resistance associated with the LS, r_{ch} is spin resistance of the n-Ge channel and r_b is the bias dependent leakage resistance at the interface between LS and n-Ge. Hence a large leakage tunnel resistance r_b can lead to a large spin accumulation in the LS layer, $\Delta\mu_{LS} \approx 2e\gamma j r_{LS}$. This occurs and can be observed experimentally when $r_b \gg r_{LS} \gg r_{ch}$. This also leads to the reduction in spin accumulation in Ge channel since $\Delta\mu_{ch} \ll 2e\gamma j r_{ch}$, compared to the direct injection into the channel without sequential tunneling. However, for low leakage resistance i.e. for $r_b \ll r_{LS}$ and $r_{ch} \ll r_{LS}$, direct tunneling into Ge channel occurs and spin accumulation in channel becomes the same as without localized states. This model was proposed by Tran et al. [105] and explains the enhancement of spin signal.

The Hanle-effect and inverted-Hanle effect curves were also fitted by estimating the local magnetostatic fields B^{ms} . In order to evaluate the local fields B^{ms} , atomic force microscopy (AFM) measurements were performed on GOI wafers after alumina deposition. The AFM images are shown in Fig. 3.15. Indeed a RMS roughness of 0.4 nm was found with a correlation

length of 45 nm. This confirms the roughness of the interface and hence the inverted-Hanle effect. Then a regular array of magnetic charges was considered with a period of 45 nm and the three components (B_x^{ms} , B_y^{ms} , B_z^{ms}) of the magnetostatic field acting on injected spins were calculated.

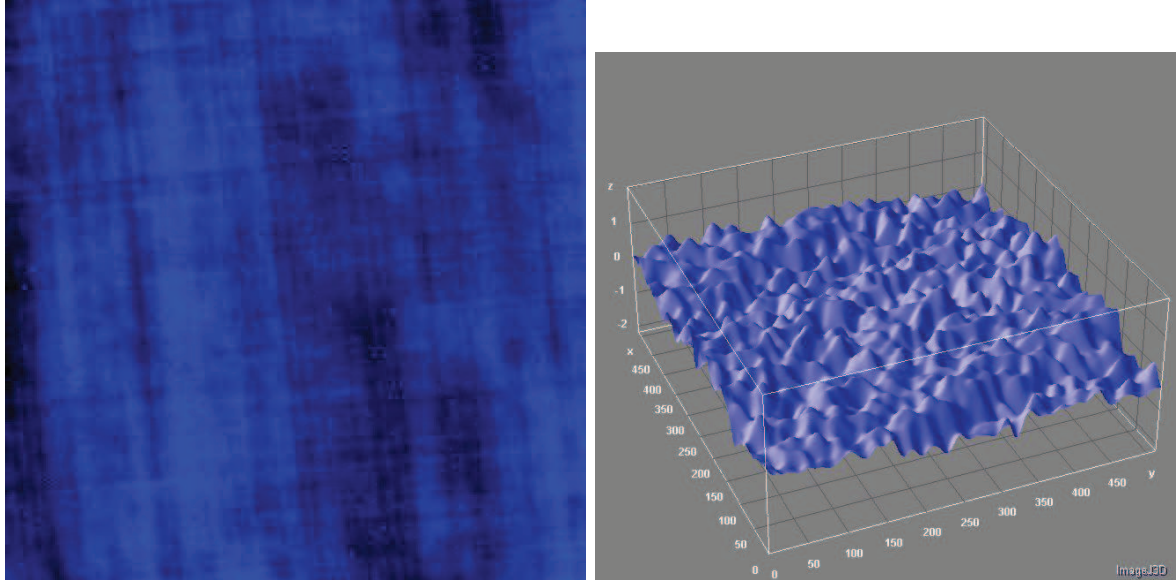


Figure 3.15 : Atomic force microscopy (AFM) images of GOI wafer after alumina deposition clearly shows that the surface is rough and a RMS roughness of 0.4 nm was observed.

The model given in ref 44 was used. The dynamics of spin density \vec{S} is given by (neglecting spin drift):

$$\frac{\partial \vec{S}}{\partial t} = \vec{S} \times \Omega_L + D \nabla^2 \vec{S} - \frac{\vec{S}}{\tau_s} \quad (3.9)$$

where $\Omega_L = (\Omega_x, \Omega_y, \Omega_z) = (g\mu_B/\hbar)(B_x, B_y, B_z)$. In case of spin accumulation in localized states, the spin diffusion term can be ignored. Therefore in presence of a homogeneous external field B^{ext} , the total field experienced by spin density will be given by: $B_i = B_i^{ext} + B_i^{ms}(x, y, z)$ with $i = x, y, z$. By solving the above equation, the steady state solution for spin density is found to be:

$$S_x = S_o \left\{ \frac{\Omega_x^2}{\Omega_L^2} + \left(\frac{\Omega_y^2 + \Omega_z^2}{\Omega_L^2} \right) \left(\frac{1}{1 + (\Omega_L \tau_s)^2} \right) \right\} \quad (3.10)$$

$$S_y = S_o \left\{ \frac{\Omega_x \Omega_y}{\Omega_L^2} - \left(\frac{\Omega_x \Omega_y}{\Omega_L^2} + \Omega_z \tau_s \right) \left(\frac{1}{1 + (\Omega_L \tau_s)^2} \right) \right\} \quad (3.11)$$

$$S_z = S_o \left\{ \frac{\Omega_x \Omega_z}{\Omega_L^2} - \left(\frac{\Omega_x \Omega_z}{\Omega_L^2} - \Omega_y \tau_s \right) \left(\frac{1}{1 + (\Omega_L \tau_s)^2} \right) \right\} \quad (3.12)$$

here $\Omega_L^2 = \Omega_x^2 + \Omega_y^2 + \Omega_z^2$ and $\Omega_i = \Omega_i^{ext} + \Omega_i^{ms}(x, y, z)$.

Now the potential related to the local magnetostatic charges is periodic and its laplacien is zero ($\nabla^2 = 0$), so at a distance z from the surface it can be written as:

$$V = \frac{M_s}{\sqrt{8w}} \exp(-\sqrt{2}wz) \sin(wx) \sin(wy) \quad (3.13)$$

The local fields perpendicular to the film plane i.e. B_z at a given distance z becomes:

$$B_z = -\frac{\partial V}{\partial z} = \frac{M_s}{2} \exp(-\sqrt{2}wz) \sin(wx) \sin(wy) \quad (3.14)$$

Similary for x-direction it can be written as:

$$B_x = -\frac{\exp(-\sqrt{2}wz) M_s \cos(wx) \sin(wy)}{2\sqrt{2}} \quad (3.15)$$

here w is given by $2\pi/\lambda$ and $\lambda = 45$ nm is the correlation length calculated from AFM images. Taking into account the total experienced field ($B^{ext} + B^{ms}$), the expression of Ω_x, Ω_y and Ω_z was replaced in eqn. 3.10. The calculations were focused on the S_x component, since in electrical detection using the same ferromagnetic tunnel contact only this component is relevant (the tunnel resistance is proportional to the projection of the spin accumulation onto the detector magnetization). For fitting the curves following parameters were used: $\tau_{sf} = 1$ ns ([101]) and $\mu_o M_s = 0.9$ T (for Py). The fits were same as long as $\tau_{sf} \gg 35$ ps. The results are shown in Fig. 3.16. The agreement with inverted Hanle effect is almost perfect whereas for Hanle measurements the spin signal seems not to reach its minimum value probably because the FM magnetization starts to rotate out-of-plane at low field as discussed previously. The best agreement with experimental curves is found at a depth of 6 nm away from the FM/ Al_2O_3 interface i.e. 3-4 nm deep in the Ge layer. This means that there is trap-assisted tunneling due to the traps located in the depletion layer of Ge. It was recently shown that in phosphorus-doped Silicon, long spin-life times of the order of 1 ns are due to the trapping and emission of spin-polarized electrons from shallow phosphorus impurity-related states [107]. Similarly, in our case, there can be two-step tunneling through localized traps due to the ionized P donors. Since the surface layers of Ge are highly doped, there is high density of traps and spin accumulation in traps may give enhanced spin signal. The real concentration profile of phosphorus dopants could be such that there is maxima at 3-4 nm from the surface.

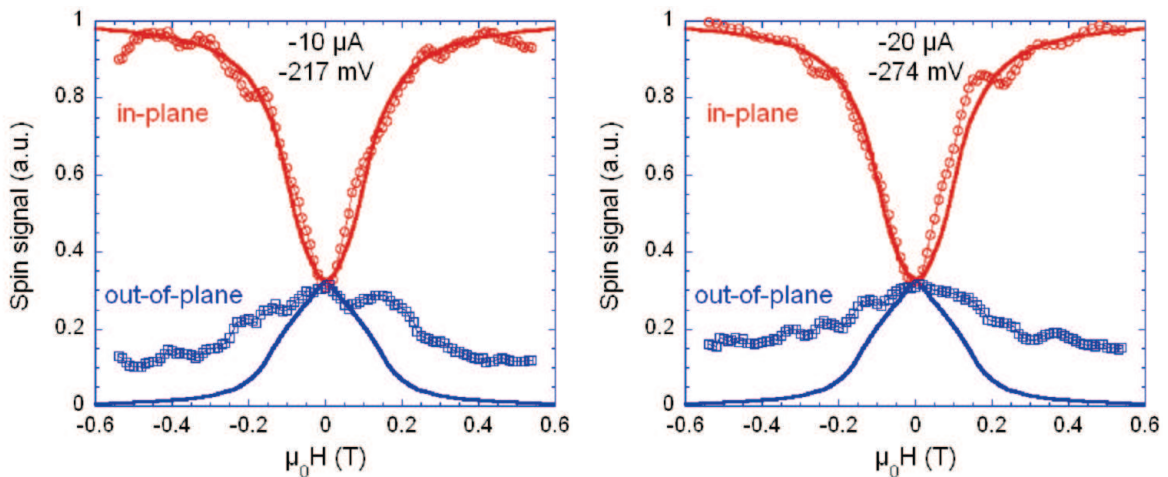


Figure 3.16 : Comparison between experimental (open symbols) and calculated (solid lines) spin signals for in-plane and out-of-plane configurations at $-10\mu\text{A}$ and $-20\mu\text{A}$. Data were normalized to the maximum value.

The bias dependence of spin signal i.e. evolution of voltage V_{BC} with different DC currents (I_{AB}) was also studied. As discussed before on reversing the bias i.e. changing the direction of current, the Hanle and inverted-Hanle curves change the sign. The variation of spin signal V_{BC}

with the bias current is shown in Fig. 3.17(a). The IV characteristics of the tunnel contact is also shown in the same plot. It is observed that the spin signal is increasing with the current density. The dependence is weaker on the injection side and this may be due to the bias dependence of the detector efficiency [108] or the spin bottleneck effect [109] i.e. the spins flowing into the Ge channel face resistance generated by spin accumulation in the Ge within the spin diffusion length which is absent on extraction of these electrons.

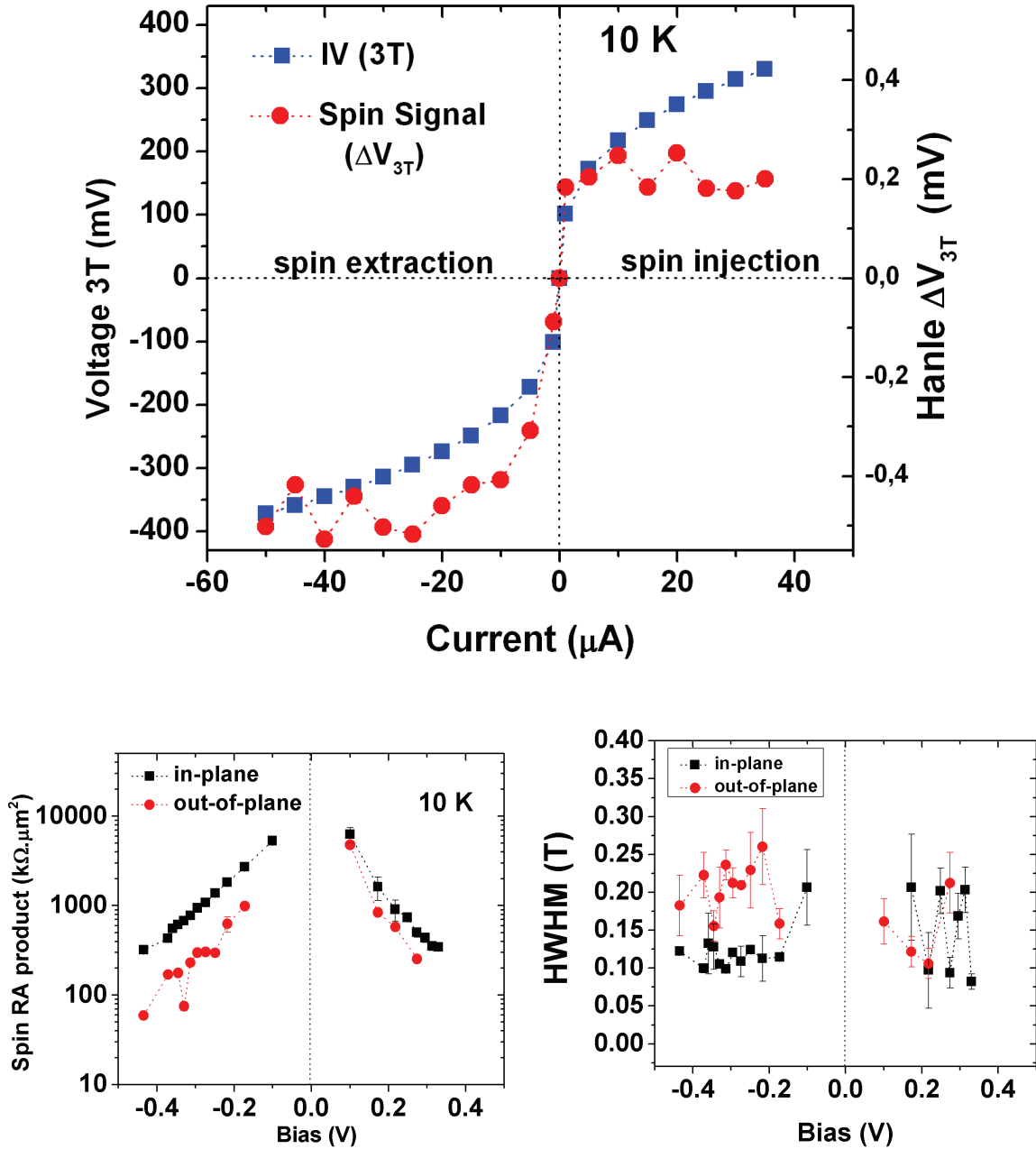


Figure 3.17 : (a) The total spin signal (ΔV_{3T}) and the I-V characteristics of the tunnel contact in 3T geometry, (b) The Spin RA product and (c) Half-width-at-half-maximum obtained for Hanle and inverted-Hanle geometry at 10 K.

The normalized spin signal i.e. $\Delta V/J$ or the spin RA product as a function of bias is shown in

Fig. 3.17(b). It is observed that spin RA product is almost symmetrical with respect to zero bias and shows a huge variation with bias. This can be explained by two-step tunneling model [105]. At lower bias, due to the depletion zone, the time taken by electrons to escape localized states and enter into Ge is long and the spin accumulation in these localized states enhances the spin signal as shown previously in Fig. 3.14. Also the effective spin lifetime is given by the localized-states spin lifetime. However on increasing the bias the direct tunneling into conduction band becomes dominant (Fig. 3.18). For high reverse bias, where the conduction band is well pulled down the FM Fermi level, the electron injection into the conduction band becomes dominant as they are taken away from the interface by strong electric field. The effective spin lifetime becomes closer to the intrinsic value. Similarly for high forward bias, the depletion layer is reduced and the electrons can easily tunnel from Ge conduction band into the FM.

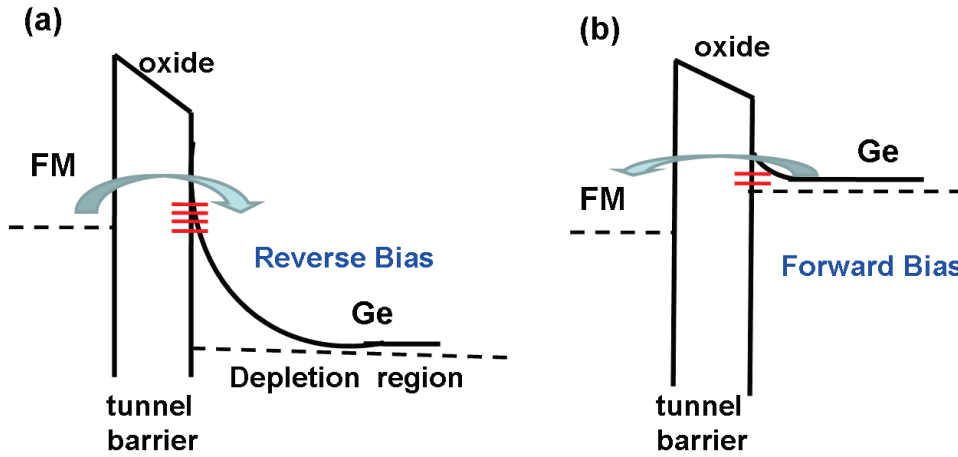


Figure 3.18 : At high forward and reverse bias the direct tunneling from conduction band becomes dominant.

In Fig. 3.17(c), full-width-at-half-maximum (FWHM) (which gives the spin lifetimes) extracted from Hanle and inverted Hanle curves are shown and they are almost constant with DC current. This behavior supports the assertion that the Hanle curve broadening leading to an underestimation of spin lifetime and inverted Hanle effect are not due to intrinsic spin relaxation mechanisms but rather to random magnetostatic fields arising from interface roughness.

The temperature dependence of spin signal and spin lifetime was also studied at bias current of $I = -10 \mu\text{A}$ and $I = -20 \mu\text{A}$. When experiments were done in Hanle geometry, the curves obtained were very noisy on increasing temperature and it was impossible to extract the true signal. Therefore, for qualitative study, the temperature dependence was studied in inverted-Hanle geometry. The inverted-Hanle effect curves for $I = -20 \mu\text{A}$ are shown for different temperatures in Fig. 3.19. After fitting these curves with Lorentzian function, the spin signal and the FWHM were extracted. In Fig. 3.19, we can see that the spin RA product is decreasing with temperature and FWHM is almost constant.

The decrease in spin RA product may imply that more electrons are directly tunnelling into the conduction band. As temperature increases, the carriers have enough energy to escape the localized states and flow into the conduction band of Ge. Another possible reason could be the change in injector/detector efficiency i.e. γ^2 with temperature. It has been shown previously that the major origin of temperature dependence of spin signal is due to characteristics of interface between oxide and semiconductor [110, 111]. The spin polarization (γ) showed a linear dependence with temperature in non-local 4T measurements and as discussed before spin signal is proportional to the square of this spin polarization, the steep reduction in spin signal is observed. The FWHM from inverted Hanle curves is again almost constant with temperature

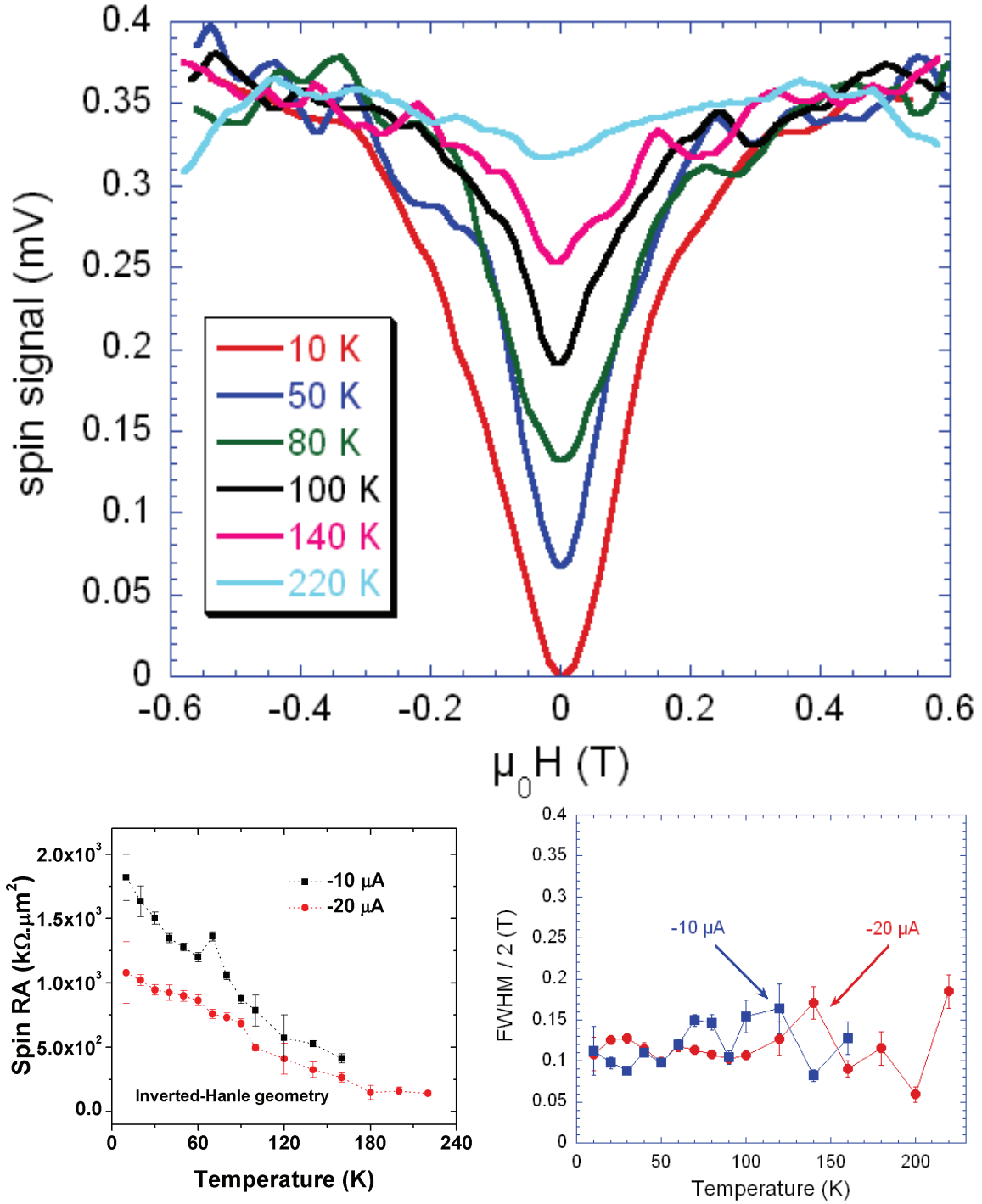


Figure 3.19 : (a) Inverted Hanle curves measured for a bias current of $-20 \mu\text{A}$ (-274 mV) at various temperatures. Spin signal is observable up to 220 K. (b) Temperature dependence of spin RA product obtained from inverted Hanle curves for two different bias currents $-10 \mu\text{A}$ (-217 mV) and $-20 \mu\text{A}$. (c) Temperature dependence of the Half-width-at-half-maximum of inverted Hanle curves for $-10 \mu\text{A}$ and $-20 \mu\text{A}$ bias currents.

and as discussed before it is due to the random magnetostatic fields arising from interface roughness.

CoFeB/MgO layers for spin injection into Ge

The growth of CoFeB/MgO layers was done in Crocus Technology, where high quality MgO junctions are grown for metal tunnel junctions for MRAMs. As in the case of Al_2O_3 tunnel barrier, the GOI substrates were treated with 10% hydrofluoric acid solution to remove the SiO_2 capping layer and quickly introduced in the sputtering machine. Magnesium layer of 1.1 nm was grown and treated in oxygen plasma for 30 seconds. This cycle was repeated three times to obtain MgO layer with thickness between 2-3 nm. Finally 5 nm of CoFeB was grown and in order to prevent oxidation 5 nm of Ta was grown as a capping layer. This stack was annealed in vacuum at 300°C for 90 mins in order to crystallize the MgO and CoFeB layers. The coercive field for these layers is known to be 15 Oe. The samples were processed in similar manner as discussed in previous section to obtain tunnel electrodes of $150 \times 400 \mu\text{m}^2$ and ohmic contacts of Ti/Au with dimensions $300 \times 400 \mu\text{m}^2$ (Fig. 3.8).

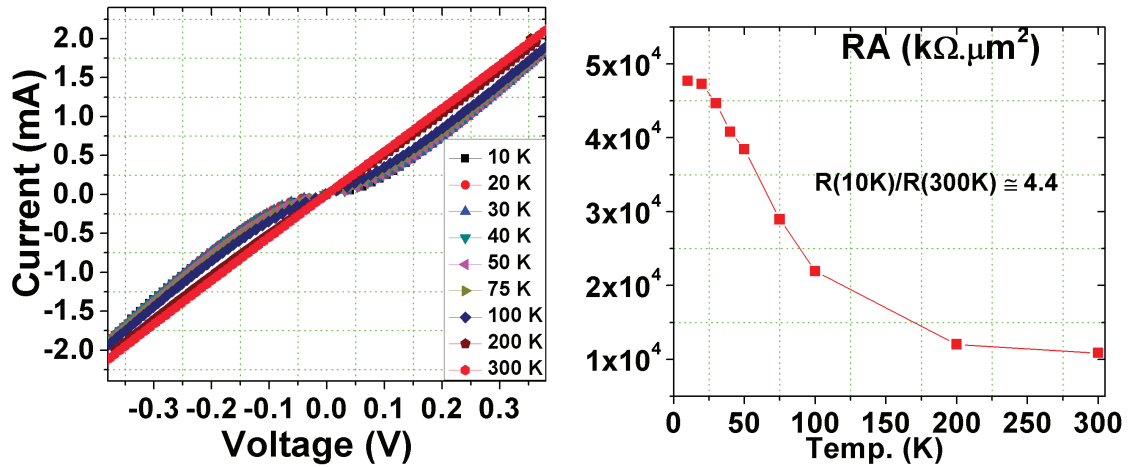


Figure 3.20 : (a) The current voltage characteristics between the tunnel contact with MgO barrier and one of the ohmic contact. (b) Dependence of the RA product of tunnel contact with temperature.

The current-voltage (I-V) characteristics between the tunnel contact (B) and one of the ohmic contacts (A) at different temperatures is shown in Fig. 3.20(a). The I-V curve is linear at room temperature however it becomes non-linear at lower temperatures. The RA products for these MgO based devices are shown in Fig. 3.20(b). A weak dependence of resistance with temperature is observed which confirms the tunneling transport ($R(10\text{K})/R(300\text{K}) \approx 4.4$). Also it can be seen that the MgO junctions are less resistive as compared to Al_2O_3 junctions, as difference of 2 orders of magnitude is observed in the RA product values. Nevertheless, this RA product exceeds the minimum interface resistance threshold required for spin injection into Ge ($10 \text{ k}\Omega \cdot \mu\text{m}^2$). This decrease in RA product implies that MgO is more efficient to release the Fermi-level pinning in Germanium as compared to Al_2O_3 . This was also recently observed by Lee et al. [92], where a drastic decrease of SBH from 0.47 to 0.05 eV was observed using CoFeB/MgO/ n^+Ge spin diodes instead of direct CoFeB/ n^+Ge ones.

The current-voltage characteristics were also performed in three-terminal geometry i.e. by varying the current I_{AB} , the voltage drop across V_{BC} was measured. The measurements are shown in Fig. 3.21. It is observed that the voltage drop across the tunnel junction is not the same in two-terminal and three-terminal measurements. This means that the tunnel contact resistance is low and of same order of the Ge-channel resistance and there is some voltage drop across the channel. This was not observed in the case of Al_2O_3 barrier where the I-V measurements were identical in 2T and 3T geometry. Hence in these MgO based devices, for the 3T measurements

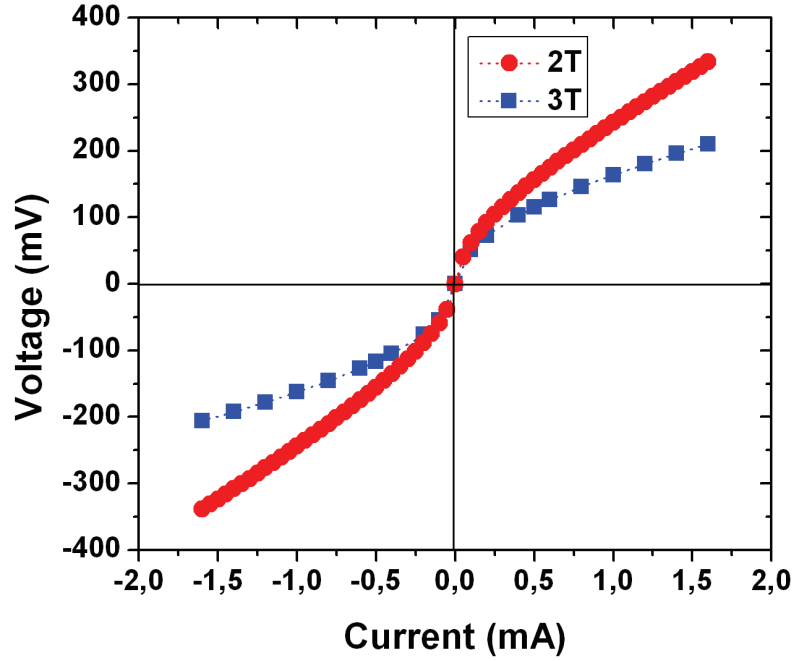


Figure 3.21 : The current voltage characteristics in two-terminal and three-terminal geometry at 10 K.

at a given current I_{AB} , the actual voltage drop at the tunnel junction V_{AB} will be higher than the voltage drop V_{BC} .

Finally spin injection experiments were performed in three-terminal geometry. A high field was applied in-plane in order to align the magnetization of the CoFeB electrodes in-plane and to obtain a single-domain state. A DC current I_{AB} was passed between contacts A and B and the voltage difference between contacts B and C was measured. The notation used for the current direction is similar to that discussed before i.e. for positive values of I_{AB} , there is injection of spin polarized electrons into the Ge channel and vice versa (Fig. 3.10). The voltage change V_{BC} was measured as a function of transverse magnetic field to observe the Hanle-effect.

For a constant DC current of $I_{AB} = -0.3$ mA (-92 mV) and varying the transverse field, the Hanle effect was observed at 10 K, hence giving proof of spin accumulation in Ge (Fig. 3.22). A voltage change of 0.19 mV was observed and spin lifetime of 136 ps was extracted after fitting the Hanle curves using simple Lorentzian function. This is the lower bound of spin lifetime and can be explained by local magnetostatic fields that give rise to inverted-Hanle effect. The inverted-Hanle curves were measured by applying in-plane magnetic field and the voltage change V_{BC} as a function of this in-plane field was measured. The inverted-Hanle curve at 10 K is shown in Fig. 3.22.

The spin RA product expected from theory is given by $R_s.A(\text{expected}) = \gamma^2 \rho l_{sf}^2 / w$, hence for $\gamma = 0.8$ at the CoFeB/MgO interface, $\rho = 10$ m Ω .cm, $l_{sf} = 1$ μ m and $w = 30$ nm, we get $R_s.A(\text{expected}) = 2.1$ k Ω . μ m². However, the spin RA product obtained from the experimental data is given by $R_s.A(\text{obtained}) = (\Delta V / I).A$, hence for $\Delta V = 0.19$ mV, $I = -0.3$ mA and contact area $A = 150 \times 400$ μ m², it becomes $R_s.A(\text{obtained}) = 38$ k Ω . μ m² (lower limit). The obtained value is still one order of magnitude higher than the predicted value but there is a drastic improvement using MgO barrier as compared to Al₂O₃ barrier. It seems that there is still some enhancement in spin signal due to the two-step tunneling through localized states but spin

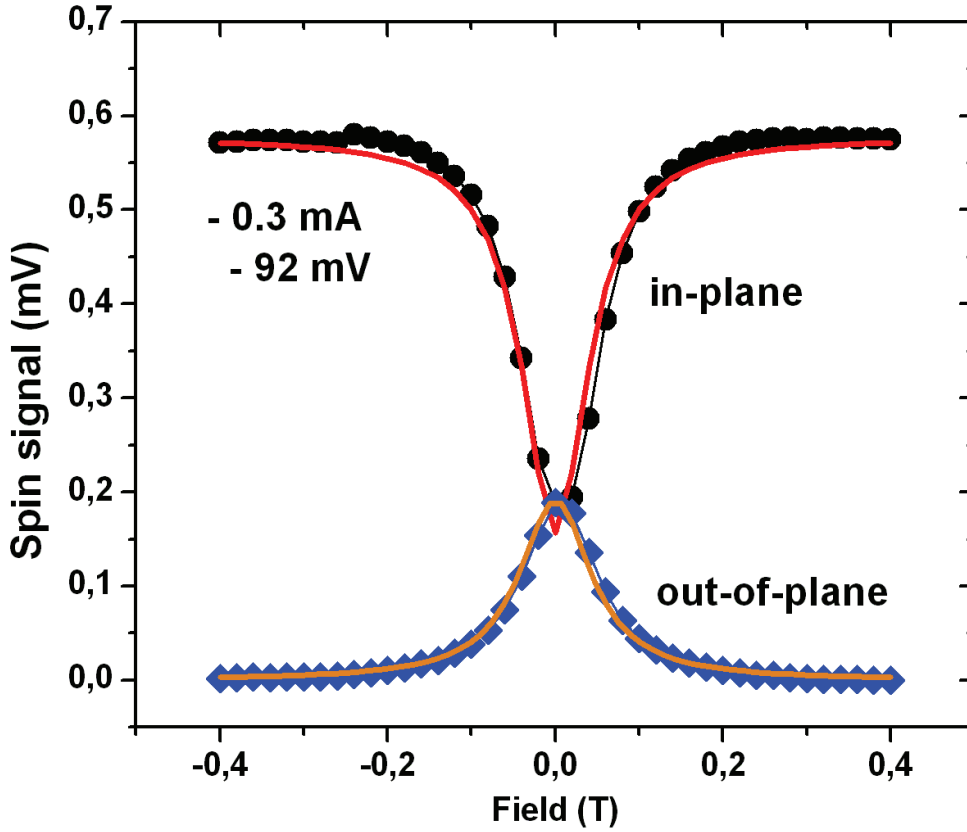


Figure 3.22 : Low magnetic field dependence of the spin signal for bias currents of -0.3 mA (-92 mV) showing both Hanle (out-of-plane) and inverted Hanle (in-plane) effects. Measurements were performed at 10 K. The curves were fitted using a Lorentzian function.

injection into the Ge channel may be more effective. As discussed before, high Schottky barrier height leads to localized states which can enhance spin accumulation signals. The negligible SBH using MgO leads to the lowering of this enhancement.

Eventually the bias dependence of spin signal was studied (for negative bias there is spin extraction and for positive bias there is spin injection). The measurements were done in out-of-plane Hanle geometry at 10 K. The Hanle curves obtained for different currents after removing the offset are shown in Fig. 3.23(a). It is observed that the spin signal is increasing with the bias. For quantitative study, the curves were fitted with a Lorentzian function to extract the magnitude of spin signal and plotted along with the I-V measurements in Fig. 3.23(b) (note the different scales). As expected the Hanle signal is increasing with the current density and follows the I-V characteristics, similar to Al_2O_3 based devices. The dependence is little weaker on the injection side and this may be due to the spin bottleneck effect or bias dependence of detector efficiency as discussed before.

The normalized spin signal i.e. $\Delta V/J$ or the spin RA products for different bias are shown in Fig. 3.24(a). It is observed that they are symmetric with bias and have weak dependence on it. The spin RA product decreases from a maximum of $64.3 \text{ k}\Omega \cdot \mu\text{m}^2$ at lower bias (-0.05 V) to a

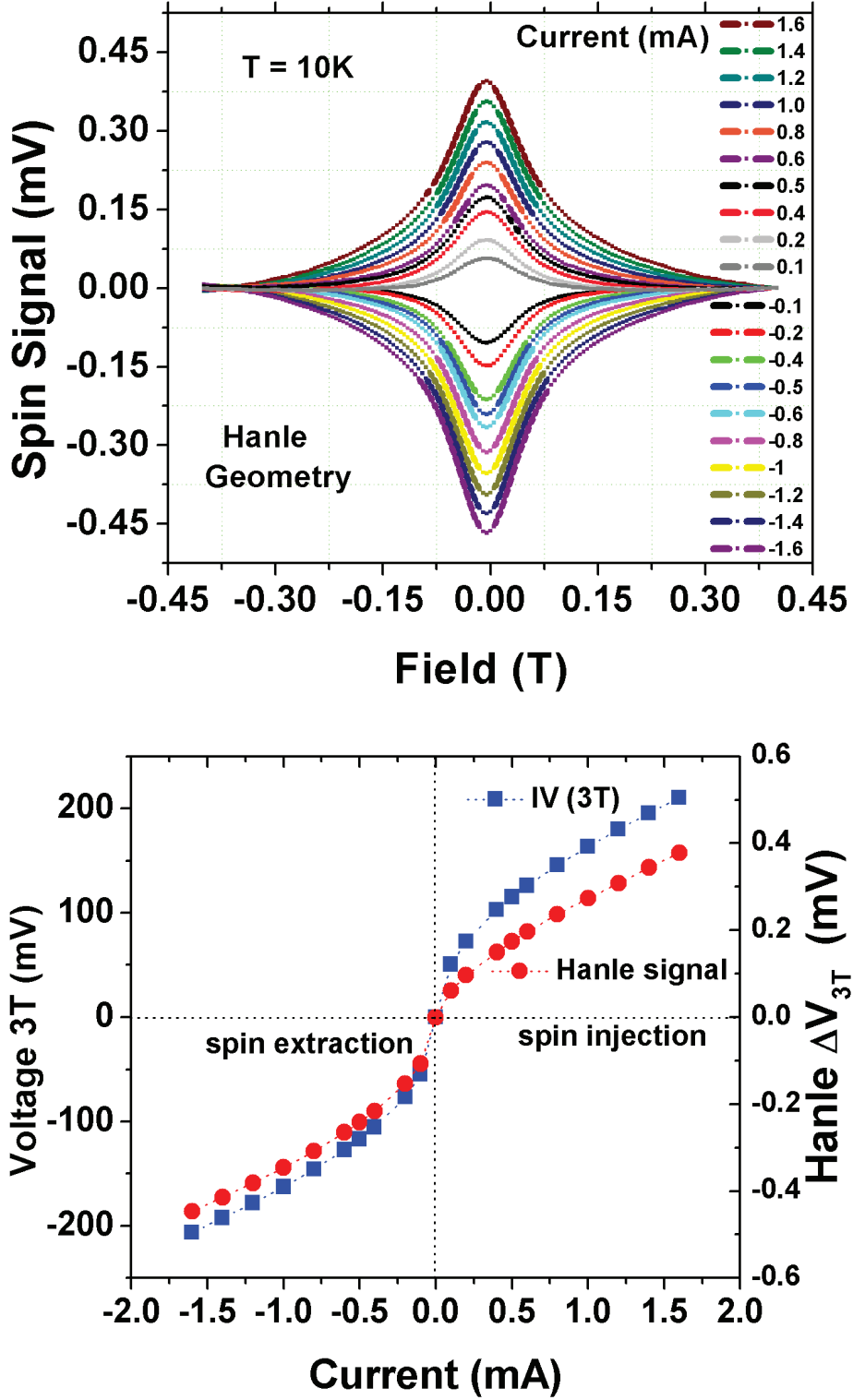


Figure 3.23 : (a) Hanle curves obtained for CoFeB/MgO/Ge tunnel junction for different currents in three terminal geometry at 10 K. (b) Amplitude of the Hanle Signal ΔV_{3T} and I-V characteristics of the tunnel barrier in 3T geometry.

minimum of $14.2\text{ k}\Omega\cdot\mu\text{m}^2$ at higher bias (0.21 V). At higher bias, the spin RA product becomes closer to the expected value. It is inferred that at lower bias, the enhancement is higher due to

spin accumulation in the localized states and it decreases on increasing the bias. At higher bias the direct tunneling into the conduction band of Ge becomes dominant. This can be explained by the model of Tran et al. [105] as discussed in the previous section. Similarly the spin lifetime shown in Fig. 3.24(b), is found to be 183.6 ps at lower bias and 87.2 ps at higher bias. The spin lifetime is higher in the localized states as compared to the bulk which agrees well with our interpretation.

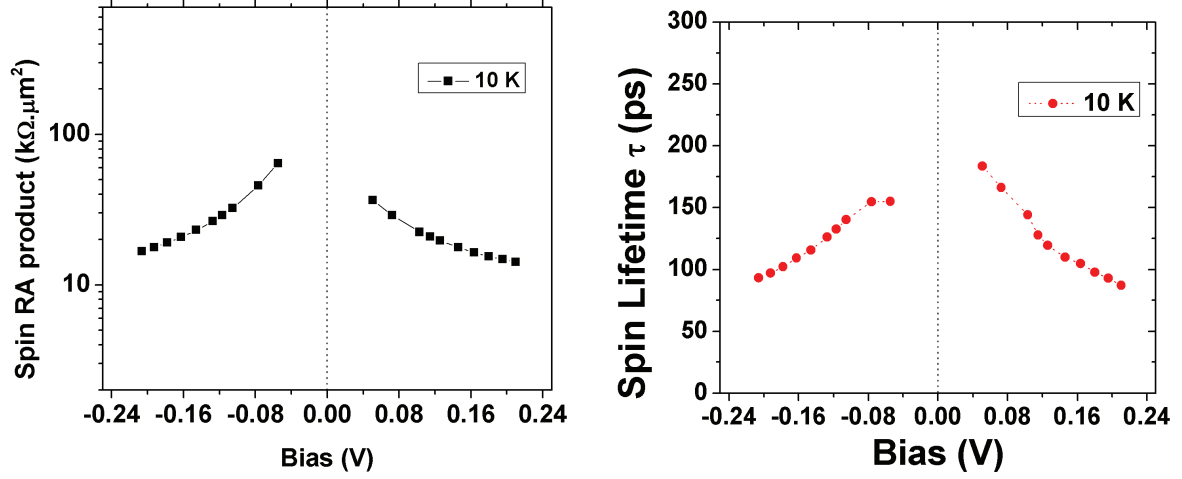


Figure 3.24 : (a) The Spin RA product and (b) The Spin lifetimes obtained at 10 K after fitting the Hanle curves using Lorentzian function.

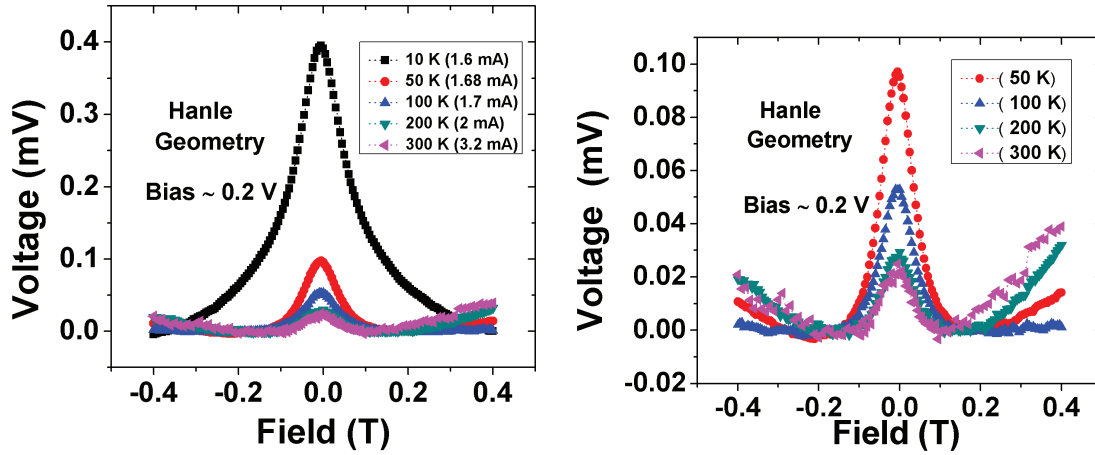


Figure 3.25 : The Hanle curves obtained for CoFeB/MgO/Ge devices at different temperatures for a fixed bias of 0.2 V.

Finally, we measured the temperature dependence of the spin signal. The Hanle curves obtained for different temperatures are shown in Fig. 3.25. The measurements were done with a fixed bias of 0.2 V. The Hanle signal is observed up to room temperature, which was not reported before in the case of Ge. Compared with Al_2O_3 based devices, the Hanle signal is observed only up to 220 K. An interesting phenomenon is also observed at lower temperature of 10 K, the Hanle signal is very large (0.38 mV) and on increasing temperature above 50 K it becomes weakly dependent on temperature (from 60 μV at 100 K to 20 μV at RT) (Fig. 3.27(a)). In a similar manner, the spin RA product varies from 14.25 $k\Omega \cdot \mu m^2$ at 10 K to 0.375 $k\Omega \cdot \mu m^2$ at RT with a weak dependence at higher temperatures (Fig. 3.27(b)). The curves obtained for

injection and extraction of carriers in Hanle geometry are shown in Fig. 3.26. The lower bound of spin lifetime lies in the range of 160-180 ps.

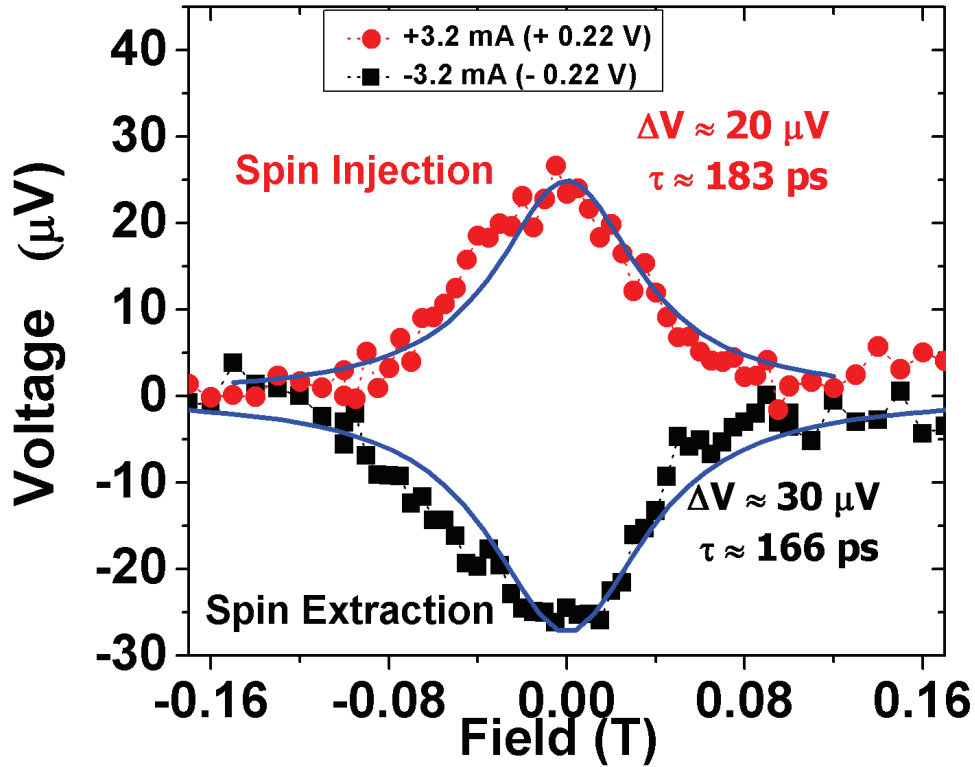


Figure 3.26 : Hanle curves obtained for CoFeB/MgO/n-Ge contact at room temperature providing evidence of spin accumulation in Ge for a current of +3.2 mA and -3.2 mA.

At higher temperatures, the obtained spin RA values lies in the same range as that of the predicted value (Considering EY relaxation mechanism, the spin-diffusion length is assumed to be same for low temperature range (10-100 K)). This may be a proof that there is direct injection of spin polarized electrons into the conduction band of Ge and the two-step tunneling through localized states becomes negligible at higher temperatures. Similar results were observed by Dash et al. [43], where they observed the enhancement of spin signal at lower temperatures corresponding to two-step tunneling in Py-Al₂O₃-Si devices. At higher temperatures the spin signal was lower and similar to devices treated with Cs which removes the SBH in Si and leads to direct tunneling. As the temperature increases, carriers have enough energy to escape the localized states and flow into the conduction band of Ge.

The spin lifetime extracted at different temperatures is shown in Fig. 3.28. The spin lifetime varies from 87.2 ps at 10 K to 206.5 ps at RT. However, due the artificial broadening of the Hanle curves, the intrinsic variation of the actual spin lifetime with temperature cannot be known. At lower temperatures, the spin relaxation in localized states is not due to the intrinsic mechanisms and one cannot totally rule out possible spin decoherence through hyperfine interaction with localized nuclear spins on Ge atoms. For direct injection into Ge channel at higher temperatures, the spin relaxation should occur by Elliot-Yafet mechanism i.e. proportional to the momentum scattering rate. As temperature increases, the spin lifetime should decrease due to increase in phonon scattering.

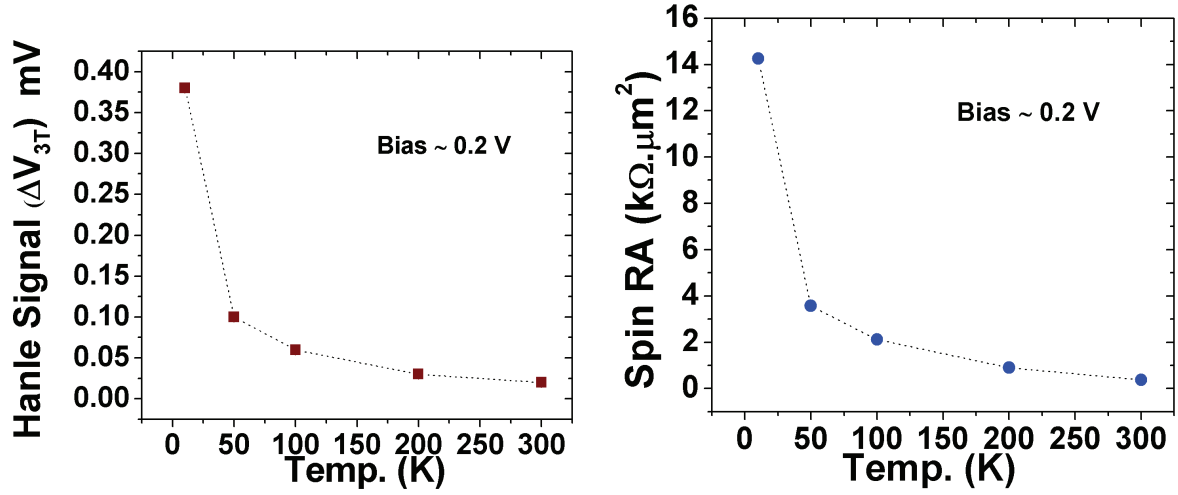


Figure 3.27 : (a) Hanle voltage in mV as a function of temperature obtained after fitting the Hanle curves with a Lorentzian curve and (b) The spin RA product as a function of temperature for CoFeB/MgO/Ge devices.

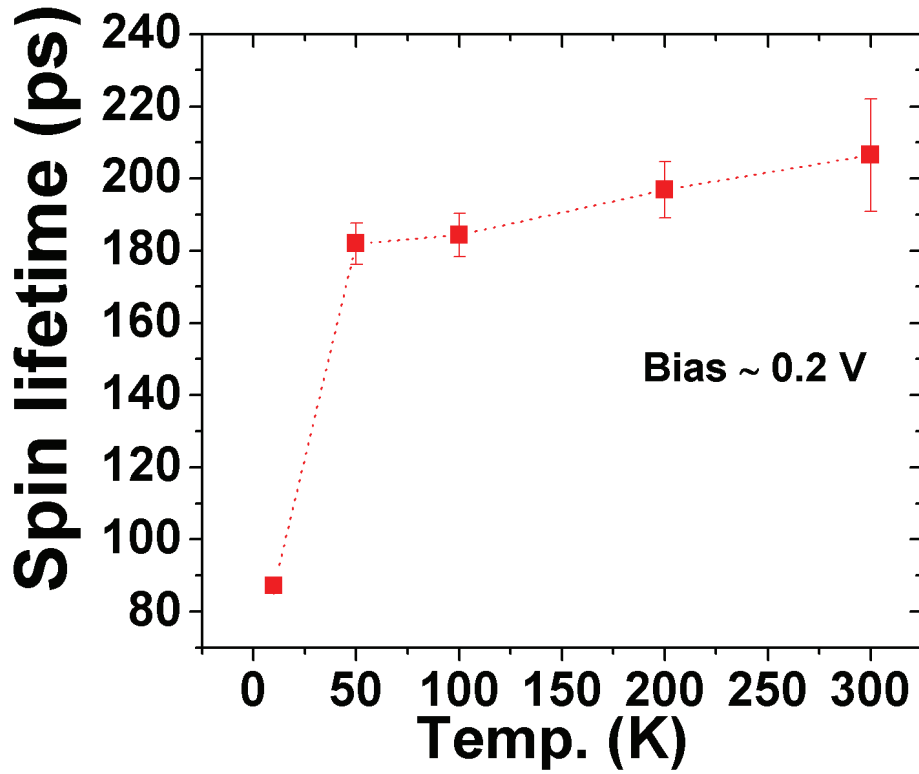


Figure 3.28 : (a) The spin life life of electrons in pico-seconds as a function of temperature obtained after fitting of Hanle curves for CoFeB/MgO/Ge devices.

3.3 Discussion

As mentioned in the previous section, the enhanced spin signal as compared to the theoretical predictions can be explained by either spin accumulation in the localized-states or presence of

inhomogeneities/pinholes in the tunnel barrier. For spin accumulation in the localized states, the interface states have to be decoupled from the SC bulk channel by large Schottky barrier. In case of metal/n-Ge contact, high Schottky barrier is present due to strong Fermi level pinning (FLP) close to the valence band. By introducing a oxide layer at the interface (FM/oxide/n-Ge), the Schottky barrier height is lowered but still not completely removed.

The spin resistance associated with the localized states (LS) based on the Tran model is given by [105]:

$$r_{LS} = \frac{\tau_{sf}^{LS}}{e^2 N^{LS}} \quad (3.16)$$

here τ_{sf}^{LS} is the spin lifetime in these LS and N^{LS} represents the two-dimensional density of states integrated over the thickness of the LS layer. For the FM/MgO/Ge interface, the value of N^{LS} from literature has been found to be $1 \times 10^{13} / \text{eVcm}^2$ [112]. For a spin life of 1 ns in the localized states, the value of $r_{LS}(\text{expected})$ becomes $62.5 \text{ k}\Omega \cdot \mu\text{m}^2$. From the experimental data, this value is given as $R_s(\text{measured})/\gamma^2$ and hence for FM/MgO/Ge interface, this becomes $r_{LS}(\text{measured}) = 38/0.8^2 = 60 \text{ k}\Omega \cdot \mu\text{m}^2$ at 10 K, same as expected. However for the FM/ Al_2O_3 /Ge interface, $r_{LS}(\text{measured}) = 1380/0.3^2 \approx 10 \text{ M}\Omega \cdot \mu\text{m}^2$, the difference from expected value can be explained by the difference in density of interface states for Al_2O_3 and MgO interface. The MIGS formation and saturation of dangling bonds can be different for different oxides and precise density can only be known with detailed Capacitance-Voltage (C-V) analysis. The high Schottky barrier due to FLP and the depletion width of order of 10 nm for the given doping concentration can give contact resistance of order of $10 \text{ M}\Omega \cdot \mu\text{m}^2$. (Moreover $r_b(\text{Al}_2\text{O}_3) > r_b(\text{MgO})$, since MgO is more efficient in lowering of SBH). This makes $r_b > r_{LS}$ and gives $\Delta\mu_{LS} \approx 2e\gamma j r_{LS}$ and $\Delta\mu_{ch} \approx 2e\gamma j \frac{r_{LS} r_{ch}}{r_b}$, leading to most of the spin accumulation absorbed in the localized states before it reaches the Ge channel.

On the other hand, the presence of inhomogeneities/pinholes in the tunnel barrier can increase the local current density and can explain the enhanced signal for direct injection in the Ge-channel. However, in the present case where the FM contact width ($150 \mu\text{m}$) is much larger than the spin diffusion length in the SC, the volume of spin relaxation in the SC is governed by l_{sf} and does not depend on the size of the contact or presence of pinholes. Hence, the measured spin signal should not change.

The temperature dependence of spin signal in case of CoFeB/MgO/Ge also confirms spin accumulation in the LS at 10 K, where one can clearly see a shift from spin accumulation in the LS to the Ge channel with increase in temperature. As the temperature increases, carriers have enough energy to escape the localized states and flow into the conduction band of Ge. The measured spin signal becomes equal to the expected signal and the 'spin lifetime' measured from the Hanle curves increases with the increase in temperature. As the carriers are shifted away from the interface, the local magnetostatic fields decrease and hence reducing the broadening of Hanle curves, giving high spin lifetimes.

The spin injection in Ge channel can be confirmed experimentally by making non-local four terminal measurements, since the the limitation of the three terminal measurements makes it difficult to determine whether the observed spin signal in this system originates from the spin accumulation in the Ge bulk channel or LSs.

3.4 Conclusion

In the beginning of this chapter, the energy band diagram of metal-Germanium contact is studied and the pinning of Fermi-level near valence band is explained. This pinning leads to high Schottky barrier heights and for moderately doped semiconductor leads to wide depletion zones

for Ge-metal contacts. A solution to remove this FLP is proposed and a tunneling transport is obtained in n-Ge.

Two different structures using oxide tunnel barriers and ferromagnetic metals: Co/Py/Al₂O₃/Ge and CoFeB/MgO/Ge are used for spin injection in Ge. The successful spin accumulation in n-doped Ge is demonstrated using Hanle-effect. The contact resistance for Al₂O₃ based devices is found to be much higher as compared to MgO based devices, indicating that MgO is more efficient in removing the Fermi-level pinning in Ge. The spin signal (spin RA product) in Al₂O₃ based devices is four orders of magnitude higher than the predicted value which led to the conclusion that there is spin accumulation in localized states at Al₂O₃/Ge interface due to high SBH. However in case of MgO based devices, the spin signal was only one order of magnitude higher than the predicted value at lower temperatures. On increasing the temperature, the enhancement decreases and the expected spin signal is observed due to thermal activation of carriers over the Schottky barrier.

We also discussed that the roughness at the FM/oxide interface leads to local magnetostatic fields. These local fields have severe effect on spin accumulation and lead to broadening to Hanle curves. The inverted-Hanle effect is the signature for this phenomenon, where in-plane magnetic field leads to recovery of spin signal.

The spin accumulation in n-Ge has been achieved up to 220 K for Al₂O₃ based devices and up to room temperature for MgO devices. For the latter, a spin signal of about $0.375 \text{ k}\Omega\cdot\mu\text{m}^2$ is observed at room temperature for spin injection in the Ge channel.

Towards (Ge,Mn) as a spin injector

As discussed in chapter 1, the ferromagnetic semiconductors as spin injectors could solve the problem of conductivity mismatch and lead to all-semiconductor devices. Similarly (Ge,Mn) system combines both magnetic and semiconducting properties and hence can be employed for spin injection in Germanium.

However the low solubility-limit of Mn in Ge, measured to be around $10^{-6}\%$ [113] can limit the use of GeMn as DMS, if grown by equilibrium growth techniques. The Ge:Mn binary phase diagram (Fig. 4.1) shows that all the stable phases are on the high Mn content side of the phase diagram [114]. This implies that Mn atoms in Ge have a strong tendency to aggregate and form high Mn concentration compounds. Several stable phases observed in equilibrium growth are $\text{GeMn}_{3.4}$ [115, 116], Ge_3Mn_7 [115], $\text{Ge}_8\text{Mn}_{11}$ [117] and Ge_3Mn_5 [118]. All these phases are metallic and last two phases are ferromagnetic. This makes out-of-equilibrium growth techniques necessary to form a diluted system or to avoid formation of stable phases.

The first experimental evidence of (Ge,Mn) as a ferromagnetic semiconductor was given by Park et al in 2002 [119]. They have grown $\text{Ge}_{1-x}\text{Mn}_x$ thin films ($0.006 < x < 0.035$) using low-temperature molecular beam epitaxy. The films were ferromagnetic with a Curie temperature from 25 to 116 K varying linearly with Mn concentration. Despite low temperature growth, they observed formation of Mn rich precipitates with 2 to 6 nm diameter. However by applying a gate voltage they could observe a change in extraordinary Hall effect (EHE), proving that the ferromagnetism was indeed mediated by the charge carriers (holes).

4.1 Literature Review

A considerable amount of research has been done in (Ge,Mn) system in last decade. This system has been investigated as a DMS and as a heterogeneous semiconductor with stable or metastable precipitates. A review of some of the experimental results is done here.

Many groups studied (Ge,Mn) as a DMS system where the local electronic structure and charge state of Mn atoms in Ge is confirmed by X-ray absorption spectroscopy (XAS). D’Orazio et al., Pinto et al. and Picozzi et al. have studied diluted (Ge,Mn) system grown by MBE [120–123]. They have observed room temperature ferromagnetism and interpretation of magnetic properties was given based on bound magnetic polaron (BMP).

Ottaviano et al. studied Mn-implanted Ge films and it was claimed that the Mn atoms occupy the substitutional positions [124–126]. With Morgunov et al. they also explained the behavior of diluted Mn^{+2} ions with the BMP model [127]. Recently they have reported room temperature ferromagnetism in Mn-implanted amorphous Ge [128].

Zeng et al. proposed a new way to synthesize homogeneously doped (Ge,Mn) and called it as *subsurfactant epitaxy* [129]. In low temperature MBE (150 K), they evaporated only Mn atoms on Ge with most of them sitting on substitutional sites. Lateral diffusion and clustering

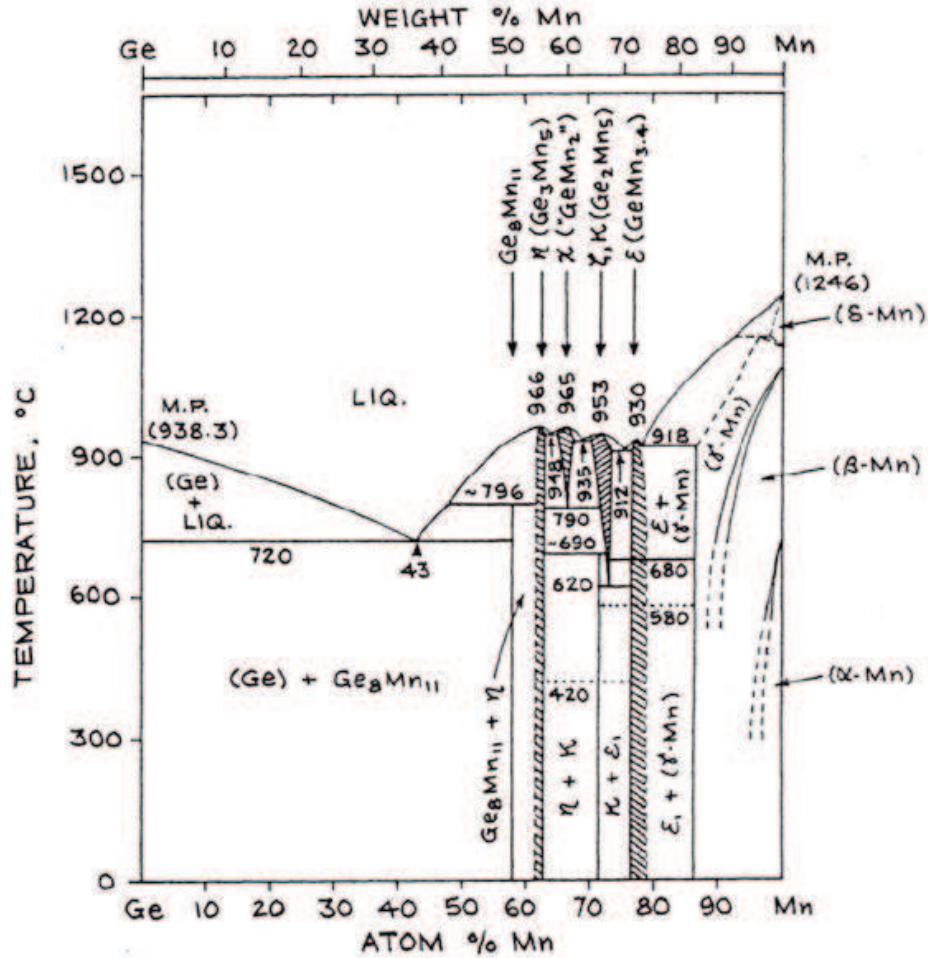


Figure 4.1 : Phase diagram of GeMn binary system [114].

was inhibited by the low temperature. Again they covered the surface with Ge atoms resulting the Mn to float on new surface due to surfactant effect, with substitutional Mn atoms staying uniformly distributed in the Ge. Doping levels of 0.25% were reached and DMS type behavior was observed with Curie temperature higher than 400 K.

Yada et al. reported the magneto-optical and the magnetotransport properties of amorphous (Ge,Mn) thin film grown by low temperature MBE on SiO₂ [130]. They concluded that the films were magnetically homogeneous, i.e. they were single-phase ferromagnetic.

Although a large percentage of Mn atoms can be incorporated in the Ge matrix, phase separation easily happens. Several groups have reported formation of intermetallic and metastable precipitates. For stable phases, mostly Ge₃Mn₅ and sometimes Ge₈Mn₁₁ or Ge₂Mn₅ clusters have been observed. Morresi et al. and Padova et al. have observed these clusters embedded in Ge matrix having 1.5% Mn [131–133].

Bihler et al. investigated the structural and magnetic properties of Ge₃Mn₅ clusters embedded in Ge matrix [134]. They have observed a coherent incorporation of the hexagonal clusters in the diamond matrix with a preferential alignment of the c-axis of both lattices. The matrix displayed a DMS-like behavior. Lechner et al. further performed a depth-resolved study of the Ge₃Mn₅ clusters in Ge [135]. They found two types of clusters : a majority is buried in the layer and c-axis aligned and a minority lies close to the surface with different but well defined orientations.

Ahlers et al. also observed precipitation of Ge₃Mn₅ clusters in Ge during the low temperature

MBE growth of (Ge,Mn) films [136]. In their case, the clusters are also mainly located near the bottom of the (Ge,Mn) layer. Zhou et al. have studied the temperature-dependent magnetic memory effect in the clusters. They explain the observed spin-glass-like features by the finite size distribution of the clusters [137].

Formation of metastable phases has also been reported by many groups in (Ge,Mn) system. Bougeard et al. observed Mn-rich clusters without any intermetallic phases in $\text{Ge}_{0.95}\text{Mn}_{0.05}$ film grown by low temperature MBE [138]. The transmission electron microscopy observation revealed areas with slightly darker contrast but still reflecting the same lattice symmetry. These areas were coherently bound to the surrounding Ge matrix and the upper limit of 15% Mn per cluster was estimated.

Around same time, Jamet et al. reported the growth of high- T_c ferromagnetic (Ge,Mn) films using LT-MBE [53]. TEM analysis showed self-assembled Mn-rich nanocolumns formed in Mn-poor single crystalline Ge matrix. This phase is similar to the Konbu phase (2D spinodal decomposition) evidenced numerically by Sato et al. [49]. The nanocolumns size, composition and crystalline structure highly depend on growth parameters leading to very different magnetic and electronic properties during growth of $\text{Ge}_{0.94}\text{Mn}_{0.06}$ thin films by LT-MBE. Numerous works have been published regarding characterization of these nanocolumns [139–144]. Similar formation of nanocolumns was also reported by Li et al. in 2007 [145]. They observed 20-30% Mn ions in the substitutional sites and a post-annealing at low temperatures increased this fraction to 40-50% implying that some interstitial Mn have been converted to substitutional Mn during the annealing process.

Xiu et al. have reported the growth of high-Curie-temperature quantum wells and dots in Ge with 5% Mn [146]. They were able to tune the magnetic properties by applying a gate voltage [147]. Room-temperature ferromagnetism in $\text{Ge}_{1-x}\text{Mn}_x$ nanowires are also observed by Kazakova et al., grown in the pores of anodized aluminium oxide membranes [148]. The nanowires were crystalline and no secondary phase could be evidenced.

To summarize, fabrication of homogeneous (Ge,Mn) films seems to be a very difficult task and there are always some inclusions that can be either known metallic compounds or new unknown phases. Some of these inclusions are embedded coherently into the semiconductor matrix and are formed in a self organized manner. They contain high density of Mn atoms and account for the persistence of ferromagnetic features up to high temperatures.

4.2 Investigation of magnetic anisotropy in (Ge,Mn) nanostructures

In this thesis the growth of (Ge,Mn) films on Ge substrates by low-temperature molecular beam epitaxy is discussed. Different nanostructures have been obtained during growth depending on the substrate orientation, substrate temperature and Mn concentration. The following (Ge,Mn) nanostructures have been studied: thin Ge_3Mn_5 films grown on Ge(111) substrate, crystalline and amorphous (Ge,Mn) nanocolumns grown on Ge(001) substrates and finally randomly distributed spherical Ge_3Mn_5 clusters on Ge(001). For future spintronics applications, the knowledge of magnetic anisotropy of (Ge,Mn) material is very important since it determines the direction of magnetization, coercive fields, and domain sizes. Magnetic anisotropy in these nanostructures has been studied using complementary techniques: ferromagnetic resonance (FMR) and superconducting quantum interference device (SQUID).

There have been only few studies regarding the investigation of magnetic anisotropy in (Ge,Mn) system and they are rather qualitative. For instance, Bihler et al. [134] investigated the uniaxial anisotropy of Ge_3Mn_5 clusters embedded in Mn-poor Germanium matrix grown by low temperature molecular beam epitaxy (LT-MBE). They showed that these clusters have easy magnetic axis along the out-of-plane direction. Deng et al. [149] also observed magnetic anisotropy in $\text{Ge}_{1-x}\text{Mn}_x$ films which they attribute to strong spin-orbit coupling originating

from reduced cubic symmetry in the crystal induced by low temperature growth using MBE or oriented substitution of Mn atoms in the matrix. Morgunov et al.[150] studied the angular dependence of resonance field in Ge:Mn films as a function of temperature and Mn concentration. At lower temperatures (4 – 60 K), the electron spin resonances were attributed to the excitation of collective spin waves in the whole film and the resulting anisotropy from magnetocrystalline and magnetoelastic components of the matrix as well as from the anisotropy of Ge_3Mn_5 clusters. However at higher temperatures (220 – 310 K) they observed in-plane anisotropy resulting from shape anisotropy of film and (Ge,Mn) clusters. In all these studies no detailed quantitative insight such as anisotropy constants was provided.

Here we have done a qualitative and quantitative study of magnetic anisotropy in (Ge,Mn) nanostructures. The complementary techniques: ferromagnetic resonance (FMR) and superconducting quantum interference device (SQUID) are used to calculate the magnetic anisotropy constants. FMR is a very sensitive spectroscopy technique with high field resolution, where the magnetization dynamics is described by the Landau-Lifschitz-Gilbert (LLG) equation:

$$\frac{1}{\gamma} \frac{d\vec{M}}{dt} = -(\vec{M} \times \vec{B}^{eff}) + \frac{\alpha}{\gamma M_s} \left(\vec{M} \times \frac{\partial \vec{M}}{\partial t} \right) \quad (4.1)$$

The first term on the right hand represents the precessional torque. The second one, called Gilbert damping term, is phenomenological and is introduced to describe the relaxation process of the magnetization. Here magnetization \vec{M} is defined as magnetic moment per unit volume, γ is gyromagnetic ratio given by $\gamma = \frac{g\mu_B}{\hbar}$, α is the damping factor and M_s is the saturation magnetization. \vec{B}^{eff} is overall effective magnetic field given by sum of external field, microwave excitation field and the internal fields.

This LLG equation can be solved to get anisotropy fields, however the solution is quite complex and an alternative way is used. Based on the free energy of the system, a formalism was introduced by Smit and Beljers [151] and independently by Suhl [152] where the equation of motion is described by the free energy density F of the system. For the derivation of this equation, please see the appendix.

$$\left(\frac{\omega}{\gamma} \right)^2 = \frac{F_{\theta\theta}F_{\varphi\varphi} - F_{\theta\varphi}^2}{M_S^2 \sin^2 \theta_0} \quad (4.2)$$

where ω is the microwave frequency and γ is the gyromagnetic ratio. M_S is the saturation magnetization of the ferromagnetic nanostructures. Here the derivatives of F ($F_{\theta\theta}$, $F_{\varphi\varphi}$ and $F_{\theta\varphi}$) are taken at equilibrium positions (θ_0, φ_0) which can be obtained from the conditions: $F_{\theta}|_{\theta_0, \varphi_0} = \partial F / \partial \theta = 0$ and $F_{\varphi}|_{\theta_0, \varphi_0} = \partial F / \partial \varphi = 0$.

The free energy density for a tetragonal symmetry is given by the summation of the Zeeman energy, demagnetization energy, uniaxial magnetic anisotropy energy, and cubic magnetocrystalline anisotropy energy. It can be written as:

$$F = -M_S B (\sin \theta \sin \theta_B \cos(\varphi - \varphi_B) + \cos \theta \cos \theta_B) \quad (4.3)$$

$$- \left(\frac{\mu_0}{2} (N_{\parallel} - N_{\perp}) M_S^2 \right) \sin^2 \theta - K_{2\perp} \cos^2 \theta \quad (4.4)$$

$$- \frac{1}{2} K_{4\perp} \cos^4 \theta - \frac{1}{8} K_{4\parallel} (3 + \cos 4\varphi) \sin^4 \theta \quad (4.5)$$

$$(4.6)$$

where θ_B, φ_B and θ, φ polar angles are defined in Fig. 4.2. \vec{B} is the applied magnetic field. $K_{2\perp}$ is the uniaxial out-of-plane anisotropy constant and reflects the difference in energy for magnetization perpendicular and parallel to the film plane. In this equation, we have neglected

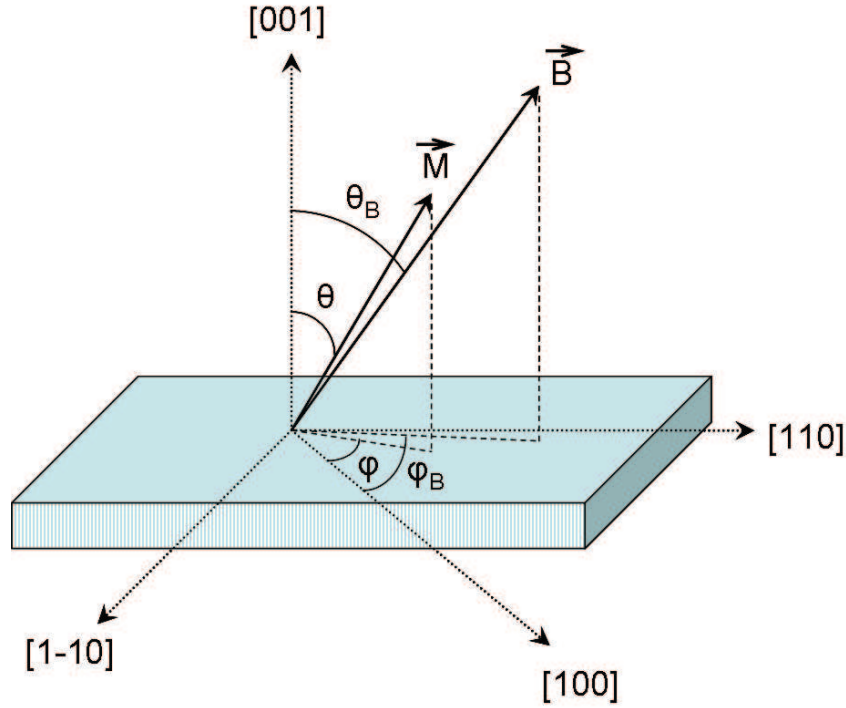


Figure 4.2 : Schematic drawing defining the polar angles θ_B, φ_B and θ, φ of the applied magnetic field \vec{B} and the magnetization $\vec{M} = M_S \vec{m}$ with respect to crystal axes. \vec{m} is a unit vector along the magnetization direction.

in-plane uniaxial magnetic anisotropy (constant $K_{2\parallel}$). It is usually very small and may result from a slight miscut of the substrate, which leads to a preferential direction in the film plane along the $[110]$ and $[1\bar{1}0]$ directions. In our case, we assume that there is no miscut of the substrate. We see further that Ge_3Mn_5 films are relaxed and exhibit bulk structure, hence making $K_{2\parallel}$ zero due to in-plane six-fold hexagonal symmetry. For Ge_3Mn_5 clusters (section 4.16), in-plane FMR measurements have shown no presence of this in-plane uniaxial anisotropy constant. Regarding crystalline nanocolumns (section 4.3.2), TEM plane views suggest the absence of this $K_{2\parallel}$ component due to in-plane four-fold cubic symmetry. $K_{4\perp}$ and $K_{4\parallel}$ are the out-of-plane and in-plane cubic anisotropy constants respectively and are equal in the case of a net cubic symmetry. N_{\perp} and N_{\parallel} are the demagnetizing factors parallel and perpendicular to the film plane respectively.

For the measurements performed with the out-of-plane applied field swept from $[001]$ to $[1\bar{1}0]$ crystal direction, the following equation is derived:

$$\left(\frac{\omega}{\gamma}\right)^2 = P_1 \cdot P_2 \quad (4.7)$$

$$(4.8)$$

where

$$P_1 = B_{res} \cos \Delta \theta + \quad (4.9)$$

$$\left(\frac{2K_{2\perp}}{M_S} - \mu_0(N_{\perp} - N_{\parallel})M_S + \frac{K_{4\perp}}{M_S} \right) \cos 2\theta_0 - \quad (4.10)$$

$$\left(\frac{K_{4\parallel}}{2M_S} \right) \cos 2\theta_0 + \left(\frac{K_{4\perp}}{M_S} + \frac{K_{4\parallel}}{2M_S} \right) \cos 4\theta_0 \quad (4.11)$$

and

$$P_2 = B_{res} \cos \Delta \theta + \left(\frac{2K_{2\perp}}{M_S} - \mu_0(N_{\perp} - N_{\parallel})M_S \right) \cos^2 \theta_0 + \quad (4.12)$$

$$\left(\frac{K_{4\parallel}}{M_S} \right) \cos^2 \theta_0 + \left(\frac{2K_{4\perp}}{M_S} + \frac{K_{4\parallel}}{M_S} \right) \cos^4 \theta_0 - \frac{2K_{4\parallel}}{M_S} \quad (4.13)$$

where $\Delta \theta = \theta_0 - \theta_B$. Hence the above equation states a relation between the resonance field B_{res} and the angle of the external magnetic field at a fixed microwave frequency. By fitting the angular dependence of resonance field, it is thus possible to deduce magnetic anisotropy constants and gyromagnetic ratio. Here due to the cubic symmetry, the fourth-order anisotropy constants are equal ($K_{4\parallel} = K_{4\perp}$). In this thesis, we denote the effective out-of-plane second-order anisotropy field by $\mu_0 H_{a2} = \frac{2K_2}{M_S} = \frac{2K_{2\perp}}{M_S} - \mu_0(N_{\perp} - N_{\parallel})M_S$ and fourth-order cubic anisotropy field by $\mu_0 H_{a4} = 2K_4/M_S$.

These equations are used to calculate the magnetic anisotropy fields. However, SQUID measurements are needed to obtain the saturation magnetization and hence calculate the anisotropy constants. This approach has proved very useful in studying magnetic anisotropy in metallic thin-films and (III,Mn)V DMS [77, 153]. In our case we have (Ge,Mn) nanostructures and the same approach has been used.

4.2.1 Superparamagnetism

Superparamagnetism is a form of magnetism, which appears in small ferromagnetic or ferrimagnetic nanoparticles. In small enough nanoparticles, magnetization can randomly flip direction under the influence of temperature. The typical time between two flips is called the Néel relaxation time (τ_N). In the absence of external magnetic field, when the time used to measure the magnetization of the nanoparticles is much longer than the Néel relaxation time ($\tau_{mes} \gg \tau_N$), their magnetization appears to be in average zero: they are said to be in the superparamagnetic state. In this state, an external magnetic field is able to magnetize the nanoparticles, similarly to a paramagnet.

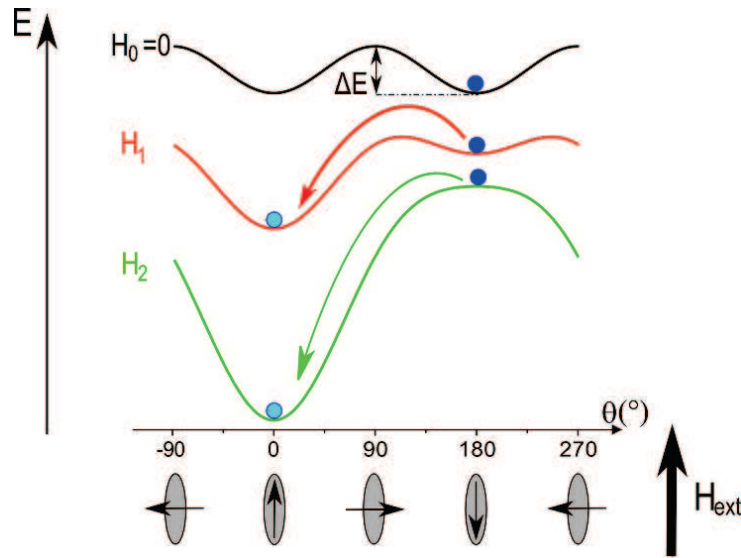


Figure 4.3 : The magnetic energy of a single domain particle having uniaxial anisotropy in an applied magnetic field H_{ext} ($0 = H_0 < H_1 < H_2$).

For a nanometer-sized single domain ferromagnetic particle where uniaxial anisotropy is dominant, the anisotropy energy is given by $KV \sin^2 \theta$, where K is the anisotropy constant, V is

the volume of the particle and θ is the angle between the magnetization and easy axis. Hence the total magnetic energy (sum of Zeeman and anisotropy energy) is given by:

$$E = KV \sin^2 \theta - \mu_o H V M_s (\theta - \varphi) \quad (4.14)$$

where φ is the angle between the easy axis and external applied field. Fig. 4.3 shows this magnetic energy of the particle as a function of the angle θ and applied field, here the field is applied along the easy axis. The equilibrium states are given by minima of this energy. In absence of external magnetic field, the two equilibrium states are given at $\theta = 0^\circ$ and $\theta = 180^\circ$ i.e. along the easy axis. An energy barrier ΔE can be defined which opposes passage from one energy state into the other. On increasing the external field, one of the states becomes more stable and eventually the magnetization direction changes into this stable state.

In case of superparamagnetism, there exists a temperature T_B for which the thermal energy becomes comparable to the energy barrier ΔE . For a temperature $T \ll T_B$, the particle is ferromagnetic and without the application of an external field there is no change in magnetization with time. However for $T \geq T_B$, the thermal energy enables the particle to shift from one stable state into another. At a given time instant, the particle is ferromagnetic but the average of magnetization over the measuring time becomes zero. The particle is said to be in a superparamagnetic state.

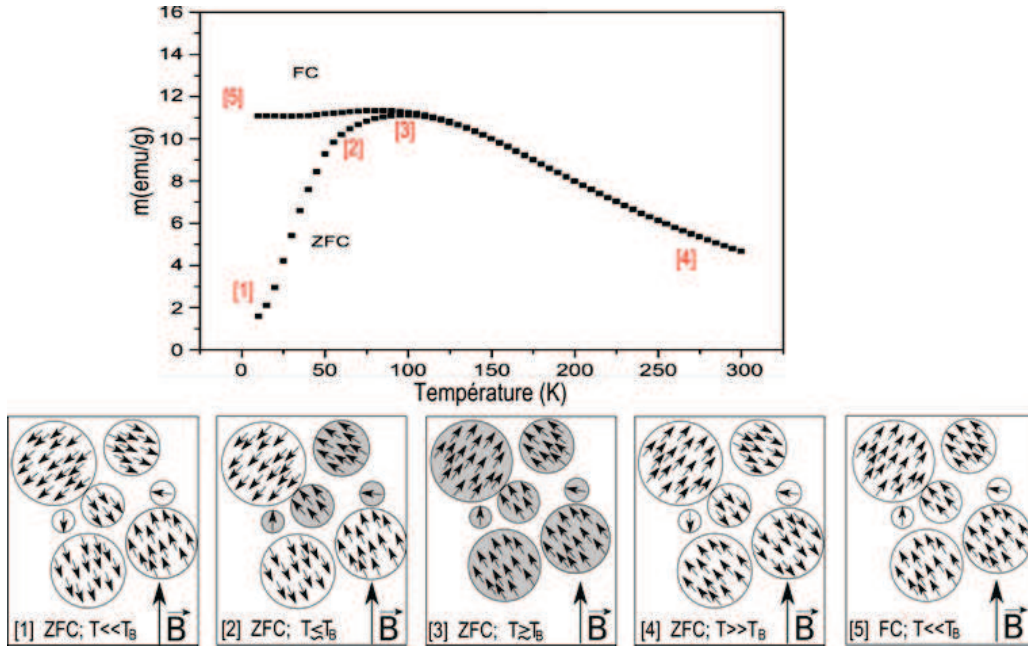


Figure 4.4 : Zero Field Cooled - Field Cooled (ZFC-FC) measurements of Fe_3O_4 particles exhibiting a blocking temperature of around 100 K. The sketches show the magnetization of superparamagnetic nanoparticles during ZFC-FC measurements.

The characteristic time for the particle magnetization to switch due to thermal fluctuations is given (Néel-Brown model [154]) by:

$$\tau_N = \tau_o \exp \left(\frac{\Delta E}{k_B T} \right) \quad (4.15)$$

here τ_o is a characteristic time of the material, called the attempt time; its typical value is 10^{-9} to 10^{-10} s. The blocking temperature for which $\tau_N = \tau_{mes}$ is given by:

$$T_B = \frac{KV}{k_B \ln(\frac{\tau_{mes}}{\tau_0})} \quad (4.16)$$

In Fig. 4.4, we show an example of the so-called ZFC-FC curves measured on Fe_3O_4 nanoparticles [155]. The sample is cooled down to the temperature below T_B without magnetic field (ZFC: zero field cooled). Then a weak field is applied, the initial magnetization is zero because the particles are randomly blocked. As the temperature increases (below T_B), some particles have enough energy to align their magnetic moment with applied field up to T_B . As the temperature keeps increasing, the magnetization decreases as $1/T$ due to thermal fluctuations. When the sample is cooled down applying an external field (FC) to block the particle magnetization, then the magnetization increases at very low temperature because it has been aligned by the applied field. These irreversible curves can be used to characterize the superparamagnetic properties of the samples. They can also be used to study their magnetic anisotropy by comparing in-plane and out-of-plane ZFC-FC measurements.

4.3 Results and Discussion

4.3.1 Ge_3Mn_5 thin films on Ge(111)

Ge_3Mn_5 is a well known and most stable phase of (Ge,Mn) and its crystalline structure is known for many years [118]. It has hexagonal structure with lattice parameters: $a = b = 7.17\text{\AA}$ and $c = 5.06\text{\AA}$. This phase is ferromagnetic with a Curie temperature of 304K [156–158] and with a magnetic moment of $2.60 \mu_B$ per Mn atom at 4K [159]. The theoretical study shows that Mn exists in two sites with different magnetic moments (Fig. 4.5). The values given by ref. [160] are $1.96 \mu_B/\text{Mn}$ for Mn^I and $3.23 \mu_B/\text{Mn}$ for Mn^{II} site. This gives an average magnetic moment of $2.72 \mu_B/\text{Mn}$.

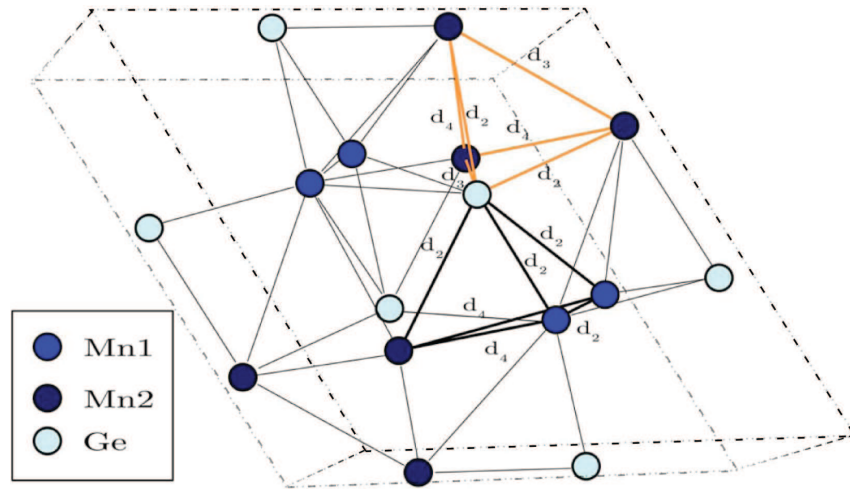


Figure 4.5 : Unit cell of Ge_3Mn_5 crystalline structure. The Mn atoms exist in two different sites with different magnetic moments. There are 6 Ge, 4 Mn^I and 6 Mn^{II} atoms.

Since Ge(111) face has hexagonal symmetry, Ge_3Mn_5 thin films with c-axis perpendicular to the film plane are known to be epitaxially grown on Ge(111) substrates [161–167]. We have used this $\text{Ge}_3\text{Mn}_5/\text{Ge}(111)$ system as a model system to check the correlation between different experimental techniques.

For the growth of Ge_3Mn_5 films, the native oxide of Ge(111) epitaxially substrate was removed by thermal desorption at 600°C in the ultra high vacuum growth chamber. After desoxidation,

the RHEED pattern was 2-D and a 8×2 reconstruction was seen [168]. Ge_3Mn_5 films were grown at 250°C by co-depositing Ge and Mn atoms according to the Ge_3Mn_5 stoichiometry. A 30nm thick Ge_3Mn_5 film was grown and the RHEED pattern was crystalline throughout the growth.

A high resolution transmission electron microscopy (HRTEM) image of grown Ge_3Mn_5 crystalline film is shown in Fig. 4.6. The c-axis of the hexagonal Ge_3Mn_5 crystal lies along the Germanium [111] growth axis. Due to a large lattice mismatch (3.7%), the Ge_3Mn_5 lattice relaxation occurs at the first stage of the film growth leading to the formation of interface dislocations between the Ge(111) substrate and the film. Hence the Ge_3Mn_5 film exhibits the bulk crystal structure. The epitaxy relationship in the film plane is Ge_3Mn_5 [100]||[1 $\bar{1}$ 0] Ge [161].

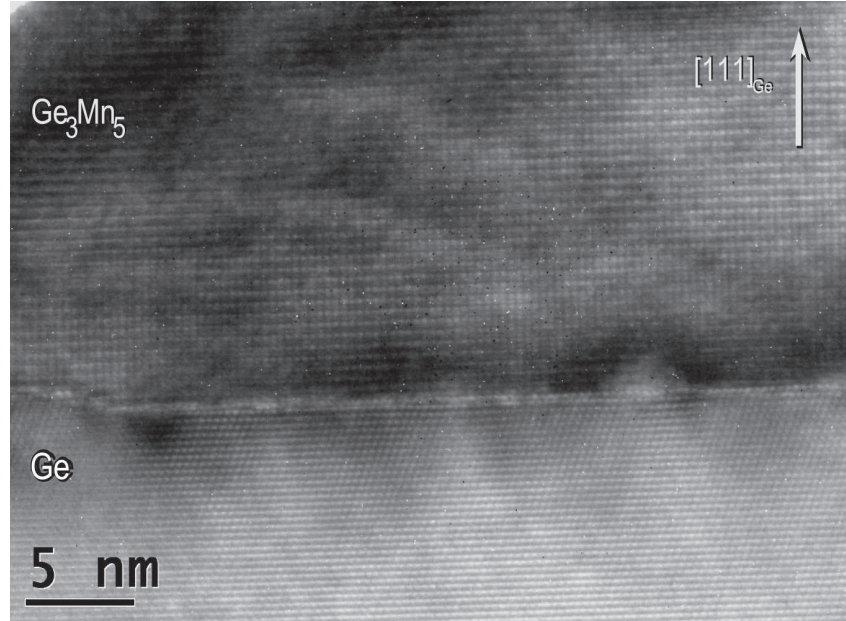


Figure 4.6 : High resolution TEM cross section of a 30 nm thick Ge_3Mn_5 film epitaxially grown at 250°C on Ge(111).

Magnetic measurements from this Ge_3Mn_5 film investigated by superconducting quantum interference device (SQUID) are displayed in Fig. 4.7(a). The temperature dependence of the magnetization yields Curie temperature $T_c = 300 \pm 5$ K and the saturation magnetization $M_S(5\text{K}) = 992$ kA/m ($2.41 \mu_B/\text{Mn}$). These values are in good agreement with the published data.

The hysteresis curves for in-plane and out-of-plane configurations at 100K is shown in Fig. 4.7(b). It is clearly visible that the grown Ge_3Mn_5 film exhibits in-plane anisotropy. In this film there exists competition between two types of magnetic anisotropies: first the magneto-crystalline anisotropy (K_{MC}) in Ge_3Mn_5 due to its crystalline structure which favors magnetization towards c-axis of hexagonal i.e. out-of-plane and second the shape anisotropy (K_{shape}) due to the morphology of the film which favors magnetization to be in-plane of the film. Hence in this Ge_3Mn_5 film, shape anisotropy overcomes the magneto-crystalline anisotropy ($K_{MC}/K_{shape} < 1$) leading to net magnetization in-plane of the film.

The difference in area between in-plane and out-of-plane magnetization curves gives an estimation of net magnetic anisotropy: $K_{shape} - K_{MC} = K = 2.1 \times 10^5$ J/m³. Moreover, the magnetic anisotropy given by the shape of a thin film is given by: $K_{shape} = \frac{1}{2} \mu_0 M_s^2 = 6.2 \times 10^5$ J/m³. Hence we deduce the magnetocrystalline anisotropy constant to be $K_{MC} = 4.1 \times 10^5$ J/m³ which is almost same as the reported bulk value ([157]).

The anisotropy in this film was then probed by ferromagnetic resonance (FMR). The FMR spectra for X-band ($f = 9.4$ GHz) were recorded as a function of the static field direction at 5 K as

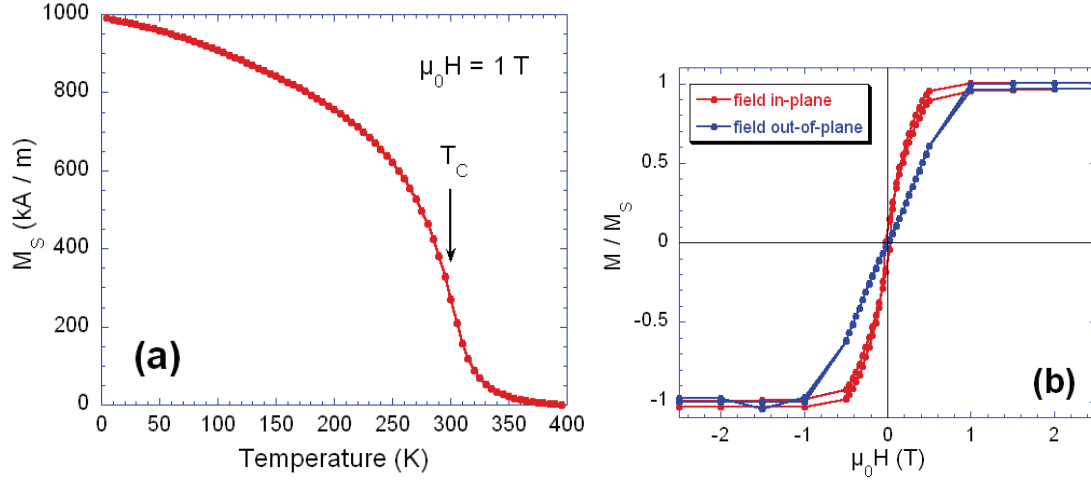


Figure 4.7 : (a) Temperature dependence of the saturation magnetization of a 30 nm thick Ge_3Mn_5 film recorded at 1 Tesla. (b) Hysteresis loops at 100K with the applied field parallel and perpendicular to the Ge_3Mn_5 film plane.

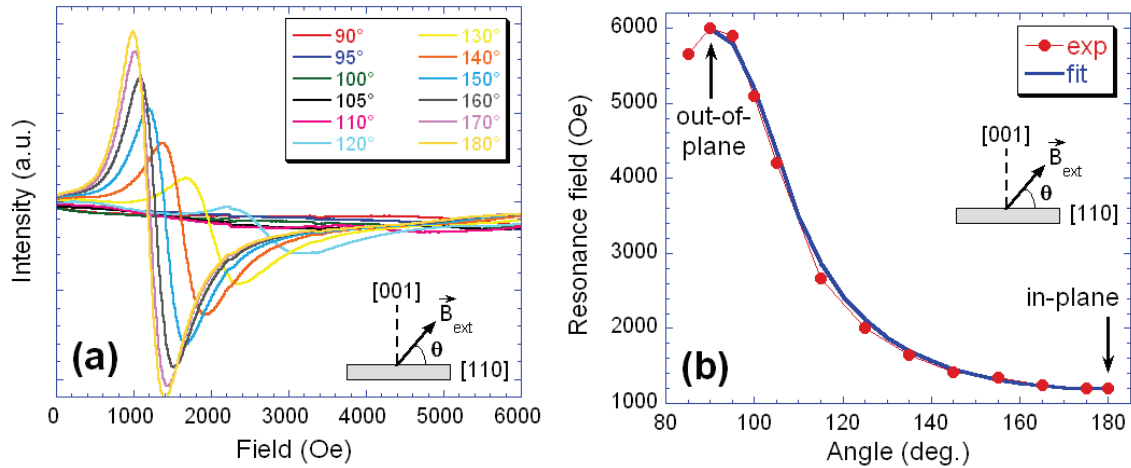


Figure 4.8 : (a) FMR spectra recorded at 5 K on a Ge_3Mn_5 film for different field directions. (b) Angular dependence of the resonance field. The angle is defined between the direction [110] and the applied magnetic field as shown in the inset.

shown in Fig. 4.7. Fitting the angular dependence of the resonance field using the Smit-Beljers formalism yields the magnetocrystalline anisotropy constant: $K_{MC} = 4.4 \times 10^5 \text{ J/m}^3$ (with $\gamma = 1.4$ where γ is electron gyromagnetic ratio) which is almost same as obtained above. This proves the high sensitivity and the calibration of the measurement techniques along with good correlation between them.

4.3.2 Crystalline (Ge,Mn) nanocolumns / Ge(001)

(Ge,Mn) thin film containing Mn-rich nanocolumns was grown on epitaxially Ge(001) substrates. The thermal desorption of the native surface oxide was done by heating the substrate in MBE chamber at 600°C, followed by growth of 40 nm thick Ge buffer layer at 250°C, resulting in a perfect 2×1 surface reconstruction as observed by in-situ RHEED. Then, 80 nm thick $\text{Ge}_{0.9}\text{Mn}_{0.1}$ film was subsequently grown, at low growth temperature of 100°C to avoid formation of stable

phases due to the low solubility of Mn in Ge. Mn-rich nanocolumns spanning the whole film thickness are observed as a consequence of two-dimensional spinodal decomposition [53, 139].

High resolution XRD $\theta/2\theta$ scans performed on the epitaxial layers show only the germanium (004) diffraction peak and revealed no secondary phases. In transmission electron microscopy, Fig. 4.9 shows the cross-sectional and plane view of a $\text{Ge}_{0.9}\text{Mn}_{0.1}$ film grown at 100°C . These nanocolumns have diameter of around 3 nm and density of $32000 \mu\text{m}^{-2}$. These nanocolumns are well crystalline and in perfect epitaxial relationship with the Ge matrix. Moreover if we assume that the Mn concentration in the Ge matrix is in between 0 and 1 %, the resulting Mn content in the columns is close to 50 %.

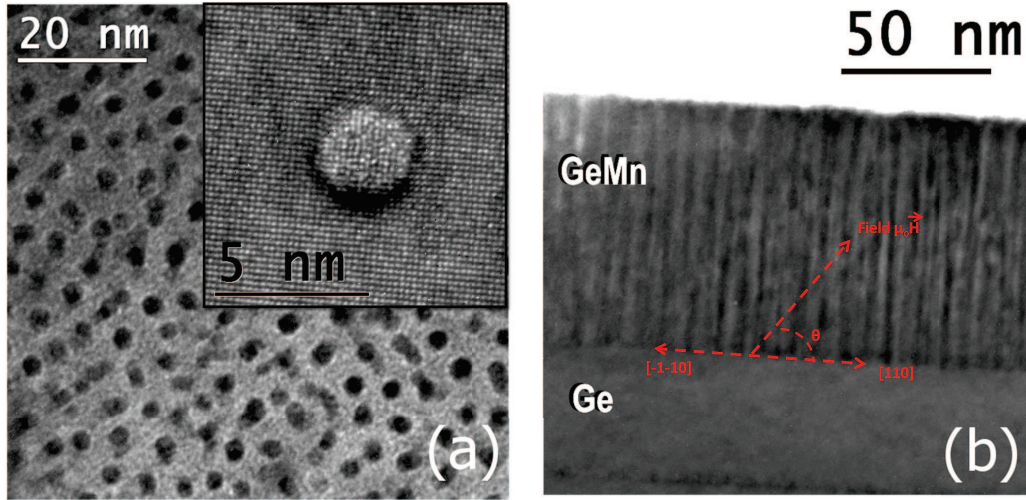


Figure 4.9 : (a) Plane view along $[001]$ and (b) cross-section view along $[110]$ TEM images of a $\text{Ge}_{0.9}\text{Mn}_{0.1}$ thin-film epitaxially grown on $\text{Ge}(001)$ at 100°C . The inset in (a) shows the core of a nanocolumn with a crystalline structure.

SQUID measurements performed on this $\text{Ge}_{0.9}\text{Mn}_{0.1}$ are reported in Fig. 4.10(a). We identify two different contributions: paramagnetic signal from Mn ions in the Ge matrix at lower temperatures and ferromagnetic signal from the nanocolumns with curie temperature between 100-200 K. The ZFC-FC measurements show that these nanocolumns are superparamagnetic with blocking temperature of 15 K and the magnetization versus field curves are reversible above 15K. In order to find the exact T_c , we tried a Curie-Weiss fitting of the magnetic susceptibility. However, the blocking temperature is much less than Curie temperature ($T_B/T_c < 0.1$) making the magnetic signal from super paramagnetic nanocolumns almost negligible when approaching T_c and the transition is not visible. Thus we used Arrott plots which gives the T_c close to 150 K. As expected it corresponds to the inflection point of the $M(T)$ curve shown in Fig. 4.10(a). The narrow shape of the ZFC peak is related to the narrow size distribution of nanocolumns grown in this temperature range [139].

To determine the magnetic anisotropy of these columns, Zero Field Cooled-Field Cooled (ZFC-FC) measurements were performed with the field parallel and perpendicular to the film plane (Fig. 4.10(c,d)). The susceptibility perpendicular to the plane seems slightly higher than that in the plane but a strong diamagnetic signal from the substrate and paramagnetic signal from diluted Mn atoms makes it difficult to quantify precisely this anisotropy.

FMR technique is hence used to differentiate the ferromagnetic signal of nanocolumns from the paramagnetic diluted Mn atoms and estimate magnetic anisotropy. The experiments were performed in Q-band (34 GHz) since cyclotron resonance peak was observed in X-band. This high intense cyclotron peak makes it difficult to follow the ferromagnetic resonance peaks (see appendix for more details). The FMR spectra are observed as a function of the angle of applied

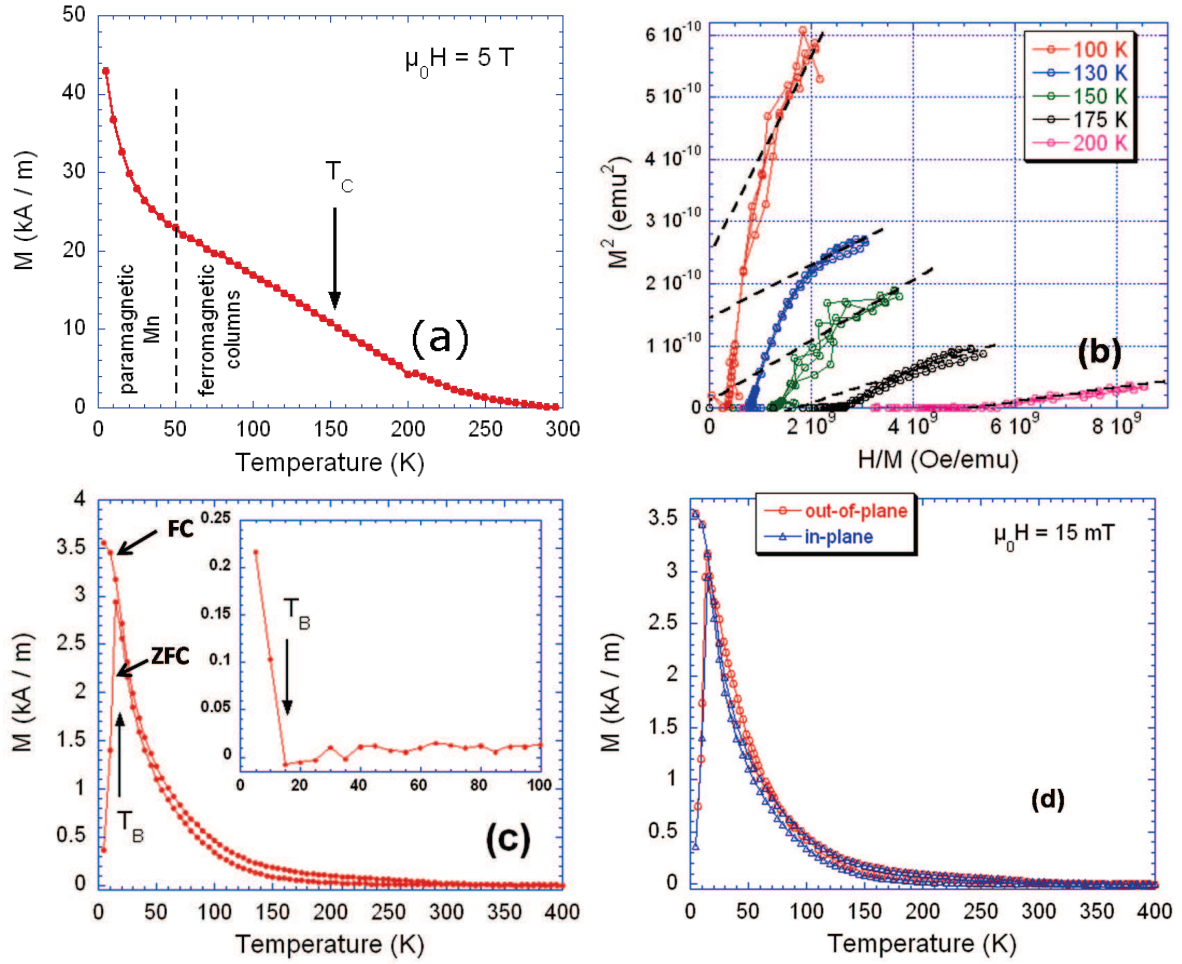


Figure 4.10 : (a) Temperature dependence of the saturation magnetization (in kA/m) of a $\text{Ge}_{0.9}\text{Mn}_{0.1}$ film grown at 100°C . The applied field is 5 T . (b) Arrott plots to estimate the Curie temperature of nanocolumns. It is found that $150 \text{ K} < T_c < 175 \text{ K}$ which is a very rough estimation of the Curie temperature (c) ZFC-FC measurements performed with the field of 15 mT parallel to the film plane. Inset: magnetic remanence after maximum field cooling under 5 T . (d) ZFC-FC measurements performed with the field parallel and perpendicular to the film plane.

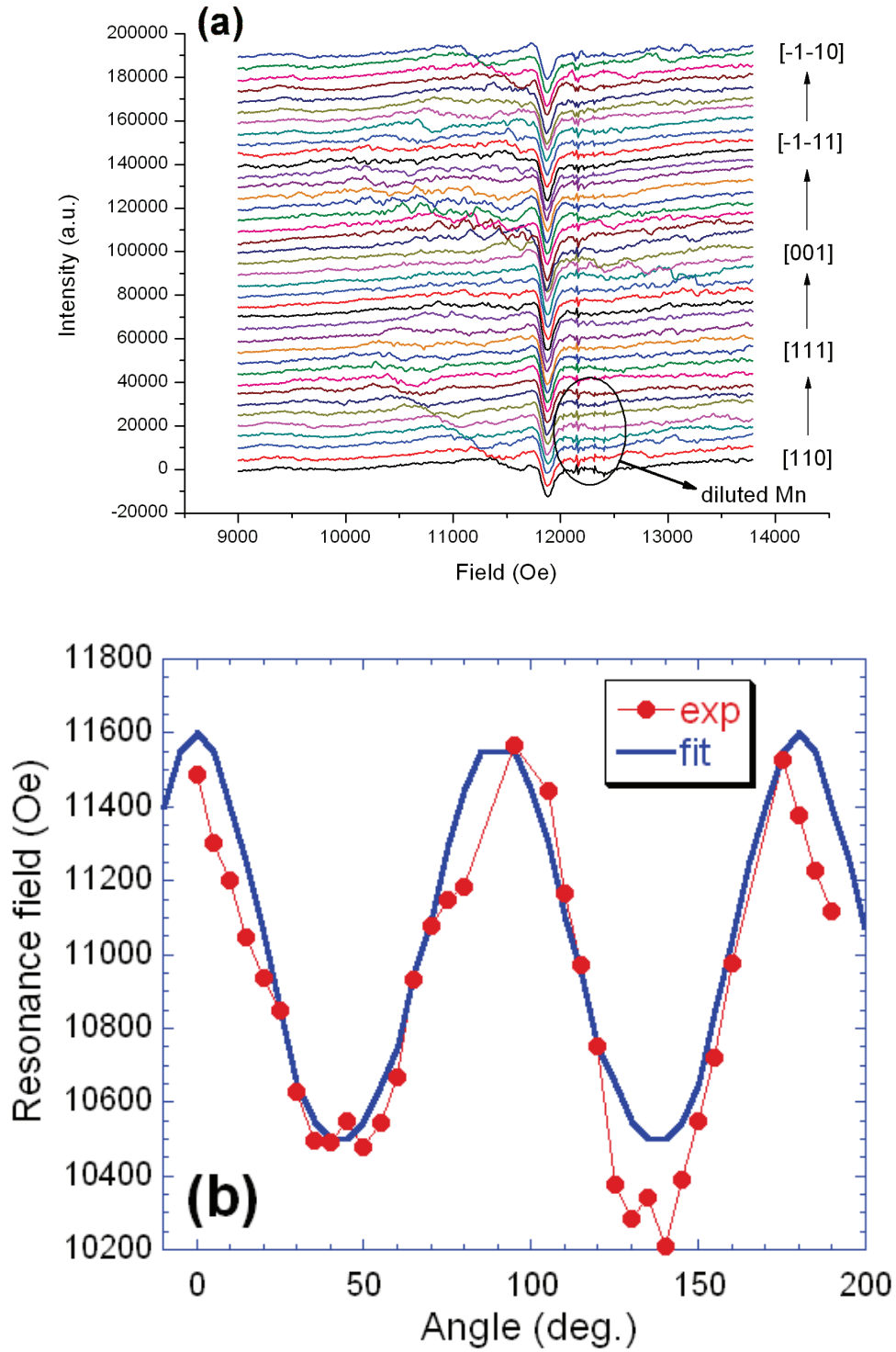


Figure 4.11 : (a) The FMR absorption spectra at Q band (34 GHz) of $\text{Ge}_{0.9}\text{Mn}_{0.1}$ sample grown at 100°C . (b) Angular dependence of the resonance field as a function of orientation of magnetic field. We observe two contributions: a ferromagnetic peak of weak anisotropy and six hyperfine peaks from diluted paramagnetic Mn ions. The angle is defined between the direction [110] and the applied magnetic field. The angular step in goniometer during measurement has been 5° . A fit with anisotropy fields $\mu_0 H_{a2} = 0.09 \text{ T}$ and $\mu_0 H_{a4} = 0.11 \text{ T}$ is also shown.

magnetic field. The field was applied in out-of-plane geometry from the direction $[110]$ to direction $[\bar{1}\bar{1}0]$ passing through the $[111]$, $[001]$ and $[\bar{1}\bar{1}1]$ direction. Fig. 4.11(a) shows the FMR spectra of the $\text{Ge}_{0.9}\text{Mn}_{0.1}$ film with crystalline nanocolumns and we observe hyperfine Mn lines [169] and also a weak ferromagnetic line we attributed to nanocolumns. The same isotropic hyperfine lines were observed in diluted paramagnetic (Ge,Mn) films containing 0.1% of Mn (Fig. 4.12). Hence, we attributed this FMR signal to diluted paramagnetic Mn in the Ge matrix.

The angular dependence of the resonance field in Fig. 4.11(b) is fitted using the Smit-Beljers formalism. We found the anisotropy fields: $\mu_o H_{a2} = 0.09$ T for the second order and $\mu_o H_{a4} = 0.11$ T for the fourth order with $\gamma/\gamma_e = 1.07$. Hence, the nanocolumns exhibit a perpendicular uniaxial anisotropy and a cubic anisotropy with easy axis along $[111]$. The presence of cubic anisotropy supports the crystallinity of nanocolumns. Also, cubic anisotropy and uniaxial anisotropy constants are of the same order of magnitude making the two crystal axes $[110]$ and $[001]$ close in energy. It thus explains the small difference between the ZFC curves for the field parallel and perpendicular to the film plane in the SQUID measurements of Fig. 4.10(b). If we consider the saturation magnetization of these small nanocolumns from SQUID $M_s = 140 \pm 20$ kA/m, we can derive the anisotropy constants to be: $K_2 = 0.63 \times 10^4$ J/m³ and $K_4 = 0.77 \times 10^4$ J/m³. The shape anisotropy of these nanocolumns given by $\mu_o M_s^2/4 = 0.62 \times 10^4$ J/m³ nicely corresponds to the uniaxial anisotropy (assuming that nanocolumns are infinite cylinders [170]).

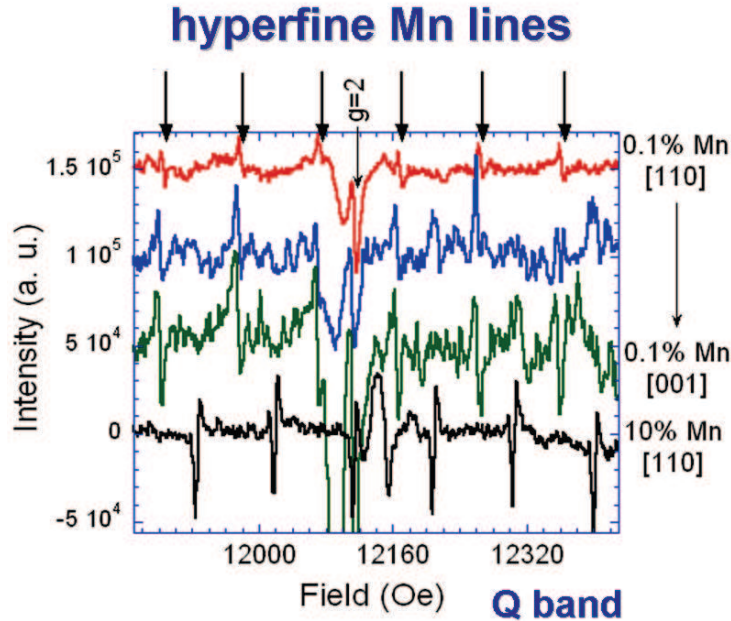


Figure 4.12 : The hyperfine lines observed for GeMn sample containing 0.1% and 10% Mn content. No FMR lines were observed in case of 0.1% Mn.

4.3.3 Amorphous (Ge,Mn) nanocolumns / Ge(001)

The (Ge,Mn) nanocolumns in $\text{Ge}_{1-x}\text{Mn}_x$ films grown at 100°C as discussed above are small in diameter and fully strained on the Ge matrix. However if the growth temperature is increased, we see some pairs of dislocations between the nanocolumns and the Ge matrix and finally for $T \approx 150^\circ\text{C}$ they relax partially and become amorphous. The TEM image of a $\text{Ge}_{0.9}\text{Mn}_{0.1}$ film grown at 150°C is shown in Fig. 4.13. The diameter of nanocolumns increases having a average diameter of 6 nm and a density of $600 \mu\text{m}^{-2}$.

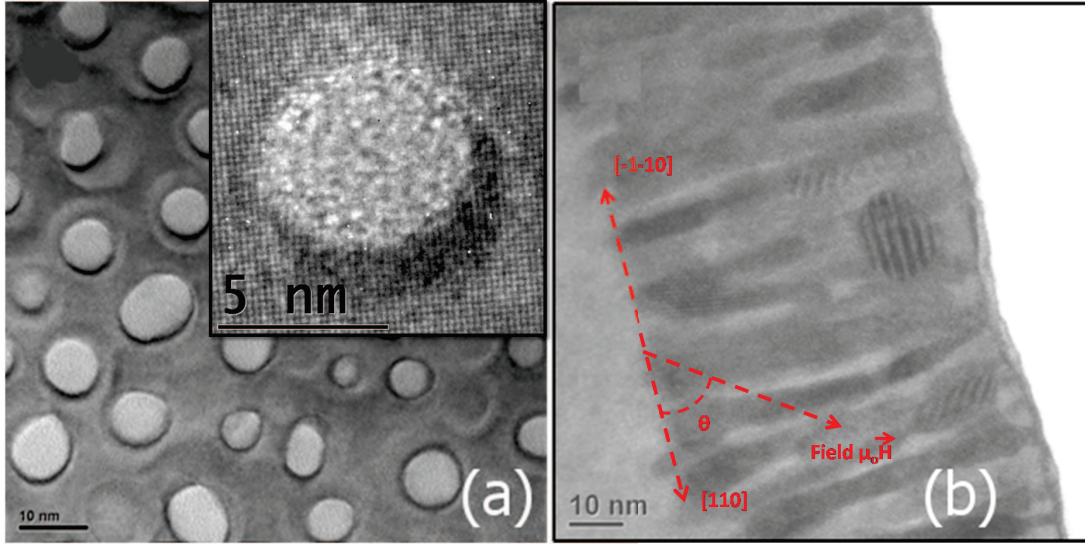


Figure 4.13 : (a) Plane view along $[001]$ and (b) cross-section view along $[110]$ high-resolution TEM image of a $\text{Ge}_{0.9}\text{Mn}_{0.1}$ film epitaxially grown at 150°C . The inset in (a) shows the core of a nanocolumn with disordered structure and appears to be amorphous.

The magnetic measurements from this layer is shown in (Fig. 4.14). These amorphous nanocolumns have a Curie temperature of 125 K. The Curie temperature is calculated by Curie-Weiss fitting of the magnetic susceptibility (In case of large amorphous nanocolumns, the inflection point is found at $T \approx 170$ K as shown in Fig. 4.14(a). Since T_B (≈ 75 K) is larger than for crystalline columns (≈ 15 K), a Curie-Weiss plot is possible). The contribution from diluted paramagnetic Mn atoms is still observed at low temperature. In ZFC-FC curves we see two peaks at around 27 K and 72 K in the ZFC curve and a weak contribution from Ge_3Mn_5 clusters. Those peaks are broad and in agreement with the broad size distribution observed by TEM [139]. The Ge_3Mn_5 clusters were also present due to growth at higher temperature. Here the T_c was estimated using Curie-Weiss plot, since it is close to T_B (around 72 K) and hence superparamagnetism to paramagnetism transition is visible.

The magnetic anisotropy of these columns is studied by FMR. The spectra are shown in Fig. 4.15 and the angular dependence of the resonance field is fitted using the Smit-Beljers formalism assuming that nanocolumns are non-interacting and single domain. A single perpendicular uniaxial anisotropy is found, the corresponding anisotropy field is: $\mu_0 H_{a2} = 0.09T$ and $\gamma/\gamma_e = 1.24$. From the saturation magnetization of amorphous nanocolumns $M_S = 220 \pm 20$ kA/m, the anisotropy constant is calculated to be $K_2 = 1.1 \times 10^4$ J/m³. This value corresponds to that of shape anisotropy $\mu_0 M_S^2/4 = 1.5 \times 10^4$ J/m³ of nanocolumns assuming their aspect ratio is high [170]. As expected for amorphous nanocolumns, no cubic magneto-crystalline contribution is found.

In the case of uniaxial magnetic anisotropy, we can easily estimate the blocking temperature of nanocolumns using the classical Néel-Brown model [154]: $KV = 25k_B T_B$, where K is the anisotropy constant, V the columns volume, k_B the Boltzmann constant and T_B the blocking temperature. From the average diameter and length of nanocolumns (6 nm and 80 nm respectively) given by TEM observations, we can estimate their volume and the blocking temperature: $T_B = 72$ K which corresponds to the second broad peak in the ZFC curve. The first peak with a maximum close to 27 K thus corresponds to shorter magnetic nanocolumns with an average length of $= (27/72) \times 80$ nm = 30 nm. We can conclude that increasing the growth temperature partly activates Mn diffusion along the growth direction which leads to the formation of

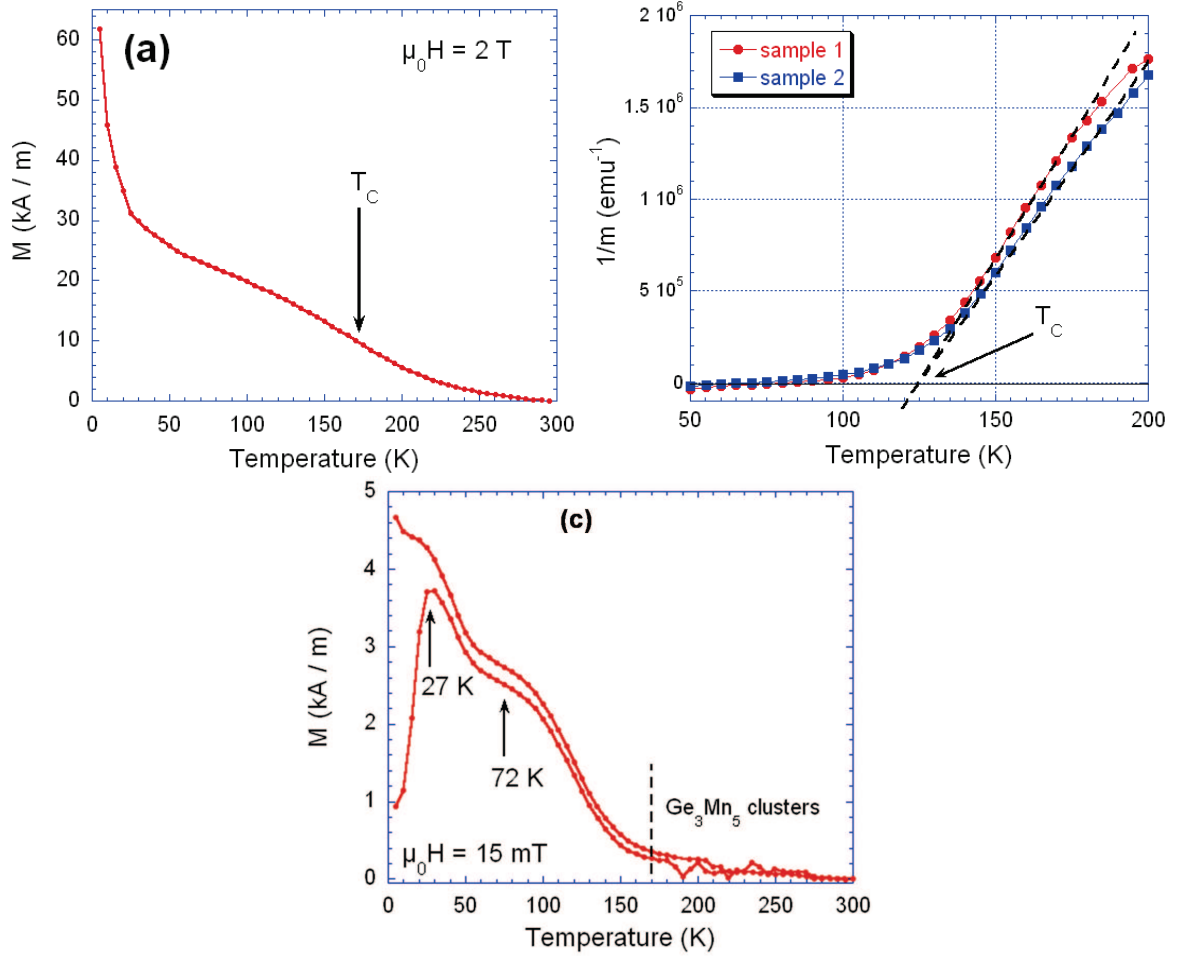


Figure 4.14 : (a) Temperature dependence of the saturation magnetization of a $\text{Ge}_{0.9}\text{Mn}_{0.1}$ film grown at 150°C . The magnetic field is 5 T and applied in the film plane along the $[110]$ direction. (b) Curie-Weiss fitting of the magnetic susceptibility which gives the Curie temperature of approximately 125 K . (c) ZFC-FC measurements performed at 0.015 T . The ZFC curve exhibits two peaks with blocking temperatures around 27 K and 72 K respectively.

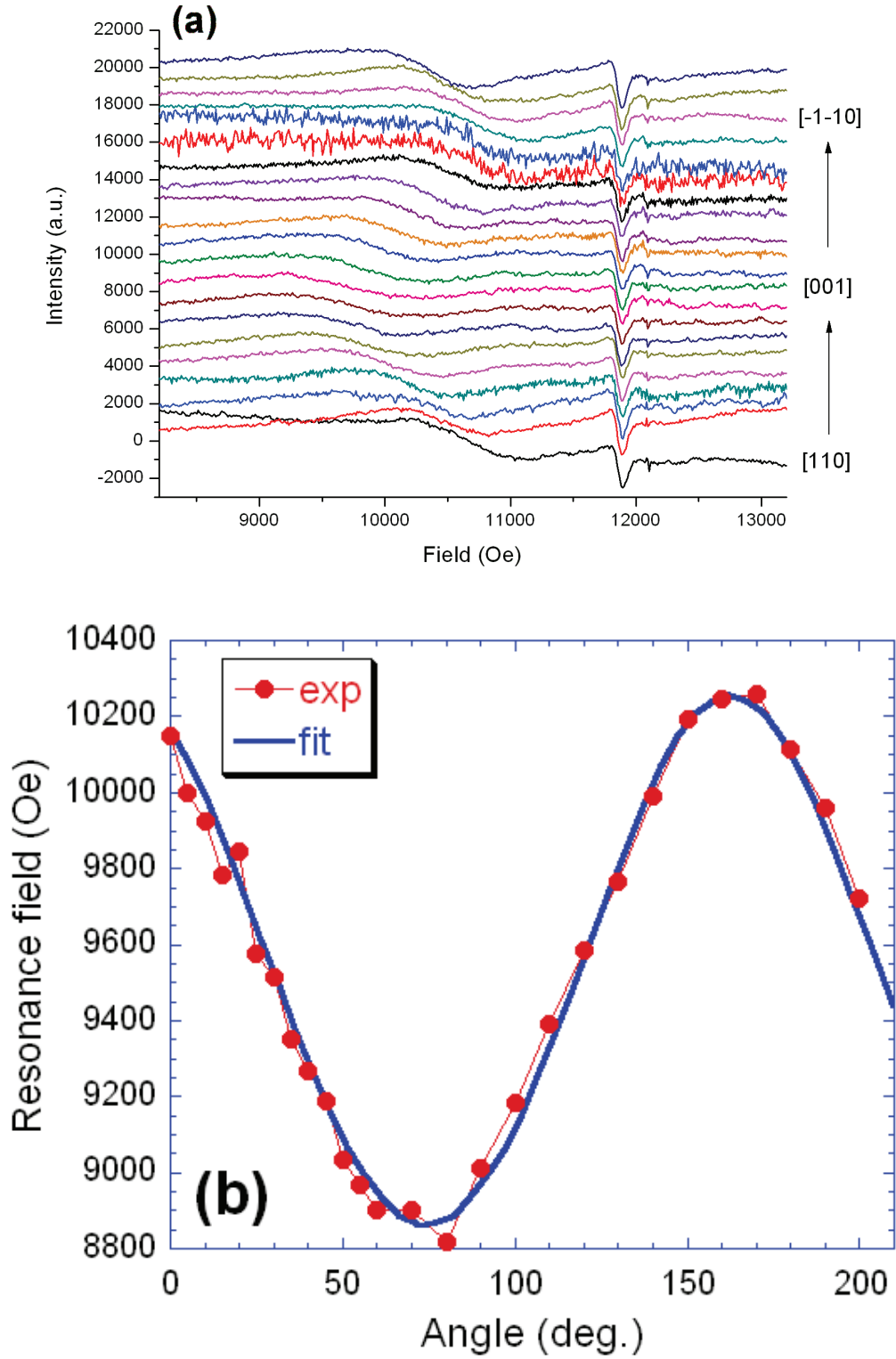


Figure 4.15 : (a) The FMR absorption spectra at Q band (34GHz) of $\text{Ge}_{0.9}\text{Mn}_{0.1}$ sample grown at 150°C . (b) Angular dependence of the resonance field as a function of orientation of magnetic field. The angle is defined between the direction $[110]$ and the applied magnetic field. The angular step in goniometer during measurement has been 5° . A fit with anisotropy fields $\mu_0 H_{a2} = 0.09\text{T}$ and $\mu_0 H_{a4} = 0$ is also shown.

elongated clusters instead of continuous nanocolumns spanning the whole film thickness.

4.3.4 Ge_3Mn_5 clusters/ $\text{Ge}(001)$

During the growth of (Ge,Mn) , there is tendency to form thermodynamically favorable ferromagnetic precipitates of Ge_3Mn_5 phase [134–137]. We observed that the growth of (Ge,Mn) films at high temperature ($> 180^\circ\text{C}$) on $\text{Ge}(001)$ or annealing (Ge,Mn) films grown at low temperature above 600°C leads to the formation of randomly distributed spherical Ge_3Mn_5 clusters.

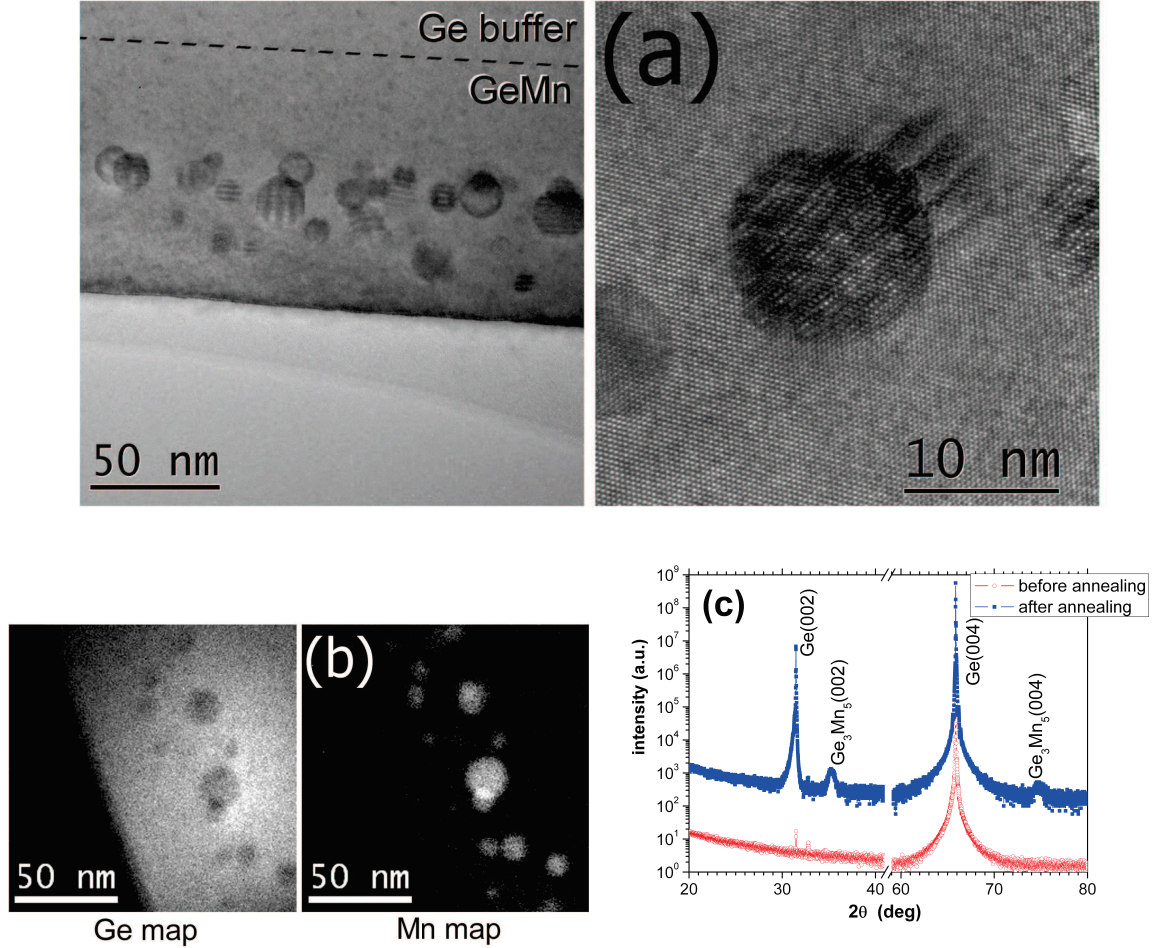


Figure 4.16 : (a) High resolution TEM image of a $\text{Ge}_{0.94}\text{Mn}_{0.06}$ thin film grown at 130°C and annealed at 650°C for 15 minutes. Spherical Ge_3Mn_5 clusters are clearly visible. (b) Energy filtered TEM images using electron energy loss spectroscopy and showing Ge and Mn rich zones and (c) $\theta/2\theta$ XRD spectra of a $\text{Ge}_{0.94}\text{Mn}_{0.06}$ film grown at 130°C before and after annealing at 650°C for 15 minutes.

The RHEED pattern of annealed samples is exactly the same as that of Ge as clusters are away from the surface, also verified in high resolution TEM image (Fig. 4.16(a)). Chemical analysis at the nanometer scale using electron energy loss spectroscopy (EELS) clearly shows Ge_3Mn_5 clusters as Mn-rich regions whereas Mn concentration in the surrounding Ge matrix is within the resolution limit of this technique (Fig. 4.16(b)). Finally x-ray diffraction measurements in $\theta/2\theta$ mode further suggest that these Ge_3Mn_5 clusters have their c-axis [001] lying along the Ge [001] direction (Fig. 4.16(c)).

In order to verify the different orientations of clusters, we performed grazing incidence x-ray diffraction at $\lambda = 0.12037$ nm, searching for all possible Ge_3Mn_5 reflections in the plane

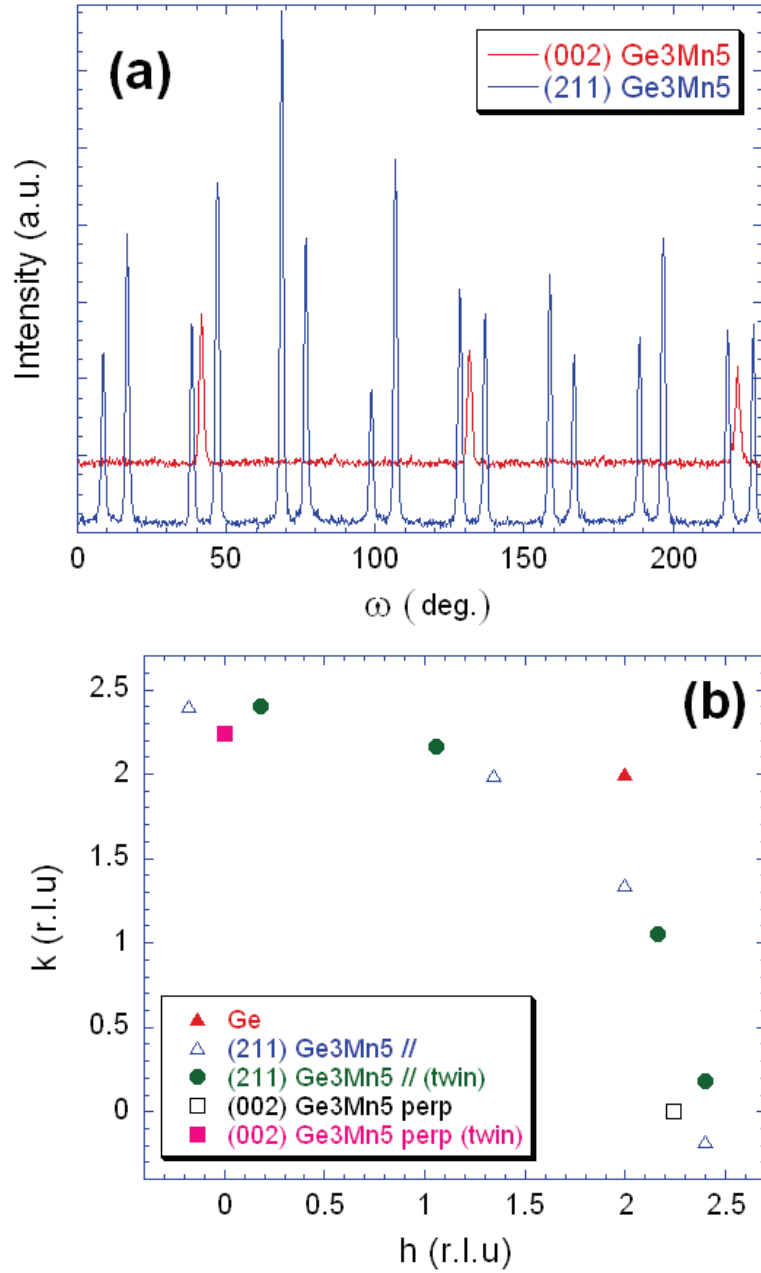


Figure 4.17 : (a) Grazing incidence X-ray diffraction angular scans performed around the 2θ Bragg angle of the $(002)_{\text{Ge}_3\text{Mn}_5}$ and $(211)_{\text{Ge}_3\text{Mn}_5}$ in-plane reflections. Four types of clusters are present, as explained in (b) with the location of all reflections relatively to the Ge lattice: two clusters with their c -axis perpendicular to the Ge surface, and their (100) direction either parallel to $(100)_{\text{Ge}}$ or $(010)_{\text{Ge}}$, and two with their c -axis either along $(100)_{\text{Ge}}$ or $(010)_{\text{Ge}}$. Small ($\approx 20\%$) intensity variations of equivalent reflections with ω in (a) are due to a small miscut in the sample, and also to the structure distortion (see text for details).

parallel to the sample surface. Measurements were performed at the European Synchrotron Radiation Facility (ESRF, Grenoble, France). The incident angle (0.3°) was chosen by maximizing the scattered intensity from the buried clusters. As is shown in Fig. 4.17, only two possible configurations are possible for the clusters:

- c -axis perpendicular to the sample surface (along $(001)_{Ge}$) and a -axis either along $(100)_{Ge}$ or $(010)_{Ge}$ as was already observed in Ref. 171.
- c -axis either along $(100)_{Ge}$ or $(010)_{Ge}$. A very small component can also be detected with the c -axis along $(110)_{Ge}$ but it is at least 20 times less intense than for the c -axis along $(100)_{Ge}$.

The relative intensities measured for a (002) reflection (for the clusters with a c -axis in-plane) and a (211) (for the c -axis out-of-plane) indicates, after taking into account theoretical intensities from bulk Ge_3Mn_5 , that there are $\approx 97 \pm 1\%$ of the clusters with a c -axis perpendicular to the sample surface. In order to avoid any effect from the sample miscut, the intensities of the (002) and (211) reflections were compared around the same azimuthal angle. The widths of radial scans around (211) reflections indicate that the cluster size is 10.6 ± 1 nm, and does not depend on the azimuth. Moreover, the exact coordinates for the (211) reflections for this main family of clusters showed that their lattice is distorted compared to the bulk hexagonal lattice. A refinement using 7 (211) reflections for the clusters with their a -axis parallel to $(010)_{Ge}$, yielded the following in-plane parameters for these clusters: $a = 0.7229$ nm, $b = 0.7197$ nm, $\gamma = 120.16^\circ$ (as compared to bulk value of 0.7184 nm). This indicates that the clusters are strained due to epitaxial strain by the germanium matrix due to lattice mismatch.

The magnetic properties of Ge_3Mn_5 clusters were studied using SQUID magnetometry. Fig. 4.18a shows the saturation magnetization of Ge_3Mn_5 clusters as a function of temperature. We can clearly observe two different phases: the Ge_3Mn_5 with a Curie temperature of 300 ± 5 K and the paramagnetic contribution of Mn ions in the Ge matrix. After subtracting the signal of Ge_3Mn_5 , the signal from diluted Mn ions is obtained and fitted using a Brillouin function. If we assume that Mn atoms are in substitutional position with a magnetic moment of $3 \mu_B$ [172], we deduce that the Mn concentration in the Ge matrix is of the order of 2 % (neglecting the volume fraction of precipitates). This value is in rather good agreement with that obtained by EELS which gives an average Mn content in the Ge matrix between 0 and 1 % which is the resolution limit of this technique. ZFC-FC measurements as well as the temperature dependence of magnetic remanence show that Ge_3Mn_5 clusters are superparamagnetic with an apparent blocking temperature of $T_B = 265 \pm 5$ K (Fig. 4.18).

Hysteresis curves at 5 K in Fig. 4.19 clearly show that most of Ge_3Mn_5 clusters exhibit perpendicular magnetic anisotropy. Since the clusters are spherical, perpendicular anisotropy arises from magnetocrystalline anisotropy. Bulk Ge_3Mn_5 crystal is hexagonal with uniaxial magnetic anisotropy along the c -axis, hence most of Ge_3Mn_5 clusters have their c -axis perpendicular to the film plane in good agreement with x-ray diffraction data. From hysteresis loops, we can estimate that 70 % of the magnetic signal corresponds to these clusters having c -axis perpendicular to the film plane.

As shown in the inset of Fig. 4.19, out-of-plane coercive fields range between 0.2 ± 0.05 T and 0.6 ± 0.05 T. This field dispersion arises from the cluster size distribution as shown in the TEM images of Fig. 4.16. Indeed for the smallest clusters, magnetization reversal is thermally activated giving the lowest coercive field value: 0.2 ± 0.05 T. On the other hand, for the largest blocked particles, the maximum coercive field gives the anisotropy field $\mu_0 H_{a2} = 0.6 \pm 0.05$ T of a single-domain cluster according to the Stoner and Wohlfarth model [154]. Using the bulk M_S value (1100 kA/m) [160], we deduce the anisotropy constant: $K_2 = \mu_0 H_{a2} M_S / 2 \approx 3.3 \times 10^5$ J/m³ which is less than the reported bulk value 4.2×10^5 J/m³ (Ref. Tawara1963). This may be explained by the distortion of Ge_3Mn_5 lattice due to the epitaxial-strain of the (Ge,Mn) matrix as observed

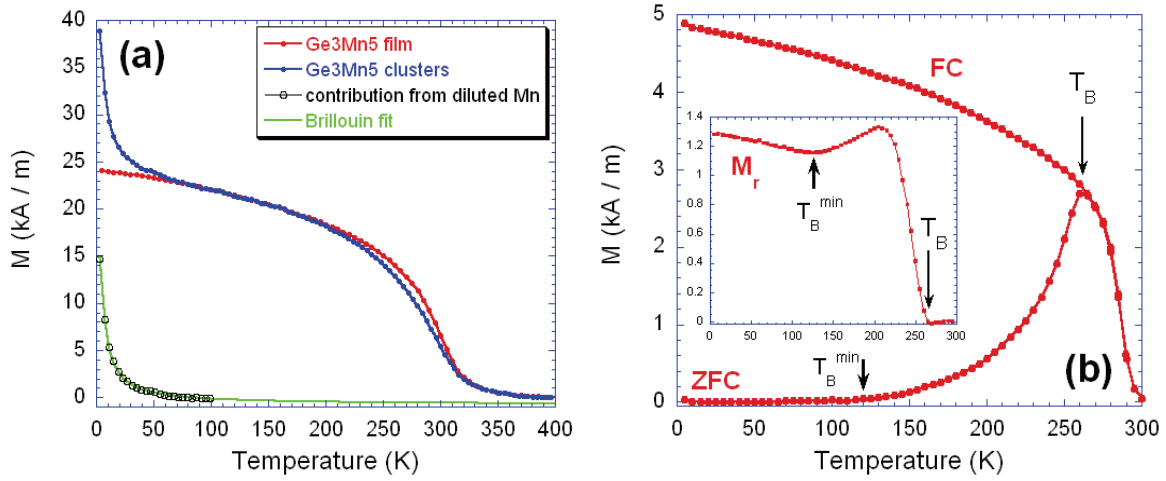


Figure 4.18 : (a) Temperature dependence of the saturation magnetization of a (Ge,Mn) thin film containing Ge_3Mn_5 clusters (in blue) compared with a Ge_3Mn_5 thin film (in red). The applied field is 2 T in the film plane. (b) ZFC-FC measurements performed on a $\text{Ge}_{0.94}\text{Mn}_{0.06}$ film grown at 100°C and annealed at 650°C for 15 minutes. The magnetic field is applied at 60° with respect to the film plane. Inset: magnetic remanence after maximum field cooling under 5 T.

in the diffraction. If we assume that undistorted clusters exhibit the bulk anisotropy constant, the effective magnetoelastic anisotropy constant K_{ME} is then simply given by: $K_{ME} = 4.2 \times 10^5 - 3.3 \times 10^5 = 0.9 \times 10^5 \text{ J/m}^3$. This result shows that magnetic anisotropy in Ge_3Mn_5 is very sensitive to slight crystal distortion. However, further systematic study is required to derive the exact dependence of magnetic anisotropy on crystal distortion.

Using the Néel-Brown model[154]: $K_2V = 25k_B T_B$ we find the actual blocking temperature of Ge_3Mn_5 clusters of average size 10.6 nm: $T_B = 596.5 \text{ K}$. This value is much higher than the Curie temperature and thus cannot be measured by ZFC-FC measurements. Moreover the lowest blocking temperature $T_B^{\min} \approx 120 \text{ K}$ (see Fig. 4.18b) yields a cluster diameter of $\approx 6.2 \text{ nm}$ which corresponds to a lower bound for the cluster size. If we further assume that the cluster size distribution is Gaussian-like and centered around 10.6 nm, we finally find the maximum cluster diameter: $\approx 10.6 + 4.4 = 15 \text{ nm}$. Hence Ge_3Mn_5 clusters grown by annealing (Ge,Mn) films exhibit a very broad size distribution.

In Fig. 4.19, we observe a magnetic signal with low coercive field which may have different origins: (i) Ge_3Mn_5 clusters with their c -axis in-plane, (ii) Ge_3Mn_5 clusters with in-plane magnetic anisotropy due to oblate shape or (iii) Mn-rich precipitates that remain despite the high annealing temperature and exhibit a very low coercive field. Case (i) is unlikely because in x-ray diffraction we observe only $3 \pm 1 \%$ of clusters having their c -axis in the film-plane along [100] and [010] directions. This population is not large enough to account for the low coercive field signal. For case (ii), we observe only spherical clusters in HRTEM image which rules out the possibility of having oblate clusters leading to in-plane shape anisotropy. We believe that case (iii) is most likely and the magnetic signal at low coercive field may originate from amorphous Mn-rich precipitates that remain in the film despite annealing at high temperature. This is supported by temperature dependent hysteresis curves (Fig. 4.20), where the low coercive field signal disappears above 200 K. This temperature is just above the Curie temperature of Mn-rich amorphous (Ge,Mn) phase [173] and this amorphous phase cannot be detected by x-ray diffraction.

The FMR spectra from (Ge,Mn) film containing Ge_3Mn_5 clusters is shown in Fig. 4.21. We observe ferromagnetic peaks only when external field is applied in the film plane, corresponding

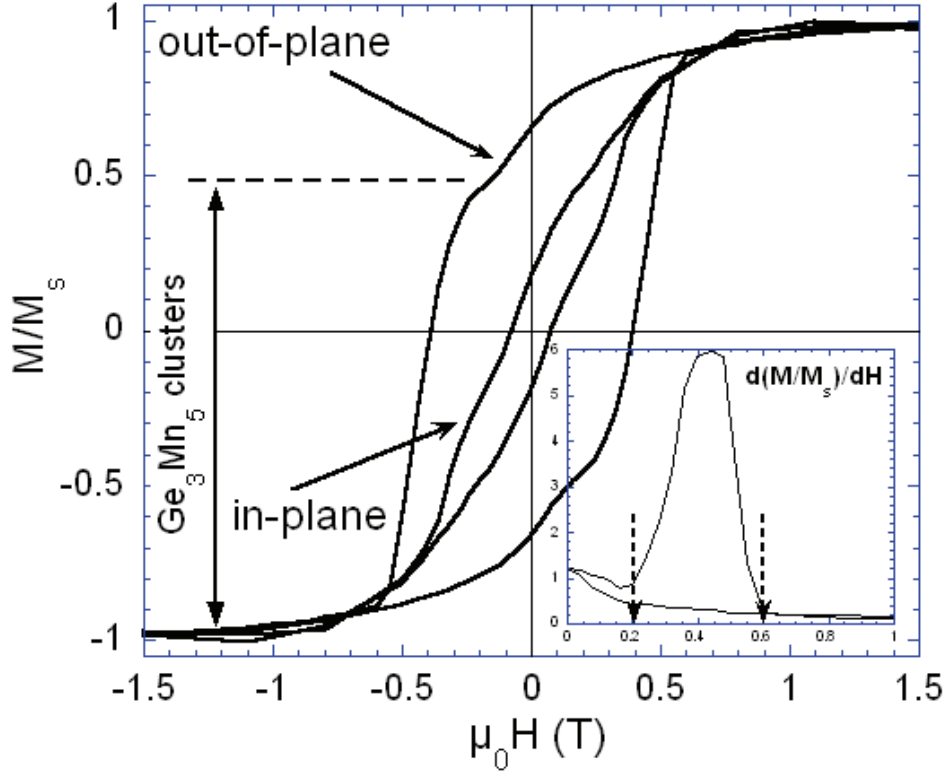


Figure 4.19 : *Hysteresis loops recorded at 5 K for the applied field parallel and perpendicular to the film plane. Inset: derivative of M/M_s for out-of-plane positive fields.*

to the clusters having out-of-plane anisotropy. These peaks are quite sensitive and disappears rapidly with change in field angle. From Smit-Beljer formalism we obtain the anisotropy field to be 0.42 T as compared to 0.4 T which is the median value obtained from SQUID measurements (see inset in Fig. 4.19), exhibiting a good correlation between the two techniques.

To summarize, we have grown Ge_3Mn_5 clusters by annealing (Ge,Mn) films grown at low temperature. This procedure leads to very broad size distributions of spherical clusters located away from the surface deep inside the germanium film. 97 % of these clusters exhibit strong out-of-plane magnetic anisotropy. However perpendicular anisotropy is less than the expected bulk value due to a clear in-plane distortion of the crystal lattice induced by epitaxial strain in the germanium matrix. These Ge_3Mn_5 clusters are thus model systems for the study of hybrid ferromagnet-semiconductor systems. In the future, new growth techniques have to be explored in order to improve the control over the size, location and magnetic anisotropy of these clusters and use them in vertical heterostructures for spintronic applications.

4.4 Growth on Germanium-on-insulator substrates

In order to define the Ge channel for spin injection from (Ge,Mn), Germanium-on-insulator (GOI) substrates are used. Another benefit of using these GOI substrates can be to study the effect of carrier concentration, charge effects and Rashba interaction on spin transport by applying gate voltage. The substrates were provided by the CEA-LETI and SOITEC company (collaboration with E. Augendre) and were fabricated using SmartCutTM technology.

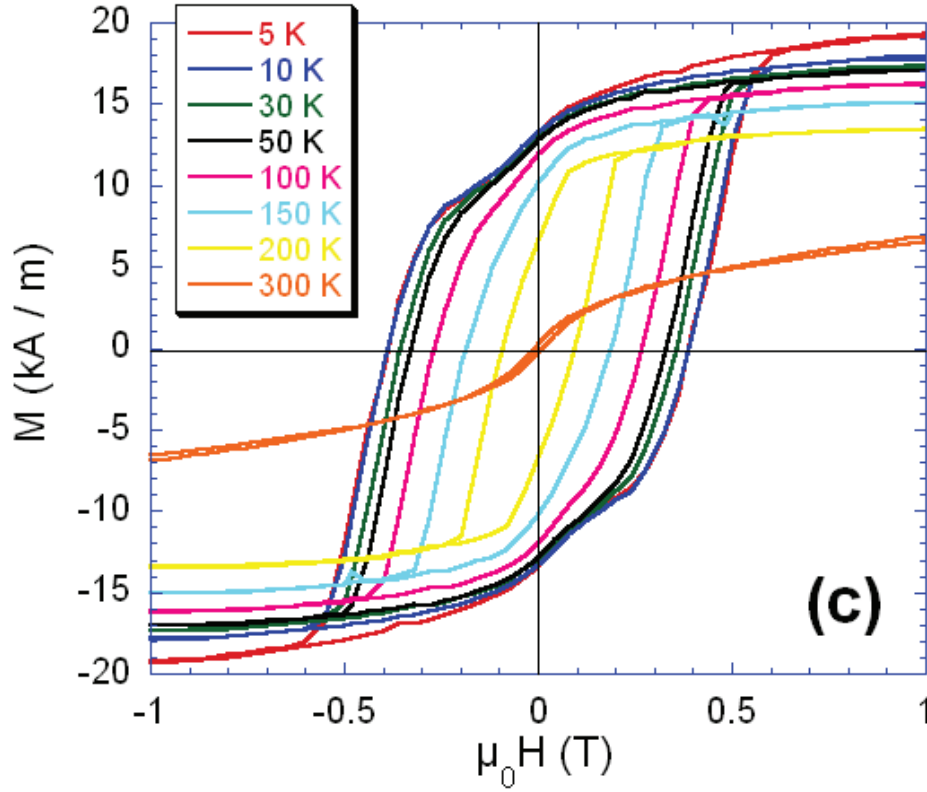


Figure 4.20 : Hysteresis loops recorded at different temperatures for the applied field perpendicular to the film plane.

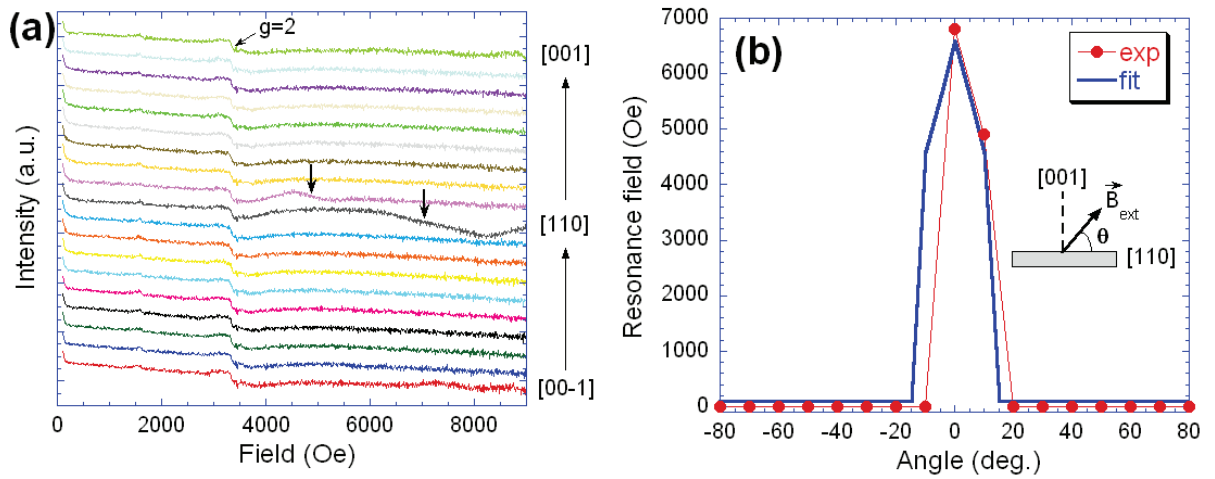


Figure 4.21 : (a) The FMR spectra for X-band (9.4 GHz) of Ge_3Mn_5 clusters at 5 K. (b) Angular dependence of the resonance field. The angle is defined between the film plane and the direction of the applied static magnetic field. The angular step in goniometer during measurement has been 10° .

4.4.1 Optimization of growth

The first step to have spin injection from (Ge,Mn) into Ge is to optimize the growth of (Ge,Mn) layers on these new substrates. The schematic diagram of GOI substrates used for (Ge,Mn)

growth is shown in Fig. 3.5. Since native Germanium oxide GeO_x is soluble in water, the direct exposure of Ge surface to air moisture can make the surface rough. To avoid this, the provided GOI substrates were covered with a SiO_2 capping layer. This capping layer was removed by treating the substrates with 10% HF solution until the surface becomes hydrophobic and finally rinsing in de-ionized water, just before introducing the sample into the MBE chamber.

In the MBE chamber, the substrate was gradually heated up to 600°C in three steps to remove moisture, organic impurities and finally the native oxide layer from $\text{Ge}(001)$. The RHEED pattern of the GOI surface after annealing is shown in Fig. 4.22(a) ; a 2×1 reconstruction is clearly seen. The substrate was then maintained at 250°C and a thin buffer layer of Ge was grown. The thickness of this buffer layer is normally 10-20 nm to make the surface smooth and also to bury the residual impurities present at the surface. This buffer layer was again annealed at 600°C and the RHEED pattern after annealing is shown in Fig. 4.22(b). The surface is now ready for (Ge,Mn) growth.

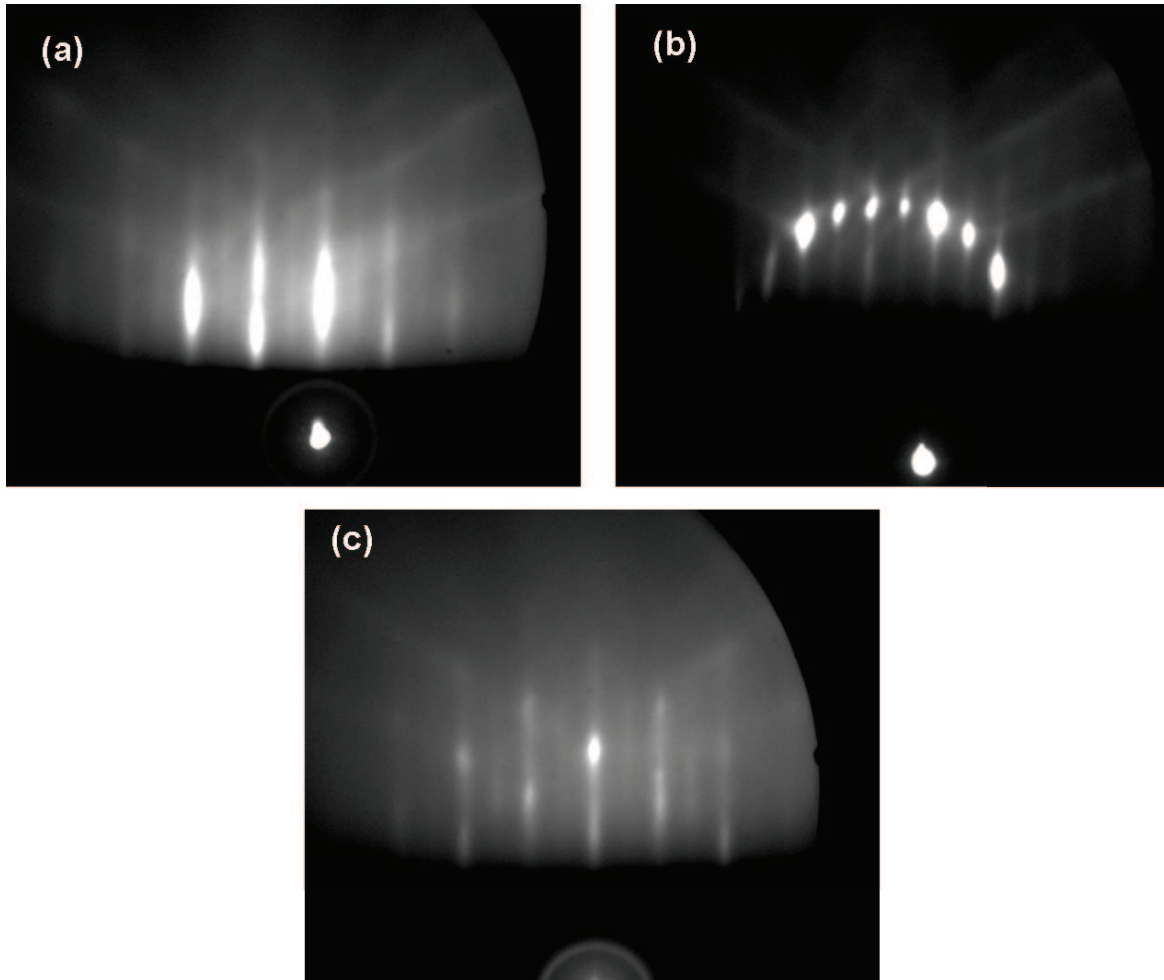


Figure 4.22 : (a) RHEED pattern of GOI substrate after annealing at 600°C along $[110]$ azimuth. After thermal desorption of the native oxide we can see a 2×1 reconstruction. (b) RHEED pattern after annealing the buffer layer. The surface is now ready for (Ge,Mn) growth. (c) The RHEED pattern after growth of 80 nm of (Ge,Mn) film. In this case the Mn concentration was 10%.

For the growth of (Ge,Mn) nanocolumns, the substrate was heated at 80°C and the Ge and Mn shutters were opened at the same time. The Ge flux which has been calculated by RHEED oscillations was around $0.2 \text{ \AA}/\text{sec}$. The Mn concentration which is known by RBS analysis can

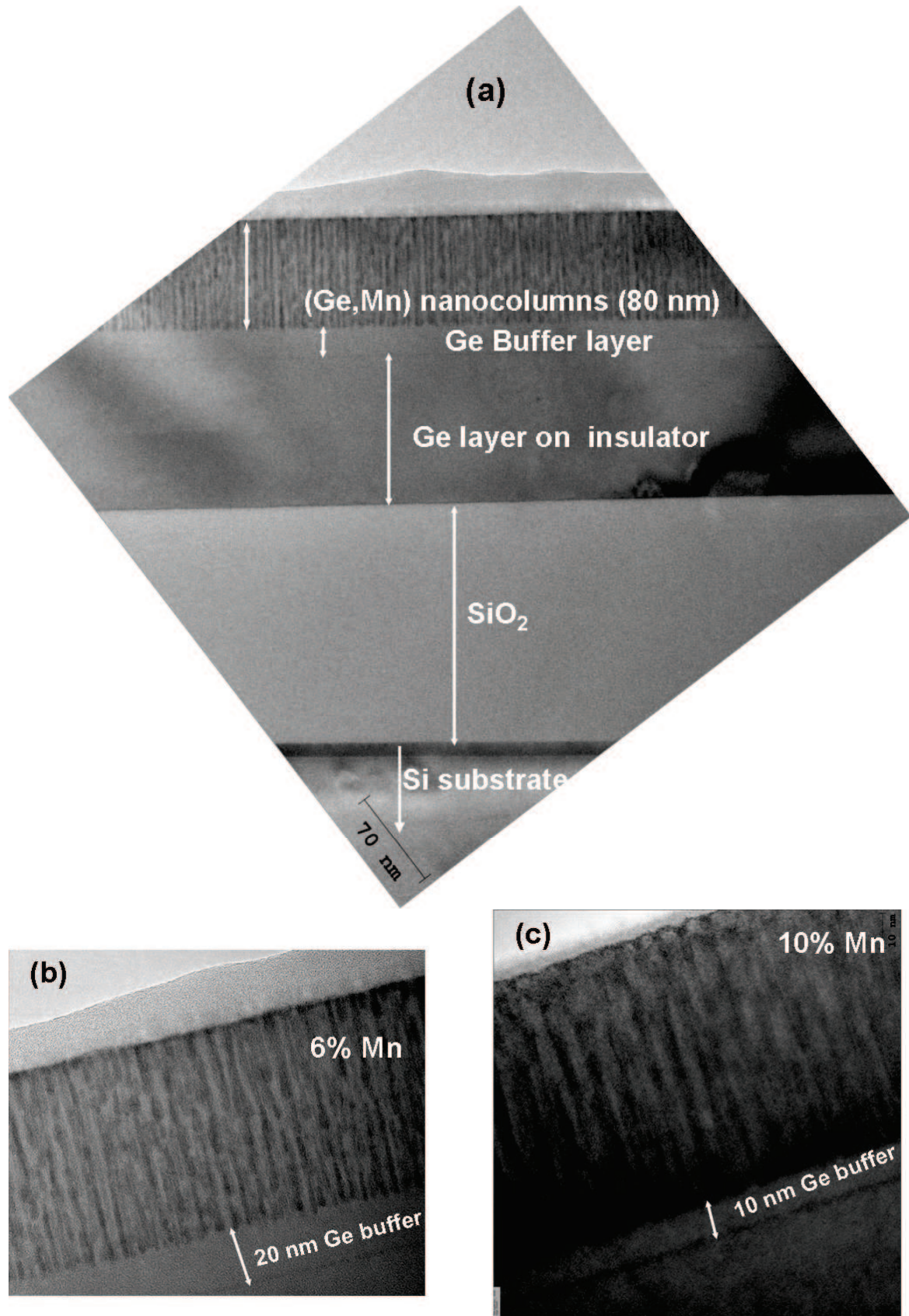


Figure 4.23 : (a) TEM images of (Ge,Mn) films in cross-section view grown on GOI substrate. Mn-rich nanocolumns are shown for Mn concentration of (b) 6% and (c) 10%.

be varied. The RHEED pattern after the growth of a 80 nm thick (Ge,Mn) film with 10% Mn concentration is shown in Fig. 4.22(c). It can be seen that the (Ge,Mn) has grown in epitaxy on Ge (001) and the surface became little rough at the end. The 2×1 reconstruction is still observed but only weaker than before.

A TEM image of this grown film is shown in Fig. 4.23. The different interfaces between Ge on GOI, the Ge buffer buffer and the grown (Ge,Mn) film can be seen. The Mn-rich nanocolumns covering the whole (Ge,Mn) film thickness which are formed similar to that of Ge(001) bulk substrate are also clearly observed. In the figure two different samples are shown: the one with 6% Mn and the other with 10% Mn concentration. This means that the successful growth of (Ge,Mn) nanocolumns was achieved on GOI substrates.

The magnetic properties of these films were studied by SQUID. Fig. 4.24 shows the measurements performed on the $\text{Ge}_{0.9}\text{Mn}_{0.1}$ film grown on GOI substrate. It is observed that (Ge,Mn) films are ferromagnetic with a Curie temperature of around 150 K. They are also superparamagnetic with a blocking temperature of 20 K, which is also confirmed by remanence measurements. These results are quite identical to crystalline nanocolumns grown on bulk Ge substrate and confirms the successful growth of (Ge,Mn) nanocolumns on these new GOI substrates.

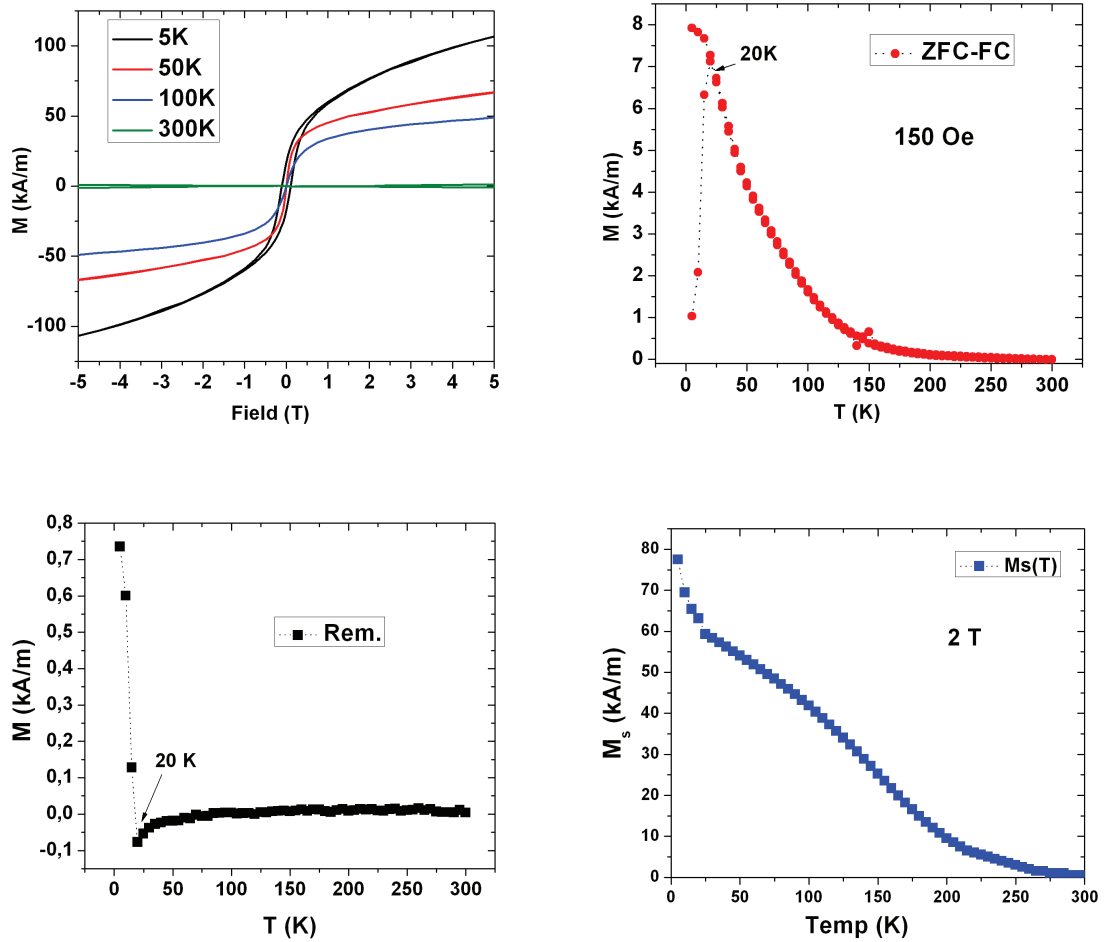


Figure 4.24 : *Magnetic measurements on (Ge,Mn) films grown on GOI: (a) Magnetization curves at different temperatures, (b) Zero-field-cooled-field-cooled curves, (c) Remanence magnetization and (d) Saturation magnetization curves.*

4.4.2 Towards (Ge,Mn) as a spin injector- A concept

(Ge,Mn) as discussed before can be epitaxially grown and employed as a spin injector into semiconductors. Theoretically it has been predicted to be a half-metal (i.e. fully spin-polarized) [174], solves the problem of conductivity mismatch and also compatible with existing semiconductor technology. It can replace the ferromagnetic metals and tunnel barrier and lead to all-semiconductor device. In addition, because ferromagnetism is driven by carriers, magnetic properties may be controlled by an electrical field through the application of a gate voltage.

As seen before different (Ge,Mn) nanostructures can be epitaxially grown on Ge. For spin injection from Ge_3Mn_5 films, the electrodes will have in-plane magnetization and a tailored Schottky barrier can be used to achieve efficient spin injection in Ge(111). Also Mn-rich nanocolumns can act as spin injector and in case of amorphous nanocolumns we have out-of-plane anisotropy. For randomly distributed spherical Ge_3Mn_5 clusters, the carriers will have to interact with the cluster magnetization to be spin polarized and injected in Ge.

Since (Ge,Mn) is a p-type semiconductor, the hole injection from (Ge,Mn) into Ge is not desired due to their short spin life-times. This problem can be solved by using inter-band Zener tunneling of electrons from the valence band of (Ge,Mn) into the conduction band of Ge. This is also known as a spin-Esaki diode. This can be done by making $\text{p}^+(\text{Ge,Mn})/\text{n}^+\text{Ge}$ junctions, where a thin depletion width is formed due to high doping. In this way, on applying reverse bias the spin polarized electrons from the valence band of (Ge,Mn) can tunnel into the conduction band of Ge. A schematic band diagram of such a device is shown in Fig. 4.25. An ideal structure would be to have $\text{p}^+(\text{Ge,Mn})/\text{n}^+\text{Ge}/\text{nGe}$ stack to have spin polarized electrons in moderately doped Ge channel to have longer spin lifetimes.

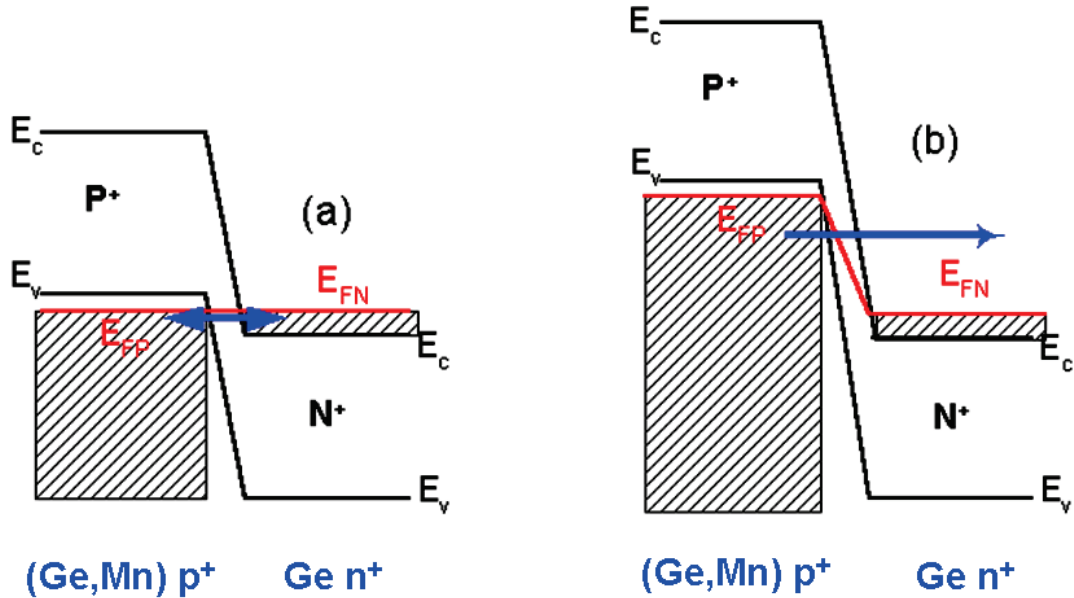


Figure 4.25 : A schematic diagram of a spin-Esaki diode showing tunneling of spin polarized electrons from the valence band of (Ge,Mn) into the conduction band of Ge on applying a small reverse bias.

The Germanium-on-insulator (GOI) substrates are ideal for this structure since it is easy to define the n-doped Ge channel and the surface layers can be highly doped by low-energy surface implantation as done in the case of FM/oxide structures in the previous chapter. The growth of (Ge,Mn) layers has been optimized on these substrates as discussed in the previous section. In the future, it would be very interesting to study the spin injection efficiency of this material.

4.5 Conclusion

In this chapter, the (Ge,Mn) magnetic semiconductor was introduced. The low solubility of Mn in Germanium leads to the segregation of metallic precipitates and thus the need of non-equilibrium growth techniques was discussed. The (Ge,Mn) thin films were grown by low temperature molecular beam epitaxy and different nanostructures were obtained depending on the growth conditions. The following (Ge,Mn) structures were studied: thin Ge_3Mn_5 films grown on Ge(111) substrate, crystalline and amorphous (Ge,Mn) nanocolumns grown on Ge(001) substrates and finally randomly distributed spherical Ge_3Mn_5 clusters on Ge(001). The structural and magnetic properties of these nanostructures were discussed.

The importance of magnetic anisotropy in this material for spintronics applications was emphasized. The qualitative and quantitative study of magnetic anisotropy with complementary techniques (SQUID and FMR) was performed. The samples were rotated in an external magnetic field at a fixed microwave frequency to study the evolution of the resonance fields. With the help of a free energy model, this behavior was fitted to extract anisotropy constants.

The Ge_3Mn_5 thin film grown on Ge(111) substrate was used as a model system to confirm the correlation between different techniques. In Ge_3Mn_5 films epitaxially grown on Ge(111), shape anisotropy is dominating and overcomes the magnetocrystalline component. For Ge_3Mn_5 precipitates on Ge(001) embedded in a Ge matrix, a hybrid ferromagnetic metal/semiconductor system is formed for nanomagnetism. The epitaxial relationship between the Ge_3Mn_5 hexagonal crystal and the Ge matrix favors perpendicular orientation of c -axis with respect to the film plane. For the first time, the effect of lattice distortion resulting in reduced anisotropy of Ge_3Mn_5 clusters as compared to bulk was detected using x-ray diffraction on synchrotron radiation facility. Furthermore crystalline (Ge,Mn) nanocolumns grown at low temperature ($T_g = 100^\circ\text{C}$), are superparamagnetic with blocking temperatures of the order of 15 K. These nanocolumns exhibit second-order perpendicular uniaxial anisotropy along with fourth-order cubic anisotropy along (111) direction. This cubic anisotropy has been expected because of the crystalline structure of nanocolumns observed in TEM. On the other hand, in amorphous nanocolumns grown at high temperature ($T_g = 150^\circ\text{C}$), this cubic anisotropy is absent and only shape anisotropy is observed. The correlation between the magnetization and the diamond lattice in these Mn-rich structures has never been evidenced before.

Finally the growth of (Ge,Mn) layers on Germanium-on-insulator substrates was shown and the concept of using (Ge,Mn) as a spin injector leading to all-semiconductor devices was discussed.

Conclusion and future outlook

In this thesis, we have discussed the importance and possible ways to create and detect non-equilibrium spin population in semiconductors. This is the first step for the realization of spintronic-based devices. Direct spin injection from ferromagnetic metals appeared to be a straightforward solution but this can not be employed due to large conductivity mismatch between the metals and semiconductors that leads to depolarization of spins before crossing the interface. This problem can however be solved by either inserting a tunnel barrier at the interface or using magnetic semiconductors as spin injectors.

Clear evidence of spin injection from ferromagnetic metals and magnetic semiconductors into semiconductors had been reported by several groups around the world, but this spin polarization was detected either optically using spin LED configuration or electrically at low temperatures. But the recent demonstration of all-electrical spin injection and detection in Si at room temperature by group of Jansen has opened up a way to integrate spintronics with electronics operating at ambient temperature. Most of the results for spin injection in semiconductors were reported in Si and GaAs, little progress was done in the case of Germanium. Germanium is interesting for spintronic applications due to its high carrier mobilities and its inversion symmetry that gives long spin lifetimes. However a strong Fermi level pinning (FLP) near the valence band edge of Ge results in high Schottky barrier heights in metal/n-Ge contacts. This leads to high contact resistance, thermionic transport and strong dependence on bias current. This is detrimental for efficient spin injection because in thermionic transport the electrons originate from the states at elevated energy (hot electrons), which have a reduced spin polarization as compared to those at lower state. Moreover, due to high contact resistance, significant magnetoresistance can not be observed.

In the first part of this thesis, various solutions to solve this problem of FLP are discussed. A tunneling transport is obtained in n-Ge by increasing the doping concentration of Ge surface layer. This leads to reduction in depletion width and electrons can tunnel through the Schottky barrier. Moreover, introduction of a oxide tunnel barrier at FM/Ge interface releases the FLP and reduces the SBH. We have successfully demonstrated electrical spin injection and detection in n-doped Germanium. Ferromagnetic metals and oxide tunnel barrier were used for spin injection. The oxide layer also solves the conductivity mismatch problem. The experiments presented here were carried out on n-doped germanium-on-insulator substrates (GOI). Spin injection in GOI rather than in bulk Ge is a step towards future practical applications with the possibility to apply gate voltage and manipulate spins through conduction channel modulation or Rashba effect.

For spin injection, two different spin injecting FM/oxide layers were used: Py/Al₂O₃ and CoFeB/MgO. The measurements were performed in three-terminal geometry and the proof of spin accumulation was given by Hanle measurements. The contact resistance for Al₂O₃ based

devices is found to be much higher as compared to MgO based devices, indicating that MgO is more efficient in removing the Fermi-level pinning in Ge. The spin signal (spin RA product) in Al_2O_3 based devices is four orders of magnitude higher than the predicted value, which led to the conclusion that there is spin accumulation in localized states at $\text{Al}_2\text{O}_3/\text{Ge}$ interface. This happens when there is a high Schottky barrier at the interface, which decouples the interface states from the bulk conduction bands. These localized states act as a confining layer through which two-step tunneling can take place and absorb most of spin accumulation before reaching Ge channel. The spin signal is observed up to 220 K.

In the case of CoFeB/MgO devices, the observed spin signal was only one order of magnitude higher than the predicted value at lower temperatures. On increasing the temperature, the enhancement decreases and the expected spin signal is observed due to thermal activation of carriers over the Schottky barrier. The spin signal of about $0.375 \text{ k}\Omega\cdot\mu\text{m}^2$ is observed up to room temperature was observed which was not reported before in the case of Ge.

Moreover, the spin lifetime extracted from Hanle curves, even for direct injection, was very short as compare to the expected values. This has been explained due to the roughness at the FM/oxide interface. This roughness creates magnetostatic charges which leads to random inhomogeneous local fields. These fields drastically reduce the spin accumulation and leads to artificial broadening of Hanle curves. This phenomenon can be verified by inverted-Hanle curves where an external field is applied in-plane to rotate the total magnetic field into the direction of the magnetization. This reduces the angle between the injected spins and the axis of precession. The precession of spins is suppressed and the spin accumulation increases as a function of applied in-plane field. Due to the broadening of Hanle curves, the intrinsic variation of the actual spin lifetime with different parameters like temperature and doping cannot be studied.

In the case of CoFeB/MgO devices, where a shift from two-step tunneling to direct tunneling is observed on increasing temperature, it would be now interesting to study bias dependence in Hanle and inverted Hanle effect geometry in these two different regimes and hopefully more physics could be explored. Moreover, by applying gate voltage and thus moving the energy bands, one may see shift from one regime to other by injecting spins close to transition temperature.

To conclude, efficient spin injection requires a high quality oxide/semiconductor interface. This depends on various factors like roughness, Schottky barrier height, depletion zone or doping concentration and interface states such as dangling bonds and their density. In the case of Germanium, one can also treat the surface with $(\text{NH}_4)_2\text{S}$ solution prior to tunnel oxide and FM growth. This is known to reduce the SBH by saturating the dangling bonds via bridge bonding formation and depinning the Fermi level.

In the second part of the thesis, the (Ge,Mn) magnetic semiconductor is investigated for its potential use as a spin injector. (Ge,Mn) thin-films have been grown by molecular beam epitaxy and different nanostructures have been obtained depending on growth conditions. Low solubility of Mn in Ge led to the precipitation of Mn-rich metastable phases. The structural and magnetic properties of these nanostructures are studied. To use (Ge,Mn) as a spin injector for future spintronics applications, the knowledge of magnetic anisotropy of (Ge,Mn) material is very important since it determines the direction of magnetization, coercive fields, and domain sizes. A qualitative and quantitative investigation of magnetic anisotropy in these structures was done using complementary techniques: FMR and SQUID.

FMR proved to be a very sensitive technique with high field resolution. Since it's a spectroscopy technique, the magnetic signal from different phases could be separated. The fitting of angular dependent measurements with a free energy model led to the determination of easy axis and anisotropy fields. With the help of SQUID measurements, saturation magnetization was known and anisotropy constants were calculated. The correlation between magnetic anisotropy and the diamond lattice in these Mn-rich structures has never been evidenced before. This information will be very useful for future spin injection experiments.

Finally, the growth of (Ge,Mn) films on GOI substrates was shown and different ways were discussed to use (Ge,Mn) as a spin injector in Ge. The growth of epitaxial (Ge,Mn) films on smooth surfaces prepared by MBE may also solve the problem of surface roughness and give true Hanle effect from which spin lifetimes could be extracted.

After successful creation of a non-equilibrium spin population in Ge at room temperature, it would be interesting to use 4-contact non-local geometry where one can study the Ge-channel and exclude the effect from the localized states. New concepts in field of Ge spintronics can also be tested. Spin injection from FM electrodes with perpendicular magnetization could confirm the concept of surface roughness (inverted-Hanle). Also in strained Ge quantum wells having direct band-gap, easy optical detection would be possible. New approaches like spin pumping (magnetization dynamics) and spin Seebeck effect with current or laser heating can also be tried.

The next step is to manipulate the spins in the channel by electric field instead of magnetic field for feasible integration into the existing technology. But with a weak spin-orbit coupling in Ge, this would be a challenge for researchers and may need a new device design. I think that this work will contribute in the quest of complete spintronic semiconductor devices.

A.1 Derivation of resonance equation

In this section, the details of calculation for equation 4.1 are given. Here the magnetization is considered as a classical gyroscope with moment of inertia I . The classical coordinate system (x,y,z) is transferred into a cartesian one (x',y',z') where z -axis rotate with the magnetization. The transformation is uniquely given by the three Euler angles φ, θ and ψ .

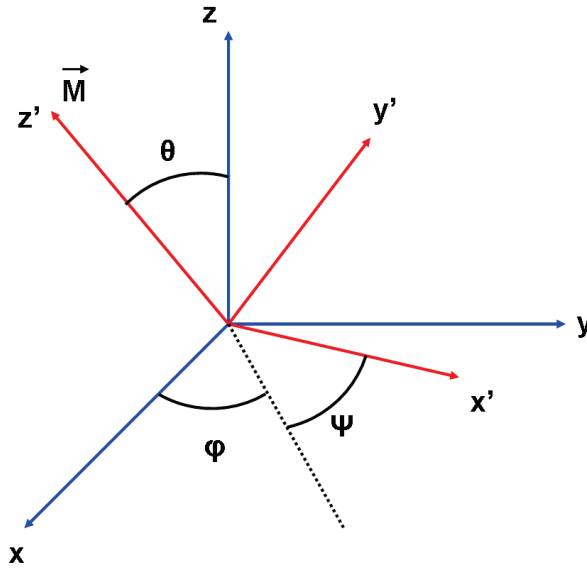


Figure A.1 : *Euler angles to describe the rotation of the coordinate system.*

The Lagrangian function of the system, that summarizes the dynamics of the system is given by $L = E_{kin} - E_{pot}(\varphi, \theta)$, here E_{kin} is the kinetic energy of the system given by $E_{kin} = \frac{I}{2} (\dot{\psi} + \dot{\varphi} \cos \theta)^2$ and E_{pot} being the potential energy. The Lagrangian equation of motion then is $\frac{d}{dt} \frac{\partial L}{\partial \dot{q}_i} - \frac{\partial L}{\partial q_i}$, where q_i are the generalized coordinates and in this case given by φ, θ and ψ . This yields the following equations:

$$\frac{d}{dt} [I(\dot{\psi} + \dot{\varphi} \cos \theta) \cos \theta] + \frac{\partial E_{pot}}{\partial \varphi} = 0 \quad (\text{A.1})$$

$$I(\dot{\psi} + \dot{\varphi} \cos \theta) \dot{\varphi} \sin \theta + \frac{\partial E_{pot}}{\partial \theta} = 0 \quad (\text{A.2})$$

$$\frac{d}{dt} [I(\dot{\psi} + \dot{\varphi} \cos \theta)] = 0 \quad (\text{A.3})$$

The term $I(\dot{\psi} + \dot{\varphi} \cos \theta)$ describes the angular momentum of the magnetization within the (x',y',z') system and thus the last equation shows the time variance of the angular momentum. The angular momentum is also given by M_s/γ from the LLG equation (here γ is the gyromagnetic ratio). Hence the above equations can be written as:

$$\frac{M_s}{\gamma} \dot{\theta} \sin \theta = \frac{\partial F}{\partial \varphi} \quad (\text{A.4})$$

$$-\frac{M_s}{\gamma} \dot{\varphi} \sin \theta = \frac{\partial F}{\partial \theta} \quad (\text{A.5})$$

Here E_{pot} is replaced by the free energy F of the system. Assuming that the precession angle of the magnetization is small, so that only small variations $\delta\theta$ and $\delta\varphi$ occur with respect to the equilibrium orientation (θ^o, φ^o) . In small angle regime, it can be given as $\theta = \theta^o + \delta\theta$, $\varphi = \varphi^o + \delta\varphi$ and the first derivatives of F can be expanded into a series of $\delta\theta$ and $\delta\varphi$ around the equilibrium position and only the linear terms have to be considered:

$$F_\theta = F_{\theta\theta}\delta\theta + F_{\theta\varphi}\delta\varphi \quad (\text{A.6})$$

$$F_\varphi = F_{\varphi\theta}\delta\theta + F_{\varphi\varphi}\delta\varphi \quad (\text{A.7})$$

Here the derivatives have to be taken at equilibrium position e.g. $F_{\theta\theta}|_{\theta^o}$. Periodic solutions $\delta\theta, \delta\varphi \propto \exp(i\omega t)$ have to be found, as the derivatives around the equilibrium position are driven by the periodic excitation due to the microwave field with a frequency ω . This yields $\dot{\theta} = i\omega\delta\theta$ and $\dot{\varphi} = i\omega\delta\varphi$. Taking into account that for small deviations $\sin(\theta^o + \delta\theta) = \sin\theta^o \cos\delta\theta + \cos\theta^o \sin\delta\theta \approx \sin\theta^o + \cos\theta^o \delta\theta \approx \sin\theta^o$. Hence from A.5, it can be written as:

$$\left(\frac{i\omega M_s}{\gamma} \sin\theta^o - F_{\varphi\theta} \right) \delta\theta - F_{\varphi\varphi} \delta\varphi = 0 \quad (\text{A.8})$$

$$\left(-\frac{i\omega M_s}{\gamma} \sin\theta^o - F_{\varphi\theta} \right) \delta\varphi - F_{\theta\theta} \delta\theta = 0 \quad (\text{A.9})$$

In the matrix form it is given by:

$$\begin{pmatrix} F_{\varphi\theta} - \frac{i\omega M_s}{\gamma} \sin\theta^o & F_{\varphi\varphi} \\ F_{\theta\theta} & F_{\varphi\theta} + \frac{i\omega M_s}{\gamma} \sin\theta^o \end{pmatrix} \cdot \begin{pmatrix} \delta\theta \\ \delta\varphi \end{pmatrix} = 0 \quad (\text{A.10})$$

The condition for a solution is $F_{\theta\varphi}^2 - F_{\theta\theta}F_{\varphi\varphi} + \omega^2\gamma^{-2}M_s^2\sin^2\theta^o = 0$, which yields the following equation for the resonance frequency:

$$\left(\frac{\omega}{\gamma} \right)^2 = \frac{F_{\theta\theta}F_{\varphi\varphi} - F_{\theta\varphi}^2}{M_s^2 \sin^2\theta_0} \quad (\text{A.11})$$

Hence from the Free energy which gives the equilibrium angles φ^o and θ^o , the eqn.A.11 give us the resonance condition and an expression for the resonance field B_{res} as a function of the angles of the external field for a fixed frequency. It shows that FMR is sensitive to curvature of the free energy surface. As the surface strongly depends on the anisotropy fields, FMR is very good tool to quantitatively determine magnetic anisotropy.

For further reading, please refer to 175.

A.2 Comment on the FMR measurements

When the FMR measurements were performed at low frequency of 9.4 GHz (X-band), a huge cyclotron resonance signal was observed at low fields. This signal makes it difficult to observe the true resonance peaks signal from GeMn films which also appears at low fields. This cyclotron signal comes from both the GeMn films and the Ge substrate as shown in the fig.A.2. This is due to the high carrier concentration of the layers. This cyclotron signal was separated from the sample signal by operating at high frequency of 34 GHz (Q band). For X-band, $g=2$ signal appears at a field of 3200 Oe but for Q-band it is observed close to 12000 Oe. At higher frequency, the true signal shifts to higher fields and the angular dependence can be studied to extract the anisotropy constants.

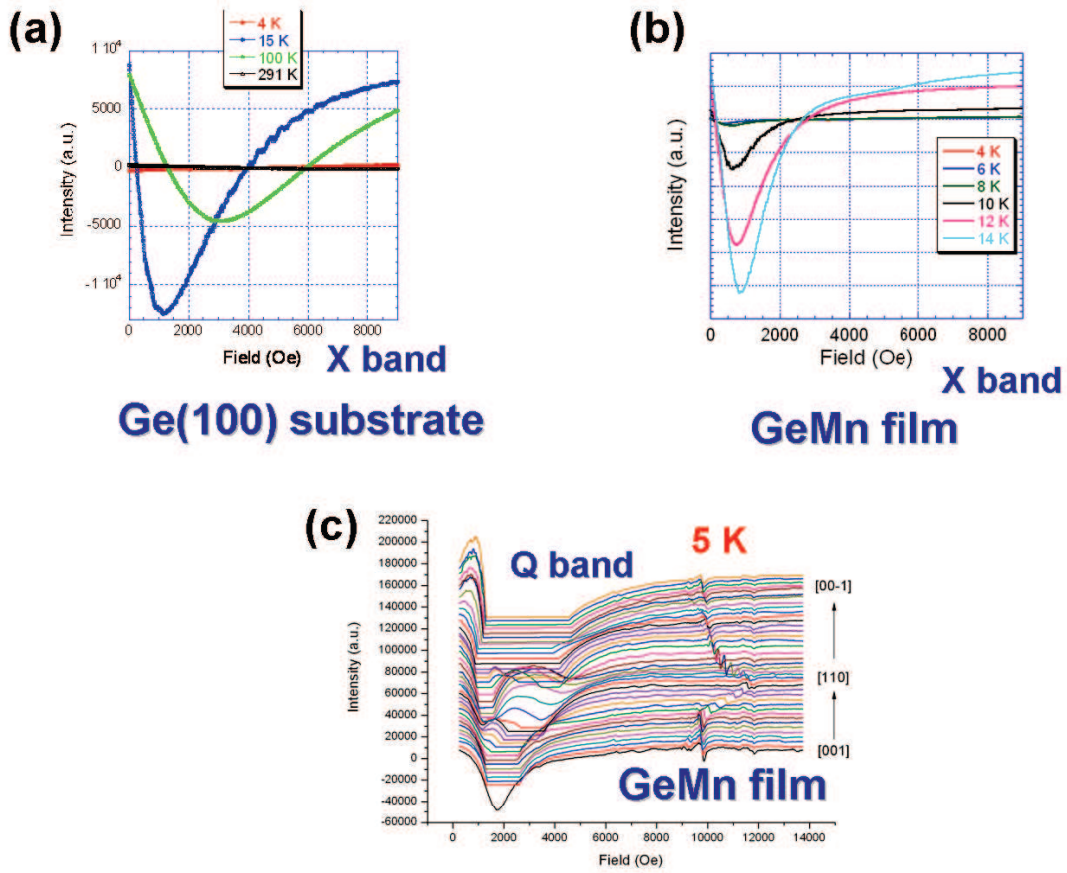


Figure A.2 : FMR spectra obtained at X-band for (a) Ge substrate and (b) GeMn film. (c) The FMR spectra obtained for same GeMn sample but at Q-band.

Bibliography

- [1] G. Moore, *Electronics* **38**, 19 (1965)
- [2] G. A. Prinz, *Science* **282**, 1660 (1998), <http://www.sciencemag.org/content/282/5394/1660.full.pdf>,
<http://www.sciencemag.org/content/282/5394/1660.abstract>
- [3] N. F. Mott, *Proc. Roy. Soc.* **153**, 699 (1936)
- [4] N. F. Mott, *Proc. Roy. Soc.* **156**, 368 (1936)
- [5] A. Fert and I. A. Campbell, *Phys. Rev. Lett.* **21**, 1190 (Oct 1968)
- [6] A. Fert and I. Campbell, *J. Phys. F* **6**, 849 (1976)
- [7] B. Loegel and F. Gautier, *J. Phys. Chem. Sol.* **32**, 2723 (1971)
- [8] P. M. Tedrow and R. Meservey, *Phys. Rev. Lett.* **26**, 192 (Jan 1971)
- [9] M. Julliere, *Physics Letters A* **54**, 225 (1975), ISSN 0375-9601, <http://www.sciencedirect.com/science/article/pii/0375960175901747>
- [10] M. N. Baibich, J. M. Broto, A. Fert, F. N. Van Dau, F. Petroff, P. Eitenne, G. Creuzet, A. Friederich, and J. Chazelas, *Phys. Rev. Lett.* **61**, 2472 (Nov 1988)
- [11] G. Binasch, P. Grünberg, F. Saurenbach, and W. Zinn, *Phys. Rev. B* **39**, 4828 (Mar 1989)
- [12] D. Hagele, M. Oestreich, W. W. Ruhle, N. Nestle, and K. Eberl, *Applied Physics Letters* **73**, 1580 (1998), <http://link.aip.org/link/?APL/73/1580/1>
- [13] J. M. Kikkawa and D. D. Awschalom, *Nature* **397**, 139 (1999)
- [14] J. M. Kikkawa and D. D. Awschalom, *Phys. Rev. Lett.* **80**, 4313 (May 1998)
- [15] R. I. Dzhioev, K. V. Kavokin, V. L. Korenev, M. V. Lazarev, B. Y. Meltser, M. N. Stepanova, B. P. Zakharchenya, D. Gammon, and D. S. Katzer, *Phys. Rev. B* **66**, 245204 (Dec 2002)
- [16] B. Jonker, *Proceedings of the IEEE* **91**, 727 (may 2003), ISSN 0018-9219
- [17] S. Datta and B. Das, *Applied Physics Letters* **56**, 665 (1990), <http://link.aip.org/link/?APL/56/665/1>

-
- [18] P. R. Hammar, B. R. Bennett, M. J. Yang, and M. Johnson, *Phys. Rev. Lett.* **83**, 203 (Jul 1999)
- [19] B. J. van Wees, *Phys. Rev. Lett.* **84**, 5023 (May 2000)
- [20] F. G. Monzon, H. X. Tang, and M. L. Roukes, *Phys. Rev. Lett.* **84**, 5022 (May 2000)
- [21] P. C. van Son, H. van Kempen, and P. Wyder, *Phys. Rev. Lett.* **58**, 2271 (May 1987)
- [22] M. Johnson and R. H. Silsbee, *Phys. Rev. Lett.* **55**, 1790 (Oct 1985)
- [23] F. J. Jedema, H. B. Heersche, A. T. Filip, J. J. A. Baselmans, and B. J. van Wees, *Nature* **416**, 713 (2002)
- [24] A. T. Filip, B. H. Hoving, F. J. Jedema, B. J. van Wees, B. Dutta, and S. Borghs, *Phys. Rev. B* **62**, 9996 (Oct 2000)
- [25] G. Schmidt, D. Ferrand, L. W. Molenkamp, A. T. Filip, and B. J. van Wees, *Phys. Rev. B* **62**, R4790 (Aug 2000)
- [26] L. GRENET, *Injection de spins dans les semi-conducteurs*, Ph.D. thesis, University of Grenoble (2006), <http://tel.archives-ouvertes.fr/tel-00508923/fr/>
- [27] E. I. Rashba, *Phys. Rev. B* **62**, R16267 (Dec 2000)
- [28] A. Fert and H. Jaffrès, *Phys. Rev. B* **64**, 184420 (Oct 2001)
- [29] H. J. Zhu, M. Ramsteiner, H. Kostial, M. Wassermeier, H.-P. Schönherr, and K. H. Ploog, *Phys. Rev. Lett.* **87**, 016601 (Jun 2001)
- [30] A. T. Hanbicki, O. M. J. van 't Erve, R. Magno, G. Kioseoglou, C. H. Li, B. T. Jonker, G. Itskos, R. Mallory, M. Yasar, and A. Petrou, *Applied Physics Letters* **82**, 4092 (2003), <http://link.aip.org/link/?APL/82/4092/1>
- [31] A. T. Hanbicki, B. T. Jonker, G. Itskos, G. Kioseoglou, and A. Petrou, *Applied Physics Letters* **80**, 1240 (2002), <http://link.aip.org/link/?APL/80/1240/1>
- [32] S. A. Crooker, M. Furis, X. Lou, C. Adelmann, D. L. Smith, C. J. Palmström, and P. A. Crowell, *Science* **309**, 2191 (2005), <http://www.sciencemag.org/content/309/5744/2191.full.pdf>, <http://www.sciencemag.org/content/309/5744/2191.abstract>
- [33] X. Lou, C. Adelmann, M. Furis, S. A. Crooker, C. J. Palmstrøm, and P. A. Crowell, *Phys. Rev. Lett.* **96**, 176603 (May 2006)
- [34] C. Ciuti, J. P. McGuire, and L. J. Sham, *Phys. Rev. Lett.* **89**, 156601 (Sep 2002)
- [35] X. Lou, C. Adelmann, S. A. Crooker, E. S. Garlid, J. Zhang, K. S. M. Reddy, S. D. Flexner, C. J. Palmström, and P. A. Crowell, *Nat Phys* **3**, 197 (Mar. 2007), ISSN 1745-2473, <http://dx.doi.org/10.1038/nphys543>
- [36] D. J. Monsma and S. S. P. Parkin, *Applied Physics Letters* **77**, 720 (2000), <http://link.aip.org/link/?APL/77/720/1>
- [37] V. F. Motsnyi, J. D. Boeck, J. Das, W. V. Roy, G. Borghs, E. Goovaerts, and V. I. Safarov, *Applied Physics Letters* **81**, 265 (2002), <http://link.aip.org/link/?APL/81/265/1>
- [38] J. Mathon and A. Umerski, *Phys. Rev. B* **63**, 220403 (May 2001)

- [39] X. Jiang, R. Wang, R. M. Shelby, R. M. Macfarlane, S. R. Bank, J. S. Harris, and S. S. P. Parkin, *Phys. Rev. Lett.* **94**, 056601 (Feb 2005)
- [40] B. T. Jonker, G. Kioseoglou, A. T. Hanbicki, C. H. Li, and P. E. Thompson, *Nat Phys* **3**, 542 (Aug. 2007), ISSN 1745-2473, <http://dx.doi.org/10.1038/nphys673>
- [41] I. Appelbaum, B. Huang, and D.J.Monsma, *Nature* **447**, 295 (2007)
- [42] O. M. J. van 't Erve, A. T. Hanbicki, M. Holub, C. H. Li, C. Awo-Affouda, P. E. Thompson, and B. T. Jonker, *Applied Physics Letters* **91**, 212109 (2007), <http://link.aip.org/link/?APL/91/212109/1>
- [43] S. P. Dash, S. Sharma, R. S. Patel, M. P. de Jong, and R. Jansen, *Nature* **462**, 491 (Nov. 2009), ISSN 0028-0836, <http://dx.doi.org/10.1038/nature08570>
- [44] S. P. Dash, S. Sharma, J. C. Le Breton, J. Peiro, H. Jaffrès, J.-M. George, A. Lemaître, and R. Jansen, *Phys. Rev. B* **84**, 054410 (Aug 2011)
- [45] H. Ohno, *Science* **281**, 951 (1998)
- [46] T. Dietl, H. Ohno, F. Matsukura, J. Cibert, and D. Ferrand, *Science* **287**, 1019 (2000), <http://www.sciencemag.org/content/287/5455/1019.full.pdf>, <http://www.sciencemag.org/content/287/5455/1019.abstract>
- [47] L. Chen, S. Yan, P. F. Xu, J. Lu, W. Z. Wang, J. J. Deng, X. Qian, Y. Ji, and J. H. Zhao, *Appl. Phys. Lett.* **95**, 182505 (2009)
- [48] T. Jungwirth, K. Y. Wang, J. Mašek, K. W. Edmonds, J. König, J. Sinova, M. Polini, N. A. Goncharuk, A. H. MacDonald, M. Sawicki, A. W. Rushforth, R. P. Campion, L. X. Zhao, C. T. Foxon, and B. L. Gallagher, *Phys. Rev. B* **72**, 165204 (Oct 2005)
- [49] K. Sato, H. Katayama-Yoshida, and P. H. Dederichs, *Jpn. J. Appl. Phys.* **44**, L948 (2005)
- [50] S. Kuroda, N. Nishizawa, K. Takita, M. Mitome, Y. Bando, K. Osuch, and T. Dietl, *Nature Mater.* **6**, 440 (2007)
- [51] A. Bonanni, A. Navarro-Quezada, T. Li, M. Wegscheider, Z. Matěj, V. Holý, R. T. Lechner, G. Bauer, M. Rovezzi, F. D'Acapito, M. Kiecana, M. Sawicki, and T. Dietl, *Phys. Rev. Lett.* **101**, 135502 (2008)
- [52] P. N. Hai, S. Ohya, M. Tanaka, S. E. Barnes, and S. Maekawa, *Nature* **458**, 489 (Mar. 2009), ISSN 0028-0836, <http://dx.doi.org/10.1038/nature07879>
- [53] M. Jamet, A. Barski, T. Devillers, V. Poydenot, R. Dujardin, P. Bayle-Guillevaud, J. Rothman, E. Bellet-Amalric, A. Marty, J. Cibert, *et al.*, *Nature Mater.* **5**, 653 (2006)
- [54] R. Fiederling, M. Keim, G. Reuscher, W. Ossau, G. Schmidt, A. Waag, and L. W. Molenkamp, *Nature* **402**, 787 (Dec. 1999), ISSN 0028-0836, <http://dx.doi.org/10.1038/45502>
- [55] B. T. Jonker, Y. D. Park, B. R. Bennett, H. D. Cheong, G. Kioseoglou, and A. Petrou, *Phys. Rev. B* **62**, 8180 (Sep 2000)
- [56] Y. Ohno, D. K. Young, B. Beschoten, F. Matsukura, H. Ohno, and D. D. Awschalom, *Nature* **402**, 790 (Dec. 1999), ISSN 0028-0836, <http://dx.doi.org/10.1038/45509>
- [57] R. Fiederling, P. Grabs, W. Ossau, G. Schmidt, and L. W. Molenkamp, *Applied Physics Letters* **82**, 2160 (2003), <http://link.aip.org/link/?APL/82/2160/1>

-
- [58] R. Mattana, J.-M. George, H. Jaffrès, F. Nguyen Van Dau, A. Fert, B. Lépine, A. Guivarc'h, and G. Jézéquel, *Phys. Rev. Lett.* **90**, 166601 (Apr 2003)
 - [59] M. Ciorga, A. Einwanger, U. Wurstbauer, D. Schuh, W. Wegscheider, and D. Weiss, *Phys. Rev. B* **79**, 165321 (Apr 2009)
 - [60] M. Kohda, Y. Ohno, K. Takamura, F. Matsukura, and H. Ohno, *Jpn. J. Appl. Phys.* **40**, L1274 (2001)
 - [61] Y. Yafet, *Phys. Rev.* **85**, 478 (Feb 1952)
 - [62] R. J. Elliott, *Phys. Rev.* **96**, 266 (Oct 1954)
 - [63] G. Dresselhaus, *Phys. Rev.* **100**, 580 (Oct 1955)
 - [64] G. Feher and E. A. Gere, *Phys. Rev.* **114**, 1245 (Jun 1959)
 - [65] G. Bir, A. Aronov, and G. Pikus, *Soviet Physics JETP* **42**, 705 (1975)
 - [66] I. Žutić, J. Fabian, and S. Das Sarma, *Rev. Mod. Phys.* **76**, 323 (Apr 2004)
 - [67] J.-C. L. Breton, S. Sharma, H. Saito, S. Yuasa, and R. Jansen, *Nature* **475**, 82 (2011)
 - [68] P. Renucci, V. G. Truong, H. Jaffrès, L. Lombez, P. H. Binh, T. Amand, J. M. George, and X. Marie, *Phys. Rev. B* **82**, 195317 (Nov 2010), <http://link.aps.org/doi/10.1103/PhysRevB.82.195317>
 - [69] E. I. Rashba, *Sov. Phys. Solid State* **2**, 1109 (1960)
 - [70] Y. A. Bychkov and E. I. Rashba, *J. Phys. C: Solid State Phys.* **17**, 6039 (1984)
 - [71] J. Nitta, T. Akazaki, H. Takayanagi, and T. Enoki, *Phys. Rev. Lett.* **78**, 1335 (Feb 1997)
 - [72] H. C. Koo, J. H. Kwon, J. Eom, J. Chang, S. H. Han, and M. Johnson, *Science* **325**, 1515 (2009), <http://www.sciencemag.org/content/325/5947/1515.full.pdf>, <http://www.sciencemag.org/content/325/5947/1515.abstract>
 - [73] A. Y. Cho and J. R. Arthur, *Prog. Solid State Chem.* **10**, 157 (1975)
 - [74] J. Klein, *Epitaktische Heterostrukturen aus dotierten Manganaten*, Ph.D. thesis, University of Cologne (2001)
 - [75] *Transmission Electron Microscopy*, edited by C. B. C. D. B. Williams (Plenum Press, New York and London, 1996)
 - [76] C. Kittel, *Introduction to Solid State Physics* (John Wiley & Sons Inc., 1996)
 - [77] X. Liu and J. K. Furdyna, *Journal of Physics: Condensed Matter* **18**, R245 (2006)
 - [78] *Electron Spin Resonance*, edited by P. C. P (New York: Interscience, 1967)
 - [79] C. O. Chui, H. Kim, D. Chi, B. B. Triplett, P. C. McIntyre, and K. C. Saraswat, *Tech. Dig. - Int. Electron Devices Meet.* **437** (2002)
 - [80] A. Dimoulas, P. Tsipas, A. Sotiropoulos, and E. K. Evangelou, *Applied Physics Letters* **89**, 252110 (2006), <http://link.aip.org/link/?APL/89/252110/1>
 - [81] T. Nishimura, K. Kita, and A. Toriumi, *Applied Physics Letters* **91**, 123123 (2007), <http://link.aip.org/link/?APL/91/123123/1>

- [82] H. K. Henisch, *Rectifying Semiconductor Contacts* (Clarendon, Oxford, 1957)
- [83] A. M. Cowley and S. M. Sze, *J. Appl. Phys.* **36**, 3212 (1965)
- [84] J. Bardeen, *Phys. Rev.* **71**, 717 (May 1947)
- [85] S. Sze, *Physics of semiconductor devices* (John Wiley & Sons, 1981)
- [86] D. Connelly, C. Faulkner, P. A. Clifton, and D. E. Grupp, *Applied Physics Letters* **88**, 012105 (2006), <http://link.aip.org/link/?APL/88/012105/1>
- [87] M. Kobayashi, A. Kinoshita, K. Saraswat, H.-S. P. Wong, and Y. Nishi, *Journal of Applied Physics* **105**, 023702 (2009), <http://link.aip.org/link/?JAP/105/023702/1>
- [88] J.-Y. J. Lin, A. M. Roy, A. Nainani, Y. Sun, and K. C. Saraswat, *Applied Physics Letters* **98**, 092113 (2011), <http://link.aip.org/link/?APL/98/092113/1>
- [89] T. Nishimura, K. Kita, and A. Toriumi, *Appl. Phys. Express* **1**, 051406 (2008)
- [90] Y. Zhou, M. Ogawa, X. Han, and K. L. Wang, *Applied Physics Letters* **93**, 202105 (2008), <http://link.aip.org/link/?APL/93/202105/1>
- [91] Y. Zhou, W. Han, Y. Wang, F. Xiu, J. Zou, R. K. Kawakami, and K. L. Wang, *Applied Physics Letters* **96**, 102103 (2010), <http://link.aip.org/link/?APL/96/102103/1>
- [92] D. Lee, S. Raghunathan, R. J. Wilson, D. E. Nikonov, K. Saraswat, and S. X. Wang, *Appl. Phys. Lett.* **96**, 052514 (2010), ISSN 00036951, <http://dx.doi.org/doi/10.1063/1.3285163>
- [93] W. E. Spicer, I. Lindau, P. Skeath, C. Y. Su, and P. Chye, *Phys. Rev. Lett.* **44**, 420 (Feb 1980)
- [94] K. Yamane, K. Hamaya, Y. Ando, Y. Enomoto, K. Yamamoto, T. Sadoh, and M. Miyao, *Applied Physics Letters* **96**, 162104 (2010), <http://link.aip.org/link/?APL/96/162104/1>
- [95] R. R. Lieten, S. Degroote, M. Kuijk, and G. Borghs, *Applied Physics Letters* **92**, 022106 (2008), <http://link.aip.org/link/?APL/92/022106/1>
- [96] A. V. Thathachary, K. N. Bhat, N. Bhat, and M. S. Hegde, *Applied Physics Letters* **96**, 152108 (2010), <http://link.aip.org/link/?APL/96/152108/1>
- [97] B. Min, K. Motohashi, C. Lodder, and R. Jansen, *Nat Mater* **5**, 817 (2006)
- [98] Y. Zhou, M. Ogawa, M. Bao, W. Han, R. K. Kawakami, and K. L. Wang, *Applied Physics Letters* **94**, 242104 (2009), <http://link.aip.org/link/?APL/94/242104/1>
- [99] E.-S. Liu, J. Nah, K. M. Varahramyan, and E. Tutuc, *Nano Letters* **10**, 3297 (2010), <http://pubs.acs.org/doi/pdf/10.1021/nl1008663>, <http://pubs.acs.org/doi/abs/10.1021/nl1008663>
- [100] C. Shen, T. Trypiniotis, K. Y. Lee, S. N. Holmes, R. Mansell, M. Husain, V. Shah, X. V. Li, H. Kurebayashi, I. Farrer, C. H. de Groot, D. R. Leadley, G. Bell, E. H. C. Parker, T. Whall, D. A. Ritchie, and C. H. W. Barnes, *Applied Physics Letters* **97**, 162104 (2010), <http://link.aip.org/link/?APL/97/162104/1>
- [101] Y. Zhou, W. Han, L.-T. Chang, F. Xiu, M. Wang, M. Oehme, I. A. Fischer, J. Schulze, R. K. Kawakami, and K. L. Wang, *arXiv* **1103.5095v1** (2011), <http://arxiv.org/abs/1103.5095>

-
- [102] H. Saito, S. Watanabe, Y. Mineno, S. Sharma, R. Jansen, S. Yuasa, and K. Ando, *Solid State Communications* **151**, 1159 (2011), <http://www.sciencedirect.com/science/article/pii/S0038109811002444>
- [103] C. Deguet, J. Dechamp, C. Morales, A.-M. Charvet, L. Clavelier, V. Loup, J.-M. Hartmann, N. Kernevez, Y. Campidelli, F. Allibert, C. Richtarch, T. Akatesu, and F. Letertre, *Electrochem. Soc. Proc.* **2005-06**, 78 (2005)
- [104] <http://www.srim.org/>
- [105] M. Tran, H. Jaffrès, C. Deranlot, J.-M. George, A. Fert, A. Miard, and A. Lemaître, *Phys. Rev. Lett.* **102**, 036601 (Jan 2009)
- [106] C. Li, O. van 't Erve, and B. Jonker, *Nat Commun* **2**, 245 (Mar. 2011)
- [107] Y. Lu, J. Li, and I. Appelbaum, *Phys. Rev. Lett.* **106**, 217202 (May 2011), <http://link.aps.org/doi/10.1103/PhysRevLett.106.217202>
- [108] S. A. Crooker, E. S. Garlid, A. N. Chantis, D. L. Smith, K. S. M. Reddy, Q. O. Hu, T. Kondo, C. J. Palmstrøm, and P. A. Crowell, *Phys. Rev. B* **80**, 041305 (Jul 2009)
- [109] M. Johnson, *Science* **260**, 320 (1993), <http://www.sciencemag.org/content/260/5106/320.full.pdf>, <http://www.sciencemag.org/content/260/5106/320.abstract>
- [110] T. Sasaki, T. Oikawa, T. Suzuki, M. Shiraishi, Y. Suzuki, and K. Noguchi, *Appl. Phys. Express* **96**, 122101 (2010), ISSN 00036951, <http://dx.doi.org/doi/10.1063/1.3367748>
- [111] T. Suzuki, T. Sasaki, T. Oikawa, M. Shiraishi, Y. Suzuki, and K. Noguchi, *Appl. Phys. Express* **4**, 023003 (2011)
- [112] K.-R. Jeon, B.-C. Min, H.-S. Lee, I.-J. Shin, C.-Y. Park, and S.-C. Shin, *Appl. Phys. Lett.* **97**, 022105 (2010), ISSN 00036951, <http://dx.doi.org/doi/10.1063/1.3454276>
- [113] H. H. Woodbury and W. W. Tyler, *Phys. Rev.* **100**, 659 (Oct 1955)
- [114] T. B. Massalski, *Binary Alloy Phase Diagrams*, Vol. 2 (American Society for Metals, Metals Park, OH, 1990) p. 1964
- [115] T. Ohoyama, *J. Phys. Soc. Jpn.* **16**, 1995 (1961)
- [116] T. Ohoyama, K. Yasukochi, and K. Kanematsu, *J. Phys. Soc. Jpn.* **16**, 352 (1961)
- [117] T. Ohba, N. Watanabe, and Y. Komura, *Acta Crystallographica Section B Structural Science* **B40**, 351 (1984)
- [118] L. Castelliz, *Monatsh. Chem.* **84**, 765 (1953)
- [119] Y. D. Park, A. T. Hanbicki, S. C. Erwin, C. S. Hellberg, J. M. Sullivan, J. E. Mattson, T. F. Ambrose, A. Wilson, G. Spanos, and B. T. Jonker, *Science* **295**, 651 (2002)
- [120] F. D'Orazio, F. Lucari, N. Pinto, L. Morresi, and R. Murri, *Journal of Magnetism and Magnetic Materials* **272-276**, 2006 (2004), <http://www.sciencedirect.com/science/article/B6TJJ-4BHT558-2F/2/02f6666906071770c4df2409f0213dc6>
- [121] N. Pinto, L. Morresi, M. Ficcadenti, R. Murri, F. D'Orazio, F. Lucari, L. Boarino, and G. Amato, *Phys. Rev. B* **72**, 165203 (2005)

- [122] N. Pinto, L. Morresi, R. Murri, F. D’Orazio, F. Lucari, M. Passacantando, and P. Picozzi, *physica status solidi (c)* **1**, 1748 (2004), ISSN 1610-1642, <http://dx.doi.org/10.1002/pssc.200304409>
- [123] S. Picozzi, L. Ottaviano, M. Passacantando, G. Profeta, A. Continenza, F. Priolo, M. Kim, and A. J. Freeman, *Appl. Phys. Lett.* **86**, 062501 (2005), ISSN 00036951, <http://dx.doi.org/doi/10.1063/1.1861127>
- [124] L. Ottaviano, M. Passacantando, A. Verna, R. Gunnella, E. Principi, A. D. Cicco, G. Impellizzeri, and F. Priolo, *Journal of Applied Physics* **100**, 063528 (2006)
- [125] A. Verna, L. Ottaviano, M. Passacantando, S. Santucci, P. Picozzi, F. D’Orazio, F. Lucari, M. De Biase, R. Gunnella, M. Berti, A. Gasparotto, G. Impellizzeri, and F. Priolo, *Phys. Rev. B* **74**, 085204 (Aug 2006), <http://link.aps.org/doi/10.1103/PhysRevB.74.085204>
- [126] L. Ottaviano, M. Passacantando, A. Verna, F. D’Amico, and R. Gunnella, *Appl. Phys. Lett.* **90**, 242105 (2007), ISSN 00036951, <http://dx.doi.org/doi/10.1063/1.2746063>
- [127] R. B. Morgunov, A. I. Dmitriev, and O. L. Kazakova, *Phys. Rev. B* **80**, 085205 (2009)
- [128] L. Ottaviano, A. Continenza, G. Profeta, G. Impellizzeri, A. Irrera, R. Gunnella, and O. Kazakova, *Phys. Rev. B* **83**, 134426 (Apr 2011), <http://link.aps.org/doi/10.1103/PhysRevB.83.134426>
- [129] C. Zeng, Z. Zhang, K. van Benthem, M. F. Chisholm, and H. H. Weitering, *Phys. Rev. Lett.* **100**, 066101 (Feb 2008), <http://link.aps.org/doi/10.1103/PhysRevLett.100.066101>
- [130] S. Yada, S. Sugahara, and M. Tanaka, *Appl. Phys. Lett.* **93**, 193108 (2008), ISSN 00036951, <http://dx.doi.org/doi/10.1063/1.3023070>
- [131] L. Morresi, J. Ayoub, N. Pinto, M. Ficcadenti, R. Murri, A. Ronda, and I. Berbezier, *Mat. Sci. Semicond. Process* **9**, 836 (2006)
- [132] L. Morresi, J. Ayoub, N. Pinto, M. Ficcadenti, R. Murri, A. Ronda, I. Berbezier, F. D’Orazio, and F. Lucari, *Surface Science* **601**, 2632 (2007), ISSN 0039-6028, international Conference on NANO-Structures Self-Assembling, International Conference on NANO-Structures Self-Assembling, <http://www.sciencedirect.com/science/article/pii/S0039602806012490>
- [133] P. D. Padova, J.-P. Ayoub, I. Berbezier, J.-M. Mariot, A. Taleb-Ibrahimi, M. Richter, O. Heckmann, A. Testa, D. Fiorani, B. Olivieri, S. Picozzi, and K. Hricovini, *Surface Science* **601**, 2628 (July 2007)
- [134] C. Bihler, C. Jaeger, T. Vallaitis, M. Gjukic, M. S. Brandt, E. Pippel, J. Woltersdorf, and U. Gösele, *Applied Physics Letters* **88**, 112506 (2006)
- [135] R. T. Lechner, V. Holý, S. Ahlers, D. Bougeard, J. Stangl, A. Trampert, A. Navarro-Quezada, and G. Bauer, *Applied Physics Letters* **95**, 023102 (2009)
- [136] S. Ahlers, D. Bougeard, N. Sircar, G. Abstreiter, A. Trampert, M. Opel, and R. Gross, *Phys. Rev. B* **74**, 214411 (2006)
- [137] S. Zhou, A. Shalimov, K. Potzger, N. M. Jeutter, C. Baetz, M. Helm, J. Fassbender, and H. Schmidt, *Appl. Phys. Lett.* **95**, 192505 (2009)
- [138] D. Bougeard, S. Ahlers, A. Trampert, N. Sircar, and G. Abstreiter, *Phys. Rev. Lett.* **97**, 237202 (2006)

-
- [139] T. Devillers, M. Jamet, A. Barski, V. Poydenot, P. Bayle-Guillevaud, E. Bellet-Amalric, S. Cherifi, and J. Cibert, *Phys. Rev. B* **76**, 205306 (2007)
 - [140] M. Rovezzi, T. Devillers, E. Arras, F. d'Acapito, A. Barski, M. Jamet, and P. Pochet, *Appl. Phys. Lett.* **92**, 242510 (2008), ISSN 00036951, <http://dx.doi.org/doi/10.1063/1.2949077>
 - [141] S. Tardif, V. Favre-Nicolin, F. Lançon, E. Arras, M. Jamet, A. Barski, C. Porret, P. Bayle-Guillevaud, P. Pochet, T. Devillers, and M. Rovezzi, *Phys. Rev. B* **82**, 104101 (Sep 2010), <http://link.aps.org/doi/10.1103/PhysRevB.82.104101>
 - [142] S. Tardif, S. Cherifi, M. Jamet, T. Devillers, A. Barski, D. Schmitz, N. Darowski, P. Thakur, J. C. Cezar, N. B. Brookes, R. Mattana, and J. Cibert, *Appl. Phys. Lett.* **97**, 062501 (2010), ISSN 00036951, <http://dx.doi.org/doi/10.1063/1.3476343>
 - [143] I.-S. Yu, M. Jamet, T. Devillers, A. Barski, P. Bayle-Guillevaud, C. Beigné, J. Rothman, V. Baltz, and J. Cibert, *Phys. Rev. B* **82**, 035308 (Jul 2010), <http://link.aps.org/doi/10.1103/PhysRevB.82.035308>
 - [144] A. Jain, M. Jamet, A. Barski, T. Devillers, C. Porret, P. Bayle-Guillevaud, S. Gambarelli, V. Maurel, and G. Desfonds, *Appl. Phys. Lett.* **97**, 202502 (2010), ISSN 00036951, <http://dx.doi.org/doi/10.1063/1.3505501>
 - [145] A. P. Li, C. Zeng, K. van Benthem, M. F. Chisholm, J. Shen, S. V. S. Nageswara Rao, S. K. Dixit, L. C. Feldman, A. G. Petukhov, M. Foygel, and H. H. Weitering, *Phys. Rev. B* **75**, 201201 (2007)
 - [146] F. Xiu, Y. Wang, K. Wong, Y. Zhou, X. Kou, J. Zou, and K. L. Wang, *Nanotechnology* **21**, 255602 (2010)
 - [147] F. Xiu, YongWang, J. Kim, A. Hong, J. Tang, A. P. Jacob, J. Zou, and K. L. Wang., *Nat Mater* **9**, 337344 (April 2010)
 - [148] O. Kazakova, J. S. Kulkarni, J. D. Holmes, and S. O. Demokritov, *Phys. Rev. B* **72**, 094415 (Sep 2005), <http://link.aps.org/doi/10.1103/PhysRevB.72.094415>
 - [149] J. X. Deng, Y. F. Tian, S. M. He, H. L. Bai, T. S. Xu, S. S. Yan, Y. Y. Dai, Y. X. Chen, G. L. Liu, and L. M. Mei, *Applied Physics Letters* **95**, 062513 (2009)
 - [150] R. Morgunov, M. Farle, M. Passacantando, L. Ottaviano, and O. Kazakova, *Phys. Rev. B* **78**, 045206 (2008)
 - [151] J. Smit and H. Beljers, *Phillips Res. Rep.* **10**, 113 (1955)
 - [152] H. Suhl, *Phys. Rev.* **97**, 555 (1955)
 - [153] M. Farle, *Reports on Progress in Physics* **61**, 755 (1998)
 - [154] M. Jamet, W. Wernsdorfer, C. Thirion, D. Mailly, V. Dupuis, P. Mélinon, and A. Pérez, *Phys. Rev. Lett.* **86**, 4676 (2001)
 - [155] W. Cai and J. Wan, *Journal of Colloid And Interface Science* **305**, 366 (2007)
 - [156] R. Quigg, G. Conard, and J.F.Libsch, *Journal of Metals* **7**, 359 (1955)
 - [157] Y. Tawara and K. Sato, *J. Phys. Soc. Jpn.* **18**, 773 (1963)
 - [158] V. Zwicker, E. Jahn, and K. Schubert, *Zeitschrift fr Metallkunde* **40**, 433 (1949)

- [159] G. Kappel, G. Fischer, and A. Jaegle, *Physics Letters A* **45**, 267 (1973), <http://www.sciencedirect.com/science/article/B6TVM-46S5J3F-2TW/2/dc87387f2080cf7faa2a5c7be7d7f461>
- [160] J. B. Forsyth and P. J. Brown, *J. Phys.: Condens. Matter* **2**, 2713 (1990)
- [161] C. Zeng, S. C. Erwin, L. C. Feldman, A. P. Li, R. Jin, Y. Song, J. R. Thompson, and H. H. Weitering, *Appl. Phys. Lett.* **83**, 5002 (2003)
- [162] Y. S. Dedkov, M. Holder, G. Mayer, M. Fonin, and A. B. Preobrajenski, *Journal of Applied Physics* **105**, 073909 (2009)
- [163] L. Sangaletti, D. Ghidoni, S. Pagliara, A. Goldoni, A. Morgante, L. Floreano, A. Cossaro, M. C. Mozzati, and C. B. Azzoni, *Phys. Rev. B* **72**, 035434 (2005)
- [164] R. Gunnella, L. Morresi, N. Pinto, R. Murri, L. Ottaviano, M. Passacantando, F. D'Orazio, and F. Lucari, *Surface Science* **577**, 22 (2005), ISSN 0039-6028
- [165] C. Zeng, W. Zhu, S. C. Erwin, Z. Zhang, and H. H. Weitering, *Phys. Rev. B* **70**, 205340 (2004)
- [166] S. Olive-Mendez, A. Spiesser, L. Michez, V. L. Thanh, A. Glachant, J. Derrien, T. Devillers, A. Barski, and M. Jamet, *Thin Solid Films* **517**, 191 (2008), ISSN 0040-6090
- [167] A. Spiesser, S. Olive-Mendez, M.-T. Dau, L. Michez, A. Watanabe, V. L. Thanh, A. Glachant, J. Derrien, A. Barski, and M. Jamet, *Thin Solid Films* **518**, S113 (2010), ISSN 0040-6090
- [168] G. Srivastava, *Reports of Progress in Physics* **60**, 561 (may 1997), <http://adsabs.harvard.edu/abs/1997RPPh...60..561S>
- [169] N. Alameleh and B. Goldstein, *Phys. Rev.* **128**, 1568 (1962)
- [170] *Introduction to the theory of ferromagnetism*, edited by J. Birman, S. Edwards, R. Friend, C. L. Smith, M. Rees, D. Sherrington, and G. Veneziano (The International Series of Monographs on Physics (Oxford Science Publications, Oxford), 1996)
- [171] V. Holý, R. T. Lechner, S. Ahlers, L. Horák, T. H. Metzger, A. Navarro-Quezada, A. Trampert, D. Bougeard, and G. Bauer, *Phys. Rev. B* **78**, 144401 (2008)
- [172] T. C. Schulthess and W. H. Butler, *J. Appl. Phys.* **89**, 7021 (2001)
- [173] S. Sugahara, K. L. Lee, S. Yada, and M. Tanaka, *Jpn. J. Appl. Phys.* **44**, L1426 (2005)
- [174] A. Stroppa, S. Picozzi, A. Continenza, and A. J. Freeman, *Phys. Rev. B* **68**, 155203 (2003)
- [175] *Magnetic Heterostructures*, edited by H. Zabel and S. Bader (Springer Tracts in Modern Physics, Vol. 227, 2008) <http://www.springer.com/materials/book/978-3-540-73461-1>

Abstract

Creation of spin polarization in non-magnetic semiconductors is one of the prerequisite for creation of spintronics based semiconductor devices. Germanium is interesting for spintronics applications due to its high carrier mobilities and its inversion symmetry that gives long spin lifetimes.

In this manuscript, we discuss two approaches for electrical spin injection and detection in Germanium. The first approach is to use a tunnel barrier and a ferromagnetic metal as a spin injector. The tunnel barrier at the interface circumvents the conductivity mismatch problem. Two different spin injectors are used: Py/Al₂O₃ and CoFeB/MgO. The measurements are performed in three-terminal geometry and the proof of spin accumulation is given by Hanle measurements. In case of Al₂O₃, the spin accumulation is predicted to be in localized states at the oxide/Ge interface and the spin signal is observed up to 220 K. However in MgO based devices, true injection in Ge channel is predicted and spin signal of 20-30 μ V is observed at room temperature.

The second approach of using ferromagnetic semiconductor (Ge,Mn) as spin injector is also discussed. The structural and magnetic properties of (Ge,Mn) thin-films grown by low-temperature molecular beam epitaxy (LT-MBE) are studied. Depending on the growth parameters, crystalline/amorphous GeMn nanocolumns and Ge₃Mn₅ thin films or nanoclusters have been observed. Magnetic anisotropy in these nanostructures is also studied. Finally, the growth of (Ge,Mn) films on GOI substrates is shown and different ways to use (Ge,Mn) as a spin injector in Ge are discussed to achieve all-semiconductor based spintronics devices.

Résumé

Le développement de nouveaux dispositifs spintroniques base de semi-conducteurs (SC) nécessite la cration d'une population électronique polarisée en spin dans ces matériaux. De ce point de vue, le germanium est un matériau prometteur pour les applications en spintronique à cause de la forte mobilit des porteurs de charge ainsi que de la symétrie d'inversion du cristal diamant à l'origine de temps de vie de spin très longs.

Dans ce manuscrit, nous discutons deux approches pour l'injection et la dtction électrique de spins dans le germanium. La première approche consiste à utiliser une barrière tunnel et un mtal ferromagnétique (FM) comme injecteur de spin. L'insertion d'une barrière tunnel à l'interface FM/SC permet de résoudre le problème fondamental du désaccord de conductivité. Nous avons utilisé deux injecteurs différents : Py/Al₂O₃ et CoFeB/MgO. Les mesures sont réalisées en géométrie à trois contacts et l'accumulation de spins dans le germanium est démontrée par la mesure de l'effet Hanle. Dans le cas d'une barrière d'Al₂O₃, les spins injectés s'accumulent sur des états localisés à l'interface oxyde/Ge et cette accumulation est observée jusqu'à 220 K. Dans le cas d'une barrière de MgO, les spins sont réellement injectés dans le canal de Ge et un signal de 20-30 μ V est encore observé à température ambiante.

Nous discutons dans la deuxième approche l'utilisation du semi-conducteur magnétique (Ge,Mn) comme injecteur de spins dans le Ge. Nous avons tout d'abord étudié les propriétés structurales et magnétiques de films minces de (Ge,Mn) fabriqués par épitaxie par jets moléculaires à basse température. En faisant varier les paramètres de croissance, nous avons pu observer des nanocolonnes de GeMn cristallines ou amorphes, ainsi que des films et des nanoparticules de Ge₃Mn₅. Nous nous sommes concentrés sur l'anisotropie magnétique de ces nanostructures. Finalement, la croissance de (Ge,Mn) sur GOI a été optimisée en vue de son utilisation comme injecteur de spins dans le germanium et différentes méthodes d'intégration de ce matriau dans les dispositifs de spintronique 'tout semi-conducteur' sont discutées.